

Electron Probe Analysis  
Society of America

**PROCEEDINGS**  
**SEVENTH NATIONAL CONFERENCE**  
**ON**  
**ELECTRON PROBE ANALYSIS**



San Francisco, California

July 17-21, 1972

Additional copies of these Proceedings and for previous  
conferences may be obtained for \$6.00 per copy plus  
postage, prepaid, from:

Dr. L. Vassamillet  
Carnegie-Mellon University  
4400 Fifth Avenue  
Pittsburgh, Pennsylvania, 15213

Make checks payable to EPASA. Payment must accompany  
order, we will not invoice.

R.L. Myklebust

**SEVENTH NATIONAL CONFERENCE ON ELECTRON PROBE ANALYSIS**

**PRESENTED BY**

**THE ELECTRON PROBE ANALYSIS SOCIETY OF AMERICA**

**JULY 17 - 21, 1972**

**SAN FRANCISCO HILTON  
SAN FRANCISCO, CALIFORNIA**

## **PREFACE**

The Seventh National Conference on Electron Probe Analysis has been expanded to a full five days to provide the most comprehensive meeting held to date. The factors behind the expansion are simple. First, the highly successful tutorial session initiated last year by the Sixth National Conference Committee is not only being held again, but is being expanded to include individual workshop sessions. Second, based upon advice from the executive council, one day is being devoted to scanning electron microscopy. Last, but not least, the large number of invited papers reflect the expanding scope of the meeting, as well as of the Society.

No conference can succeed without the aid of a large number of people. The help and assistance of the Northern California Microprobe Users Group, the hosting EPASA affiliate, is greatly appreciated. The willingness and dedication of individuals such as Dave Kyser - vice chairman, Ralph Gutmacher - arrangements, Gordon Cleaver - printing and publicity, and Herman Rosenbaum, Ted Lannin - program, can never be fully appreciated or realized. A special thanks to the employers of all the individuals who have contributed to the Conference for allowing these people to participate.

The companies who are exhibitors at the Conference have once again shown their faith in the Society by signing up in greater numbers than ever before. Needless to say, the success of each conference depends greatly on their participation.

On behalf of the Seventh National Conference Committee and the National Society, I would like to extend our thanks to the authors of the papers to be given at this Conference. Further expansion of the Society depends upon its members. We sincerely hope that the papers given at this Conference provide the stimulation to meet this end.

Robert Ruscica  
General Chairman



**THE ELECTRON PROBE ANALYSIS SOCIETY OF AMERICA**

**NATIONAL OFFICERS - 1972**

**PRESIDENT**

K. Keil  
University of New Mexico

**PRESIDENT-ELECT**

D. R. Beaman  
Dow Chemical Company

**SECRETARY**

J. W. Colby  
Bell Telephone Laboratories

**TREASURER**

D. B. Brown  
U. S. Naval Research Laboratory

**MEMBERS AT LARGE**

J. B. Woodhouse  
University of Illinois

D. B. Wittry  
University of Southern California

J. I. Goldstein  
Lehigh University

## SEVENTH NATIONAL CONFERENCE COMMITTEE MEMBERSHIP

General Chairman	R. J. Ruscica	Materials Analysis Company
Vice Chairman	D. F. Kyser	IBM Research Division
Program	H. S. Rosenbaum T. E. Lannin A. J. Saffir	G.E. Vallecitos Nuclear Center G.E. Vallecitos Nuclear Center University of the Pacific
Arrangements	R. G. Gutmacher	Lawrence Livermore Laboratory
Secretary	R. Meisenheimer	Lawrence Livermore Laboratory
Treasurer	H. R. MacQueen Mrs. G. Cleaver	IBM Research Division
Exhibits	H. F. Harnsberger	Chevron Research Company
Printing & Publicity	G. Cleaver	G.E. Vallecitos Nuclear Center
Registration	W. Traber M. Mitchell	IBM Systems Development Division Stanford University
Photographic Exhibit	W. Estill	Sandia Laboratory
Ladies Program	Mrs. R. Ruscica	

## INVITED SPEAKERS

W. C. Nixon  
Cambridge University  
Cambridge, England

L. L. Marton  
Smithsonian Institution  
Washington, D. C.

B. L. Henke  
University of Hawaii  
Honolulu, Hawaii

T. E. Everhart  
University of California  
Berkeley, California

O. C. Wells  
IBM Corporation  
Yorktown Heights, New York

E. D. Wolf  
Hughes Research Laboratory  
Malibu, California

G. Judd  
Rensselaer Polytechnic Institute  
Troy, New York

T. Hall  
Cavendish Laboratory  
Cambridge, England

K. Keil  
University of New Mexico  
Albuquerque, New Mexico

**ELECTRON PROBE ANALYSIS SOCIETY OF AMERICA**

**SUSTAINING MEMBERS**

**1972**

**AMR CORPORATION**  
Burlington, Massachusetts

**APPLIED RESEARCH LABORATORIES**  
Sunland, California

**CAMECA INSTRUMENTS INC.**  
Elmsford, New York

**CANBERRA INDUSTRIES, INC.**  
Meriden, Connecticut

**COATES AND WELTER INSTRUMENT CORPORATION**  
Sunnyvale, California

**CORNING GLASS WORKS**  
Corning, New York

**CPS, INC.**  
Sunnyvale, California

**ETEC CORPORATION**  
Hayward, California

**HI-REL LABORATORIES**  
San Marino, California

**ELECTRON PROBE ANALYSIS SOCIETY OF AMERICA**

**SUSTAINING MEMBERS**

**1972**

**JEOL USA INCORPORATED**  
Medford, Massachusetts

**KENT CAMBRIDGE SCIENTIFIC INC.**  
Morton Grove, Illinois

**KEVEX CORPORATION**  
Burlingame, California

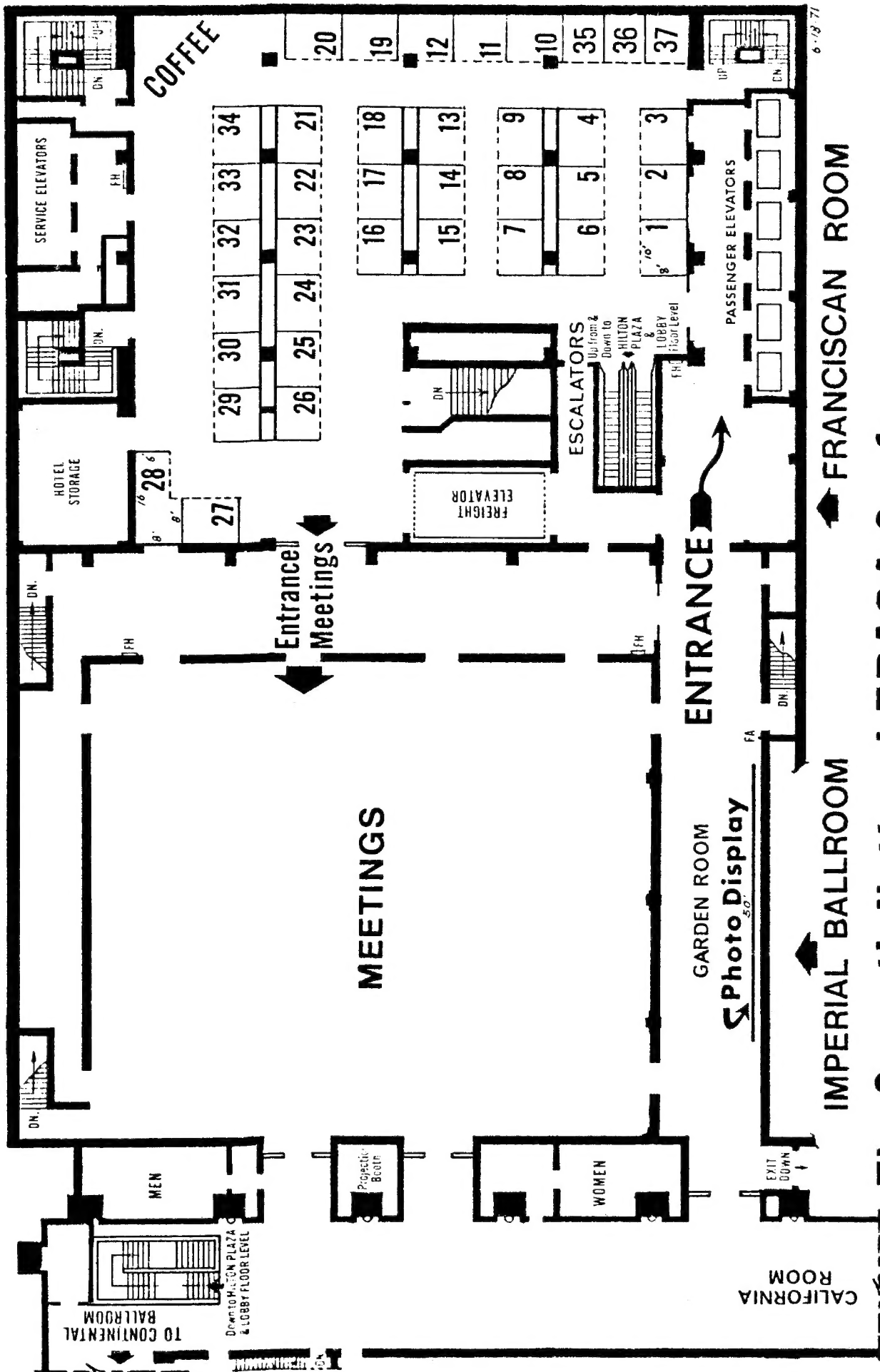
**McCRONE ASSOCIATES**  
Chicago, Illinois

**NUCLEAR DATA, INC.**  
Palatine, Illinois

**EDAX INTERNATIONAL**  
Prairie View, Illinois

**ORTEC INC.**  
Oak Ridge, Tennessee

**ULTRASCAN COMPANY**  
Cleveland, Ohio



# The Seventh National EPASA Conference

JULY 17-21, 1972

**SAN FRANCISCO HILTON Hotel ★ SAN FRANCISCO**

**Ballroom Floor Level**

## EXHIBITORS AND BOOTH ASSIGNMENTS

COMPANY NAME	ADDRESS	BOOTH LOCATION
Advanced Metals Research Corp.	Burlington, Massachusetts	19-20
Applied Research Laboratories	Sunland, California	1-6
Biodynamics Research Corporation	Rockville, Maryland	7
Cameca Instruments, Inc.	Elmsford, New York	14-15
Canberra Industries	Meriden, Connecticut	37
Coates & Welter Instrument Corp.	Sunnyvale, California	10-12
CPS, Inc.	Sunnyvale, California	27
Denton Vacuum, Inc.	Cherry Hill, New Jersey	32
EDAX International	Prairie View, Illinois	16
Ernest F. Fullam, Inc.	Schenectady, New York	21
Etec Corporation	Hayward, California	29-31
JEOL U.S.A., Inc.	Medford, Massachusetts	35-36
Kent Cambridge Scientific	Morton Grove, Illinois	26
KeveX Corporation	Burlingame, California	33
Materials Analysis Company	Palo Alto, California	24-25
Nuclear Data, Inc.	Palatine, Illinois	34
Nuclear Equipment Company	San Carlos, California	28
Nuclear Semiconductor	Menlo Park, California	18
Princeton Gamma - Tech Inc.	Princeton, New Jersey	17
Qanta/Metrix	San Carlos, California	13
3M Company	St. Paul, Minnesota	8-9

## **MEETING ANNOUNCEMENT**

### **EIGHTH NATIONAL CONFERENCE ON ELECTRON PROBE ANALYSIS**

This meeting will be held at the Jung Hotel in New Orleans, Louisiana (USA); August 13-17, 1973.

This meeting will be a joint meeting of the Electron Microscope Society of America and the Electron Probe Analysis Society of America. Attendance at the meeting is estimated between 1000 and 1500.

For general information pertaining to this meeting contact:

Paul Lublin  
GTE Laboratories Inc.  
Waltham, Massachusetts

The topics of the technical sessions will include:

Electron Microprobe X-Ray Analysis, Techniques and Instrumentation. Principles of Electron Scattering and X-Ray Generation, Quantitative Correction Procedures, Soft X-Ray Emission, Computer Control and Data Reduction, Energy Dispersion Analysis, Ion Microprobe Analysis, Scanning Electron Microscopy, New Methods and Instrumentation in Micro-Analysis, and Applications.

Contributed papers will be considered and a "call for papers" will be issued through direct mailing and meeting announcements six or eight months in advance of the meeting. The deadline for papers will be April 1, 1973. Everyone is invited to contribute papers. Abstracts must be submitted in English and sent to:

Arnold Hakkila  
P.O. Box 1663  
Los Alamos, New Mexico 87544

Exhibitors should contact:

Fred G. Kettlekamp  
Professional Associates  
6710 Clayton Road  
St. Louis, Missouri 63117



## **STUDENT AWARD PAPERS**

### **JEOLCO AWARD**

K. Y. Chiu - Abstract # 14  
University of Southern California

### **EPASA AWARDS**

B. J. Panessa - Abstract #20  
New York University

H. C. Marciniak - Abstract #27  
University of Southern California

R. R. Warner - Abstract #41  
University of Rochester

T. E. Keller - Abstract #80  
Case Western Reserve University

## PROGRAM

### SEVENTH NATIONAL CONFERENCE ON ELECTRON PROBE ANALYSIS

---

MONDAY JULY 17, 1972

#### TUTORIAL SESSION

Imperial Ballroom

T. E. Lannin, H. S. Rosenbaum, Co-Chairmen

- |         |  |
|---------|--|
| 8:00 AM | Registration - West Lounge   |
| 10:00   | Introductory Remarks by D. R. Beaman, President-Elect EPASA  |
| 10:10   | "The Generation and Detection of X-Rays in the Electron Microprobe and Scanning Electron Microscope"; Eric Lifshin - General Electric Company.             |
| 10:50   | "Data Collection and Reduction. (a) MAGIC IV Computer Program, (b) Resolution Enhancement of Spectral Emission"; John Colby - Bell Telephone Laboratories. |
| 11:30   | Lunch  |
| 1:30 PM | "Applications of Soft X-Ray Analysis"; Eugene White - Pennsylvania State University.   |
| 2:10    | "Techniques for Electron Probe Analysis of Biological Samples"; James Coleman - University of Rochester-Medical Center.                                    |
| 3:00    | Workshop at conclusion of Session  |
| 7:00    | Executive Council Meeting - Toyon Suite  |
- 

TUESDAY JULY 18, 1972

#### SESSION I - KEYNOTE

Imperial Ballroom

David B. Wittry, Chairman

- |   |         |  |
|---|---------|--|
|   | 9:00 AM | Introduction by EPASA Officers   |
| 1 | 9:15    | INVITED PAPER: "The Use of Electron Beams for Characterizing or Understanding Materials"; L. Marton - Smithsonian Institution.                               |
| 2 | 9:40    | INVITED PAPER: "Characterization of Material Surfaces by Scanning Electron Microscopy"; W. C. Nixon - Engineering Department, Cambridge University, England. |

	10:30	Intermission
3	10:50	"The Correction for Absorption of Primary X-Rays"; K. F. J. Heinrich, H. Yakowitz, and D. L. Vieth - National Bureau of Standards.
4	11:05	"The Effect of the Mean Depth of X-Ray Production on the Continuum Fluorescence"; G. Springer - Falconbridge Metallurgical Laboratories.
5	11:20	"A Comparison of $\varphi(\rho z)$ Curves Measured on Instruments of Different Geometries"; J. D. Brown and L. Parobek - University of Western Ontario.
6	11:35	"Practicality of Monte Carlo Technique to Quantitative Microanalysis in Inclined Target"; R. Shimizu, K. Murata, N. Nishigori, N. Fujino, and T. Shirawa - Osaka University, Suita, Osaka, Japan.
7	11:50	"The Solid Solubility of Gd, Tb, Dy, Ho, Er and Yb in Mg: Systems with a Large Atomic Number Correction"; D. R. Beaman, L. F. Solosky, D. Mizer and B. C. Peters - Dow Chemical Company.
	12:05	"Analysis of Light Elements"; I. B. Borovskii - Baikov Institute of Metallurgy, Moscow (Tentative).
	12:20	END SESSION - Vendor and Photo Exhibits Open

---

TUESDAY JULY 18, 1972

## SESSION II - SOFT X-RAYS AND ELECTRON SPECTROSCOPY

Imperial Ballroom  
Eugene W. White, Chairman

8	2:00 PM	INVITED PAPER: "The Measurement of Low Energy Electron and X-Ray Interaction Coefficients for Solids"; B. L. Henke - University of Hawaii.
9	2:45	"Elucidation of the Damage Mechanism of Synthetic Sodalites by ESCA"; J. S. Brinen - American Cyanamid and L. A. Wilson - Varian Associates.
10	3:00	"New Absorption Correction for Soft X-Rays in Quantitative Electron Probe Microanalysis"; D. F. Kyser and H. R. MacQueen - IBM Research Laboratory, San Jose.
	3:15	Intermission

- |    |       |  |
|----|-------|--|
| 11 | 3:35  | "Some Examples of Materials Characterization by Soft X-Ray Electron Microprobe Analysis"; James S. Solomon - University of Dayton Research Institute and William L. Baun - Air Force Materials Laboratory (WPAFB). |
| 12 | 3:50  | "Characterization of Surface and Interfacial Oxide Films by Soft X-Ray Spectroscopy"; Charles G. Dodd - Phillip Morris Research Center.  |
| 13 | 4:05  | "Use of Bremsstrahlung and Characteristic X-Ray Spectra to Study the Surface Potential Produced on Insulators"; W. B. Estill, S. Gair, and J. L. Wirth - Sandia Laboratories.                                      |
| 14 | 4:20  | "An Electron Spectrometer for Quantitative Measurements of Surface Voltages with Electron Microprobe Instruments"; K. Y. Chiu and D. B. Wittry - University of Southern California.                                |
|    | 4:35  | END SESSION  |
|    | 7:00  | AEC Probe User's Meeting - Toyon Suites A and B  |
|    | 10:00 | END SESSION  |
- 

WEDNESDAY JULY 19, 1972

### SESSION III - SCANNING ELECTRON MICROSCOPY

Imperial Ballroom  
P. R. Thornton, Chairman

- |    |         |  |
|----|---------|--|
| 15 | 8:30 AM | INVITED PAPER: "Limits of Resolution in Electron Probe Instruments"; T. E. Everhart and J. C. Wiesner - University of California (Berkeley).                                   |
| 16 | 9:15    | INVITED PAPER: "Low Loss Image Formation in the Surface SEM"; Oliver C. Wells - IBM Research Center, New York.   |
| 17 | 9:45    | "On the Conditions Necessary to Observe Crystalline Defects in the Scanning Electron Microscope Using Back Scattered Electrons"; D. R. Clarke - Cavendish Laboratory, England. |
|    | 10:05   | Intermission   |
| 18 | 10:25   | "Anomalous Contrast Effects Encountered in SEM Studies of Cubic Boron Nitride"; E. Lifshin and R. C. DeVries - General Electric Company, Schenectady.                          |

- |    |       |  |
|----|-------|--|
| 19 | 10:40 | "Scanning Electron Microscope Collection of Secondary Electrons Using a Small Aperture Probe"; R. K. Matta and G. L. Kusic - University of Pittsburgh.                                 |
| 20 | 10:55 | "SEM Comparison of the Intracellular Ultrastructure of Botanical Specimens Prepared by Metal Coating and a New Technique for Surface Conduction"; B. J. Panessa - New York University. |
| 21 | 11:10 | "Enzyme Etching in Scanning Electron Microscopy"; R. Lin and P. Lublin - GTE Laboratories Incorporated.  |
| 22 | 11:25 | "Changes in Morphology of Polymers as a Result of Gamma Irradiation: Low Density Bulk Polyethylene"; T. Besmann and R. Greer - Iowa State University.                                  |
| 23 | 11:40 | "Electron Microscopy in the Education and Training of Allied Medical Members of the Clinical Laboratory Team"; William R. Bishop - American Medical Association.                       |
|    | 11:55 | END SESSION  |
|    | 12:00 | Invited Speakers and Session Chairmen Luncheon - Continental Ballroom #1.  |
- 

WEDNESDAY JULY 19, 1972

#### SESSION IV - USE OF ELECTRON AND ION BEAMS

Imperial Ballroom  
Noel MacDonald, Chairman

- |    |         |  |
|----|---------|--|
| 24 | 1:30 PM | INVITED PAPER: "Computer-Controlled Electron Beam Microfabrication"; E. D. Wolf - Hughes Research Laboratories.  |
| 25 | 2:15    | "A Charge Storage Memory with Read-Out and Erasure Using YbFeO <sub>3</sub> "; S. J. Ingreby and W. Westwood - Bell Northern Research.                                       |
| 26 | 2:30    | "Voltage Dependent Parameters in Negative Electron Resist Exposure"; R. D. Heidenreich, L. F. Thompson and C. M. Melliar-Smith - Bell Telephone Laboratories.                |
| 27 | 2:45    | "Temperature Dependence of Cathodoluminescence of GaAs, GaP, and GaAs <sub>x</sub> P <sub>1-x</sub> "; H. C. Marciniak and D. B. Wittry - University of Southern California. |
|    | 3:00    | Intermission   |

28	3:20	"Ion Neutralization at Insulator Surfaces"; D. V. McCaughan, R. A. Kushner and V. T. Murphy - Bell Telephone Laboratories.
29	3:35	"Ion Mobilization by Ion Bombardment"; R. A. Kushner, D. V. McCaughan and V. T. Murphy - Bell Telephone Laboratories.
30	3:50	"Surface Composition by Analysis of Neutral Impact Radiation"; C. W. White, D. L. Simms, and N. H. Tolk - Bell Telephone Laboratories.
31	4:05	"Hemispherical Triode: A Device and Technique for Measuring Electron Emission"; A. R. Frederickson - AFCRL-LQR.
	4:20	END SESSION
	4:25	Business Meeting
	4:55	END Business Meeting
	6:00	Hosted Reception - Continental Ballroom #4

---

THURSDAY JULY 20, 1972

# SESSION V - SPECIAL APPLICATIONS AND ION MASS SPECTRA

Imperial Ballroom  
T. E. Lannin, Chairman

32	8:30 AM	INVITED PAPER: "Application of Scanning Electron Microscopy and Electron Probe Microanalysis Techniques to the Forensic Sciences"; G. Judd - Rensselaer Polytechnic Institute.
33	9:15	"Quantitative Analysis of Ultra-Thin Sections: A Model Experiment"; M. I. Corlett and R. S. Thomas - Queen's University, Canada.
34	9:30	"The Ionization Function and Its Application to the Electron Probe Analysis of Thin Films"; Wilhad Reuter - IBM Research Center, New York.
35	9:45	"An Electron Microprobe Study of Gold Films"; R. B. Bolon and E. Lifshin - General Electric Company, Schenectady.
	10:00	Intermission
36	10:20	"The Effect of Take-Off Angle on Particle Analysis With the Electron Microprobe"; J. T. Armstrong, P. R. Buseck and E. F. Holdsworth - Arizona State University.

- |    |       |   |
|----|-------|---|
| 37 | 10:35 | "Ion Microprobe Analysis of Small Particles"; M. A. Bayard - W. C. McCrone Associates, Inc.   |
| 38 | 10:50 | "Secondary Ion Emission and Auger Spectroscopy for the Surface and In-Depth Analysis of Sputtered Tantalum Thin Films"; J. M. Morabito and R. H. Minetti - Bell Telephone Laboratories, R. L. Lewis - Cameca Instruments. |
| 39 | 11:05 | "CARISMA - A Quantitative Correction Procedure for the Ion Microprobe Mass Analyzer"; C. A. Andersen and J. R. Hinthorne - Hasler Research Center.  |
|    | 11:20 | END SESSION   |
- 

THURSDAY JULY 20, 1972

SESSION VI A - BIOLOGICAL APPLICATIONS

Continental Parlors 7, 8, 9  
Arthur Saffir, Chairman

- |    |         |   |
|----|---------|---|
| 40 | 1:00 PM | INVITED PAPER: "Preparation and Examination of Biological Samples"; T. A. Hall - Cavendish Laboratory, England.   |
| 41 | 1:40    | "A Computer Program for Quantitative Microanalysis of Thin Biological Material"; R. R. Warner and J. R. Coleman - University of Rochester.                |
| 42 | 1:55    | "Enzyme Localization in Mouse Intestine by Electron Probe Analysis"; R. B. Lyons, R. Ruscica, A. W. Cook and R. Bundtzen - Arctic Health Research Center. |
| 43 | 2:10    | "Thickness and Mass Thickness Measurements Within Biological Sections"; J. W. Edie and U. L. Karlsson - University of Iowa.                               |
| 44 | 2:25    | "Calcium Transport in the Small Intestine"; R. R. Warner and J. R. Coleman - University of Rochester.   |
|    | 2:40    | Intermission  |
| 45 | 3:00    | "Secondary Ion Microanalysis of Biological Tissues"; A. J. Tousimis - Biodynamics Research Corporation.   |
| 46 | 3:15    | "Trace Metal Analyses of Human Serum with an Electron Probe Micro Analyzer"; P. S. Ong, P. K. Lund and W. M. Conrad - University of Texas.                |

47	3:30	"Electrolytes in Cells of Biologic Tissues"; A. J. Tousimis - Biodynamics Research Corporation.
48	3:45	"Elemental Analysis of Refractile Bodies in <u>Amoeba Proteus</u> "; J. R. Coleman, R. R. Warner and J. R. Nilsson - University of Rochester.
	4:00	END SESSION
	7:00	Banquet - Continental Ballroom, 1 through 5

---

THURSDAY JULY 20, 1972

SESSION VI B - PHYSICAL APPLICATIONS

Imperial Ballroom  
W. D. Donnelly, Chairman

49	1:00 PM	INVITED PAPER: "Application of the Electron Microprobe in Geology"; K. Keil - University of New Mexico.
50	1:35	"Microprobe Analysis of Glasses in Lunar Soils"; R. W. Brown, W. I. Ridley, J. L. Warner and A. M. Reid - NASA Manned Spacecraft Center.
51	1:50	"Intracrystalline Variations of Major and Minor Elements in Lunar Pyroxenes"; A. E. Bence - State University of New York.
52	2:05	"Vapor Phase Crystallization in Lunar Breccias"; D. S. McKay, U. S. Clanton and G. H. Ladle - NASA Houston Space Center.
53	2:20	"Low KeV Analysis of Silicate Minerals Using Pure Element Standards"; G. Cunningham, T. Palmer, K. Snetsinger and M. Blanchard - NASA-Ames Research Center.
54	2:35	"Electron Probe Investigation of Hydrogen-Induced Blisters and Internal Cracks in Iron"; I. M. Bernstein - Carnegie-Mellon University and J. L. Bombard - United States Steel Corporation.
	2:50	Intermission
55	3:10	"Examination of Medium Rank Coals by SEM"; L. F. Vassamillet - Mellon Institute of Science.
56	3:25	"Examination of Low Grade Uranium Ores by Electron Beam Techniques"; G. S. Maurer, L. F. Vassamillet and T. B. Massalski - Oberlin College.



57	3:40	"Electron Microprobe Techniques for Determination of the Oxygen Potential in Irradiated Mixed Oxide Fuels"; C. E. Johnson, C. A. Seils, and M. S. Foster - Argonne National Laboratory.
58	3:55	"Interdiffusion Between Uranium Dioxide and Uranium-Plutonium Dioxide During Irradiation;" E. M. Butler, R. O. Meyer and D. R. O'Boyle - Argonne National Laboratory.
59	4:10	"Microanalysis of Fission Products in Uranium or Uranium-Plutonium Irradiated Oxide Fuels"; J. Bazin, M. Perrot, N. Vignesoult, C. Conty and J. Guernet - Commissariat a l'Energie Atomique.
60	4:25	"Electron Probe Analysis of Corroded Cr-Ni Alloys in Combination with a Light Optical ZnSe Interference Method"; A. P. von Rosentiel - Metaalinstituut TNO, Delft-Nederland and A. G. van Zuilichem - Koninklijke/Shell-Laboratorium, Amsterdam.
61	4:40	"Bonding in Porcelain Enamel-Metal Systems"; J. B. Woodhouse and A. I. Nedeljkovic - University of Illinois.
	4:55	END SESSION
	7:00	Banquet - Continental Ballroom, 1 through 5

---

FRIDAY JULY 21, 1972

## SESSION VII - AUTOMATED AND COMPUTATIONAL TECHNIQUES

Imperial Ballroom  
David Kyser, Chairman

62	8:30 AM	"Location and Identification of Small Particles Within Large Samples"; J. Gavrilovic - Walter C. McCrone Associates, Inc.
63	8:45	"Measurement and Analysis of Scanning Electron Microscope Images"; Roger R. A. Morton - Bausch and Lomb, Inc.
64	9:00	"Quantitation of SEM and Electron Probe Images with the Quantimet 720"; R. A. Swenson, B. C. Partridge and R. H. Heil - Image Analyzing Computers, Inc.
65	9:15	"Electron Microprobe Automation: X-Ray Peak Location"; F. Kunz and E. Eichen - Ford Motor Company.

66	9:30	"An Automated Crystal Spectrometer System for Qualitative Microprobe Analysis"; E. Lifshin - General Electric Company, Schenectady.
67	9:45	"Microprobe Analysis Integrated Automation Computer System"; J. W. Colby - Bell Telephone Laboratories.
	10:00	Intermission
68	10:15	"Computer Automation of an Electron Microprobe"; L. W. Finger and C. Hadidiacos - Carnegie Institution of Washington.
69	10:30	"The Program CYCLOPS for the Quantitative Analysis of Electron Microprobe X-Ray Data"; H. R. Thresh and T. E. Keller - Chase Brass and Copper.
70	10:45	"Improved Deconvolution Technique to Study Electron Microprobe Concentration Profiles"; Z. Mencik - Ford Motor Company.
71	11:00	"Nonparametric Analysis Applied to the SEM and Microprobe Study of Induced-Arc and Resistive Welds"; A. J. Saffir - University of the Pacific and D. I. Zenobia - Precision Metallurgical Company.
72	11:15	"The Effect of Carbon Film Thickness on the Intensity of Selected K $\alpha$ Radiation"; J. F. Villaume, D. M. Kerrick and L. B. Eminhizer - Pennsylvania State University.
73	11:30	"Mirror-Mode Electron Probe Microanalysis"; J. Ordonez and E. K. Brandis - IBM Components Division.
74	11:45	"Microprobe Technique for Determination of Thickness and Phosphorous Concentration of Gate Oxide Phosphosilicate Glass in FET Devices"; Guilio Di Giacomo - IBM Components Division.
	12:00	END SESSION

FRIDAY JULY 21, 1972

SESSION VIII A - ENERGY DISPERSIVE TECHNIQUES AND  
NONCONVENTIONAL APPLICATIONS

Imperial Ballroom  
Gregg F. Melde, Chairman

75	1:30 PM	"Non-Dispersive X-Ray Data Analysis by Computer"; W. G. Miller - Illinois State Geological Survey.
----	---------	--

76	1:45	"Background Subtraction for Energy Dispersive X-Ray Spectra"; J. C. Russ - EDAX Laboratories.
77	2:00	"Mathematical Smoothing of X-Ray Fluorescence Spectra"; M. W. Vannier and L. V. Sutfin - Orthopedic Research Laboratories.
78	2:15	"An Approach to Quantitative SEM Analysis"; H. P. Hotz - Qanta/Metrix.
79	2:30	"Escape Peaks in Si(Li) Detectors"; J. B. Woodhouse - University of Illinois.
80	2:45	"A Method for the Automatic Location and Identification of Peaks Observed in Energy Dispersive X-Ray Spectra"; T. E. Keller and H. R. Thresh - Case Western Reserve University.
81	3:00	"The Rapid Identification of Microconstituent Phases in Commercial Silicon"; A. F. Kolb and D. R. Beaman - Dow Corning Corporation.
82	3:15	"Retrospective Identification - The Analysis of Microspheres"; H. Edward Mishmash - 3M Company.
83	3:30	"NbC Microprobe Reference Materials - An Effort in Development"; F. W. Postma, Jr. and James E. Ferguson - Union Carbide Nuclear Corporation.
	3:45	END SESSION

---

FRIDAY JULY 21, 1972

SESSION VIII B - LATE BREAKING DEVELOPMENTS AND  
SPECIAL INTEREST ITEMS

Continental Parlors 7, 8, 9  
H. R. MacQueen, Chairman

1:30 PM	"New Apparatus for Analysis of Light Elements"; I. B. Borovskii - Baikov Institute of Metallurgy, Moscow (Tentative).
1:45	"Auger Electron Spectroscopy in a Diffusion Pumped SEM"; E. K. Brandis and R. A. Hoover - IBM Components Division.
2:00	"What Good is Microprobe Automation? Result of a Survey of Users"; H. G. Matthews - Canberra Industries.

**2:15**

**OPEN - Consult with Program Chairman in Advance to Arrange Contributions During this Time Interval.**

**Executive Council Meeting - to be announced**

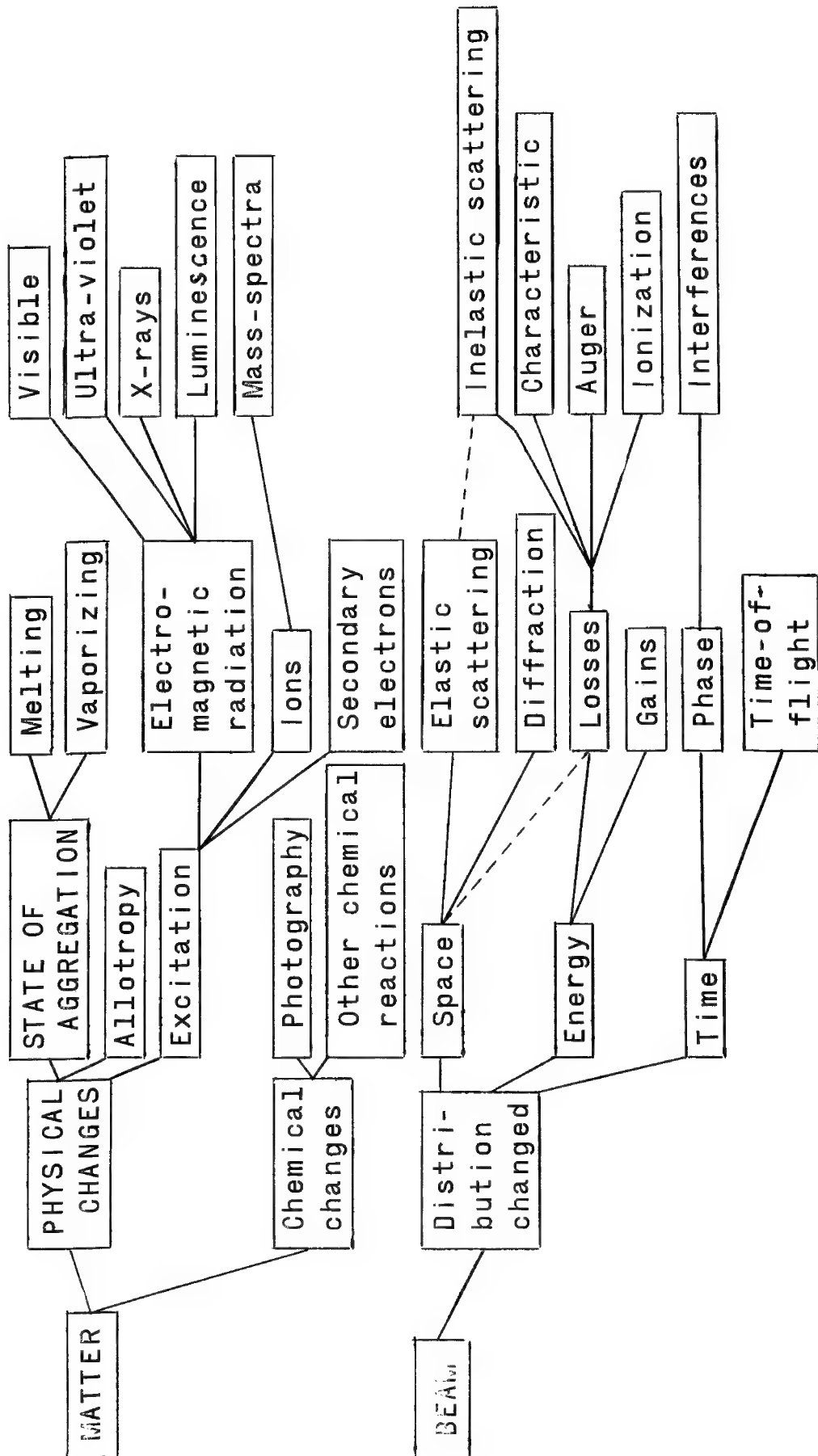
# **Summaries of Papers**



The Use of Electron Beams for Characterizing or Understanding Materials,  
by L. Marton, Smithsonian Institution, Washington, D. C.

When electron beams interact with matter, the interaction results in two classes of observable (measurable) effects. In one group we can look at the product of interaction in or around the substance itself; either changes wrought in the material or products issuing from it; and the conclusions about the material are the results of measuring these changes. In the second class belong all observations where our conclusions are derived from the measured changes in the properties of the interacting beam. The following tabulation gives a rough listing of the major observable changes. This tabulation is by no means complete, there are many cases where two or more effects combine and complete characterization or understanding results from linking together the various effects.

The historical background of representative examples shall be given. It is possible in many cases to trace back the origins of current techniques to very modest beginnings. In the presentation of the historical details the logical order will follow more or less the order given in the tabulation.





## CHARACTERIZATION OF MATERIAL SURFACES BY SCANNING ELECTRON MICROSCOPY

W.C. Nixon  
Engineering Department  
Cambridge University  
England

X-ray Microanalysis

The areas considered to be within the scope of the Seventh National Conference of the Electron Probe Analysis Society of America show the breadth of interest of those members working with scanning electron beams which can produce much wider results than the original electron probe x-ray micro-analysers. Nevertheless, the spread of solid state energy dispersive x-ray detectors as simple attachments to scanning electron microscopes has ensured the central position of x-ray microanalysis in elemental characterization of material surfaces. Improved resolution of solid state detectors has brought most of the periodic table within reach and the large solid angle of collection means rapid point analysis or less noisy x-ray scanning images. When very thin specimens are used analysis of a single surface without the underlying solid is possible with improved spatial resolution. In particular, the solid state detector may be placed on the opposite side of the thin specimen from that first struck by the electron beam so producing the desirable combination of large solid angle of x-ray collection plus very short electron optical focal length.

Cathodoluminescence

Among other forms of signal produced at the specimen surface the electron induced emission of light has been widely used. In this case the elemental sensitivity is sometimes better than for x-rays due to the slight wavelength shift in light output for minute impurities. In addition, the quantity of light emitted by cathodoluminescence may be linked directly to the state of strain of the sample. In this way a cathodoluminescent image may give information about the past history of the specimen without the need for attached strain gauges during the straining process which with mineral samples could have taken place over a geological time scale.

## Contrast

Contrast and resolution are intimately linked in scanning electron microscopy but in many cases high contrast and high resolution do not go together. In particular, if a smooth surface is to be characterized contrast of any kind may be very low. Back scattered or, for shallow angles of impact, forward scattered electrons without energy loss may yield new information. The electrons that have lost some energy may be analysed or the low voltage secondary electrons controlled to show detail on the surface including geometrical features. Various forms of secondary electron detector permit emphasis to be placed on this form of contrast selection which in some ways is analogous to point reference interference or Nomarski optical microscopy. Indeed, at very low magnification it is possible to see some features in the optical microscope that are very difficult to see in the scanning electron microscope unless this type of contrast enhancement is used.

## Signal Processing

The same approach of secondary electron control will also give electrostatic and magnetic contrast from suitable specimens and this type of information is also part of a full characterization of the material surface. Combined images with electronic processing of several channels of video signals can be used to show relationships between electrostatic and elemental information, for example. Signal differentiation, integration, addition, subtraction and other forms of channel mixing are all of value once the basic electron beam interaction has occurred. A further understanding of electron scattering behaviour within the specimen surface is of help in knowing the exact point of origin of x-rays or secondary electrons. The Monte Carlo techniques adapted for use with the largest new computers are giving us a much more detailed insight into electron interaction with the material in question.

## Computer Analysis

Small computers may be used on line to analyse the information produced by scanning electron beam systems to give quantitative stereological information about the surface shapes, areas, perimeters, etc. The third dimension is perhaps even more important and some progress has been made in measuring photogrammetric details from stereographic pairs of micrographs. Recently, direct stereographic viewing has been demonstrated with the possibility of not only seeing the full solid surface without the need for photography but also measuring the third dimension directly by use of the electron optical analogue of the floating dot method in aerial mapping.

## Computer Control

Computer control of the electron beam before it reaches the specimen is now well established for microfabrication within the scanning electron microscope, either by electron resist exposure or direct metallic deposition. The position of the electron beam and the degree of beam blanking may be carried out at a rate of many megahertz. For other applications of scanning electron microscopy this same type of electron beam control may be of value. Computer programming by punched tape or other store permits electron beam exposure only where chosen with instantaneous movement from one part of the field to another. Analysis of a pre chosen electron path is then possible, either to increase the speed of information collection by only tracking the electron beam along a specific grain boundary, for example, or by positive avoidance of parts of a thin and electron sensitive specimen that might be altered by the larger beam currents used for adjacent x-ray analysis.

## Dynamic Events

Dynamic methods of characterizing material surfaces are now more widespread with the universal use of TV scanning and special specimen stages for heating, cooling, stressing, straining, etc. Micromanipulation within the scanning microscope comes into this category where microhardness tests may be made on one micrometer or less of the surface in a calibrated manner. Electrical probing may be combined with electrostatic contrast or biological dissection carried out within the specimen chamber, Ion etching and surface coating are also possible in situ.

## Displays

Newer forms of image display are being investigated such as the halftone storage tubes of the scan convertor type where a full range of grey levels is maintained coupled with a slow scan input for good signal integration and fast TV readout for a flicker free display. Beam switching can give simultaneous display of two different magnifications or an image and its diffraction pattern, for example.

## Crystallography

Crystallographic information from a specimen surface can supply much further information to go with the topographic, elemental and mechanical properties already referred to above. Broad area scanning gives rise to a general crystallographic map of the surface and selected area beam rocking shows the crystal state over the same one micrometer region as analysed by the x-ray emission. Since x-ray production and back scattered primary emission are occurring simultaneously both signals can be collected and displayed at once.

## Electron Optics

All of these characterization methods depend on effective and efficient electron optical instrumentation. Electron sources are still being improved such as thermionic emission from lanthanum hexaboride. This type of electron gun is now of low wattage and is compatible with the normal scanning electron microscope vacuum, yet gives an improvement of a least ten times in beam brightness. This can be used for better operation in TV scanning, low voltage operation, less noise for the same photographic exposure, etc. Field emission sources are more difficult to handle but in some cases can give even higher brightnesses which may mean some improvement in resolution from solids. Electron lenses and deflection systems are also being studied and improved by computational methods using the finite element approach. In this way electron lenses have been designed for specific purposes such as long working distance, high take off angle, low leakage magnetic field at the specimen or very short focal length for transmission.

## Conclusions

The characterization of material surfaces by scanning electron microscopy involves and requires an understanding of the engineering of the instrumentation, the physics of the interaction and the psychology of image interpretation. The bandwidth of the modulation transfer functions of all the links in the communication chain from specimen preparation to final photographic viewing might appear to be impossibly limited if the subject were approached only from a theoretical standpoint. However, we know that apparently noisy x-ray micrographs can yield useful information when taken together with a scanning electron image of the same field. Similarly, restricting the number of lines per field can still produce interpretable information although the number of picture points might be considered too low by theory. By combining experimentation and experience with theory and imagination we can extract the maximum information from our specimen surface within a reasonable time.

## The Correction for Absorption of Primary X-Rays

K. F. J. Heinrich, H. Yakowitz, D. L. Vieth  
National Bureau of Standards, Washington, D. C. 20234

Several analytical expressions (e.g. 1-4) have been proposed for the calculation of the absorption factor for primary radiation ( $f_p, f(\chi)$ ). These equations are derived from approximate, and sometimes unrealistic, physical models; they are all complicated and usually require tabulation and/or machine calculation. As will be shown, such complexity is not warranted by the existing physical evidence or required for quantitative determination at presently attainable accuracy levels.

It is commonly agreed that the absorption factor is dependent on the respective mass absorption coefficient,  $\mu$ , the x-ray emergence angle,  $\psi$ , the operating voltage,  $E_0$ , the critical excitation voltage,  $E_q$ , and the mean atomic weight and mean atomic number of the target,  $A^*$  and  $Z^*$ :

$$f_p = f(\chi \equiv \mu \cdot \csc \psi, E_0, E_q, A^*, Z^*)$$

The Philibert equation [1,2] with an "electron deceleration coefficient",  $\sigma = C/(E_0^n - E_q^n)$ , is frequently used to express this dependence. The equation can be written as follows:

$$1/f_p = a_0 + a_1 \gamma + a_2 \gamma^2; (a_0 = 1, \gamma = (E_0^n - E_q^n) \chi)$$

According to Philibert, and Duncumb and Shields [1,2],

$$a_1 = \frac{1+2h}{(1+h) (2.39 \times 10^5)} \quad (h = 1.2 \frac{A}{Z^2}).$$

$$a_2 = \frac{h}{(1+h) (2.39 \times 10^5)^2}$$

As reported previously [5], it is permissible, without serious consequences, and useful in empirical adjustment, to postulate that  $a_2 \approx 0$ , so that  $1/f_p - 1 \approx a_1 \gamma \approx a_1 (E_0^n - E_q^n) \chi$ .

This approximation permits a convenient analysis of experimental values for  $f_p$ , which are thus characterized by the slope  $d(1/f_p)/d\chi^*$ . The coefficient  $a_2$  can be reintroduced at a later stage, if the absorption loss is large. ( $f_p < 0.7$ ).

The factor  $h$  presumably describes the variation of the absorption law as a function of atomic number and weight. Philibert, as well as other authors [e.g. 3], have used a considerable spread of values for  $h$ . However, the need for an expression for the "atomic number effect on absorption" cannot be proven with the aid of available  $f(\chi)$  curves or by the analysis of standards. The following expression

$$1/f_p = 1 + 3 \times 10^{-6} (E_0^{1.65} - E_q^{1.65}) \chi + 4.5 \times 10^{-14} (E_0^{1.65} - E_q^{1.65})^2 \chi^2$$

which contains no dependence on  $Z^*$  and  $A^*$  appears to be as accurate as the original Philibert equation, with Heinrich's  $\sigma$  [13]. For moderate absorption, the last term can be neglected.

The improvement over Philibert's original equation which is obtained with expressions for  $\sigma$  of the type  $\sigma = C(E_0^n - E_q^n)^{-1}$  is usually attributed to the inclusion of the critical excitation potential  $E_q$ . However, the effect of this inclusion is small except at low over-voltage: where  $E_q$  is larger, the absorption correction is usually small, and vice versa. Therefore, a simple expression of the form:

$$1/f_p = 1 + 3 \times 10^{-6} E_0^{1.65} \chi$$

does not produce serious errors in the absorption calculation. This means that Birk's concept of a universal absorption correction curve for each operating voltage [14] is quite effective provided that the parameters of these curves are well chosen.

Duncumb et al. [2] have shown that the exact value of  $n$  in the expression for  $\sigma$  is not critical if  $n$  is between 1.5 and 2, so long as the appropriate coefficient,  $C$ , is chosen. It is, in fact, difficult to extract much information concerning the value of  $n$  from the available experimental evidence.

We have tested the efficiency of the following simple equation for the absorption factor

$$1/f_p = 1 + 1.15 \times 10^{-6} (E_0^2 - E_q^2) \chi$$

which can be easily calculated by hand. Such a calculation is most useful in establishing appropriate excitation conditions.

The largest deviations from the experimental results occur for short-wave radiation, (such as  $UL\alpha$  or  $MoK\alpha$ ), for which the absorption correction is typically insignificant.

#### References

1. J. Philibert, X-ray Optics and X-ray Microanalysis, (Proc. Third Intern. Symp., Stanford Univ., H. H. Pattee, V. E. Cosslett, and A. Engström, eds.), Academic Press, New York, p.379 (1963).
2. P. Duncumb and P. K. Shields, The Electron Microprobe, (Proc. Symp. Electrochem. Soc., Washington, D. C., 1964, T. D. McKinley, K. F. J. Heinrich and D. B. Wittry, eds.), Wiley & Sons, New York, p.284 (1966).
3. R. Theisen, Quantitative Electron Microprobe Analysis, Springer-Verlag, New York (1965).
4. C. A. Andersen and D. B. Wittry, Brit. J. Appl. Physics, Ser. 2, 1, p.529 (1968).
5. K. F. J. Heinrich, 2nd National Conference EPASA, Paper No. 7, Boston (1967).
6. P. Duncumb, P. K. Shields-Mason, and C. daCasa, Proc. Vth International Congress on X-ray Optics and Microanalysis, G. Möllenstadt and K. H. Gaukler, eds., Springer-Verlag, Berlin, p.146 (1969).
7. R. Castaing & J. Hénoc, X-Ray Optics and Microanalysis, (Proc. Fourth Intern. Symp., Orsay, R. Castaing, P. Deschamps, J. Philibert, eds.), Hermann, Paris, p.120 (1966).
8. K. F. J. Heinrich, R. L. Myklebust, S. D. Rasberry, and R. E. Michaelis, NBS Spec. Publ. 260-28, 89pp (1971).
9. J. Goldstein, F. J. Majeske, and H. Yakowitz, Advances in X-ray Analysis 10, 431 (1967).
10. H. Yakowitz, C. E. Fiori, and R. E. Michaelis, NBS Spec. Publ. 260-22, 22pp. (1971).
11. H. Yakowitz, R. E. Michaelis, and D. L. Vieth, Advances in X-ray Analysis 12, 418 (1969).
12. M. J. Berger and S. M. Seltzer, Nat. Acad. Sci., Nat. Res. Council Publ. 1133, 205 (1964).
13. K. F. J. Heinrich, Anal. Chem. 44, 350 (1972).
14. L. S. Birks, J. Appl. Phys. 32, 387 (1961)

Table I  
Typical Results for Various Binary Alloys  
Using Four Different Expressions for  $f_p$

Alloy	Line Measured	Voltage Relative		I	II	III	IV	$f_p$
		$E_0$ (kv)	Intensity k					
Ag-Au containing 0.3992 Ag*	Ag-L $\alpha$	5	0.466	0.416	0.418	0.428	0.416	0.97
Ag-Au containing 0.3992 Ag*	Ag-L $\alpha$	10	0.385	0.382	0.391	0.398	0.387	0.87
Ag-Au containing 0.3992 Ag*	Ag-L $\alpha$	20	0.310	0.374	0.394	0.394	0.398	0.64
Ag-Au containing 0.3992 Ag*	Ag-L $\alpha$	30	0.250	0.358	0.384	0.376	0.392	0.46
Ag-Au containing 0.3992 Ag*	Ag-L $\alpha$	40	0.207	0.343	0.371	0.356	0.377	0.34
Ag-Au containing 0.3992 Ag*	Ag-L $\alpha$	48.5	0.182	0.334	0.364	0.342	0.364	0.27
Ag-Au containing 0.6005 Au*	Au-M $\alpha$	5	0.584	0.643	0.643	0.643	0.643	0.97
Ag-Au containing 0.6005 Au*	Au-M $\alpha$	10	0.567	0.613	0.614	0.614	0.613	0.88
Ag-Au containing 0.6005 Au*	Au-M $\alpha$	20	0.556	0.599	0.599	0.598	0.599	0.68
Ag-Au containing 0.6005 Au*	Au-L $\alpha$	20	0.573	0.606	0.598	0.606	0.606	0.97
Ag-Au containing 0.6005 Au*	Au-M $\alpha$	30	0.548	0.593	0.592	0.591	0.592	0.51
Ag-Au containing 0.6005 Au*	Au-M $\alpha$	40	0.535	0.583	0.581	0.579	0.581	0.38
Ag-Au containing 0.6005 Au*	Au-M $\alpha$	48.5	0.529	0.580	0.576	0.574	0.575	0.31
Al-Mg containing 0.251 Al <sup>+</sup>	Al-K $\alpha$	10	0.184	0.266	0.274	0.275	0.263	0.67
Al-Mg containing 0.251 Al <sup>+</sup>	Al-K $\alpha$	15	0.140	0.262	0.269	0.266	0.264	0.49
Al-Mg containing 0.251 Al <sup>+</sup>	Al-K $\alpha$	20	0.101	0.247	0.250	0.241	0.249	0.36
Fe-Si containing 0.0322 Si <sup>++</sup>	Si-K $\alpha$	10	0.0281	0.0314	0.0327	0.0331	0.0318	0.76
Fe-Si containing 0.968 Fe <sup>++</sup>	Fe-K $\alpha$	10	0.963	0.969	0.969	0.970	0.969	0.99
W-Mo containing 0.215 Mo**	Mo-L $\alpha$	10	0.212	0.225	0.235	0.239	0.229	0.76
W-Mo containing 0.215 Mo**	Mo-L $\alpha$	15	0.164	0.207	0.222	0.222	0.219	0.60
W-Mo containing 0.215 Mo**	Mo-L $\alpha$	20	0.143	0.209	0.228	0.223	0.228	0.48
W-Mo containing 0.785 W**	W-M $\alpha$	10	0.726	0.761	0.761	0.761	0.761	0.85
W-Mo containing 0.785 W**	W-L $\alpha$	15	0.742	0.772	0.772	0.772	0.771	0.98
W-Mo containing 0.785 W**	W-L $\alpha$	20	0.772	0.795	0.794	0.794	0.794	0.96



- \* See Ref. [8], Specimen Analysis Certified by NBS  
 + See Ref. [9], Specimen Analysis Performed at NBS  
 ++ See Ref. [10], Specimen Analysis Certified by NBS  
 \*\* See Ref. [11], Specimen Analysis Certified by NBS

All concentrations in this table were calculated from program COR. This program uses mass absorption coefficients according to Heinrich, mean ionization potentials according to Berger and Seltzer [12], back-scatter factors according to Duncumb and Reed, and correction for continuous radiation due to Henoc. For further details of COR and specific references, see Ref. [13].

I Absorption correction according to Philibert with  

$$\sigma = 4.5 \times 10^5 / (E_o^{1.65} - E_q^{1.65}) \quad \text{See Ref. [13]}$$

II Absorption correction calculated from  

$$\frac{1}{f_p} = 1 + 3 \times 10^{-6} (E_o^{1.65} - E_q^{1.65})_X + 4.5 \times 10^{-14} (E_o^{1.65} - E_q^{1.65})^2_X^2$$

III Absorption correction calculated from  

$$\frac{1}{f_p} = 1 + 3 \times 10^{-6} E_o^{1.65}_X$$

IV Absorption correction calculated from  

$$\frac{1}{f_p} = 1 + 1.15 \times 10^{-6} (E_o^2 - E_q^2)_X$$

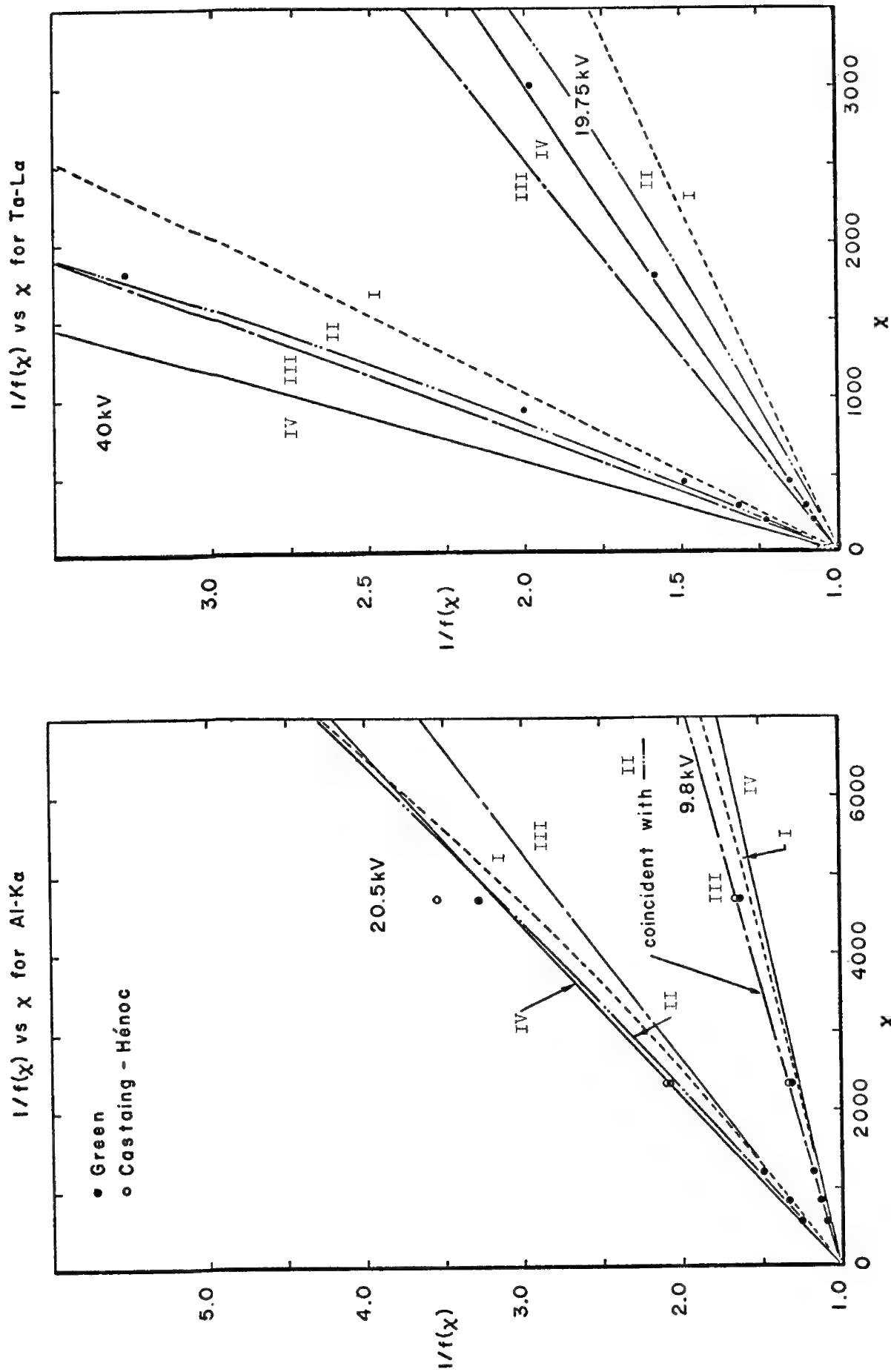


Fig. 1  $f(\chi)$  vs  $\chi$  for Al-K $\alpha$  calculated by the four equations listed in Table I

Fig. 2  $f(\chi)$  vs  $\chi$  for Ta-L $\alpha$  calculated by the four equations listed in Table I

## THE EFFECT OF THE MEAN DEPTH OF X-RAY PRODUCTION ON THE CONTINUUM FLUORESCENCE

G. Springer  
 Falconbridge Metallurgical Laboratories  
 Thornhill, Ontario, Canada

A procedure has been advocated by the author (Springer, 1967) to correct for fluorescence by the X-ray continuum in electron probe analysis. This approach is simpler to apply than a procedure used by Henoc (1962). Objections have been raised against some of the assumptions that lead to the simplifications and these will be dealt with in this context.

Henoc assumed that the continuous X-radiation arises from a point at the surface of the sample whilst in the author's approach the origin was considered to be at the same depth as the characteristic radiation. This latter assumption leads to the cancellation of an absorption term and by further ignoring the continuum fluorescence in the part of the target between the mean depth of primary X-ray production and the surface, a substantially simplified expression for the correction of the continuum fluorescence can be derived.

Obviously neither Henoc's nor the author's approach are entirely correct. But, as will be shown, the assumptions adopted by the author do not entail serious inaccuracies. Mathematical treatment of the problem reveals that a minor fraction of the measured characteristic X-ray intensity produced by continuum fluorescence comes from the surface layer of the target. Since the total continuum fluorescence correction hardly ever exceeds 5%, this fraction is generally within the limits of experimental error and can be neglected, which is very convenient because the surface portion of the fluorescence intensity is very difficult to compute.

The other objection that will be dealt with briefly concerns the choice of the method to calculate the directly produced X-ray intensity; knowledge of this quantity is required for the evaluation of the continuum fluorescence correction. It will be shown that it is not necessary to introduce elaborate functions for electron back scattering and electron deceleration, since these effects are unimportant in this connection.

The differences caused by the various degrees of approximation will be demonstrated for several elements. Furthermore, the calculated values will be compared with measurements published in the literature. It appears from the results that the originally proposed formula (Springer, 1967 and 1971) is adequate for most practical applications.

1. Henoc, J. (1962): Etude No. 655, P.C.M., Issy-les-Moulineaux, France.
2. Springer, G. (1967): Neues Jahrbuch f. Mineralogie, Abhandlungen, 106, 241-256.
3. Springer, G. (1971): Proc. VI. International Congress on X-ray Optics and X-ray Microanalysis, Osaka, Japan.

A COMPARISON OF  $\phi(\rho z)$  CURVES MEASURED ON INSTRUMENTS  
OF DIFFERENT GEOMETRIES

by

J.D. Brown and L. Parobek  
Faculty of Engineering Science  
The University of Western Ontario  
London Canada

The measurement of  $\phi(\rho z)$  curves provides primary experimental data for calculating the corrections to be applied to x-ray intensity data to obtain quantitative electron probe microanalysis. These curves can be measured using a sandwich sample technique first described by Castaing and Descamps.<sup>1</sup> The technique has been used by other authors to establish the absorption correction,<sup>2,3</sup> the correction for fluorescence by characteristic lines,<sup>4</sup> and the atomic number correction.<sup>5</sup> Few measurements have been made on probes with different geometries to establish the effect of geometry on these  $\phi(\rho z)$  curves and hence the quantitative corrections in electron probe microanalysis. Castaing measured his  $\phi(\rho z)$  curves in an instrument in which the electron beam was inclined at an angle of 80° with respect to the sample surface. Brown<sup>4</sup> has described some measurements in which the electron beam was inclined at an angle of 60° to the sample and others have measured the  $\phi(\rho z)$  curves with the incident electron beam normal to the sample surface.

Using the same set of samples which originally were prepared to examine the atomic number effect, the  $\phi(\rho z)$  curves were measured in three different instruments: a Cambridge Microscan in which the electron beam is normal to the sample surface and the x-ray take-off angle is 75°; an Applied Research Laboratories Microprobe\* in which the electron beam is again normal to the sample surface but the x-ray take-off angle is 52½°; and finally, in a Materials Analysis Co. Microprobe in which the normal to the sample surface is inclined at an angle of 30° with the electron beam and the x-ray take-off angle 38.5°.

---

\* Measurements in the ARL Microprobe were made through the courtesy of the Industrial Laboratory, Eastman Kodak Co., Rochester, N.Y.

Figure 1 shows a comparison of the depth distribution measured on the Microscan and ARL microprobes. Corrections have been made for absorption in the sample and the excellent agreement between the sets of data is a good indication that, first, the thicknesses of the matrix layers as well as the mass absorption coefficient are accurately known and, second, that the intensity distributions are indeed known to an accuracy of approximately 1%. Figure 2 shows a comparison of the Microscan data with that from the Materials Analysis Microprobe. Both distributions have been corrected for absorption but no adjustment has been made for the inclined specimen. The decrease in average depth of x-ray generation for the inclined specimen is clearly seen. These data are extremely important in establishing the proper form for the absorption correction when applied to data from microprobes with an inclined specimen.

### References

1. Castaing, R., and Descamps, J., J. Phys. Radium 16, 304 (1955).
2. Castaing, R., Advances in Electronics and Electron Physics 13, 317 (1960).
3. Vignes, A., and Dez, G., Brit. J. Appl. Phys., Ser. 2, 1, 1309 (1968).
4. Brown, J.D., Ph.D. Thesis, University of Maryland (1966).
5. Brown, J.D., and Parobek, L., 6th International Conference on X-Ray Optics and Microanalysis, Osaka, Japan (1971).

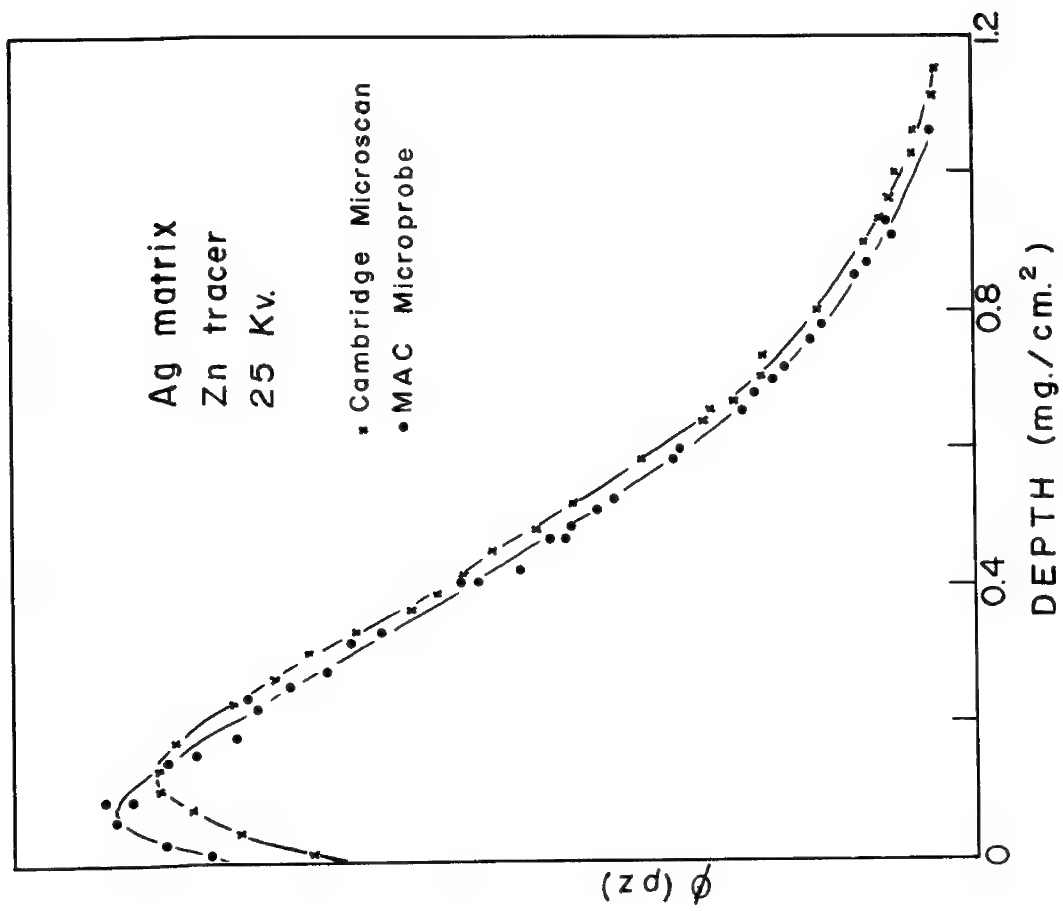


FIGURE 1

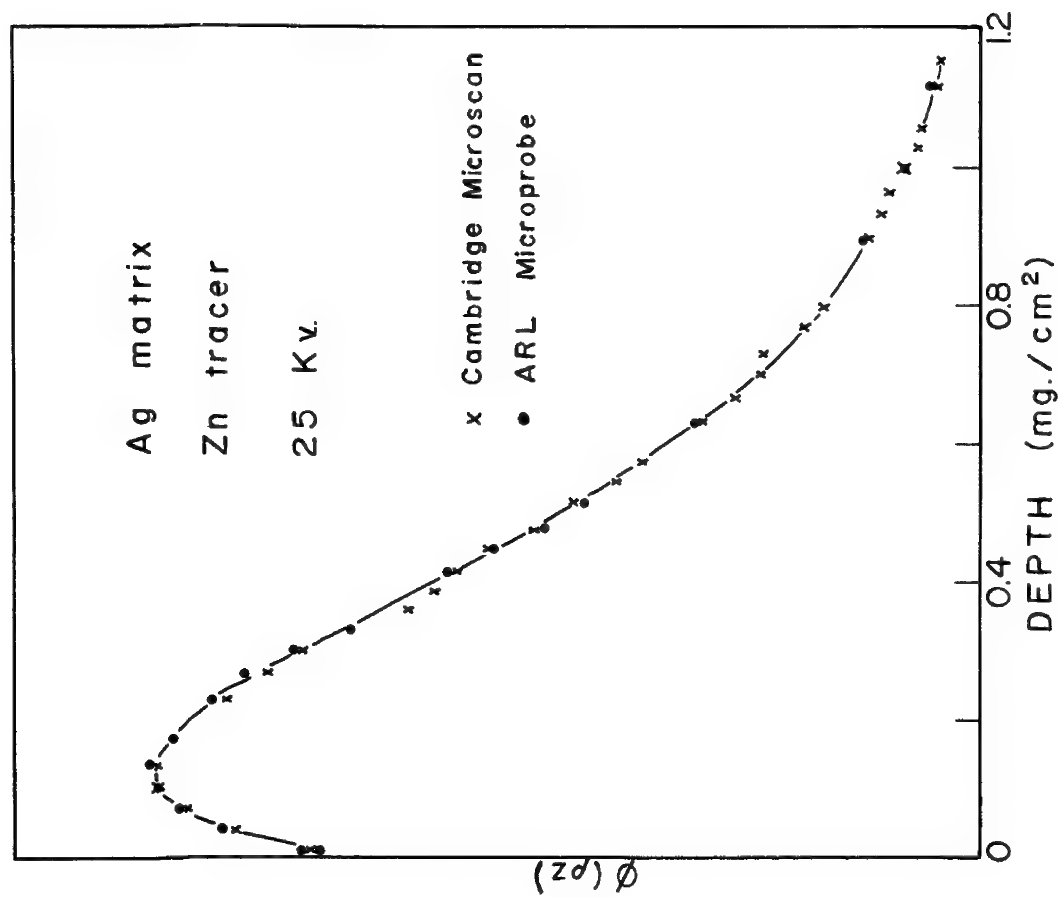


FIGURE 2

PRACTICALITY OF MONTE CARLO TECHNIQUE TO QUANTITATIVE  
MICROANALYSIS IN INCLINED TARGET

by

R. Shimizu, K. Murata and N. Nishigori  
Department of Applied Physics, Osaka University, Suita, Japan

N. Fujino and T. Shiraiwa  
Central Research Laboratories, Sumitomo Metal Industries, Ltd., Japan

Although the quantitative microprobe analysis has been widely used, some problems still remain unsolved. One of them is necessity of further investigation on the uncertainty of the absorption coefficients, specifically, for characteristic X-rays of light elements, and the other is to develop a more general correction procedures applicable to the case of oblique incidence as well as that of normal incidence usually found in common electron probe micro-analysers of commercially available types.

In the present paper the rotating inclined target method<sup>(1)</sup> has been adopted to access the practicality of the correction procedures by Monte Carlo technique, and it is intended to examine the adaptability of the values of absorption coefficients published by different authors from standpoint of quantitative analysis.

In practice the quantitative microanalysis in the inclined target, is becoming more important in the SEM with X-ray spectrometer in which the specimen surface is usually inclined against the incident beam. Monte Carlo technique has been successfully utilized for the normal incidence<sup>(2)</sup>, and has potentiality, in principle, to be easily applied to a particular boundary condition, e. g. inclined target. Hence the first investigation was attempted to access the practicality of the Monte Carlo technique to the more generalized quantitative corrections covering the inclined target. Such an application is also of interest in the sense that adaptability of the model of the calculation can be discussed more widely.

We also carried out the practical analysis by the rotating inclined target method measuring intensity from the alloy targets of the known composition at various take off angles. Procedures of calculation and experiment are given below.

Theoretical;

The Monte Carlo calculation is the same as that already published<sup>(3)</sup>, namely it is based on the Lewis' multiple scattering theory which is modified to be applicable to compounds. The theory is given by the following equation,

$$f(\theta) = \frac{1}{4\pi} \sum_{\ell=0}^{\infty} (2\ell+1) P_{\ell}(\cos \theta) \exp\left(-\int_0^s \sum K_{\ell i} ds\right),$$

where

$$K_{\ell i} = 2\pi N_i \int_0^{\pi} G_i(\theta) [1 - P_{\ell}(\cos \theta)] \sin \theta \cdot d\theta,$$

$G_i(\theta)$ : single scattering cross section.

For energy loss we used the Bethe's equation as following,

$$\frac{dE}{d(\rho s)} = - \frac{2\pi e^4 N_{\text{Avog}}}{E} \sum_{i=1}^n C_i \frac{Z_i}{A_i} \ln \frac{1.166 E}{J_i}$$

The calculated results of  $f(\theta)$ -curves for Fe-Al alloy (Al 24.09wt%) and pure Al at 30 KV are shown in Fig.1 with the result of normal incidence. In order to leave the fluorescence correction out of consideration, which is not directly related to the argument on the Monte Carlo simulation of the electron behavior in the target, the experiment was made for the elements of  $Z < 30$ , and in this paper the examination on Fe-Al alloy and Cu-Al alloy is described.

Experimental;

The schematic diagram of the experiment is shown in Fig.2. The inclined target was rotated around the axis of electron beam instead of rotating the spectrometer to detect the X-rays at various take off angles in the Shimadzu-ARL-7 channel type EMX. The rotation axis is fit to the focus point of the electron beam and the deviations of the irradiated point from the axis of rotation were confirmed to be less than several microns by the examination of the contamination under optical microscope. Denoting  $\varphi$  the angle of rotation and  $\psi_0$  the take off angle of the instrument for the horizontal plane ( $52.5^\circ$ ), the take off angle  $\psi$  of X-rays for a given angle of rotation  $\varphi$  can be derived from,

$$\sin \psi = \sin \psi_0 \sin \Phi - \cos \psi_0 \cos \Phi \cos \varphi,$$

where  $\Phi$  is the angle between specimen surface and electron beam axis.

In the present experiment  $\psi_0$  is  $52.5^\circ$ . Intensities of Characteristic X-rays were measured at several points between  $0^\circ$  and  $180^\circ$  of the rotation angle.

Typical measurements by this rotating inclined target method are shown in Fig. 3. Making quantitative correction by Monte carlo calculation to each datum one can access both the validity of Monte Carlo simulation and the influence of the uncertainty of absorption correction systematically.



The discrepancy in the quantitative analysis incurred by the difference in the absorption coefficient and the accuracy of the Monte Carlo quantitative correction procedures will be discussed.

#### References

- (1) N. Gennai, K. Murata and R. Shimizu; Jap. J. Appl. Phys. 10, 491 (1971)  
N. Gennai; Jap. J. Appl. Phys. 10, 1125 (1971)
- (2) H. E. Bishop; X-ray Optics and Microanalysis, eds. R. Castaing,  
P. Decamps and J. Philibert, (Hermann, Paris, 1966) p.112.  
R. Shimizu, K. Murata and G. Shinoda; --- ibid p.127.
- (3) N. Nishigori, R. Shimizu and K. Murata; to be published in J. Appl. Phys.

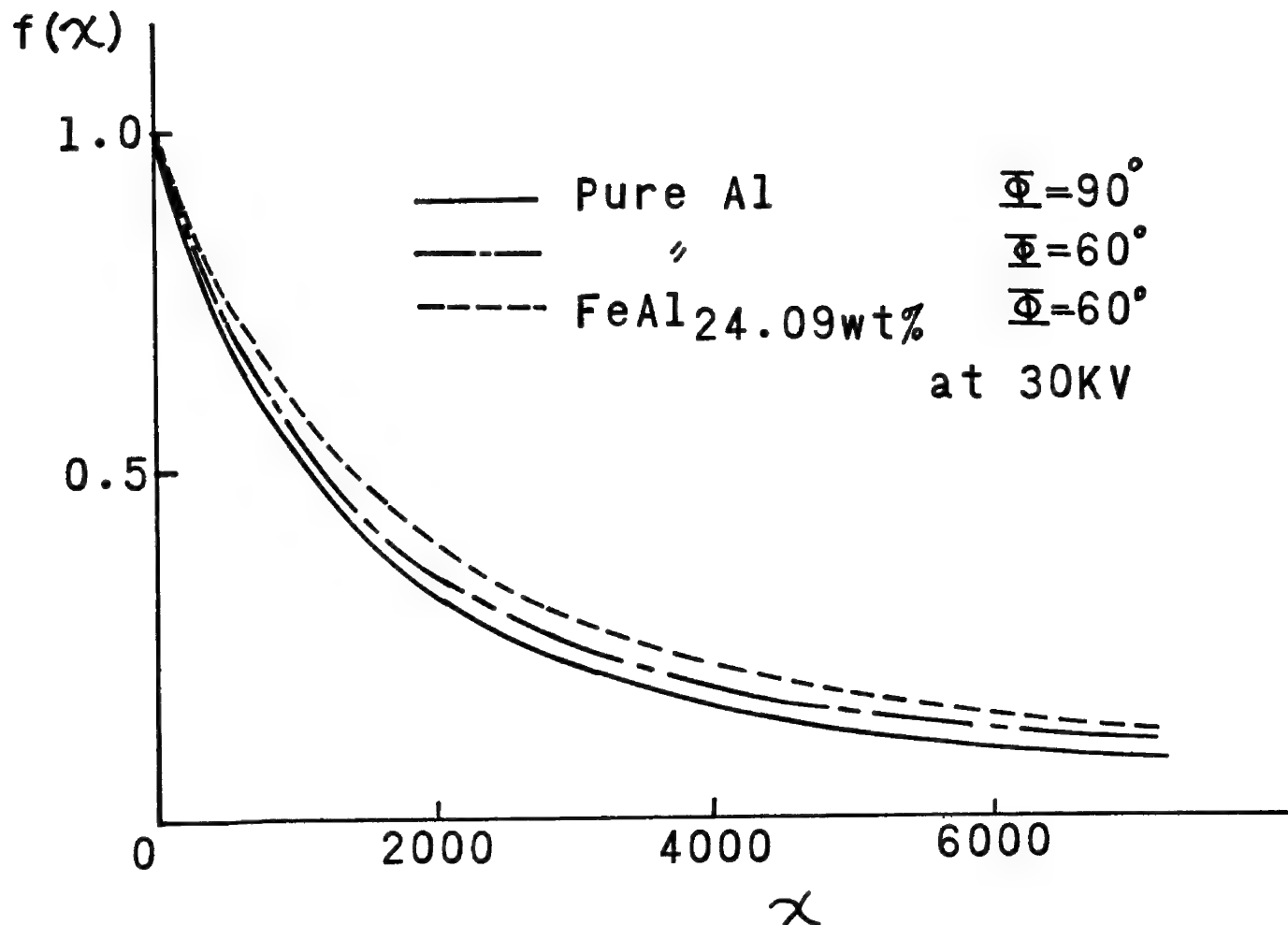


Fig. 1 Calculated  $f(\chi)$ -curves of Al  $K\alpha$  X-rays in pure Al and Fe-Al alloy (Al 24.09wt%) target

Incident  
Electron Beam

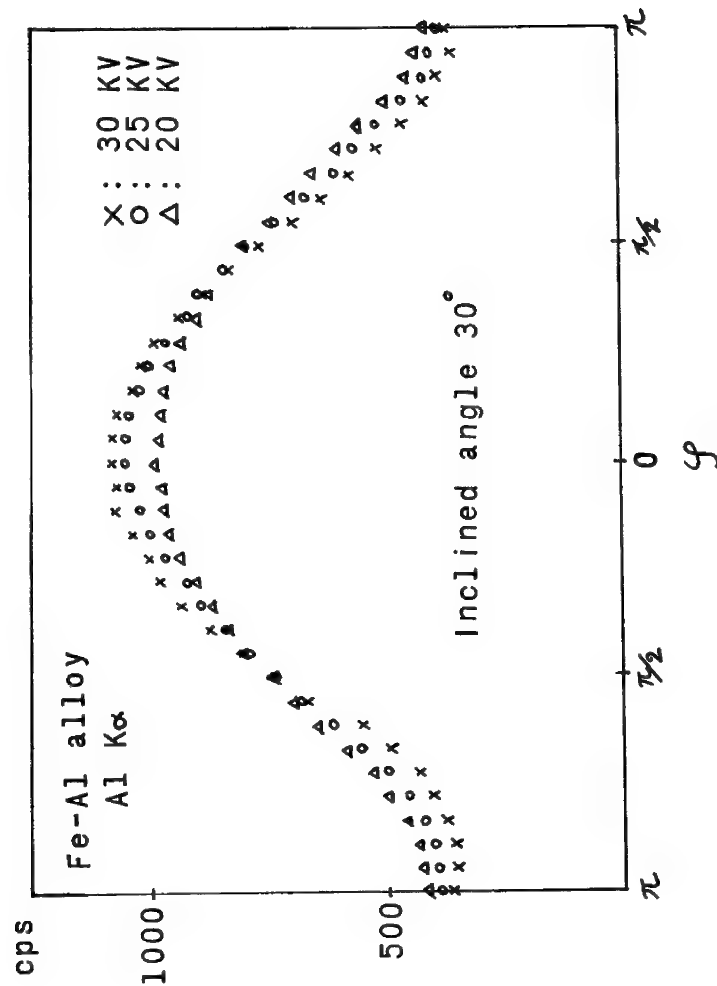
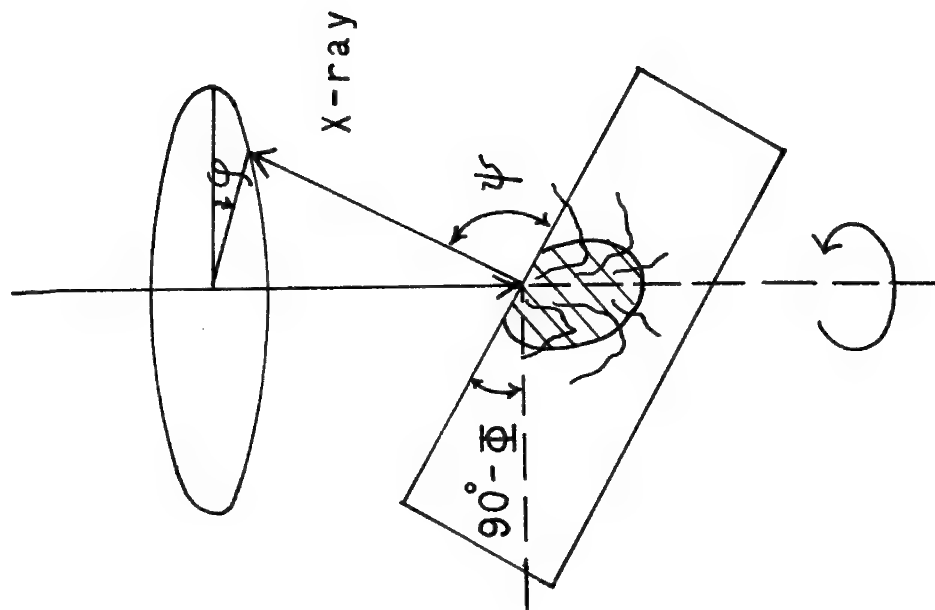


Fig. 3 Intensities of Al  $K\alpha$  from Fe-Al alloy (Al 24.09wt%) measured by rotating inclined target method at 20, 25 and 30 KeV.

Fig. 2 Diagram showing the direction of X-rays detection.

The Solid Solubility of Gd, Tb, Dy, Ho, Er and Yb in  
Mg: Systems with a Large Atomic Number Correction.

D. R. Beaman, L. F. Solosky, D. Mizer and B. C. Peters  
Dow Chemical U.S.A.  
Midland, Michigan 48640

The solid solubility of several rare earth metals in Mg was determined using the electron probe. A eutectic reaction occurs on the Mg-rich side of the phase diagram for Mg alloys containing Gd(Z=64), Tb(Z=65), Dy(Z=66), Ho(Z=67), Er(Z=68) and Yb(Z=70). The following characteristics were determined for each alloy system: the eutectic solubility, the solid solubility of the rare earth metal in Mg from the eutectic temperature to 260°C, the eutectic temperature, and the composition of the intermetallic compound. The samples were prepared by melting, casting, extruding for homogeneity, and heat treating in Argon at high temperatures and in an oil bath at low temperatures for long times near and below the eutectic temperature. Following metallographic examination, samples with the appropriate structure were examined in an electron probe operated at 15 kV with a take-off angle of 18°. The analyses were straightforward for samples heat-treated at and above 427°C but more ambiguous for lower temperatures because of the small size and fine distribution of second phase.

The solvus determinations shown in the figure indicate good results in all systems except Ho. The eutectic solubilities and intermetallic compound compositions are given in the table. Note that there are some wide discrepancies between these results and those previously reported.<sup>1,2</sup> The compound data indicate a broad composition range, and any dependence of the compound composition on temperature was obscured by the experimental precision. The compound in the Mg-Gd system has not been identified by x-ray diffraction but Mg<sub>9</sub>Gd (41.7% Gd in reference 1) appears unlikely in view of the 52.5% Gd measured; the broad ranges of composition encountered precludes identification on the basis of chemistry.

These materials are interesting from a theoretical point of view because: 1) The atomic number and absorption corrections can be studied in the absence of characteristic and continuous fluorescence effects. In calibration calculations the absolute intensity ratio was altered by less than 0.02% Mg, 0.10% Gd through Er, and 0.20% Yb. 2) The rare earth element is subject to a large atomic number correction in the absence of all other effects. 3) The Mg is subject to a large absorption correction and also a significant atomic number correction. In computing the rare earth concentration, considerable

uncertainty is introduced through the selection of the correction model and the mean ionization potential,  $J$ . For example, in the Mg-Gd system for a measured intensity ratio of 18% Gd, the Philibert-Tixier<sup>3</sup> atomic number correction used in conjunction with the Duncumb and Shield's<sup>4</sup> absorption correction (Heinrich's<sup>5</sup>  $\sigma$  value) yields concentrations of 23.4, 24.6 and 25.9 wt.% Gd when using the Berger and Seltzer,<sup>6</sup> 11.5  $Z$ , and Duncumb and Reed<sup>7</sup>  $J$  values respectively. This relative compositional error of over 10% is caused by a 10% variation in the stopping power correction. The Duncumb and Reed<sup>7</sup> atomic number correction yields 26.3% Gd.

The results shown in the figure and table are those obtained using the Philibert-Tixier<sup>3</sup> correction with the Berger and Seltzer<sup>6</sup>  $J$  values, because this combination gave the most reasonable results for all six alloy systems when the measured Mg concentrations were also considered. Using this ZAF scheme the 23.4% Gd is obtained from  $C=k \cdot (\text{stopping power, } S) \cdot (\text{backscatter, } R) \cdot (\text{absorption, } A)$ , where  $k=18.0$ ,  $S=1.61$ ,  $R=0.84$  and  $A=0.96$ , corresponding to an atomic number correction factor of 1.36. The mass absorption coefficients for the rare earth radiations were small and consistent within several sources so those of Heinrich<sup>8</sup> were used; however, the mass absorption coefficients for MgK $\alpha$  radiation by the rare earth metals varied considerably. Those published by Kelly<sup>9</sup> were used except for the absorption of MgK $\alpha$  by Tb in which case Frazer's<sup>10</sup> was used. Using these values led to concentration totals varying from 99-103%, except in the case of the Mg-Tb system where the higher totals encountered due to a high Mg concentration were presumably caused by an inaccurate mass absorption coefficient. While these problems may appear disconcerting, the accuracy of the solubility determinations is satisfactory and the alloy systems should be useful in the evaluation of atomic number correction procedures. This work was carried out as part of a research program supported by Frankford Arsenal Contract No. DAAG-11-69-C-0626.

#### References

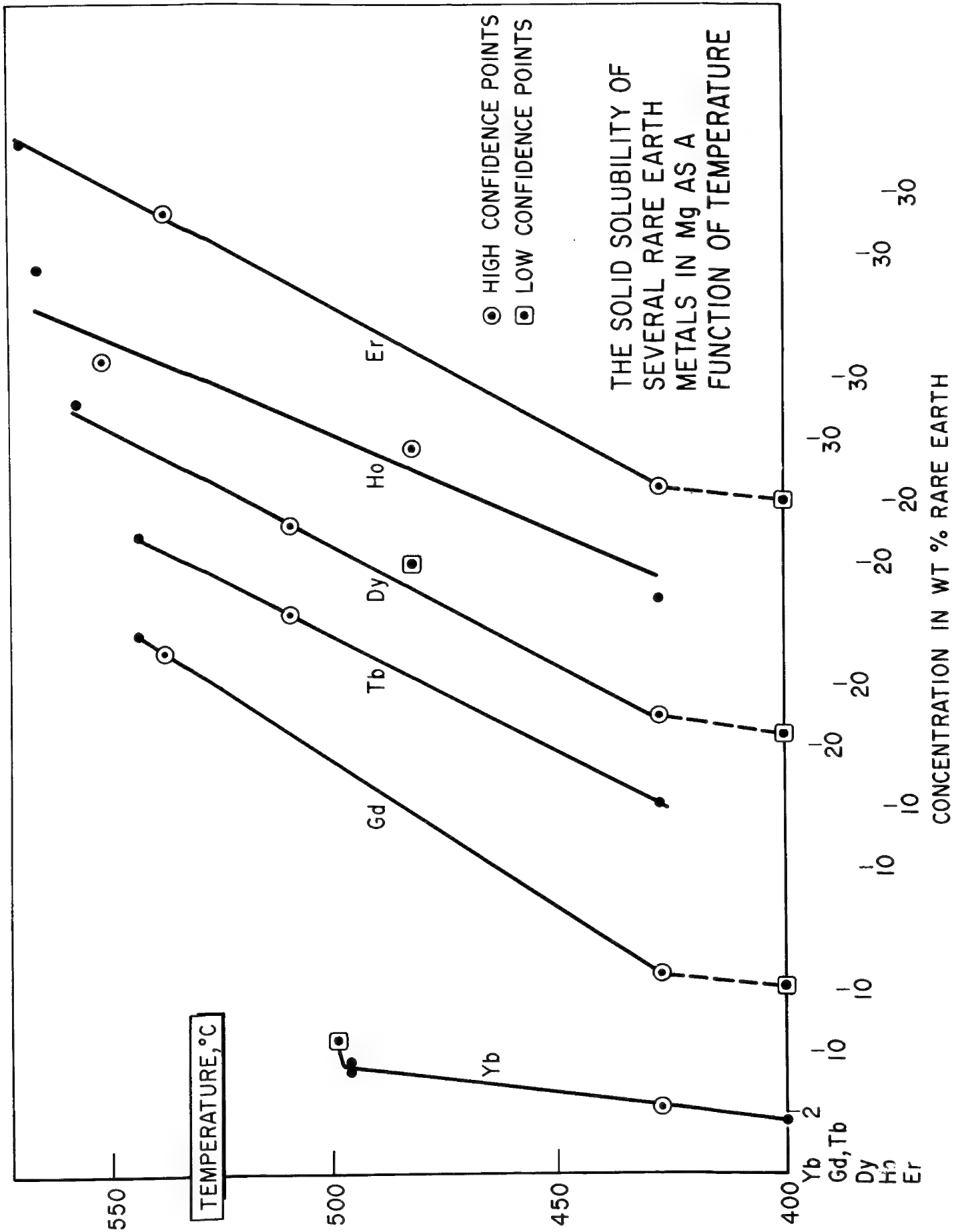
- 1) R. P. Elliott, Constitution of Binary Alloys, First Supplement, McGraw Hill, N.Y., 1965.
- 2) O. D. McMasters and K. A. Gschneidner, Jr., J. Less-Common Metals, **8**, 1965, p. 289.
- 3) J. Philibert and R. Tixier, in Quantitative Electron Probe Microanalysis, K. F. J. Heinrich, Ed., NBS Special Publ. 298, 1968, p. 13.
- 4) P. Duncumb and P. K. Shields, in The Electron Microprobe, T. D. McKinley, K. F. J. Heinrich and D. B. Wittry, Eds., Wiley, N. Y., 1966, p. 284.
- 5) K. F. J. Heinrich, in Advances in X-Ray Analysis, J. Newkirk, G. Mallett and H. Pfeiffer, Eds., Plenum Press, N. Y., Vol. 11, 1968, p. 40.
- 6) M. J. Berger and S. M. Seltzer, National Academy of Sciences-National Research Council Publ., NASRA, Vol. 1133, 1964, p. 205.
- 7) P. Duncumb and S. J. B. Reed, in Quantitative Electron Probe Microanalysis, K. F. J. Heinrich, Ed., NBS Special Publ. 298, 1968, p. 133.

- 8) K. F. J. Heinrich, in The Electron Microprobe, T. D. McKinley, K. F. J. Heinrich and D. B. Wittry, Eds., Wiley, N. Y., 1966, p. 296.
- 9) T. K. Kelly, Trans. Institution of Mining and Metallurgy, B75, 1966, p. 59.
- 10) J. Frazer, Un. of Calif. at LaJolla, S.I.O. Ref. No. 67-29, 1967.

TABLE: EUTECTIC CHARACTERISTICS OF SEVERAL Mg-RARE EARTH ALLOYS

<i>atomic number</i>	<i>element</i>	<i>eutectic temperature, °C</i>	<i>eutectic solubility, wt.% rare earth</i>	<i>maximum reported solubility, wt.% rare earth</i>	<i>measured compound composition, wt.% rare earth</i>	<i>compound formula*</i>	<i>stoichiometric composition, wt.% rare earth</i>
64	Gd	543	23.4	2.5 <sup>1</sup>	52.5		
65	Tb	543	26.8		48.8	Mg <sub>24</sub> Tb <sub>5</sub>	57.7
66	Dy	557	29.2		50.7	Mg <sub>24</sub> Dy <sub>5</sub>	58.3
67	Ho	566	29.6		49.8	Mg <sub>24</sub> Ho <sub>5</sub>	58.5
68	Er	571	31.5	0.7 <sup>1</sup>	51.5	Mg <sub>24</sub> Er <sub>5</sub>	59.0
70	Yb	499	4.4	8.0 <sup>2</sup>	71.4	Mg <sub>2</sub> Yb	78.0

\*identified by x-ray diffraction



# THE MEASUREMENT OF LOW-ENERGY ELECTRON AND X-RAY INTERACTION COEFFICIENTS FOR SOLIDS

Burton L. Henke  
Department of Physics and Astronomy  
University of Hawaii  
Honolulu, Hawaii 96822

The quantitative chemical analysis of surfaces using, for example, the electron microprobe, the scanning electron microscope, and photoelectron spectroscopy requires a considerably greater knowledge of the x-ray and electron interaction processes within matter than currently is available--particularly for the low-energy region of 100-1000 eV. In this region, the elastic scattering of both the x-ray photons and the electrons contributes relatively little to the total interaction cross sections for which the predominant contributions are from photoionization and electron ionization.

In recent years total photoionization cross sections have become more available from several laboratories for the 10-100 A region. (Reviews of available photoionization data for the 10-100 A region are contained in Refs. 1 and 2.) However, experimental data on the total electron ionization cross sections (or the mean-free-path values) for low-energy electrons within solids are nearly nonexistent. The subshell photo and electron ionization cross sections and the associated angular distributions of the emitted electrons are also needed, often as much as are the total cross sections, and a considerably smaller amount of data is available for these.

The measurement of low-energy x-ray and electron interaction cross sections is usually difficult. This is mostly because of the requirement for very thin sample thicknesses. (Typical low-energy electron mean-free-path values are of the order of 50 A.) Described in this paper are several methods which are being used in this laboratory for these measurements, including the method of photoelectron spectroscopy.

Finally, the important role of recent theoretical work in obtaining detailed knowledge of low-energy interactions is reviewed here. Using standard theoretical models (as, for example, Hartree-Fock-Slater calculations) and with large computers, a considerable amount of calculated cross section data for a large range of elements has become available. (See, for example, Refs. 3, 4, and 5.) These include differential and total photoionization cross sections, photoelectron angular distributions, and electron ionization cross sections.

## References

1. B. L. Henke, et al., Technical Report, AFOSR 67-1254, June 1967; also Advances in X-Ray Analysis, Vol. 13 (Plenum Press), New York, 1970), p. 639 (with R. L. Elgin).
2. B. L. Henke, in Proceedings, International Conference on Inner Shell Ionization Phenomena, Atlanta, Ga., April 1972 (in press).
3. E. J. McGuire, Phys. Rev. 175, 29 (1968).
4. D. J. Kennedy and S. T. Manson, Phys. Rev. A 5, 227 (1972).
5. E. J. McGuire, Phys. Rev. A 3, 267 (1971).

ELUCIDATION OF THE DAMAGE MECHANISM OF SYNTHETIC SODALITES BY ESCA

by

J.S. Brinen

Central Research Division, American Cyanamid Company,  
Stamford, Connecticut 06904

and

L.A. Wilson

Instrument Division, Varian Associates,  
Palo Alto, California 94303

Sodalite, long known to be photochromic,<sup>1</sup> is an aluminosilicate represented by the ideal formula  $\text{Na}_8\text{Al}_6\text{Si}_6\text{O}_{24}\text{X}_2$  ( $\text{X} = \text{Cl}, \text{Br}$  or  $\text{I}$ ). It is characterized by a framework of alternating silicon and aluminum atoms linked through their surrounding oxygen tetrahedra. The structure contains numerous cavities in which the sodium and halogen ions are located at specific positions. Some specially prepared synthetic sodalites exhibit reversible photochromism.<sup>2,3</sup> When these materials are irradiated with ultraviolet light they become colored; magenta, purple or blue when the halogens present are respectively chlorine, bromine or iodine. Bleaching is achieved by irradiation with visible light into these newly generated absorption bands. Under mild conditions of electron bombardment these same materials are reversibly cathodochromic, i.e., the color is produced by electron bombardment and can be bleached by visible light.<sup>4-8</sup> With increasing levels of electron bombardment the sodalite is "damaged" so that the color generated cannot be bleached optically. In this case bleaching can only be achieved by heat treatment.<sup>9</sup> ESR studies have demonstrated that the same F-center (an electron trapped at a halogen vacancy interacting with four equivalent sodiums) is responsible for both the photochromic and cathodochromic behavior.<sup>10</sup> In attempting to discover the nature of the damaging process and its reversal by heat we have



investigated the surface chemistry of these sodalites in the colorless, damaged and bleached states, by ESCA. It is estimated that these measurements may be sampling as much as  $\sim 40 \text{ \AA}$  deep into surface of the materials under study.

Experiments were performed on a Varian IEE Spectrometer utilizing Al K $\alpha$  (1486.6 eV) and Mg K $\alpha$  (1253.6 eV) radiation. The sodalite powders were mounted on stainless screens. Electron damage was achieved by exposing the sample to 2 KeV electrons from a Tungsten filament in the spectrometer reaction chamber for 15 minutes. Thermal bleaching was achieved by heating the screens containing the damaged sodalite in air for  $\sim 1$  hour at 300°C.

Figure 1 shows part of the ESCA spectrum obtained for bromosodalite in the 50-100 eV binding energy region. This narrow region facilitates comparison of two elements directly involved in the color mechanism (sodium and bromine) with one which is not (aluminum). The top spectrum is that obtained from a colorless sample of bromosodalite.<sup>11</sup> The Al 2p; Br 3d and Na 2s electron lines are all of comparable intensity. The weak line at  $\sim 54$  eV is Fe 3p line from the stainless screen. The middle spectrum is that obtained from the same sample after damage in the reaction chamber with 2 KeV electrons. A dramatic loss of bromine and, to a lesser extent, sodium relative to aluminum is observed for the damaged bromosodalite. Similar changes in the Na 2p and Br 3p photoelectron lines were observed. Electron bombardment also cleans the surface of the stainless screen leading to an increase in the Fe 3p and Fe 3s (93 eV) lines.<sup>12</sup> The sodium line appears to be broadened which may be an artifact attributable to either Ni 2p or Cr 2p electrons from the screen material. At this stage the sodalite is highly colored and cannot be bleached by visible light. The bottom spectrum was obtained from the same sample after bleaching at approximately 300°C. The

spectrum of the now colorless sample clearly shows the return of both bromine and sodium to the surface. The iron lines have shifted to higher binding energies reflecting oxidation during this treatment.

Similar results were obtained for iodosodalites and chlorosodalites prepared in different procedures, although the changes observed were not as pronounced as for the bromosodalite.

The above measurements clearly demonstrate that the permanent coloration (damage) produced by electron bombardment results in a substantial decrease of surface halogen and sodium. It is quite clear then that the F centers resulting the optically bleachable coloration and the damaged sodalite coloration, although identical as evidenced by their optical and ESR spectra, are different in origin. In the photochromic sodalites (light bleachable) coloration may be explained in terms of reversible electron transfer from one center to a halogen vacancy while reversible coloration produced by mild conditions of electron bombardment may be explainable in terms of electrons trapped by the same halogen vacancy.

The authors wish to thank Dr. J.R. Leto for preparing the samples and Dr. R. Bhalla and Prof. F.E. Williams for many stimulating discussions.

## REFERENCES

1. D.B. Medved, Am. Mineralogist 39, 615 (1954).
2. W.G. Hodgson, J.S. Brinen and E.F. Williams, J. Chem. Phys. 47, 3719 (1967).
3. E.F. Williams, W.G. Hodgson and J.S. Brinen, J. Am. Ceramic Soc. 52, 139 (1969).
4. W. Phillips, Z.J. Kiss, Proc. IEEE 56, 2072 (1968).
5. P.A. Forrester, D.J. Marshall, S.D. McLaughlan and M.J. Taylor, "Colour Centers in Sodalites for Storage Displays," North American Treaty Organization, AGARD Conference Proceedings, N. 50, pg. 14-1 (1970).
6. W. Phillips, J. Electro Chem. Soc. 117, 1557 (1970).
7. R. Duncan, B. Faughner and W. Phillips, Appl. Optics 9, 2236 (1970).
8. I. Gorog, Appl. Optics 9, 2242 (1970).
9. P.M. Heyman, I. Gorog and B.W. Faughnan, IEEE International Electron Device Meeting, Oct. 28-30, 1970, Washington, D.C.
10. J.S. Brinen, unpublished results.
11. A slight color is produced by the x-ray excitation. This fades rapidly in room light.
12. These lines were not observed when similar measurements were performed with the samples mounted on sticky tape.

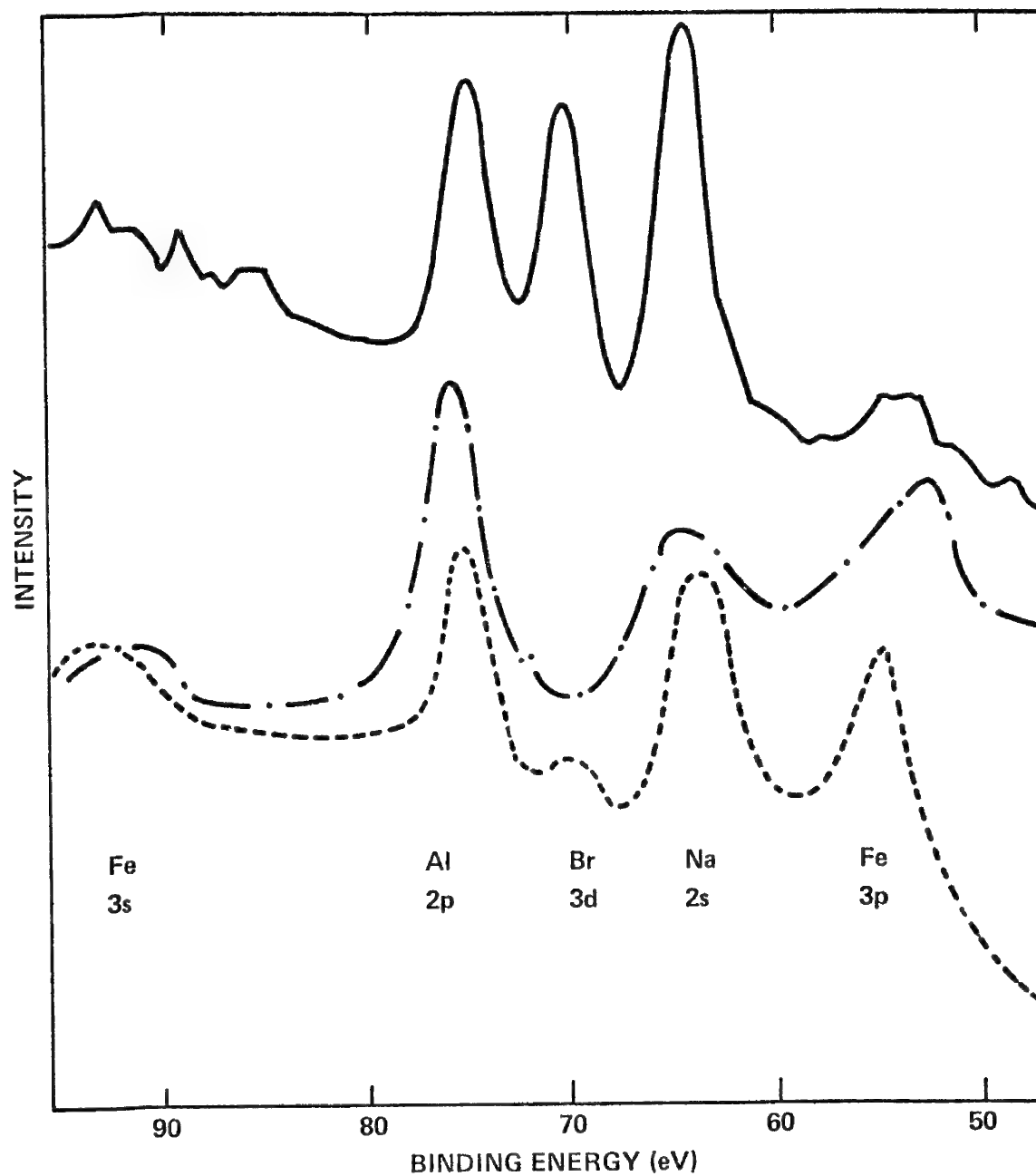


Figure 1. ESCA spectrum of bromosodalite in the 50-100 eV binding energy region. The top spectrum (—) was that obtained from a colorless sample, the middle spectrum (— . —) was obtained from a sample which was damaged by electron bombardment and the bottom spectrum (----) was from a damaged sample bleached by heating.

# NEW ABSORPTION CORRECTION FOR SOFT X-RAYS IN QUANTITATIVE ELECTRON PROBE MICROANALYSIS

D. F. Kyser and H. R. MacQueen

IBM Research Laboratory  
San Jose, California

One of the most important corrections required for quantitative electron probe microanalysis, especially for "soft" X-rays, is that for absorption by the target. The magnitude of the correction, and hence the error possible in the correction, increases with increasing overvoltage  $U_0$  and absorption coefficient  $\mu/\rho$ . According to Yakowitz and Heinrich,<sup>1</sup> the absorption correction  $f(\chi)$  should be maintained between 0.8 and 1.0 by choosing an appropriately low beam voltage  $E_0$  and high takeoff angle  $\psi$ . The error in  $f(\chi)$  will then be less than 1% typically.

However it is often necessary to utilize high overvoltages and emission lines which are strongly absorbed, especially in multi-element targets, which results in  $f(\chi) \ll 1$ . The analyst is then faced with placing confidence in a particular model for  $f(\chi)$  and utilizing questionable values for  $\mu/\rho$  which can produce large errors in quantitative results.

Because many of the tabulated values for  $\mu/\rho$  were simply calculations extrapolated or interpolated over large ranges in  $\lambda$  and atomic number  $Z$  of the absorber, Kyser<sup>2,3</sup> developed an experimental method for the determination of  $\mu/\rho$  for soft X-rays in a mid-Z target. The method involves a measurement of X-ray intensity versus beam voltage  $E_0$ , with target current maintained constant. The experimental details are published elsewhere.<sup>4</sup> A simple relation was deduced between the value of  $\mu/\rho$  in the target and the value of  $E_0 = E_p$  which produced a maximum observed intensity. A truncated Gaussian distribution of  $\Phi(\rho z)$  scaled with  $E_0$  was utilized to provide an expression for  $f(\chi)$ . This Gaussian  $f(\chi)$  was easier to incorporate in subsequent calculations of  $\mu/\rho$  than the popular expression for  $f(\chi)$  due to Philibert<sup>5</sup> which is presently widely used in quantitative analysis with hard X-rays. The Gaussian  $f(\chi)$  was also more satisfying physically since it did not require that  $\Phi(0) = 0$  like the Philibert  $f(\chi)$  does. The Gaussian  $f(\chi)$  for soft X-rays ( $E_c \leq 1$  kV) is

$$f(\chi) = \left\{ \frac{\exp[-(z_0/\Delta z)^2] \exp(u^2) [1 - \operatorname{erf}(u)]}{1 + \operatorname{erf}(z_0/\Delta z)} \right\} - 0.029 \quad (1)$$

where

$$u = \left[ \frac{\chi \rho \Delta z}{2} - \frac{z_0}{\Delta z} \right], \quad \rho z_0 = 0.125 R, \quad \rho \Delta z = 0.350 R,$$

and

$$R = 2.56 \times 10^{-3} (E_0/30)^{1.68} \text{ gm/cm}^2 \quad (E_0 \text{ in kV}).$$

The subtractive constant 0.029 in Eq. (1) represents an approximate correction for asymmetry in  $\Phi(\rho z)$  about  $\rho z_0$  and is derived in the appendix of reference 3.

This new expression for  $f(\chi)$  has now been used in quantitative calculations with Cu L $\alpha$  and large  $U_0$  in a series of Cu-Au alloy standards available from the U.S. National Bureau of Standards.<sup>6</sup> Strictly speaking, Eq. (1) should only apply to a target with average atomic number near Cu ( $Z = 29$ ), since the constants in Eq. (1) which describe the shape of  $\Phi(\rho z)$  were deduced by fitting to a curve of energy loss in Cu via TEP calculations.<sup>7</sup> However atomic number dependence in  $f(\chi)$  is suggested by comparison with the work of Andersen and Wittry,<sup>8</sup> whereby the electron range  $R$ , and hence the mean depth of X-ray production  $\bar{\rho z} = 2\rho z_0 = 0.25 R$ , is scaled as  $A/[Z^{1.33} \ln(174 E_0/Z)]$ . This scaling factor is nearly identical for Cu and Au at large  $E_0$  which results in Eq. (1) being applicable to the Cu-Au system without an atomic number dependence in  $f(\chi)$ . However in other alloy systems this weak dependence may have to be included.

Experimental values of relative intensity  $k$  for Cu L $\alpha$  and Au L $\alpha$  were taken from Heinrich,<sup>6</sup> and the MAGIC 4 computer program described by Colby<sup>9</sup> was used for calculations of weight fraction  $C$ . MAGIC 4 was modified to allow a choice between the use of the Gaussian  $f(\chi)$  or Philibert  $f(\chi)$  for Cu L $\alpha$  and also external input of  $\mu/\rho$  (Cu L $\alpha$ , Cu) and  $\mu/\rho$  (Cu L $\alpha$ , Au). The Au L $\alpha$  line was calculated only with the Philibert  $f(\chi)$ , since it is a hard X-ray. The results are shown in Table 1. An improved analysis was obtained with the KABSCO matrix for  $\mu/\rho$  and the use of the Gaussian  $f(\chi)$  for Cu L $\alpha$  (Case I). The KABSCO values of  $\mu/\rho$  for Cu L $\alpha$  were suggested previously by Kyser.<sup>3</sup> The value of  $\mu/\rho$  (Cu L $\alpha$ , Au) = 5,810 cm<sup>2</sup>/gm is very close to the value of 6,000 provided by Colby<sup>10</sup> in a recent literature review.

An alternative method suggested by Kyser<sup>3</sup> would take advantage of the direct measurement of  $\chi$  for each X-ray line in a composite target via the relation between  $\chi$  and  $E_p$ :

$$\chi_{\text{total}} (\text{cm}^2/\text{gm}) = \left( \frac{2660}{E_p} \right)^{1.68} (E_p \text{ in kV}). \quad (2)$$

This value for  $\chi$  can then be used in Eq. (1) without iteration of  $f(\chi)$ , except of course for any  $Z$ -dependence. The same  $Z$ -dependence used for  $f(\chi)$  should also be used in Eq. (2), which is presently accurate for mid- $Z$

targets only. The potential advantage of this technique is that it is not necessary to use questionable values of  $\mu/\rho$  to calculate  $X_{total}$ , since it is directly measured. The value of  $E_p$  for Cu  $L\alpha$  was measured for each of the alloys in Table 1 and in a pure Cu target. A correction to  $E_p$  was made for electron gun bias. Values of  $X$  were then calculated from Eq. (2), and  $f(X)$  from Eq. (1). This fixed value of  $f(X)$  for Cu  $L\alpha$  was then used in an APL computer program<sup>11</sup> which was modified to accept a fixed absorption correction for any element, but let the other ZAF corrections iterate to convergence. This interactive APL program contained the same correction formulae, parameters, and iteration scheme as MAGIC 4. Table 3 shows the results obtained with the same  $k$  values as those used in Table 1. The results are best for the Cu-rich alloys, but in any case comparable to or better than the results found in cases II to VI of Table 1. This alternative method may be very useful, especially in those cases where the tabulated values of  $\mu/\rho$  are very inaccurate or completely unknown.

- 
1. H. Yakowitz and K. F. J. Heinrich, *Microchim. Acta* 1968, 182 (1968).
  2. D. F. Kyser, *Proc. 5th Nat. Conf. on Electron Probe Analysis* (New York, 1970), paper no. 12.
  3. D. F. Kyser, *Proc. 6th Int. Congress on X-Ray Optics and Microanalysis* (Osaka, 1971), to be published. Also IBM Research Report RJ 911 (Sept. 1971).
  4. D. F. Kyser and D. E. Horne, *Rev. Sci. Instr.* (to be published). Also IBM Research Report RJ 1011 (April 1972).
  5. J. Philibert, *Proc. 3rd Int. Congress on X-Ray Optics and Microanalysis* (Stanford, 1962), p. 379.
  6. K. F. J. Heinrich, N.B.S. Spec. Pub. No. 260-28 (1971).
  7. D. B. Brown, U.S. Naval Research Laboratory (private communication).
  8. C. A. Andersen and D. B. Wittry, *Brit. J. Appl. Phys., Ser. 2*, 1, 529 (1968).
  9. J. W. Colby, *Proc. 6th Nat. Conf. on Electron Probe Analysis* (Pittsburgh, 1971), paper no. 17.
  10. J. W. Colby, Bell Telephone Laboratories (private communication).
  11. R. Lasky, IBM Corp. (private communication).

Table 1

Comparison of corrections for Cu  $L\alpha$  at  $E_0 = 25$  kV,  $\psi = 52.5^\circ$ .  
The values in parentheses are  $f(\chi)^\circ/f(\chi)$  for Cu  $L\alpha$  in each alloy.

19.8Cu - 80.2Au			39.6Cu - 60.4Au			59.9Cu - 40.1 Au			79.9Cu - 20.1Au		
$\underline{k}$	$\underline{\sigma}$		$\underline{k}$	$\underline{\sigma}$		$\underline{k}$	$\underline{\sigma}$		$\underline{k}$	$\underline{\sigma}$	
Cu $L\alpha$ = 0.097	0.001		0.219	0.001		0.387	0.002		0.632	0.004	
Au $L\alpha$ = 0.745	0.002		0.529	0.003		0.331	0.002		0.154	0.003	
I	$\underline{C(\%)}$	$\underline{f(\chi)}$	$\underline{C(\%)}$	$\underline{f(\chi)}$		$\underline{C(\%)}$	$\underline{f(\chi)}$		$\underline{C(\%)}$	$\underline{f(\chi)}$	
	21.0	0.1546	41.0	0.1866		60.8	0.2307		80.4	0.2936	
	<u>79.3</u>		<u>59.4</u>			<u>39.0</u>			<u>19.0</u>		
$\Sigma =$	100.3	(2.48)	100.4	(2.06)		99.8	(1.66)		99.4	(1.31)	
II	$\underline{C(\%)}$	$\underline{f(\chi)}$	$\underline{C(\%)}$	$\underline{f(\chi)}$		$\underline{C(\%)}$	$\underline{f(\chi)}$		$\underline{C(\%)}$	$\underline{f(\chi)}$	
	16.4	0.2171	34.3	0.2452		54.0	0.2860		75.8	0.3443	
	<u>78.4</u>		<u>58.8</u>			<u>38.8</u>			<u>19.0</u>		
$\Sigma =$	94.8	(1.96)	93.1	(1.73)		92.8	(1.48)		94.8	(1.23)	
III	$\underline{C(\%)}$	$\underline{f(\chi)}$	$\underline{C(\%)}$	$\underline{f(\chi)}$		$\underline{C(\%)}$	$\underline{f(\chi)}$		$\underline{C(\%)}$	$\underline{f(\chi)}$	
	23.9	0.1274	44.9	0.1580		64.4	0.2000		82.8	0.2624	
	<u>79.2</u>		<u>59.3</u>			<u>39.0</u>			<u>19.0</u>		
$\Sigma =$	103.1	(2.82)	104.2	(2.28)		103.4	(1.80)		101.8	(1.37)	
IV	$\underline{C(\%)}$	$\underline{f(\chi)}$	$\underline{C(\%)}$	$\underline{f(\chi)}$		$\underline{C(\%)}$	$\underline{f(\chi)}$		$\underline{C(\%)}$	$\underline{f(\chi)}$	
	18.3	0.1859	37.6	0.2143		58.2	0.2553		79.5	0.3149	
	<u>79.2</u>		<u>59.4</u>			<u>39.1</u>			<u>19.0</u>		
$\Sigma =$	97.5	(2.16)	97.0	(1.88)		97.3	(1.57)		98.5	(1.28)	
V	$\underline{C(\%)}$	$\underline{f(\chi)}$	$\underline{C(\%)}$	$\underline{f(\chi)}$		$\underline{C(\%)}$	$\underline{f(\chi)}$		$\underline{C(\%)}$	$\underline{f(\chi)}$	
	22.8	0.1220	43.7	0.1500		63.6	0.1884		82.6	0.2440	
	<u>79.6</u>		<u>59.6</u>			<u>39.1</u>			<u>19.0</u>		
$\Sigma =$	103.4	(2.68)	103.3	(2.18)		102.7	(1.74)		101.6	(1.34)	
VI	$\underline{C(\%)}$	$\underline{f(\chi)}$	$\underline{C(\%)}$	$\underline{f(\chi)}$		$\underline{C(\%)}$	$\underline{f(\chi)}$		$\underline{C(\%)}$	$\underline{f(\chi)}$	
	17.3	0.1807	35.7	0.2061		55.7	0.2428		77.2	0.2959	
	<u>78.6</u>		<u>58.9</u>			<u>38.9</u>			<u>19.0</u>		
$\Sigma =$	95.9	(2.06)	94.6	(1.80)		94.6	(1.53)		96.2	(1.26)	



Table 2

Mass absorption coefficients and  $f(x)$  formulae used in Table 1.

KABSCO <sup>3</sup>		HABSCO <sup>6</sup>		CABSCO <sup>9</sup>	
<u>CuL<math>\alpha</math></u>	<u>AuL<math>\alpha</math></u>	<u>CuL<math>\alpha</math></u>	<u>AuL<math>\alpha</math></u>	<u>CuL<math>\alpha</math></u>	<u>AuL<math>\alpha</math></u>
Cu = 1910	245	2080	245	2340	245
Au = 5810	127	7030	127	7168	127

I.	KABSCO with Gaussian $f(x)$ for Cu L $\alpha$ only:	$f(x)_{\text{CuL}\alpha}^0 = 0.3834$
II.	KABSCO with Philibert $f(x)$ for Cu L $\alpha$ , Au L $\alpha$ :	$f(x)_{\text{CuL}\alpha}^0 = 0.4243$
III.	HABSCO with Gaussian $f(x)$ for Cu L $\alpha$ only:	$f(x)_{\text{CuL}\alpha}^0 = 0.3594$
IV.	HABSCO with Philibert $f(x)$ for Cu L $\alpha$ , Au L $\alpha$ :	$f(x)_{\text{CuL}\alpha}^0 = 0.4019$
V.	CABSCO with Gaussian $f(x)$ for Cu L $\alpha$ only:	$f(x)_{\text{CuL}\alpha}^0 = 0.3271$
VI.	CABSCO with Philibert $f(x)$ for Cu L $\alpha$ , Au L $\alpha$ :	$f(x)_{\text{CuL}\alpha}^0 = 0.3713$

Table 3

Quantitative results for  $E_0 = 25$  kV,  $\psi = 52.5^\circ$  with fixed  $f(x)$  method for Cu L $\alpha$ 

Target	$E_p$ (kV)	$x$ (cm <sup>2</sup> /gm)	$f(x)$	$f(x)^0/f(x)$	C(%)
Cu	25.48	2,450	0.3786	1.000	100.0
79.9 Cu 20.1 Au	21.07 -	3,400	0.2896	1.307	80.7 19.0 $\Sigma = 99.7$
59.9 Cu 40.1 Au	18.42 -	4,200	0.2377	1.593	58.8 39.1 $\Sigma = 97.9$
39.6 Cu 60.4 Au	17.44 -	4,650	0.2147	1.763	35.4 59.4 $\Sigma = 94.8$
19.8 Cu 80.2 Au	15.73 -	5,500	0.1798	2.106	17.8 79.2 $\Sigma = 97.0$

SOME EXAMPLES OF MATERIALS CHARACTERIZATION  
BY SOFT X-RAY ELECTRON MICROPROBE ANALYSIS

James S. Solomon  
University of Dayton Research Institute, Dayton, Ohio 45409

and

William L. Baun  
Air Force Materials Laboratory (LN), WPAFB, Ohio 45433

Often specimens submitted for microprobe analysis innately limit semiquantitative or quantitative analysis. An example of this sometimes occurs in failure analysis in which the microprobe analyst may not disturb the surface, which means restricting or even prohibiting the usual specimen preparation techniques such as mounting and polishing. Another example is the analysis of oxide scales or coatings which are restrictive because of surface porosity, poor conductivity, density, and thickness. Light element quantitative analysis has always been a problem to the microprobe analyst because of large discrepancies and disagreement in mass absorption coefficients, except for specifically and operationally defined measurements.<sup>1</sup>

Soft x-ray spectroscopy is a tool that can often yield the required analytical information from specimens such as those described above. The electron microprobe, in general, is capable of soft x-ray spectroscopy investigations for both research and practical analytical applications.<sup>2,3</sup> Very often microprobe operators neglect certain analytical information contained in x-ray line and band profiles. Instead, they are usually concerned only with the quantitative measurement of peak intensities. In many cases x-ray line and band spectra yield very important chemical and structural information for materials characterization when the usual techniques fail or are subject to large sources of error.

Figure 1 is an illustration of electron microprobe characterization of an oxide ring around a copper wire coated with silver. The silver (the lighter contrast area between the two curved sections of copper wire) did not properly wet the copper surface during coating and consequently tended to agglomerate along the walls of the wire upon heating. The copper then became subject to oxidation. The electron image is presented with a superimposed x-ray line scan of oxygen showing the presence of oxygen in the outer edge of the copper as well as in the silver. At the top of the electron image are the  $\text{CuL}\alpha$  x-ray band profiles from the oxide layer adjacent to the copper center and from an area well within the copper center. Comparing these with the  $\text{CuL}\alpha$  spectra to the left from  $\text{Cu}$ ,  $\text{Cu}_2\text{O}$ , and  $\text{CuO}$ , the analyst was able to identify the oxide ring adjacent to the  $\text{Cu}$  as  $\text{Cu}_2\text{O}$ .

The electron image in Figure 2 shows a two phase chromium, chromium-nitrogen specimen. To the right of the electron image are the  $\text{CrL}\alpha$  and  $\text{CrL}\beta$  x-ray band profiles from each of the two phases. Comparing them with the  $\text{CrL}$  emission bands to the left from  $\text{Cr}$ ,  $\text{Cr}_2\text{N}$ , and  $\text{CrN}$  identifies the nitrogen containing phase as  $\text{Cr}_2\text{N}$  and the second smaller phase is unreacted chromium metal. A point count quantitative analysis using the chromium  $\text{K}\alpha$  line would probably be difficult since there is a large difference between the mass absorption coefficients involved, and the mass absorption coefficient of nitrogen absorbed by chromium would have to be accurately determined for this particular specimen in order to do a quantitative analysis for the nitrogen content.

Characterization in the two examples in Figures 1 and 2 was accomplished by visually comparing x-ray band profiles from unknowns with the profiles from standards. One advantage with this method is that once the profiles from standards are recorded, it is not necessary to repeat this measurement each time an analysis is to be performed. In other words, a microprobe facility could record numerous x-ray spectra from various elements, alloys, and compounds and catalog them for future reference similar to the routine methods used by infrared spectroscopists. However, unlike infrared spectra, soft x-ray spectra are often significantly affected by instrumental and experimental parameters such as take-off angle and excitation conditions. This necessitates the recording of spectra by the individual facility. Comparison with spectra from other instruments for accurate materials characterization must be cautioned against, although where similar equipment is used and operational conditions are kept the same, comparison of results from one laboratory to another is quite good.

Specific features in some emission spectra could also be used for characterization. For example, in the Al-Cu alloy system the effect of alloying splits the AlK band into two components and the separation between the components is a function of concentration.<sup>4,5</sup>

In some cases the change in relative intensity of one or more components of an x-ray band or line compared to another component or to another band or line can be used for the analysis. An example of this is found in the changes of the intensity ratio of  $K\alpha_3$  and  $K\alpha_4$  satellite emission lines from some Al, Si, and Mg compounds.<sup>6</sup>

Numerous other examples of soft x-ray application to materials characterization have been reported in the literature, all of which give strong support for the routine application of this technique to microprobe analysis.

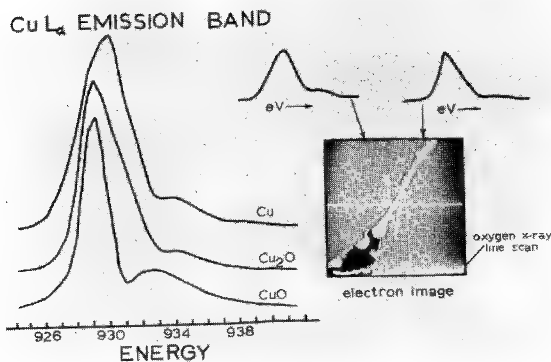


Figure 1. Characterization of Copper Oxide Layer by  $\text{CuL}\alpha$  Band Profile Comparison

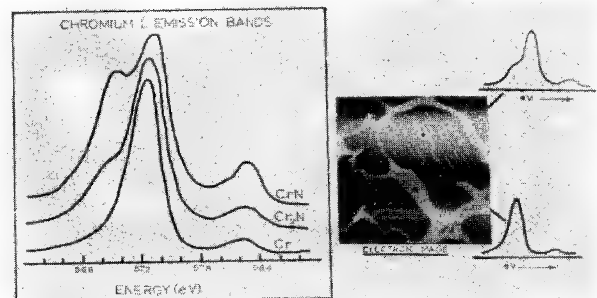


Figure 2. Characterization of a Chromium Nitride Phase by  $\text{CrL}$  Band Profile Comparison

## REFERENCES

1. B. L. Henke in Advances in X-Ray Analysis 7, 460 (Plenum Press, New York, 1964)
2. W. L. Baun and J. S. Solomon, "Bonding and Chemical Combination Studies Using the Electron Microbeam Probe," Air Force Materials Laboratory Technical Report AFML-TR-70-80 (1970)
3. J. S. Solomon and W. L. Baun, "Electron Microprobe Instrumentation for Soft X-Ray Spectroscopy Applications," Sixth National Conference on Electron Probe Analysis, Pittsburgh, Pennsylvania, July 1971
4. W. L. Baun and D. W. Fischer, J. Appl. Phys. 38, 2092 (1967)
5. J. S. Solomon and W. L. Baun, "Electron Microbeam Probe Characterization of Al-Cu Alloys with Al and Cu Soft X-Ray Spectra," Air Force Materials Laboratory Technical Report AFML-TR-70-253 (1970)
6. W. L. Baun and D. W. Fischer, "The Effect of Chemical Combination on K X-Ray Emission Spectra from Magnesium, Aluminum, and Silicon," Air Force Materials Laboratory Technical Report AFML-TR-64-350 (1964)

## CHARACTERIZATION OF SURFACE AND INTERFACIAL OXIDE FILMS BY SOFT X-RAY SPECTROSCOPY

Charles G. Dodd

Philip Morris Research Center, Richmond, Virginia 23206

Oxide films occur on iron and steel surfaces under ambient conditions. When thin metallic films are deposited on these surfaces (by evaporation or sputtering), an interfacial oxide layer generally remains, and it affects the bonding of the surficial thin film to the substrate. Experimental techniques, utilizing electron microprobes, have been developed for the measurement of iron L soft X-ray spectra to characterize such interfacial films. Surface film thickness measurements on the metallic films were made independently by micro X-ray fluorescence and multiple beam interferometry. X-ray parameters used for characterization included spectral line peak intensity ratios and line widths at half maximum. A proposed model (of the surface film-interfacial oxide layer-metal substrate composite) has been developed that is consistent with the data. This model may be used to design soft X-ray spectroscopy experiments to fully characterize interfacial and/or surface oxide films in terms of composition, thickness, and inferred adhesion bonding properties.

Measurements on metallic thin film-steel substrate systems tend to support Holliday's proposal<sup>1</sup> that increases in the Fe  $L_{II}/L_{III}$  peak intensity ratio with decreasing  $E_0$ , for iron and steel at low  $E_0$  values (less than 4 keV), are caused mainly by surface oxides rather than by self absorption<sup>2</sup>. The use of measured Fe  $L_{III}$  line widths, as an additional characterization parameter, helps to explain variations of Fe  $L_{II}/L_{III}$  ratios with  $E_0$  for X-rays emitted from varying depths through the interfacial film region. In order to study adhesive bonding at the surficial film-oxide film interface, and to avoid the need to use inconveniently low  $E_0$  values for an electron probe, one should deposit a surface film with a thickness corresponding to its extrapolated mass range  $\rho R_x$ , at the  $E_0$  used<sup>3</sup>. This yields X-ray spectra that characterize a volume element of the interfacial oxide film immediately below the overlying metal film. On a plot of  $L_{II}/L_{III}$  peak intensity ratios vs.  $E_0$ , the  $E_0$  value at which the points for a given specimen intersect the reference iron metal line correspond roughly to the  $E_0$  value that should be used with the specific mass ( $\mu\text{g cm}^{-2}$ ) of the metallic film required to accomplish this objective. In a similar manner, experiments can be designed for characterizing thin layers at varying depths in a surface film, providing a stable electron beam can be attained at the

requisite  $E_0$  values, and that each  $E_0$  required is appreciably above  $E_{\text{Fe-L}}$ . Refer to figure 1.

A plot of  $L_{\text{II}}/L_{\text{III}}$  peak intensity ratios vs.  $L_{\text{III}}$  line widths also has been found to be useful for supporting the above model and for identifying film, bulk, and composite samples of various iron compounds, and of those of other first series transition metals. Ribble<sup>4</sup> used this type of plot to distinguish unambiguously between copper metal and copper compounds of varying valence states. Copper, however, is a true metal with a filled 3d shell. For other elements of the first transition group, such as iron, the interpretation depends on understanding variations in L spectra with  $E_0$  for elements with incomplete 3d shell electrons available for chemical bonding. An example of this type of plot is shown in figure 2, on which points are shown for reference iron metal standards at varying  $E_0$  values, together with corresponding points for  $\text{Fe}_2\text{O}_3$  and  $\text{Fe}_3\text{O}_4$ .

In another sense, the type of information displayed in figures 1 and 2 relates to a determination of a modified  $\Phi(\rho Z)$  function, measuring not primary X-ray line emission, but, rather, emission of chemical-bond-characterizing X-ray spectra with depth.

#### REFERENCES:

1. Holliday, J.E., "The effect of surface oxides on the changes in the Fe  $L_{\text{II}}/L_{\text{III}}$  ratio with accelerating voltage," in C. S. Barrett, J.B. Newkirk, and C. O. Ruud, editors, Advances in X-ray Analysis, Vol. 14, p. 243-249, Plenum Press (1971).
2. Chopra, D., "Ni L self-absorption spectrum," Phys. Rev. A, 1, p. 230-235 (1970).
3. Cosslett, V.E. and R. N. Thomas, "Multiple scattering of 5-30 keV electrons in evaporated metal films. II. Range-energy relations," Brit. J. Appl. Phys., 15, p. 1283-1300 (1964).
4. Ribble, T. J., " $L_{\text{II}}$  and  $L_{\text{III}}$  emission spectra of copper compounds," Phys. Stat. Sol. (a), 6, p. 473-478 (1971).

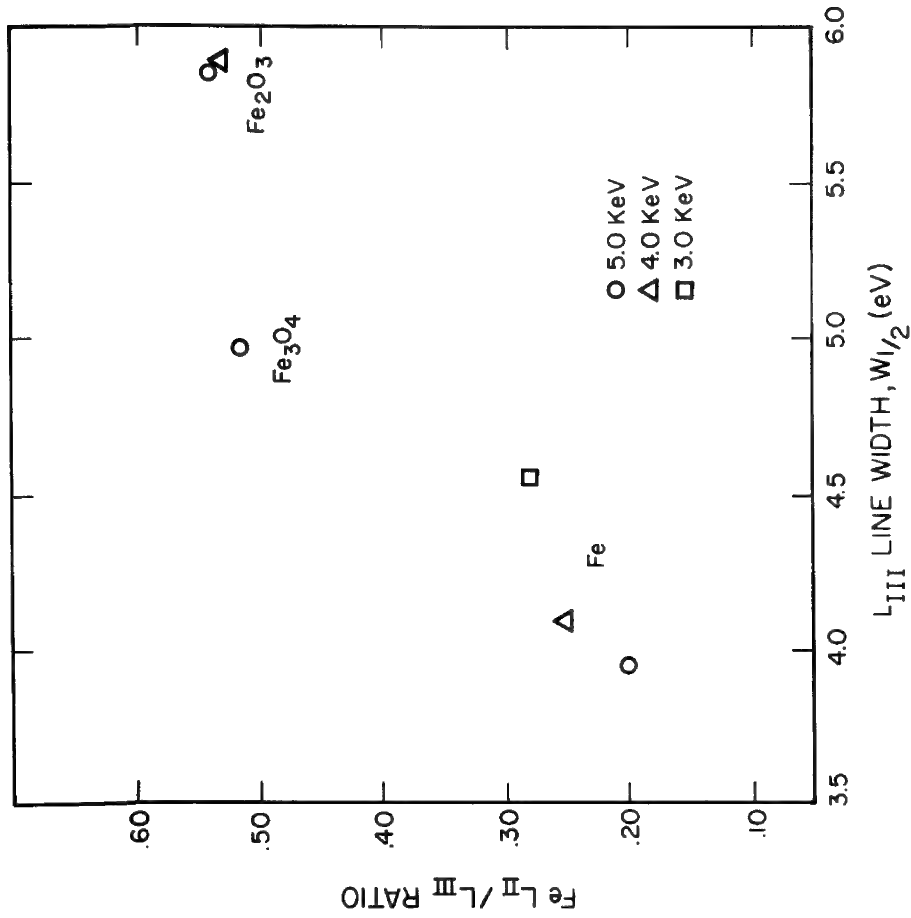


FIGURE 2. Fe  $L_{II}/L_{III}$  intensity ratios versus  $L_{III}$  peak width at half maximum, for Fe,  $Fe_3O_4$  and  $Fe_2O_3$  at varying  $E_0$ .

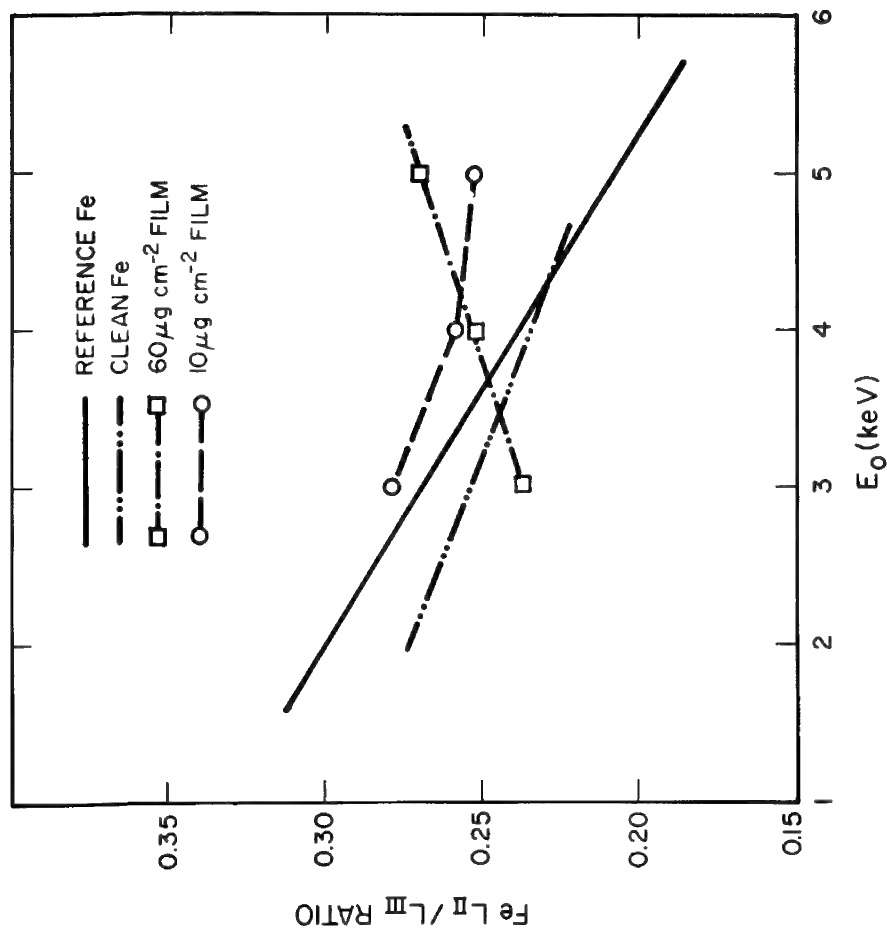


FIGURE 1. Fe  $L_{II}/L_{III}$  intensity ratio versus accelerating electron beam voltage for reference iron, Holliday's "clean" iron, and deposited-film-on-steel samples.

"Use of Bremsstrahlung and Characteristic X-ray Spectra  
to Study the Surface Potential Produced on Insulators"

by

W. B. Estill  
S. Gair  
J. L. Wirth  
Sandia Laboratories  
Livermore, California 94550

ABSTRACT

A technique has been developed to study the electrical potential of a dielectric surface as it is irradiated by a monoenergetic beam of electrons. The technique, which is described in detail, facilitates the measurement of field dependent secondary electron emission coefficients of dielectric materials and serves as a convenient method for assessing charge buildup during routine electron microprobe studies.

The technique has several variants, all of which are based upon the relationship between the electron energy at impact and various features of the Bremsstrahlung and characteristic X-ray emission from the irradiated zone. First, the maximum energy of the Bremsstrahlung continuum equals the electron impact energy; hence the surface potential is determined by the difference between the electron accelerating potential and the maximum Bremsstrahlung energy. Second, the surface potential can be measured by observing the apparent shift in the known characteristic X-ray appearance potential during irradiation.

Surface equilibrium potentials of from 4000 to 8000 volts have been observed in fused quartz and fiberglass samples irradiated by 15 to 30 keV electrons. The potentials were independent of beam current and increased slowly with beam energy. It is believed that field enhanced secondary emission is the limiting factor in the buildup of potential on the irradiated samples.



# AN ELECTRON SPECTROMETER FOR QUANTITATIVE MEASUREMENTS OF SURFACE VOLTAGES WITH ELECTRON MICROPROBE INSTRUMENTS \*

K. Y. Chiu and D. B. Wittry

Departments of Materials Science and Electrical Engineering  
University of Southern California, Los Angeles, California 90007

The measurement of surface voltages by measuring the absolute energy of secondary electrons with an electrostatic energy analyzer between the specimen and the detector has previously been suggested.<sup>1</sup> In this paper, a simple electron spectrometer using a parallel plate geometry is described. The parallel plate electrostatic analyzer with 30° entrance angle provides second order focusing and an angular aberration proportional to  $(\Delta\theta)^3$ . This principle was recently described by Green and Proca<sup>2</sup>. The energy resolution of this type of energy analyzer is  $\Delta E/E = 1.6(\Delta\theta)^3$  which is higher than other electrostatic analyzers.

The spectrometer was made of brass except for the top plate which was made of ARMCO iron to shield the magnetic field produced by the objective lens. All metallic parts are gold plated to minimize contact potential effects. The geometry is such that the spectrometer fits into the bore of the objective lens and the secondary electrons produced by electron bombardment can be collected by the secondary electron detector normally provided for the SEM mode in the electron microprobe instrument used.<sup>3</sup> The sample position and the exit slit are adjustable so that the sensitivity and resolution of the spectrometer can be altered. The thickness of the spectrometer was designed so that the specimen can be bombarded by a light beam focussed by the optical viewing system of the instrument. This makes it possible to study surface photovoltaic effects which result from a decrease in the barrier height due to drift of excess carriers in the "band bending" region near the surface.

When the spectrometer is in the position shown in Fig. 1, the top plate is grounded. The secondary electron signal is measured by the scintillator-photomultiplier through a microammeter, frequency-voltage converter and scaler and typed out by electric typewriter. At first, it was found that the peak position and amplitude changed with time because of contamination and contact potential effects. After careful cleaning and degassing the spectrometer by leaving it in vacuum for several hours before each test, it was found that contamination could be reduced. A secondary electron spectra of brass using a 10kV electron beam is shown in Fig. 2.

For quantitative measurements of changes of surface potential due to electron or photon bombardment, we calibrated the shift of the peak of the secondary electron curve with applying voltage between specimen and energy

analyzer. To prevent any significant change in the  $30^\circ$  entrance angle of the electrons because of this applied voltage, a grid which is at the same potential as entrance plate was placed above the sample.

As indicated by Wittry<sup>4</sup>, spurious effects due to contact potentials and residual fields are usually present. To diminish these effects and to separate the collection efficiency of spectrometer from energy analysis performed by the spectrometer, tests are being made using a composite sample holder as shown in Fig. 3.

---

\* Research sponsored by the National Science Foundation under Grant No. GK 3904 and by the Joint Services Electronics Program through the Air Force Office of Scientific Research under Contract F 44620-71-C-0067.

<sup>1</sup> O. C. Well and C. G. Bremer, J. Sci. Inst. Ser. 2, 1, 902 (1968).

<sup>2</sup> T. S. Green and G. A. Proca, Rev. Sci. Inst. 41, 1409 (1970).

<sup>3</sup> Model EMX-SM manufactured by Applied Research Laboratories, Inc., Sunland, California 91040.

<sup>4</sup> D. B. Wittry, X-Ray Optics and Microanalysis, R. Castaing et al. ed., Hermann Pres, (Paris), p. 168 (1966).

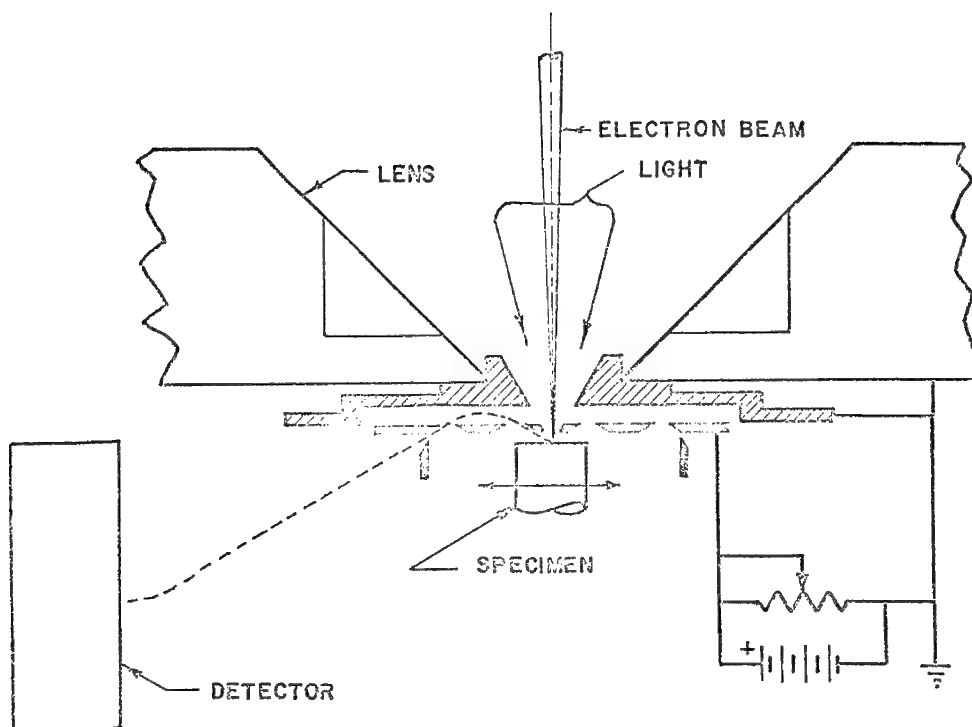


FIG. 1

14C

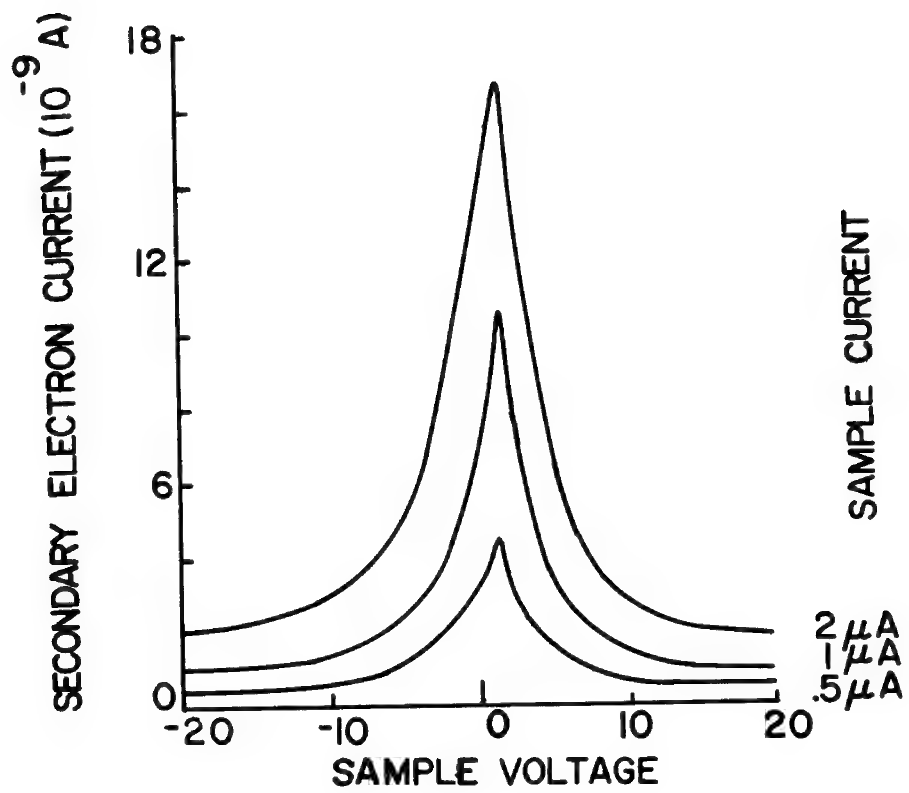


FIG. 2

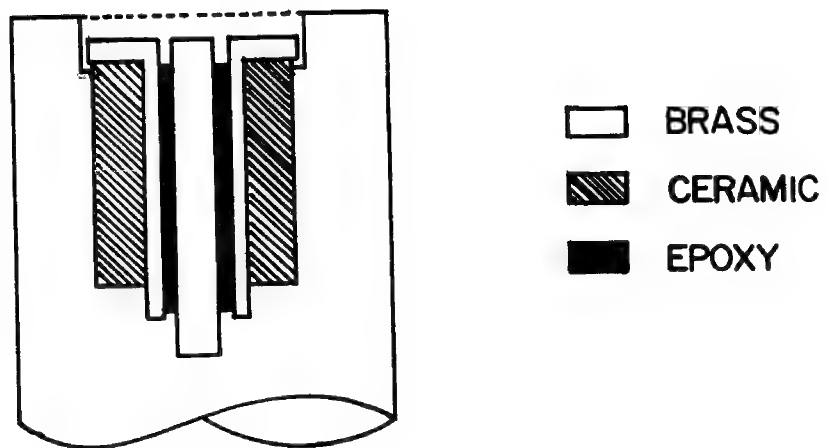


FIG. 3

ABSTRACT for Electron Probe Analysis Society of America  
Seventh National Conference, San Francisco, California  
July 1972

INVITED PAPER: Limits of Resolution in Electron Probe Instruments

T. E. Everhart and J. C. Wiesner  
Department of Electrical Engineering  
and Computer Sciences  
University of California, Berkeley, California  
94720

The resolution that can be achieved in electron probe instruments is limited by five basic and inter-related considerations. First, how small can one make the electron probe? Second, what information is desired from the sample? Third, how small a volume in the sample produces information? Fourth, what physical constraints are imposed by the gathering of this information? Fifth, how long is one willing or able to wait for the information to be collected?

The first problem depends upon electron optics: a source of a given size can be demagnified until its size is limited by diffraction and by the aberrations of the demagnifying system. However, source demagnification reduces the probe current, and hence the rate at which information is generated in the sample. This information rate depends upon the information desired: X-ray production is much less efficient than secondary electron production, for example. The nature of the sample and the information desired determines the volume from which the information comes. In general, the thinner the sample, the smaller this volume, and the higher the possible resolution. The nature of the information also influences the geometrical arrangement of the specimen and the final lens which produces the probe. A large solid angle is required between the sample and an energy-dispersive X-ray detector, for example, which establishes a minimum working distance, hence a minimum focal

length of the final lens, and hence its spherical and chromatic aberration constants. Finally, operator patience and instrumental stability are two limitations on the length of the time required to gather the desired information. Anything that increases the information rate will reduce this time, and hence improve the possibility of better resolution. Source brightness (Richtstrahlwert), information generation efficiency, and information collection efficiency are three parameters that should be maximized to optimize the resolution capability of any electron probe instrument for any given information.

The brightest electron source known today is the field emission cathode. Although a simple approximate formula is often used to estimate the source size of this cathode, a complete analysis of the source size to be expected from the field emission diode has been recently completed by Wiesner<sup>1</sup>. His analysis predicts that an optimum tip size exists, and that as the emission angle increases, the apparent source size increases linearly at first, and then as the third power of emission angle. Since diffraction effects (and lack of beam current) prevent one from reducing the emission angle too far an optimum half angle of emission exists in the neighborhood of 0.005 to 0.01 radian.

The accelerating fields of the electron gun also have aberrations associated with them.<sup>2</sup> A principal aberration of accelerating lenses is associated with the aperture lens effect. This can be minimized by clever electrode design<sup>3</sup>. Even so, the aberrations associated with the accelerating structure and not the source size of the field-emission tip presently limit the diameter of the probe formed by this lens. This will be shown for typical values cited by Crewe et. al.<sup>4</sup> The improved gun of Komeda and Saito<sup>5</sup> should behave similarly.

The source produced by the gun is demagnified by electron lenses to produce the final probe. For scanning transmission electron microscopy, the sample is very thin, and can be inserted between the pole-pieces of a condenser-objective lens. The resolution is normally limited by the aberrations of that lens, and by diffraction. If the electron optical demagnification is too great, the current in the final probe is decreased below its optimum value, and the information rate is unduly low. Hence, for a given source, and a given final lens, an optimum demagnification exists. Experimentally, it is easiest to arrive at this optimum value for a given source by using an auxiliary lens<sup>5,6</sup>. At this optimum value, which will have significant current in the probe, the probe diameter is given approximately by  $C_s^{1/4} \lambda^{3/4}$ , as was shown first by Smith<sup>7</sup>. If the demagnification is greater, the information rate decreases, and the resolution can improve somewhat. The best performance reported to date is a resolution of five Angstroms<sup>8</sup>.

Information generation in the sample is related to electron energy loss, and to the probability of escape of the generated information, whether this consists of X-rays or other photons, secondary, backscattered or Auger electrons, etc. First let us consider the electron energy loss. The volume of energy loss has been measured more accurately recently using a new method<sup>9</sup>. Recent results will be reported. In addition, the previous work of Wells,<sup>10</sup> which gives a distribution function for the escape of secondary electrons as a function of the distance from the point of entry of the primary beam, has been extended to oblique incidence<sup>11</sup>. These results will be presented. They show that resolutions of the order of the mean free path of secondary electrons in the sample material should be obtained with solid materials, that is, resolutions of about ten Angstroms should be possible with the proper

choice of material. These results have particular importance in view of coating procedures used in preparing biological samples for scanning electron microscope examination. Recently, resolutions of thirty to forty Angstroms have been reported using secondary electrons in scanning electron microscopes<sup>5,12</sup>.

While this value will probably be improved upon with better samples and higher signal currents made possible by brighter sources, the best resolutions will be obtained in the transmission scanning electron microscopy of thin samples. This will require increased beam voltage to reduce  $\lambda$ , the electronic wavelength.

#### REFERENCES

1. J. C. Wiesner - Point-Cathode Electron Sources, Report No. ERL-70-6, (Electronics Research Laboratory, University of California, Berkeley, 94720).
2. T. E. Everhart, J. Appl. Phys. 38, 4944-4957, 1967.
3. A. V. Crewe, D. N. Eggenberger, J. Wall, and L. M. Welter, Rev. Sci. Instr. 39, 576-583, 1968.
4. A. V. Crewe, J. Wall, L. M. Welter, J. Appl. Phys. 39, 5861-5869, 1968.
5. T. Komoda and S. Saito, Scanning Electron Microscopy/1972, (IIT Research Institute, Chicago, 1972) pp. 130-136.
6. R. Speidel, T. E. Everhart, and C. S. Kim, Electron Microscopy 1970, Vol. 1, P. Favard, ed., (Soc. Francaise de Microscopie Electronique, Paris, 1970) pp. 211-212.
7. K.C.A. Smith, Encyclopedia of Microscopy, G. L. Clark, ed., (Reinhold, New York, N.Y. 1961) pp. 241-251.
8. A. V. Crewe, Phil. Trans. Roy. Soc. Lond. B. 261, 61-70, 1971.
9. R. F. Herzog, J. S. Greeneich, T. E. Everhart, and T. Van Duzer, IEEE Trans. Electron Devices, EO-19, 635-641, 1972.
10. T. E. Everhart, O. C. Wells, and C. W. Oatley, J. Electronics and Control 1, 97-111, 1959.
11. T. E. Everhart and M. S. Chung, to be published in J. Appl. Phys.
12. A. N. Broers, Electron Microscopy 1970, Vol. 1, P. Favard, ed., (Soc. Francaise de Microscopie Electronique, Paris, 1970) pp. 239-240.

## LOW-LOSS IMAGE FORMATION IN THE SURFACE SEM

Oliver C. Wells

IBM Thomas J. Watson Research Center, Yorktown Heights, N. Y.

In commercial SEM's, a solid specimen is examined by collecting the secondary electrons when the surface is scanned by an electron beam.<sup>(1)</sup> The resolution as measured at a sharp edge is limited by the beam diameter, which can be in the range 30 Å to 50 Å.<sup>(2)</sup> The ability of the SEM to see details close to the sharp edge is limited at about 100 Å by the escape depth of the secondary electrons. Also, there is a bright fringe for a distance of a micron or so from a sharp edge caused by penetration.

An alternative approach to high resolution surface scanning microscopy is to collect electrons having a small energy loss.<sup>(5,6)</sup> Typically, with 15 kv operating potential, electrons are collected if they have lost less than 400 ev. With aluminum, this corresponds to a path length of 1200 Å. The collected current is only 0.1% of the beam current, but it is still possible to obtain an image.

The properties of the low-loss image are as follows:

Side-by-side resolution. This was tested using a sample described by Broers<sup>(3)</sup> and Blakeslee.<sup>(4)</sup> Figure 1 shows lines etched in GaAs with a center-to-center spacing of 220 Å. These lines can be seen in both the secondary electron and the low-loss image. This shows that the low-loss image has the potential for high resolution surface microscopy.

Shallow depth perception. The low-loss signal is generated in a thin surface layer. This has been used to show the presence of a thin self-supported alumina layer across the top of cavities formed in aluminum by electromigration.<sup>(5,6,7)</sup> The thinness of the escape layer has been explained by a scattering model in which the electron is deflected by a single Rutherford wide-angle event in the specimen.<sup>(8)</sup> Figure 2 shows a corrosion spot in passivated chrome. The secondary electron image shows a dark region round the edge of the cavity. This is not present in the low-loss image, which shows that the edge is overhanging in this sample.

Reduced penetration effect at sharp edges. The bright band at a sharp edge in the low-loss image has a width of about 1200 Å for the operating condition described above. This is narrower than it is in the secondary electron image by an order of magnitude.

High contrast from surface topography. The surface scratches on the sample shown in Figure 2 are shown more clearly in the low-loss image. In the same way, in Figure 4 there is a line present in the low-loss image which is not visible in the secondary electron image. We believe that this is caused by a shallow surface step. An improved contrast has also been found with some other samples.



As compared with the above advantages, the low-loss image cannot show parts of the specimen surface that are shielded from the detector, neither can it show voltage or magnetic contrast.

The low-loss image is approximately the reciprocal of the image of a solid specimen obtained by reflection in the conventional transmission electron microscope. (True reciprocity requires that there should be no energy loss.) This can be seen by reversing the path of the rays in the specimen, and then equating the source in one case to the detector in the other. The advantage of the low-loss image as compared with the TEM reflection image arises because: (1) The collector in the surface SEM subtends a larger solid angle than the illuminating system in the TEM. (2) A larger energy band can be accepted. (3) The heating of the specimen is reduced. A similar relationship exists between the TEM and the transmission SEM when examining specimens in transmission.<sup>(9,10)</sup> As opposed to this, there does not seem to be a reciprocal version of the secondary electron image.

I would like to thank C. G. Bremer for technical help.

#### References:

- (1) K. C. A. Smith and C. W. Oatley, Brit. J. Appl. Phys., 6 391-399 (1955).
- (2) A. N. Broers, Rev. Sci. Inst., 40, 1040-1045 (1969).
- (3) A. N. Broers, Sept. Cong. Int. Mic. El., Grenoble 1970. 1 239-240.
- (4) A. E. Blakeslee, 3rd Int. Symp. GaAs, Aachen 1970, 283-291.
- (5) O. C. Wells, Appl. Phys. Letters, 19 232-235 (1971).
- (6) O. C. Wells and C. G. Bremer, Proc. 6th Int. Conf. on x-ray optics and microanalysis, Osaka Sept. 1971, in press.
- (7) N. G. Ainslie, F. M. d'Heurle and O. C. Wells, Appl. Phys. Letters, 20, 173-174 (1972).
- (8) O. C. Wells, 5th Annual SEM Symp., Chicago, Apr. 1972, 169-176.
- (9) J. M. Cowley, Appl. Phys. Letters, 15 58-59 (1969).
- (10) A. V. Crewe and J. Wall, J. Mol. Biol., 48 375-393 (1970).

Fig. 1 Resolution test specimen with 220 Å ridge-to-ridge spacing: (a) Secondary electron image. (b) Low-loss image.

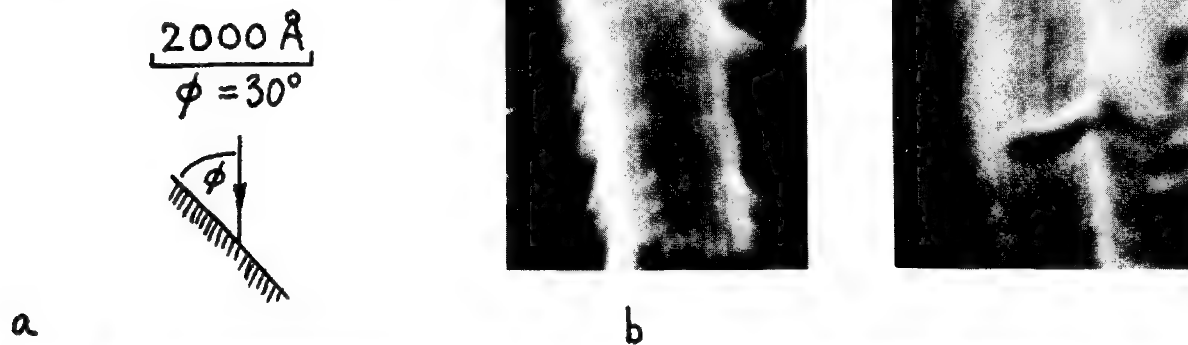


Fig. 2 Corrosion spot in passivated chrome: (a) Secondary electron image. (b) Low-loss image.

$$\frac{25 \mu}{\phi = 40^\circ}$$

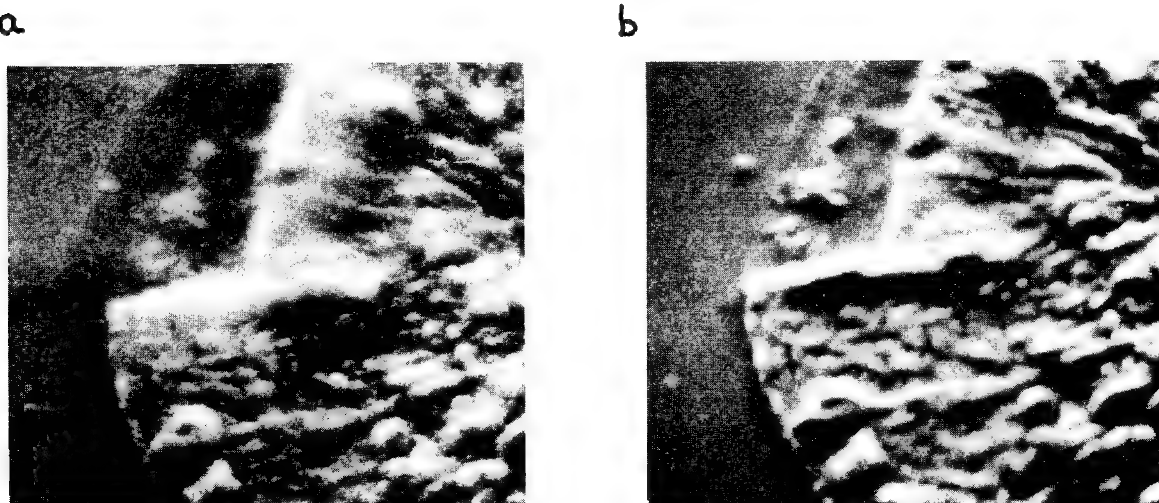


Fig. 3 Contaminant spots on silicon dioxide: (a) Secondary electron image. (b) Low-loss image.

$$\frac{2 \mu}{\phi = 40^\circ}$$

On the Conditions Necessary to Observe Crystalline Defects in the  
Scanning Electron Microscope Using Back Scattered Electrons

D. R. Clarke

Cavendish Laboratory, Cambridge, England.

The application of the scanning electron microscope to the study of the microstructure of materials would be significantly extended beyond the present surface structure and morphological investigations if the underlying crystal defects could be detected. Until recently this had not been possible and a simple calculation by Booker (1970) indicates that with the contrast available the scanning times required are prohibitive in microscopes having a conventional electron gun and operating at 20 or 30 keV. The recent construction of scanning microscopes with field emission guns of brightness greater by about  $10^4$  than that of conventional guns however changes the situation and makes the detailed calculation of the conditions necessary to observe defect images timely.

A few results of these calculations and some of their consequences are presented in this summary for the particular case of dislocations.

The basis of the calculations is that the strain field of the defect causes local transitions between Bloch wave states which have differing probabilities of being back scattered. The total back scattered intensity is then the integral of the square of the back scattered amplitude over the primary electron penetration depth. The problem is formulated by a slight extension of the existing dynamical electron diffraction theory (see HHNPW, 1965). As an initial approximation a two beam model was considered in which it was assumed that at each atomic site the back scattering probability was independent of the diffraction vector  $g$ . The diffraction data used corresponds to copper at an electron energy of 20 keV (Humphreys and Hirsch, 1968).

As an example of the computed dislocation profiles, Fig. 1 shows the influence on the image of the Bragg reflection used. Apart from variations in the background intensity the profiles are relatively insensitive to the deviation  $w$  from the exact Bragg condition, and changes approximately as  $\exp(-w^2)$ . An image screw dislocation was used in order to render the surface tractions zero and it is interesting that in this case the qualitative model based on local lattice tilts at the surface (Booker, 1970) would show no contrast.

The dynamical diffraction theory calculations lead to a theoretical contrast value but what is really required is the contrast attainable using a beam of finite width and of finite divergence. From the image profiles it can be deduced by convoluting with various beam sizes that most of the theoretical contrast will be attained provided a probe of width  $d$  and illumination semi-angle  $\alpha$  is chosen to satisfy the conditions

$$d \leq (g \cdot b) \xi_g / 5$$

$$\alpha = \frac{\Delta w}{g \xi_g} \leq \frac{1}{g \xi_g}$$

These necessary conditions for the observation of dislocations may be displayed as in Fig. 2 for  $g \cdot b = 1$  and used to determine the electron beam parameters required for different Bragg reflections. The aberration limitations marked refer to conventional scanning microscopes. A set of lines satisfying the equation  $d = A/\alpha$  has been indicated where  $A$  is given by

$$A^2 = (1.22\lambda)^2 + 0.4 \frac{I}{B}$$

and determines the current  $I$  that a gun of brightness  $B$  will deliver into a spot of diameter  $d$ .

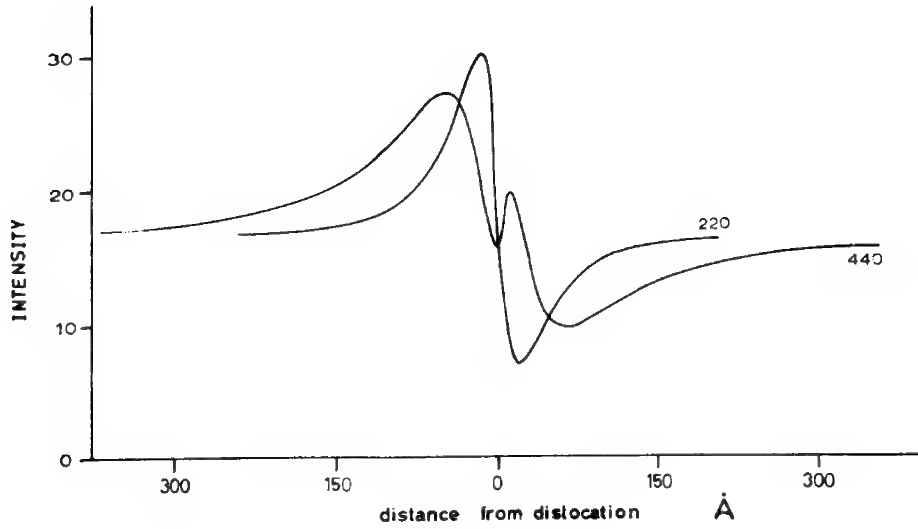
In general the curves indicate that it is better when studying thin foils to use as high a voltage as possible, in a microscope of low aberration. This has been substantiated by the author using a microscope fitted with a conventional gun at 80 keV to observe weak images of dislocations in polycrystalline aluminium and more recently by Hashimoto, Kimoto and Stern (private communication) in  $\text{MoS}_2$  at 100 keV.

The calculations however illustrate that except in these special circumstances, of high voltages, energy selective detectors and very long exposures, it is not possible to observe crystal defects using conventional electron guns. The use of field emission sources, concentrating on higher current than a conventional gun into spot sizes below  $1000\text{\AA}$ , will shorten the recording times to routinely convenient values. It remains to be seen however whether the defect contrast will be observable in the presence of morphological contrast without the use of energy selective detectors especially when studying bulk crystals.

D.R.C. wishes to acknowledge the guidance of Dr A. Howie with whom the initial results of these calculations were published.

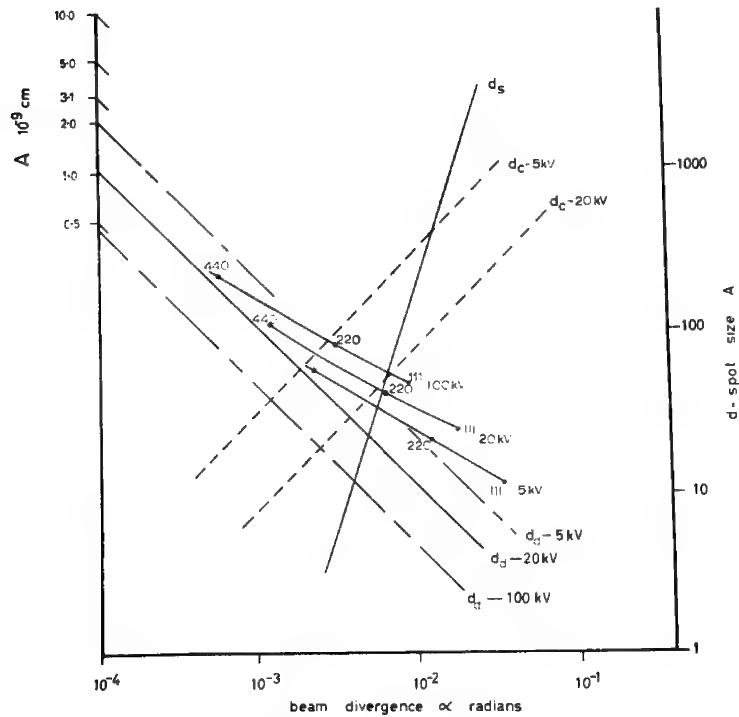
#### References

- Booker, G.R., 1970, "Modern Diffraction and Imaging Techniques in Materials Science" edited by S. Amelinckx, R. Gevers, G. Ramut and J. Van Landuyt (North- Holland).
- Clarke, D.R., 1971, *Phil. Mag.*, 24, 973.
- Clarke, D.R. and Howie, A., 1971, *Phil. Mag.*, 24, 959.
- Hirsch, P.B., Howie A., Nicholson R.B., Pashley D.W. and Whelan M.J., "Electron Microscopy of Thin Crystals" (Butterworths).
- Humphreys, C.J. and Hirsch, P.B., 1968, *Phil. Mag.*, 18, 115.



The image profiles of a screw dislocation for both 220 and 440 reflections satisfying the conditions  $\mathbf{g} \cdot \mathbf{b} = 1$  and 2 respectively.

FIGURE #1



A graph of probe spot size against beam divergence indicating the limits due to spherical and chromatic aberrations  $d_s$  and  $d_c$ , and diffraction,  $d_d$ . Also plotted are the lines satisfying the attainable contrast conditions at different accelerating voltages, and labelled with a number of various reflections.

FIGURE #2

ANOMALOUS CONTRAST EFFECTS ENCOUNTERED IN  
SEM STUDIES OF CUBIC BORON NITRIDE

by

E. Lifshin and R. C. DeVries  
General Electric Corporate Research and Development

In the scanning electron microscope secondary electron image contrast arises principally from point by point variations in either the number of secondary electrons emitted or collected from a specimen. The first category includes the dependence of the secondary electron yield on surface topography and work function. These effects are easily detected by the conventional Everhart-Thornley<sup>1</sup> detector which uses a biased grid to attract secondary electrons to the tip of an even more strongly biased scintillation detector. The second category includes voltage and magnetic contrast effects which cause variations in the detector collection efficiency by altering secondary electron trajectories and, consequently, the number which ultimately reach the detector. While these effects are observable with the conventional detector, they may be enhanced by the use of directional detectors which more carefully define the electrostatic field in the vicinity of the sample, as have been developed by Banbury and Nixon.<sup>2</sup>

Backscattered electron image contrast also depends strongly on surface topography, but tends to be much more directional (as exemplified by shadowing effects), depends on the average atomic number of the specimen, and is relatively insensitive to local magnetic and electrostatic fields. With these factors in mind, it was quite surprising to observe a series of unusual secondary electron images, typified by figure 1, which were encountered during a study of a polished section of cubic boron nitride grains mounted in a conducting glass matrix, especially when the dark regions shown in figure 1 appeared only faintly outlined in a backscattered electron image of the same area as shown in figure 2. Starting with figure 2, one would conclude that there are no significant variations in either surface topography or average atomic number except for some surface relief in polishing which is shown in a Nomarski interference micrograph (figure 3) of the same region. This is to be expected, since the grains are single phase with a very limited range of stoichiometry.

If major compositional effects and surface topography are eliminated as sources of contrast, then voltage contrast or altered electron yield remain, either of which would require the presence of some impurity in the specimens which were found to be semiconducting. Ion microprobe analysis showed the presence of the order of 100 PPM of Li in the dark-appearing

regions as shown in figure 4. Several possible explanations of the origin of this contrast will be proposed.

### References

1. Everhart, T. E., Thornley, R. F. M., J. Sci. Instrum. 37, 246-48 (1960).
2. Banbury, J.R. and Nixon, W. C., J. Sci. Instrum. Ser 2, 2, 1367-72.

### Acknowledgements

The authors wish to thank J. Westbrook for supplying the original sample which showed this effect, J. McHugh of the Knolls Atomic Power Laboratory for the ion microprobe analysis, and M. McConnell for the specimen preparation and Nomarski micrographs.

### Figure Captions

1. Secondary electron image 500X
2. Backscattered electron image
3. Nomarski interference micrograph
4. Li ion distribution image

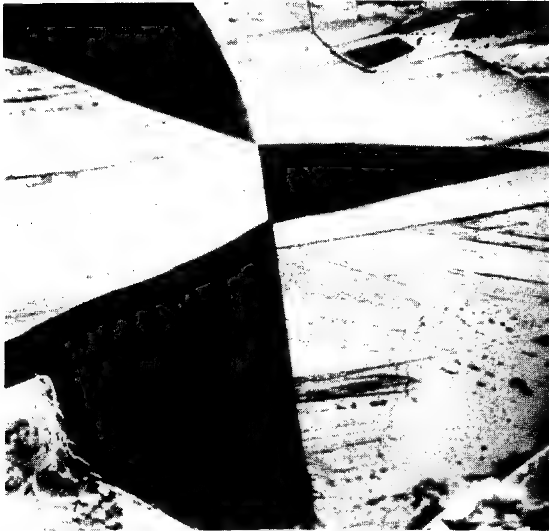


FIGURE 1



FIGURE 3



FIGURE 2



FIGURE 4



Scanning Electron Microscope Collection of  
Secondary Electrons Using a Small Aperture Probe

R.K. Matta, Department of Radiation Health, University of Pittsburgh  
G.L. Kusic, Department of Electrical Engineering, University of Pittsburgh

Abstract

It has been shown by several investigators that low energy electrons, or 'true' secondary electrons of energy in the range 0-30 eV are the most desirable in scanning microscopy.<sup>(1)(2)</sup> Typical secondary electron collectors used have large numerical apertures and effectively collect about 65% of the electrons with initial energies below 50 eV. Such probes, if located near the bombarded sample, also collect a significant amount of backscattered electrons, i.e. those above 50 eV initial energy. Everhart<sup>(3)</sup> has shown that a combination of suitable location and adjustable slot aperture allows one to select secondary electrons of a specific energy as modified by initial angle and location at the sample. However, the efficiency of collecting secondary electrons decreases in such schemes.

In the experimental and theoretical results presented herein, a small aperture cylindrical probe is used which focuses secondary electrons into the detector. (See figure 1). The small aperture detector is positioned close to the sample, effectively collecting all the secondary electrons, but a significant increase in probe scintillator gain is obtained when a voltage bias is applied to the sample. Figure 2 indicates relative gain as the specimen bias is varied. Preliminary measurements as well as a two-dimensional digital computer simulation indicate the increased gain may be due to the low energy (secondary electrons) being reflected and multiplied at the inside surface of the collector. At lower sample bias the secondary electrons do not reach the collector wall. At a high sample bias either the angle of incidence is too large for suitable multiplication or the secondary electrons are drawn to the bottom pole of the piece.

The increase in gain more than compensates for backscattered electrons which may enter the probe. The location of the probe is not critical for the bias may be varied to attain suitable focus conditions. In figure 3A, the signal is shown when the probe was positioned for 'best contrast' and in figure 3B, the bias is applied. There may be other effects present, but the result of the bias shows a significant improvement in image contrast.

The digital computer simulation utilized an integral equation approach described in reference 3, breaking up an approximate boundary into the 41 segments indicated in figure 1. The integral equation technique<sup>(4)(5)(6)</sup> readily lends itself to irregular domains; it offers a significant reduction in computation time for larger problems, plus provides an analytical expression for the field and gradient at any point. Thus, a specific region, such as around the sample and probe entrance, may be selectively detailed without increasing the detail in other parts of the simulation. The analytical results qualitatively agree with the experimental data.

### References

1. Pease, R.F.W., "Fundamentals of Scanning Electron Microscopy", Proceedings of the Fourth Annual SEM Symposium, IIT Research Institute, Chicago, Illinois, April, 1971.
2. Thornton, P.R., "Scanning Electron Microscopy", Chapman and Hall Limited, London, 1968.
3. Everhart, T.E., "Reflections on Scanning Electron Microscopy", Proceedings of the SEM Symposium, IIT Research Institute, Chicago, Illinois, April, 1968.
4. Kusic, G.L., "Optimal Design of Electrostatic Lenses Using Integral Equation Field Methods", IEEE Transactions on Electron Devices, October, 1971.
5. Singer, B. and Braun, M., "Integral Equation Method for Computer Evaluation of Electron Optics", IEEE Transactions on Electron Devices, October, 1970.
6. Mautz, J.R. and Harrington, R.F., "Computation of Rotationally Symmetric Laplacian Potentials", Proceedings Institute of Electrical Engineering, (London), April, 1970.

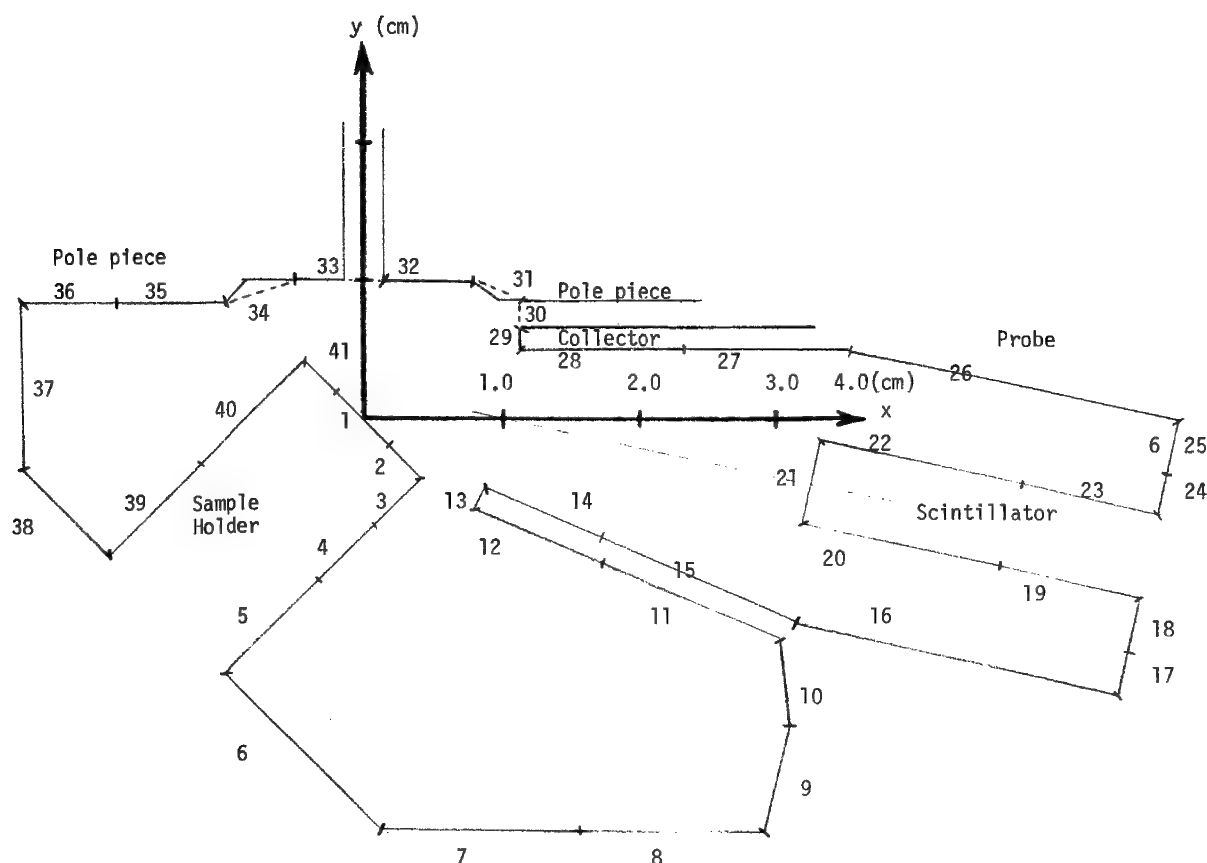


Figure 1. Two-Dimensional View of the Sample Holder, Pole Piece, and Probe with Integral Equation Boundary Segments Shown

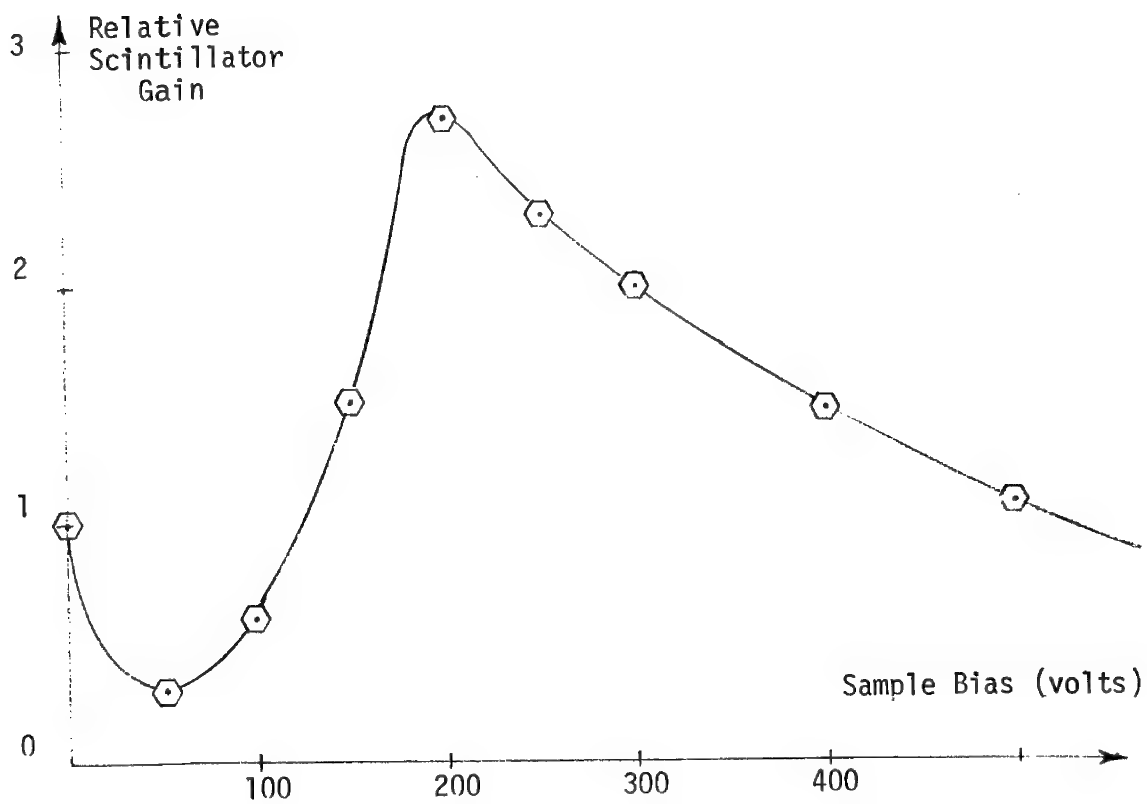


Figure 2. Scintillator Gain as a Function of Sample Bias

3A  
Without  
Sample Bias

3B  
With  
Sample Bias

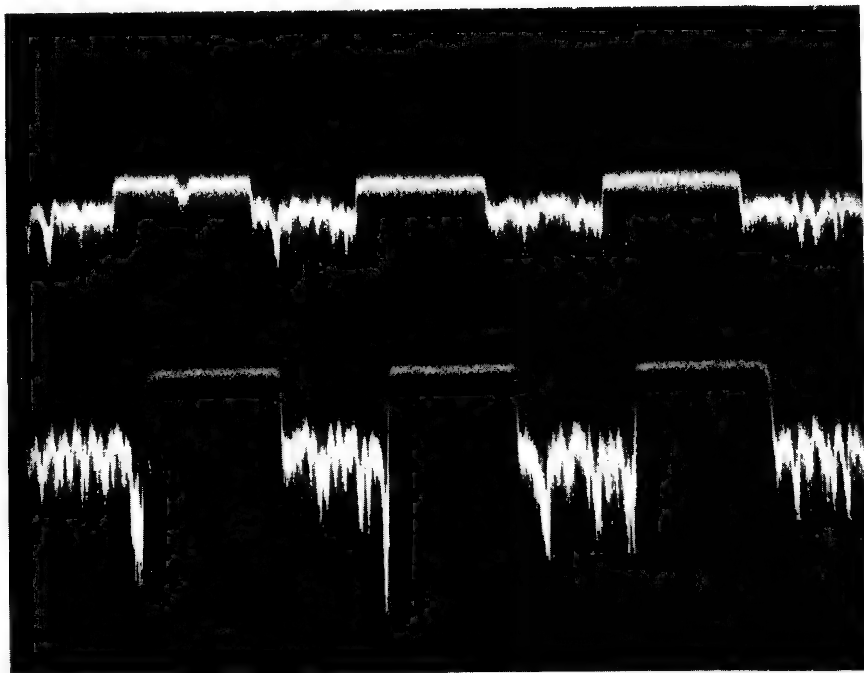


Figure 3. Scintillator Signal With and Without Sample Bias

## SEM Comparison of the Intracellular Ultrastructure of Botanical Specimens Prepared by Metal Coating and a New Technique for Surface Conduction

B.J. Panessa

Biology Department, New York University, 100 Washington Square East, N.Y.N.Y. 10003

By their physical nature, most biological specimens do not lend themselves readily to examination in the SEM. Most tissues are quite soft and may shift or distort during dessication, which occurs in the scope vacuum or under the electron beam at high accelerating voltages. To obviate this, investigators have subjected specimens to periods of long fixation followed by dehydration in solvents (ethanol, acetone, ether...), or freeze drying. Delicate tissues, such as botanicals, do not withstand alcoholic dehydration or freeze drying well, and for this reason, in our laboratory they have been examined after glycerol infiltration(1). The glycerol replaces tissue-bound water and prevents dessication-induced distortions. Since most biologicals are non-conducting, metal is usually evaporated onto the surface of the tissue to prevent charging.

In our studies of the various structure-function relationships of the tissues of carnivorous plants (Sarracenia purpurea, Drosera rotundifolia, Pinguicula vulgaris and Dionea muscipula), the material is trimmed in such a way as to expose the cellular interior. These plants, especially Sarracenia, have cells with extremely large, central cell sap vacuoles, and very little cytoplasm; two factors which simplify observation of intracellular organelles as they are not obscured by cytoplasm (Fig. 1).

In the past, to avoid charging we examined these organelles at low accelerating voltages, but found this to be inadequate because the amount of information obtainable is limited by poor resolution. By coating the tissue with carbon (25-50 Å) -gold-palladium (175-300 Å) we were able to use higher accelerating voltages (5-10 Kv), however we found that the coating procedure often produced tissue damage. Furthermore, a comparison of scanning images obtained from tissue prepared in this manner (Fig. 2) and tissue prepared by treatment with aqueous iodine followed by lead acetate(2), showed that the coated tissue presents quite a different appearance than directly observed material (Fig. 3). Metal coated specimens exhibited a smooth cytoplasm with few cytoplasmic strands or channels. Organelles also appeared somewhat flattened. Uncoated specimens, on the other hand, possessed numerous cytoplasmic strands and large networks of anastomosing strands believed to be endoplasmic reticulum. Mitochondria, chloroplasts and nuclei could be easily distinguished, many of which possessed complex surface configurations. Frequently mitochondria and chloroplasts were observed to be joined by thin cytoplasmic strands; a rare occurrence in coated preparations. Membranes as well as the elements of the cell walls were clearly apparent.

In order to specifically identify structures observed in scanning images, the scanning specimen was removed from its stub, embedded in plastic, sectioned and examined by transmission electron microscopy, TEM(3). TEM micrographs showed no plasmolysis in either the coated or uncoated SEM specimens. The increased information obtainable from uncoated

specimens was a result of the direct visualization of the cell surface.

Not only does treatment of tissue with iodine-lead acetate permit direct observation of tissues, resulting in more information, but it increases the specimen's conductivity permitting long periods of examination(3-5 hours)with little or no charging.Specimens appeared to be more stable under the electron beam, and after removal from the specimen chamber were still green and turgid.

## References

- 1.B.J.Panessa and J.F.Gennaro, Jr.1972.IITRI Symposium, Chicago. (Proceed.)
- 2.B.J.Panessa and J.F.Gennaro, Jr.1972.EMSA, Los Angeles. (Proceed.)
- 3.B.J.Panessa 1971.Amer.Soc.for Cell Biol., New Orleans.(Proceed.):215

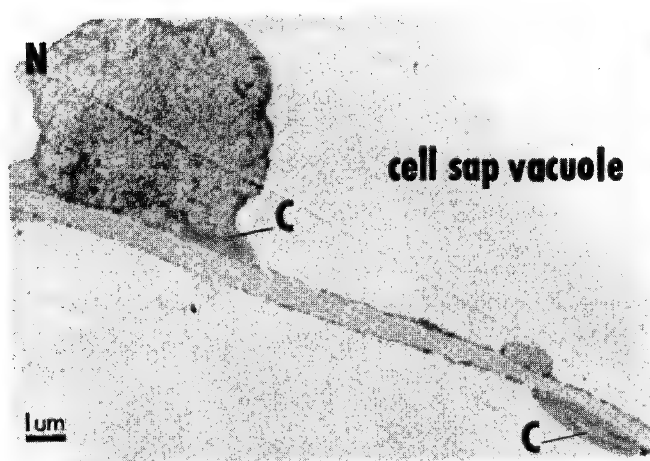


Figure 1.Sarracenia cells routinely prepared for TEM show paucity of cytoplasm and large empty vacuole.N;nucleus, C;chloroplast.

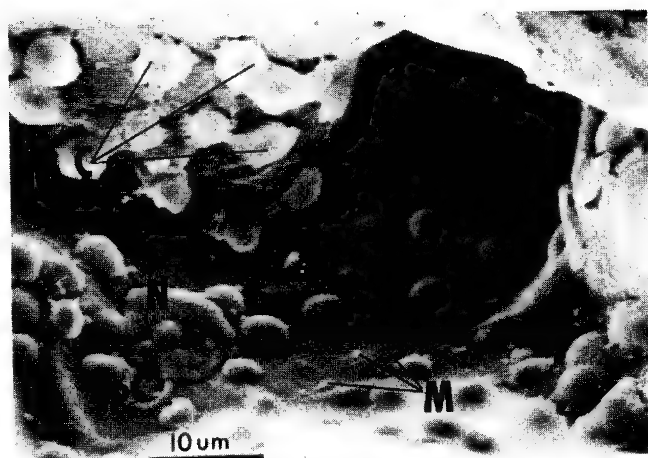


Figure 2.SEM of single cell of Sarracenia. Coated preparation showing nucleus(N), chloroplasts(C), pit field(P)and mitochondria (M).

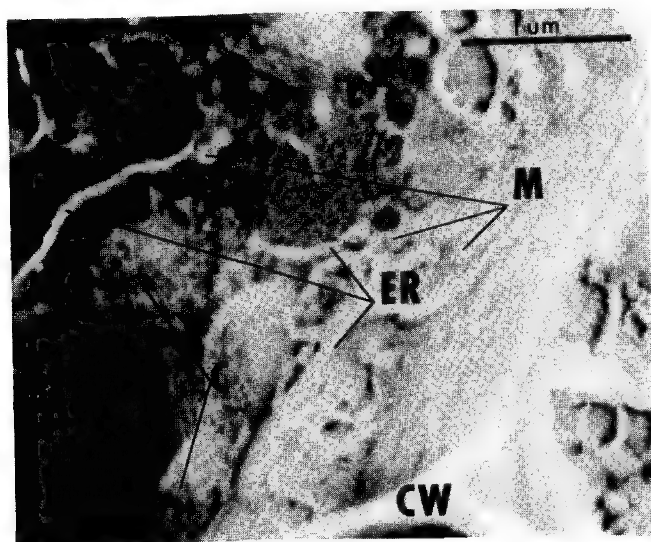


Figure 3.Iodine -lead treated cell of Sarracenia with chloroplasts(C), ER, mitochondria(M) and cell wall(CW).

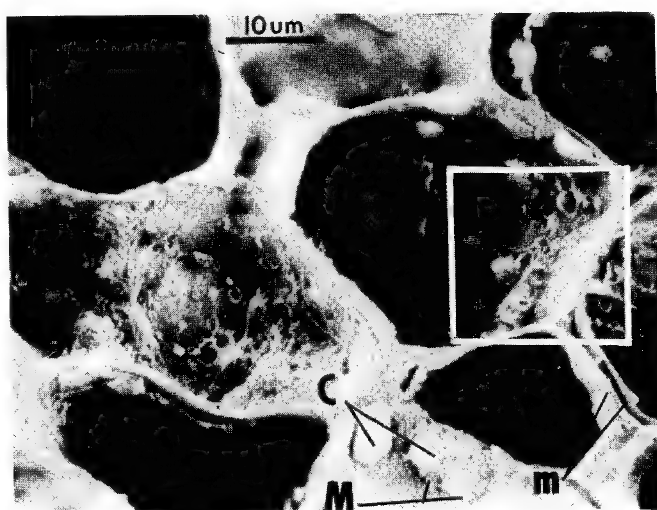


Figure 4.Low magnification of Fig.3(in enclosed area).Note the membranes(m).

# ENZYME ETCHING IN SCANNING ELECTRON MICROSCOPY

Robert I. Lin and Paul Lublin  
GTE Laboratories Incorporated  
Bayside, New York 11360

Most of the biological substances we see after fixation are polymerized macromolecules, such as proteins, cellulose, nucleic acids, glycoproteins, and lipoproteins. These materials, in their natural state, and some other synthetic organic substances are substrates for various enzymes. Selective removal of a certain component from a biological sample or a synthetic organic substance by a specific enzyme can reveal the ultrastructures in a way related to their chemical nature. By combining this technique with scanning electron microscopy, the anatomy at macromolecular level may be achieved.

In the present study the following enzymes were used on samples from various biological sources: pronase,<sup>1,2</sup> (a very potent, wide spectrum, protein hydrolyzing enzyme from a fungus), trypsin<sup>3</sup> (a protein hydrolyzing enzyme from pig pancreas), ribonuclease<sup>4-9</sup> (RNA and DNA hydrolyzing enzymes, respectively, from pancreas), cellulase (cellulose digesting), chitinase (chitin digesting), and lysozyme<sup>12-15</sup> (which digests bacterial cell wall polysaccharides).

Most fixative agents, such as glutaldehyde and formaldehyde, operate as cross-linking agents bridging amino groups or other functional groups. After fixation the susceptibility of the substances to enzyme can be changed drastically, either due to alteration of functional groups or stereo conformation.

The etching was done either before fixation, after fixation, and both before and after. The observed results on various materials will be discussed in the light of cytochemistry and fixative effects.

## References

1. Nomoto et al., J. Biochem (Tokyo) 48, 598 (1960).
2. Hashimoto, et al., Ann. N.Y. Acad. Sci. 106, 233-246 (1964).
3. Travis, J. and I.E. Liener, J. Biol. Chem. 240, (1962).
4. Schmidt, G.R., et al., J. Biol. Chem. 192, 715 (1951).
5. Hirs, C.H.W., J. Biol. Chem. 235, 625 (1960).
6. Hirs, C.H.W., S. Moore and W.H. Stein, J. Biol. Chem. 235, 633 (1960).
7. Crestfield, A.M. in Abs. Comm., 5th Intern. Congr. Biochem. London: Pergamon Press, p. 37 (1966).
8. Kunitz, M., J. Biol. Chem., 164, 563 (1946).

9. Scherago, H.A. and J.A. Rupley in *Advances in Enzymology*: F.F. Nord: Ed., New York: Interscience, Vol. XXIV, p. 161 (1962).
10. Laskowski, M., Sr., in *the Enzymes*, Boyer, Lardy and Myrback, Eds., New York: Academic Press Vol 5, p. 123 (1961).
11. Kunitz, M.J., *J. Gen. Physiol.*, 33, 349 (1950).
12. Shugar, D., *Biochim. Biophys. Acta* 8, 302 (1952).
13. Hamaguchi, K. et al., *J. Biochem.* 46, 1659 (1959).  
Hayahi, K. et al., *Ag. Biol. Chem. (Japan)* 28, 517 (1964).
14. Litwack, G., *Proc. Soc. Exptl. Biol. Med.* 87, 401 (1955).
15. Parra, R.M. et al., *ibid* 119, 384 (1961).

## CHANGES IN MORPHOLOGY OF POLYMERS AS A RESULT OF GAMMA IRRADIATION: LOW DENSITY BULK POLYETHYLENE

Theodore Besmann and Raymond Greer  
Department of Nuclear Engineering and Engineering Research Institute,  
Iowa State University, Ames, Iowa 50010

The morphology of unirradiated and irradiated low density bulk polyethylene, with and without an inorganic filler, has been investigated using scanning electron microscopy. Surface features of polyethylene specimens containing several percentages of  $\text{CaCO}_3$  filler have been characterized as a function of gamma irradiation doses between 0 and 100 megarads and of tensile strength measurements at the various levels of irradiation and filler concentration.

DYNH-4 pellets (Union Carbide Corporation, Bound Brook, New Jersey) were used as the raw material for compression molding of plaques of polyethylene, without filler, from which samples were cut. The samples that contained a percentage of filler were mixed by conventional methods before molding. Tensile testing specimens were produced by stamping them out of the plaques of polymer. Prior to tensile testing the samples were placed in an oven at  $50^\circ\text{C}$  for 48 hours in order to remove any molecular orientations that developed as a result of the compression molding.

A cobalt-60 radiation source was utilized for the irradiations. Cobalt glass dosimetry was chosen as a practical method of determining the dose rate within the irradiation chamber<sup>1</sup>. In accord with the ASTM standards for irradiation of polymers<sup>2</sup>, the radiation field was not allowed to deviate more than 30% between the most highly irradiated area and the least irradiated area of the gage length of the tensile testing pieces, and of the entire specimen that would be used for scanning electron microscopy. The entire irradiation container was constantly purged with pre-purified nitrogen at 50 cc/min. The high intensity of radiation caused some heating in the specimens ( $38^\circ\text{C} \pm 1^\circ\text{C}$ ) but was not high enough to alter the properties of the polymer<sup>3</sup>.

Fracturing polyethylene at liquid nitrogen temperatures produces a granular surface in the unirradiated material and in samples irradiated to only 0.1 megarad. The fracture across lamellae was seen to cause local drawing that resulted in spherical structures being observed in the edges of the lamellae. These spherical features observed by means of scanning electron microscopy (Figure 1) are approximately 0.15 microns in diameter and represent small areas which had been drawn, became fibrillar, melted, and retracted onto the fracture surface of the polyethylene lamellae. The fracture is not entirely brittle, but rather is a function of local melting across fractured lamellae. These findings are in agreement with transmission electron microscope studies of a fracture surface of low density polyethylene<sup>4</sup> which indicated spherical units in the edges of the lamellae.

Fracture surfaces of the irradiated specimens of the present study do not contain spherical units. An example is shown in Figure 2. At higher irradiation doses, 0.1 micron voids are observed. Void concentration is observed to vary with no apparent change in void size. Void concentration increases from 1 megarad to 5 megarads. With increasing irradiation from 5 to 100 megarads the lamellae structure is sufficiently altered to subdue surface features.



Tensile strength results for unfilled polyethylene are in good agreement with those of Lyons and Vaughn<sup>5</sup>. For all filler concentrations (0 - 25%) there has been an initial increase in tensile strength with irradiation that peaks at about 10 megarads. Peak tensile strength appears to trend to higher doses at higher filler concentrations until at 20% filler the tensile strength peaks at 20 megarads. A 50% increase in tensile strength due to the irradiation is the maximum for the unfilled polyethylene. Increase in tensile strength decreases with increasing filler concentrations until at 20% filler the maximum increase is only 30%. An example of the influence of the physical presence of the filler in accomplishing a change in mechanical properties by diverting a crack or by stopping a crack from continuing to propagate is shown in Figure 3. The identification of and distribution of filler aggregates was monitored by using energy dispersive analysis techniques in conjunction with the scanning electron microscope analyses.

#### REFERENCES:

1. J. S. Crudele, "Cobalt Glass Dosimetry and Gamma Ray Dose Measurements in A.L.R.R. Facilities", ALRR-14, Ames, Laboratory of the U.S. Atomic Energy Commission (1970).
2. American Society for Testing Materials, Committee D-20 on Plastics, ASTM Standards on Plastics - General Methods of Testing, Nomenclature, Philadelphia, Pa., ASTM (1970).
3. W. O. Statton and P. H. Geil, J. Appl. Polym. Sci., 3, 356-361 (1960).
4. P. H. Geil, J. Polym. Sci., 149, 47, 65-74 (Nov. 1960).
5. B. J. Lyons and C. R. Vaughn, in Irradiation of Polymers, R. F. Gould, Ed., pp. 139-155, American Chemical Society Publications, Washington, D. C. (1967).

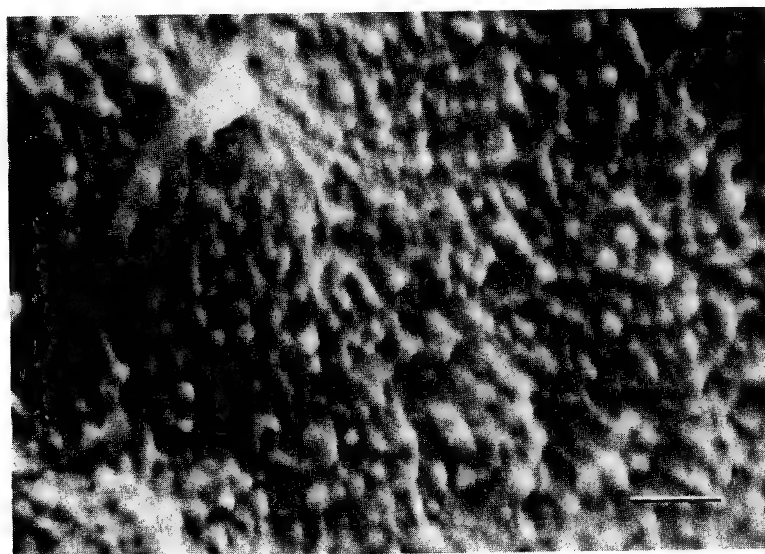


Figure 1. Secondary electron image of a granular fracture surface of unirradiated polyethylene. 0% filler. Scanning electron microscope (SEM) accelerating voltage was 10 kV. A vacuum deposited 100 Å thick conductive gold coating was applied to the specimen surface for all SEM specimens. Scale bar represents 0.5  $\mu\text{m}$ .

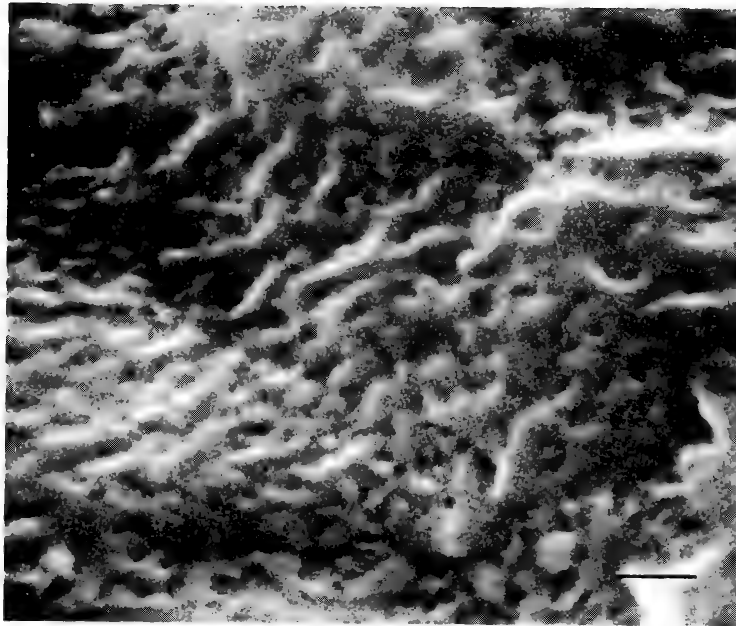


Figure 2. Secondary electron image of a fracture surface of polyethylene irradiated to 10 megarads illustrating the presence of voids. SEM accelerating voltage was 10 kV. 0% filler. Scale bar represents  $0.5\text{ }\mu\text{m}$ .

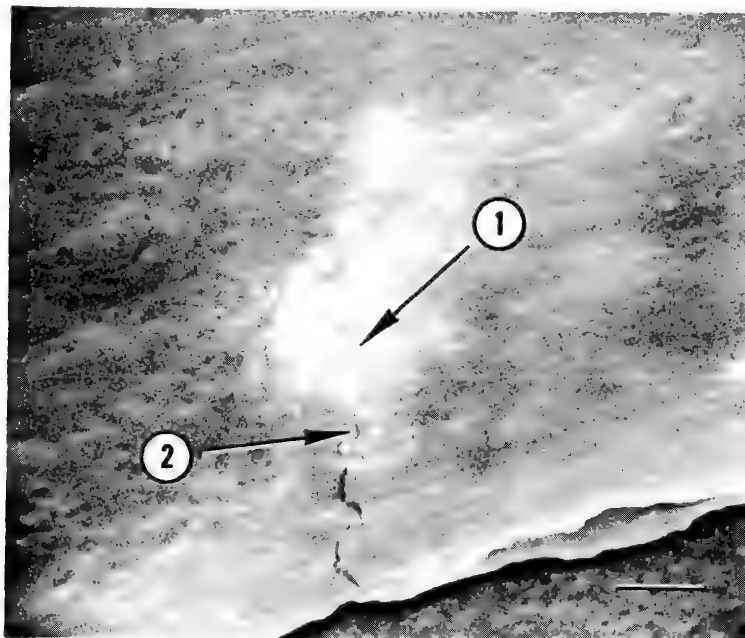


Figure 3. Fracture surface of 2.5%  $\text{CaCO}_3$  filled polyethylene. Arrow 1 indicates a filler aggregate. Arrow 2 indicates a crack which has halted at the filler aggregate. SEM accelerating voltage was 10 kV. Scale bar represents  $1\text{ }\mu\text{m}$ .

# ELECTRON MICROSCOPY IN THE EDUCATION AND TRAINING OF ALLIED MEDICAL MEMBERS OF THE CLINICAL LABORATORY TEAM

WILLIAM R. BISHOP, PH.D.  
DIVISION OF MEDICAL EDUCATION  
AMERICAN MEDICAL ASSOCIATION  
CHICAGO, ILLINOIS

THE COUNCIL ON MEDICAL EDUCATION OF THE AMA IN COLLABORATION WITH THE AMERICAN SOCIETY OF CLINICAL PATHOLOGISTS, THE AMERICAN SOCIETY OF MEDICAL TECHNOLOGISTS, AND AMERICAN ASSOCIATION OF BLOOD BANKS EMPLOYS NATIONAL STANDARDS OR ESSENTIALS FOR THE EVALUATION AND APPROVAL OF MORE THAN 1200 PROGRAMS NATIONALLY FOR THE EDUCATION AND TRAINING OF CLINICAL LABORATORY ALLIED MEDICAL TEAM MEMBERS, INCLUDING MEDICAL TECHNOLOGISTS, CYTOTECHNOLOGISTS, MEDICAL LABORATORY TECHNICIANS, HISTOLOGIC TECHNICIANS, CERTIFIED LABORATORY ASSISTANTS AND SPECIALISTS IN BLOOD BANK TECHNOLOGY. THE MEDICAL TECHNOLOGY PROGRAMS ARE 4-YEAR BACCALAUREATE LEVEL, THE CYTOTECHNOLOGY PROGRAMS -- 3 YEARS, THE MEDICAL LABORATORY TECHNICIAN -- 2 YEARS ASSOCIATE DEGREE, THE SPECIALIST IN BLOOD BANKING -- 1 YEAR, POST-GRADUATE, AND THE HISTOLOGIC TECHNICIAN AND CERTIFIED LABORATORY ASSISTANT PROGRAMS ARE 1 YEAR, POST-HIGH SCHOOL. THESE EDUCATIONAL PROGRAMS ARE LOCATED IN HOSPITALS, CLINICS, 4 YEAR COLLEGES AND UNIVERSITIES, AND 2-YEAR COLLEGES (JUNIOR OR COMMUNITY).

IN ADDITION TO THESE CATEGORIES OF EDUCATION AND TRAINING, NATIONAL STANDARDS ARE BEING PROPOSED FOR THE POSSIBILITY OF AMA APPROVAL OF EDUCATIONAL PROGRAMS IN HEMATOLOGY AT THE POST-GRADUATE LEVEL. ALL OF THESE HEALTH TEAM MEMBERS ASSIST THE PATHOLOGIST IN THE CLINICAL LABORATORY IN THE COLLECTION OF PERTINENT DATA UTILIZING A VARIETY OF MEDICAL INSTRUMENTATION AS A CONTRIBUTION TOWARD THE TOTAL DIAGNOSIS BY THE ATTENDING PHYSICIAN. MANY CLINICAL LABORATORY ALLIED MEDICAL PERSONNEL ARE ALSO INVOLVED IN AREAS OF BIOMEDICAL RESEARCH AND BIO-ENGINEERING. IT IS WITHIN THOSE LIMITED AREAS OF THE APPLICATION OF THE ELECTRON MICROSCOPE (TRANS. AND SCANNING) WITH HISTO- AND CYTO-PATHOLOGIC APPROACHES TO THE DEVELOPMENT OF DATA WHICH MAY CONTRIBUTE TO THE DIAGNOSIS OF DISEASE, AND THE DISCOVERY OF NEW KNOWLEDGE OF DISEASE PROCESSES THROUGH ELECTRON MICROGRAPHY, THAT MEDICAL TECHNOLOGISTS, CYTOTECHNOLOGISTS, TECHNICIANS AND ASSISTANTS COULD BENEFIT FROM THE INCORPORATION OF SOME BASICS OF SPECIMEN PREPARATION, RESIN COMPOSITION, EMBEDMENT AND CURING, CONTRAST DENSITY STAINING, THIN SECTIONING, SPECIMEN MOUNTING, AND TECHNIQS FOR THE PREPARATION OF SPECIMENS FOR SCANNING MICROSCOPY THROUGH THIN-FILM VACUUM DEPOSITION METHODS. THESE AREAS OF EDUCATIONAL CONTENT COULD BE VALUABLE IN THE TOTAL TRAINING PROGRAM, ESPECIALLY IF THE ALLIED MEDICAL PROFESSIONAL OR OCCUPATIONAL IS TO ENTER RESEARCH ENTERPRISE WITH RESEARCH ORIENTED PHYSICIANS AND BIOMEDICAL SCIENTISTS. THEREFORE, IT IS IMPORTANT TO REVIEW PERTINENT ASPECTS OF THE CURRICULUM FOR THE EDUCATION AND TRAINING OF CLINICAL LABORATORY PERSONNEL IN THE ALLIED MEDICAL OCCUPATIONS FOR DETERMINATIONS OF THE MOST APPROPRIATE AREAS FOR THE INCLUSION OF ULTRASTRUCTURAL CURRICULAR CONTENT.

## COMPUTER-CONTROLLED ELECTRON BEAM MICROFABRICATION

E. D. Wolf  
 Hughes Research Laboratories  
 Malibu, California 90264

Introduction

The primary function of both the electron microprobe analyzer and the scanning electron microscope is information transfer from a specimen surface to an operator (observer) via tabular and/or one-or two-dimensional display(s) of electron-beam-stimulated response(s) of that surface. This function is also a very important part of the required two-part capability of electron beam microfabrication systems. In fact, one premise of this paper is that precise scanning electron microscopy (registration) is as fundamental a requirement for precision microfabrication as the writing of the high resolution pattern (exposure). Thus, computer-controlled electron beam microfabrication deals with precision bi-directional information transfer between a target specimen and the computer (operator). Utilization of much related work in information theory and image (signal) enhancement schemes is possible and advantageous.

Beam "contamination", first observed in the transmission electron microscope and later in the microprobe analyzer and scanning electron microscope, suggested the possibility of focused electron beams for information "recording". Early work by Christy,<sup>1</sup> Möllenstadt *et al.*,<sup>2</sup> Wells, Everhart and Matta,<sup>3</sup> Broers,<sup>4</sup> Chang<sup>5</sup> and others set the stage for the present high level of laboratory accomplishment enjoyed by electron beam microfabrication.<sup>6</sup> The minimum linewidths obtained by Broers<sup>4</sup> and Chang<sup>5</sup> stand as significant accomplishments as does the self-registration of an electron beam demonstrated by Wells, Everhart and Matta.<sup>3</sup> Review papers have been written on electron beam microfabrication.<sup>7-9</sup>

The need for high frequency, high density, low-power devices and circuits for various communication, navigational and surveillance systems has recently added impetus to the field of electron-beam microfabrication. The high performance capability of commercially available scanning electron microscopes and minicomputers has at least suggested the probability of realizing some of these system needs with perhaps modified but similarly configured systems.

It is the purpose of this paper to review some of the basic concepts of electron beam microfabrication, to discuss briefly some of the advantages and disadvantages, and then to illustrate with specific

devices some areas best served by electron beam microfabrication, e.g., acoustic surface wave devices, discrete microwave semiconductor transistors, charged-coupled devices and integrated optics.

#### Definition - Electron-beam Lithography

Electron beam microfabrication is defined here as non-thermal electron-beam exposure of a thin polymeric film which after appropriate development serves as a contact mask. Electron beam microfabrication is thus defined simply as electron-beam lithography combined with one or more different methods for transforming high resolution electron-beam-created masks into device structures. Combinatorial processes which retain or transform the original edge definition and linewidth such as ion implantation doping and ion sputtering are of special importance (Fig. 1). Because there is a wide variety of mask usages, electron-beam lithography can be applied to many different types and classes of microelectronic devices and circuits. Electron-beam microfabrication, or better, electron-beam lithography, has most of the utility of conventional photolithography but with one-to two-orders of magnitude reduction in linewidth; a direct result from the fact that an electron beam can be focused to a spot whose diameter is well below the diffraction wavelength limit of visible (UV) radiation normally used for mask exposure.

#### Advantages -Disadvantages

Most of the advantages of computer-controlled electron beam microfabrication have already been discussed in the literature. Briefly, the principal advantages over photolithography are: narrower linewidth, greater precision of line placement and edge accuity, and potentially faster turn-around times with more extensive automation. The main disadvantage is that it takes longer to expose an array (wafer) of patterns. Both Brewer<sup>8, 9</sup> and Chang<sup>10</sup> have reviewed writing speeds so this topic will not be discussed in detail. However, it should be remembered that density of elements (component complexity) increases proportionally to the square of the linewidth decrease. Therefore, the  $(\rho_{el} \times \tau_{exp})$  product may remain nearly constant for certain devices, i. e., it may take longer but there is an associated increase in the device functional complexity so that the number of functional units produced per unit time may remain about constant. This is an important rationale for electron beam microfabrication. For certain types of devices it will be economical to use electron-beam exposure. Furthermore, there are certain classes of devices whose operating frequency just can not be reached any other way. For these devices the same economic guidelines used for conventional microelectronic devices may not be directly applicable.

## Registration and Resist Exposure

Electron-beam lithography offers the desirable feature of "hands-off" processing, thereby eliminating many human-induced failures. Preliminary alignment experiments by Ozdemir, Wolf and Buckey<sup>11</sup> have demonstrated closed-loop computer-controlled electron-beam registration to better than  $\pm 0.1 \mu\text{m}$  over a field of  $\sim 1 \text{ mm-square}$ . This degree of alignment precision should be attainable on a routine basis and is generally required when linewidths of  $1 \mu\text{m}$  or less are needed.

Sufficient empirical data exists<sup>12, 13</sup> on electron beam energy dissipation profiles to allow programmable linewidths on a given substrate. Figure 2 represents some energy dissipation profiles in Elvacite 2041, a very high weight average molecular weight ( $> 300,000$ ) polymethyl methacrylate, presented earlier<sup>12</sup> for variable line charge density,  $q_l = 1 \times 10^{-8} \text{ coulombs cm}^{-1}$  at 10, 15, and 20 keV primary beam energy, respectively. These data were obtained by taking scanning electron micrographs of cross-sectioned samples which had been exposed and developed. Figure 3 shows aluminum electrodes with variable linewidths obtained on lithium niobate using the metal deposition technique shown in Fig. 1. Each interdigital electrode structure is part of a high frequency acoustic surface wave transducer.

## Areas of Applicability

Figure 3 illustrated one class of high frequency device. For certain applications, broadband acoustic surface wave delay lines are desirable. Figure 4 shows a transducer with 244 electrodes whose spacing decreases every  $2\lambda$  by  $153 \text{ \AA}$  for a total change of  $0.93 \mu\text{m}$  in  $\sim 450 \mu\text{m}$ . When combined with a similar transducer a delay line with 450 MHz bandwidth centered at 1.0 GHz was obtained.

Figure 5 shows an aluminum gate on gallium arsenide Schottky barrier field effect transistor which is expected to have a predicted cut-off frequency of about 60 GHz. The source and drain (large pads on either side of aluminum gate) are silver.

Figure 6 shows a metallization pattern for a 16-bit shift register using a 3-phase charge-coupled device. The electrode gap is  $0.3 \mu\text{m}$  and should improve field-aided transfer of charge.

Figure 7 shows a planar phase grating coupler on an optical wave guide. The phase grating was fabricated using electron beam lithography, conventional photolithography and ion beam micromachining. The grating periodicity is  $3600 \text{ \AA}$  and the groove width is just under  $1000 \text{ \AA}$ .

In summary, electron beam microfabrication portends much for the future where submicron linewidths are needed. These several examples of prototype devices demonstrate general applicability.

The author acknowledges collaboration with several colleagues at Hughes Research Laboratories where these device structures are being fabricated, tested and evaluated. Specific fabrication details and device performance will be published elsewhere.

### References

1. R. W. Christy, J. Appl. Phys. 31, 1680 (1960).
2. G. Mollenstadt and R. Speidel, "Newer Developments in Micro-miniaturization", Proc. 3rd Symposium on Electron Beam Technology, ed., R. Bakish, Alloyd Electronic Corp., 23-24 March 1961, pp. 340-357.
3. O. C. Wells, T. E. Everhart, and R. K. Matta, IEEE Trans. on Electron Devices ED-12, 556 (1965).
4. A. N. Broers, Microelectronics and Reliability 4, 103 (1965).
5. T. H. P. Chang, Ph.D. Dissertation, Cambridge University, England, 1967.
6. See special section in IEEE Trans. on Electron Devices ED-19, (No. 5) May 1972 and also Record of 11th Symposium on Electron, Ion and Laser Beam Technology, ed., R. F. M. Thornley, San Francisco Press, Inc., 12-14 May 1971.
7. O. C. Wells, "Electron Beams in Micro-electronics", Proc. 3rd Symposium on Electron Beam Technology, ed., R. Bakish, Alloyd Electronic Corp., 23-24 March 1961, pp. 291-321.
8. G. R. Brewer, IEEE Spectrum 8, 23 (1971).
9. G. R. Brewer, Solid State Technology 15 (No. 7), July 1972 Special issue.
10. T. H. P. Chang, "Device Fabrication Using a Scanning Electron Beam System", Proc. 4th Ann. Scanning Electron Microscope Symposium, ed., O. Yohari, IIT Research Institute, April 1971, pp. 417-424.
11. F. S. Ozdemir, E. D. Wolf and C. R. Buckey, "Computer-Controlled Scanning Electron Microscope System For High Resolution Micro-electronic Pattern Fabrication", Record 11th Symp. on Electron, Ion and Laser Beam Technology, ed., R. F. M. Thornley, San Francisco Press, Inc. 12-14 May 1971, pp. 463-470.
12. E. D. Wolf, F. S. Ozdemir, W. E. Perkins and P. J. Coane, "Response of the Positive Electron Resist Elvacite 2041 to Kilo-volt Electron Beam Exposure", Record 11th Symp. on Electron, Ion and Laser Beam Technology, ed., R. F. M. Thornley, San Francisco Press, Inc., 12-14 May 1971, pp. 331-336.
13. M. Hatzakis, Appl. Phys. Lett. 18, 7 (1971).

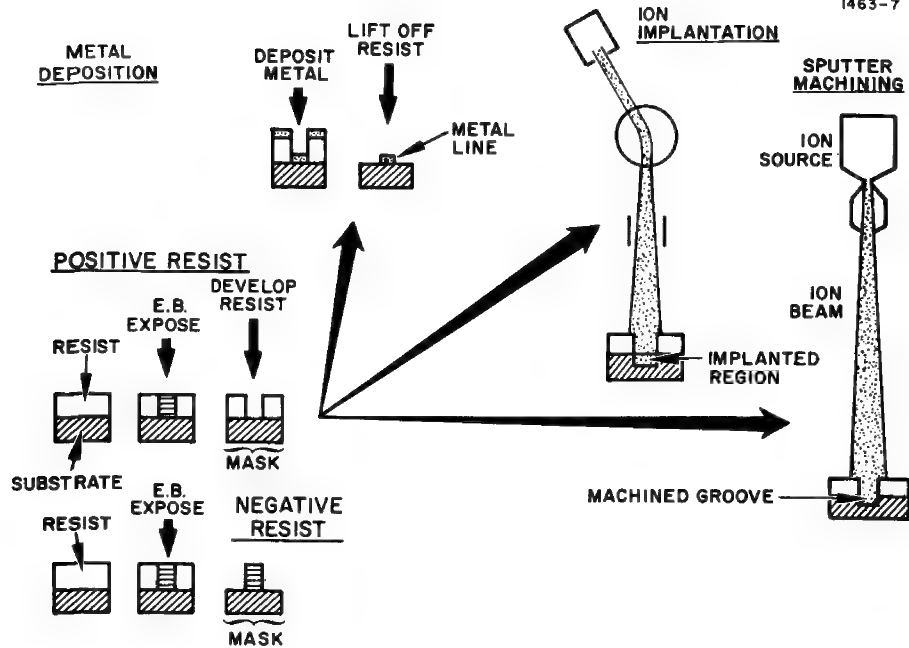


Fig. 1. Transformation of electron beam lithographic mask into device structures.

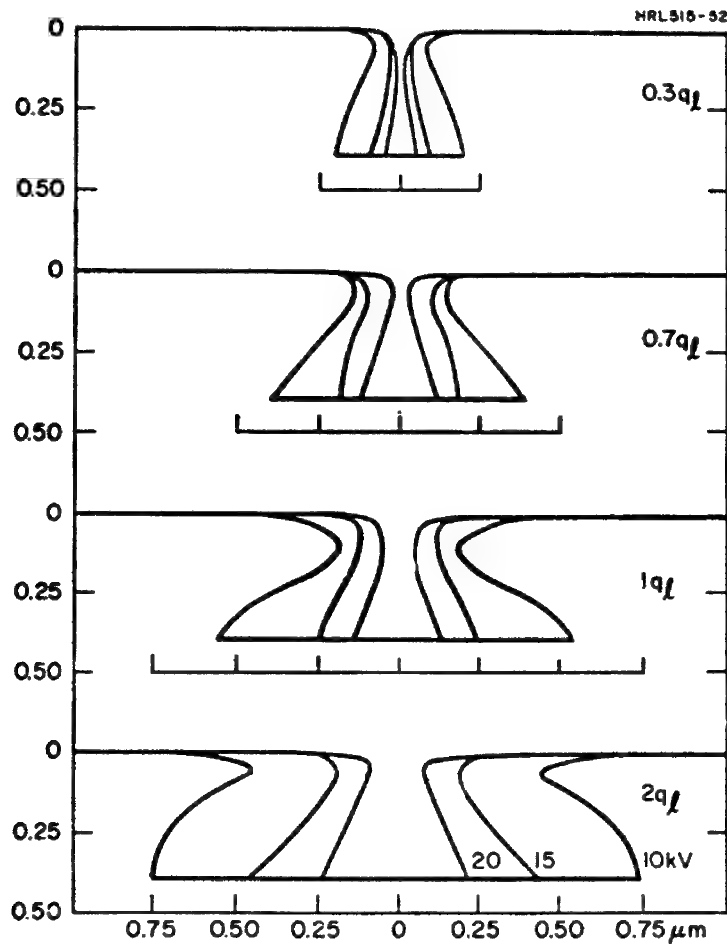


Fig. 2. Critical energy dissipation profiles in Elvacite 2041 (ref. 12).



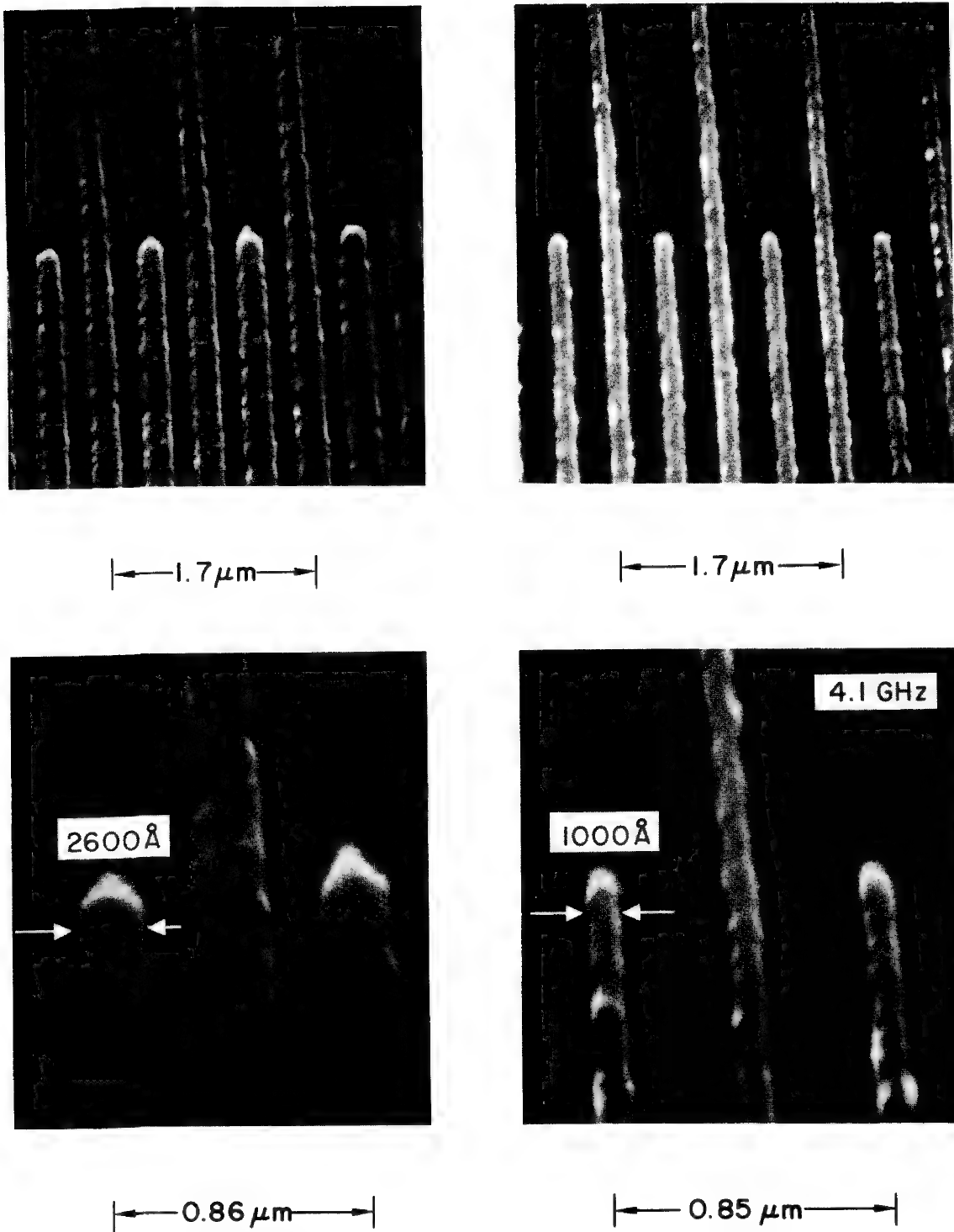


Fig. 3. Programmable electrode widths on same center-to-center spacing for 4.1 GHz acoustic surface wave transducer.

1219-1

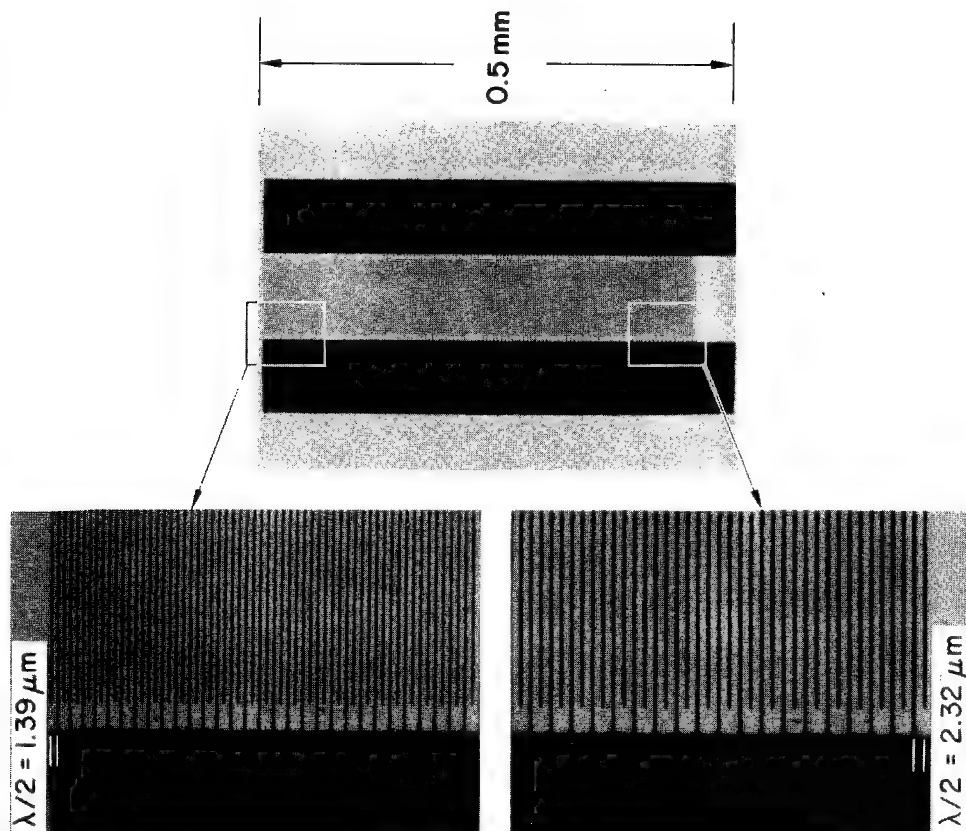


Fig. 4. Broad bandwidth acoustic surface wave transducer with 244 electrodes (optical transmission photographs).

1369-39

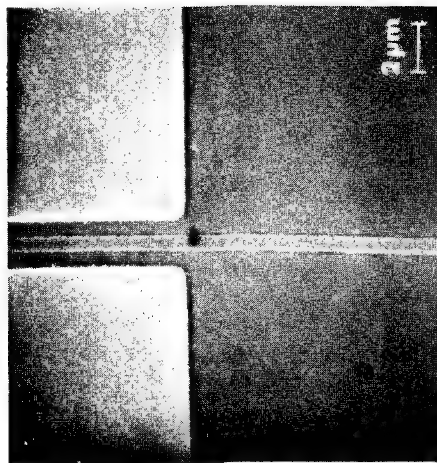


Fig. 5. GaAs Schottky barrier FET. Aluminum gate is  $0.6 \mu\text{m}$  in width.

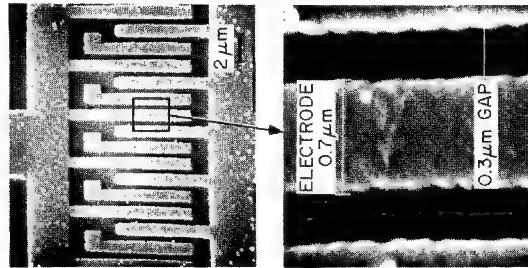


Fig. 6. Aluminum metallization pattern for a 3-phase 16-bit shift register CCD.

1493-1

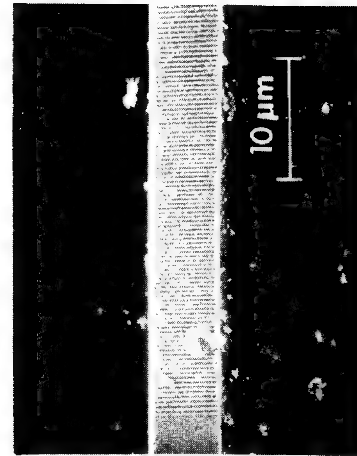


Fig. 7. Planar phase grating coupler with  $1000 \text{ \AA}$  grooves ion-beam machined into an optical waveguide. Periodicity is  $3600 \text{ \AA}$ .

A CHARGE STORAGE MEMORY WITH READ-OUT AND  
ERASURE USING YbFeO<sub>3</sub>

by

S.J. Ingrey & W. Westwood

Bell Northern Research

Box 3511 Station "C", Ottawa, Ontario, Canada

Some of the major requirements for a material to be useful in an electron beam induced charge memory application include permanence, short "write-in" time and high storage density. We have found that the charge storage mechanism in ytterbium orthoferrite<sup>(1)</sup> (YbFeO<sub>3</sub>) meets to some extent these requirements. These charging effects are produced by irradiation of the material with high energy electrons. Using an electron probe with a beam energy, current and spot size of 20keV, 0.2  $\mu$ A and 2000 $\text{\AA}$  respectively, information was written into the surface regions of single crystal platelets of YbFeO<sub>3</sub> and YbFeO<sub>3</sub> doped with CaO.

Fig. 1(a) is a specimen current electron micrograph of an area of the platelet, regions of which had previously been irradiated by moving the electron beam spot across the sample at a speed of approximately  $20 \times 10^{-4} \text{cm.S}^{-1}$ . In the micrograph the irradiated areas appear brighter due to a higher electron conductivity. The width of the lines produced during the "write-in" are of the order of 5000 $\text{\AA}$ , this dimension is larger than the beam diameter because of electron scattering in the material but is still dependent in part upon the electron beam spot size. Figs. 1(c) and (d) show an area immediately after the "write-in" cycle and after 21 days exposure to atmosphere respectively. The pattern was still evident after 40 days.

The speed at which the beam moves across the sample during the 'read' cycle is approximately  $1-5 \text{cm.S}^{-1}$  so that the time required to read a 5000 $\text{\AA}$  diameter spot is less than 100  $\mu$ s. Since the time required to write the information into the sample is approximately two orders of magnitude greater than this, the memory may be read many times without a reduction in the contrast of the pattern. The pattern may, however, be erased by heating the platelet at approximately 500°C for a few seconds.

When a single crystal platelet of Ca-doped YbFeO<sub>3</sub> was examined in the same way, it was found that the electron conductivity was lowered in the areas where the electron beam was used to 'write' information. Fig. 1(b) shows a specimen current electron micrograph of the sample; the area irradiated during the write cycle appears dark. This pattern was still evident after exposure to the atmosphere for a few days.

The occurrence of these opposite effects in the doped and undoped crystals makes it possible to 'erase' a single 'bit' of information.

The information written in an undoped platelet would be 'erased' by irradiating a corresponding position in the doped platelet and adding the specimen currents from the two platelets when they are 'read' by separate but synchronized electron beams.

Before this 'erasure', the sum of the specimen currents would change at the storage position whereas there would be no change after 'erasure'.

Charging effects are often observed when specimens are irradiated with high energy electrons in electron microscopes and microprobes and this charging is usually associated with high resistivity materials. Irradiation of the material with high energy electrons (5-50kV) results in an intense localized ionization and the creation of vacancies and interstitials. When a specimen of high resistivity is irradiated, neutralization of the surface charge is delayed because of the low carrier mobility between the specimen surface and ground. This surface charge can be positive, due to the production of interstitials, or negative, due to excess electrons remaining in the surface region, and has a decay time which depends on the specimen, (structural characteristics, conductivity, etc.)

These decay times are usually of the order of minutes. As a first approximation the increase in carriers generated by the beam under equilibrium situations is<sup>(2)</sup>

$$\Delta_n = \Delta_p = \frac{i_b}{eZ} \frac{E}{J}$$

where:  $i_b$  is the beam current  
 $Z$  is the penetration depth of the electron beam  
 $E$  is the energy of the incident electrons  
 $J$  is the mean ionization potential

If the charge introduced into the surface region is negative then the energy ( $E$ ) of the incident electron will no longer be equal to the operating voltage ( $E_0$ ) but will be less i.e.  $E = (E_0 - \Delta E)$  and, from the above equation the number of carriers produced will decrease upon irradiation. If positive charging occurs, then  $E = (E_0 + \Delta E)$  and there is an increase in the number of carriers produced. A finite time is required to reach the equilibrium state i.e. when the specimen current is equal to the number of carriers produced at the surface.

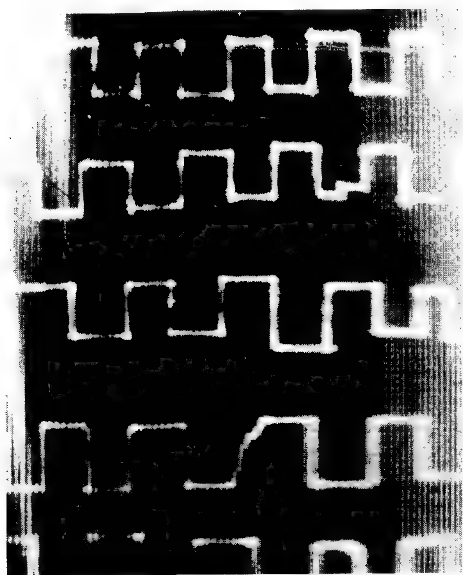
These types of charging effects usually require much longer irradiation times than observed for the  $\text{YbFeO}_3$  samples and they also have decay times which are of the order of minutes rather than days. Therefore, these charging effects do not seem adequate to explain the results observed for the  $\text{YbFeO}_3$ . These may instead be due to a change in the ratio of  $\text{Fe}^{2+}$  and  $\text{Fe}^{3+}$  ions in the  $\text{YbFeO}_3$ . Conduction can occur in these materials by electron hopping between  $\text{Fe}^{2+}$  and  $\text{Fe}^{3+}$  ions<sup>(3)</sup>. In  $\text{YbFeO}_3$ , nearly all the iron is in the  $\text{Fe}^{3+}$  state so that the conductivity will be increased by the formation of  $\text{Fe}^{2+}$  ions. While the bulk resistivity of the  $\text{YbFeO}_3$  platelet was  $10^9 \mu\text{cm}$ , the calcium-doped platelet had a resistivity of  $10^6 \mu\text{cm}$ , probably due to the presence of divalent ions. If the electron beam irradiation causes further ionization of these, the resistivity may increase, as observed. Much more detailed investigation will be required to determine whether these are, in fact, the mechanisms responsible for the observed memory effect.

#### Acknowledgement

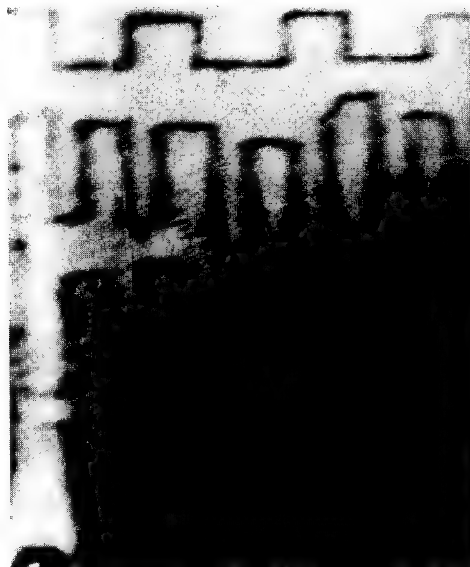
We would like to thank Dr. H.H. Quon and A. Potvin for supplying the ytterbium orthoferrite platelets.

# References

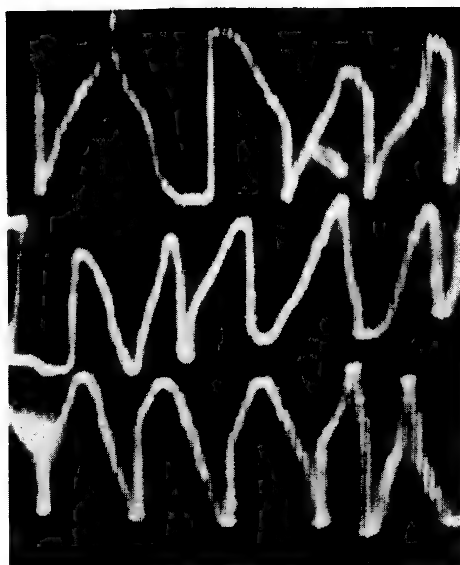
- (1) H.H. Quon, A. Potvin and S.D. Entwistle, Mat. Res. Bull. V.6, 1175-1184, 1971
- (2) P.R. Thornton, Scanning Electron Microscopy, 1968, pp.116, Chapman and Hall.
- (3) J. Smit, H.P.J. Wijn, Ferrites, pp. 229-234, 1959, J. Wiley and Sons.



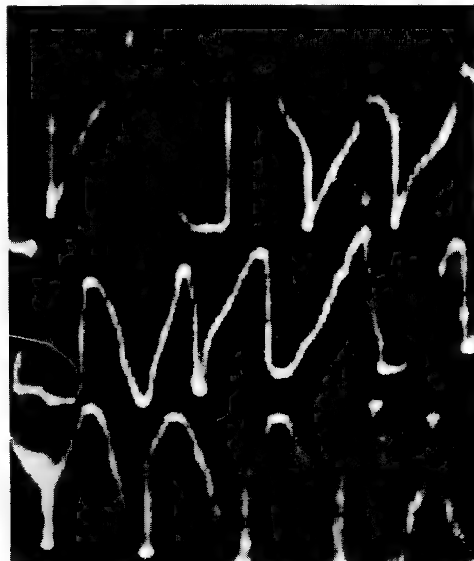
(a)



(b)



(c)



(d)

Fig. 1. Conduction mode electron micrographs of electron beam writing in

- (a) Undoped  $\text{YbFeO}_3$
- (b) Doped  $\text{YbFeO}_3$
- (c) Undoped  $\text{YbFeO}_3$
- (d) Same area as in (c) after being exposed to atmosphere for 21 days.

VOLTAGE DEPENDENT PARAMETERS IN NEGATIVE  
ELECTRON RESIST EXPOSURE

by

R.D. Heidenreich, L.F. Thompson and C.M. Melliar-Smith  
Bell Telephone Laboratories, Incorporated  
Murray Hill, New Jersey 07974

ABSTRACT

The successful application of electron lithography techniques to microcircuit fabrication depends heavily upon the properties of resist materials including sensitivity, resolution, adhesion, flaws, pinholes, etc. This paper is concerned primarily only with the sensitivity and resolution obtainable with negative resists, i.e. resists which are rendered insoluble by electron irradiation.

The sensitivity of negative resists is determined by the number of cross linking events produced by an incident electron. It varies over a range of several orders of magnitude depending upon the functional groups present in the resist and the cross section for the chemical event which is voltage dependent.

The resolution or line width is determined by the lateral or transverse electron flux resulting from scattering in the resist itself. The maximum width and penetration of a fine electron beam is set by the Bethe range which is voltage dependent.

Studies with four negative resist materials are presented here; polyvinyl ferrocene, polyglycidyl methacrylate,<sup>(1)</sup> epoxidized polybutadiene<sup>(1)</sup> and Riston<sup>(2,3)</sup>. These materials have been evaluated for sensitivity, resolution and as etching masks for SiO<sub>2</sub> and tungsten. They all show the same general behavior of increasing sensitivity (as shown in Figure 1) and decreasing line width (as shown in Figure 2) as the accelerating voltage is reduced.

To prevent an excessive number of pinholes in the resist, a film thickness of 4000<sup>o</sup>Å was required. This limited the minimum usable accelerating voltage to 5kV or above. If the voltage was reduced below 5kV the electrons had insufficient energy to penetrate the resist throughout its depth and the pattern would not adhere to the substrate during development.

#### References

1. T. Hirai, Y. Hatano and S. Nonogaki; J. El. Soc., 118 669 (1971).
2. A. C. Schoenthaler; U.S. Patent 3,418,295 (December 1968).
3. J. R. Celeste; U.S. Patent 3,469,982 (September 1969).

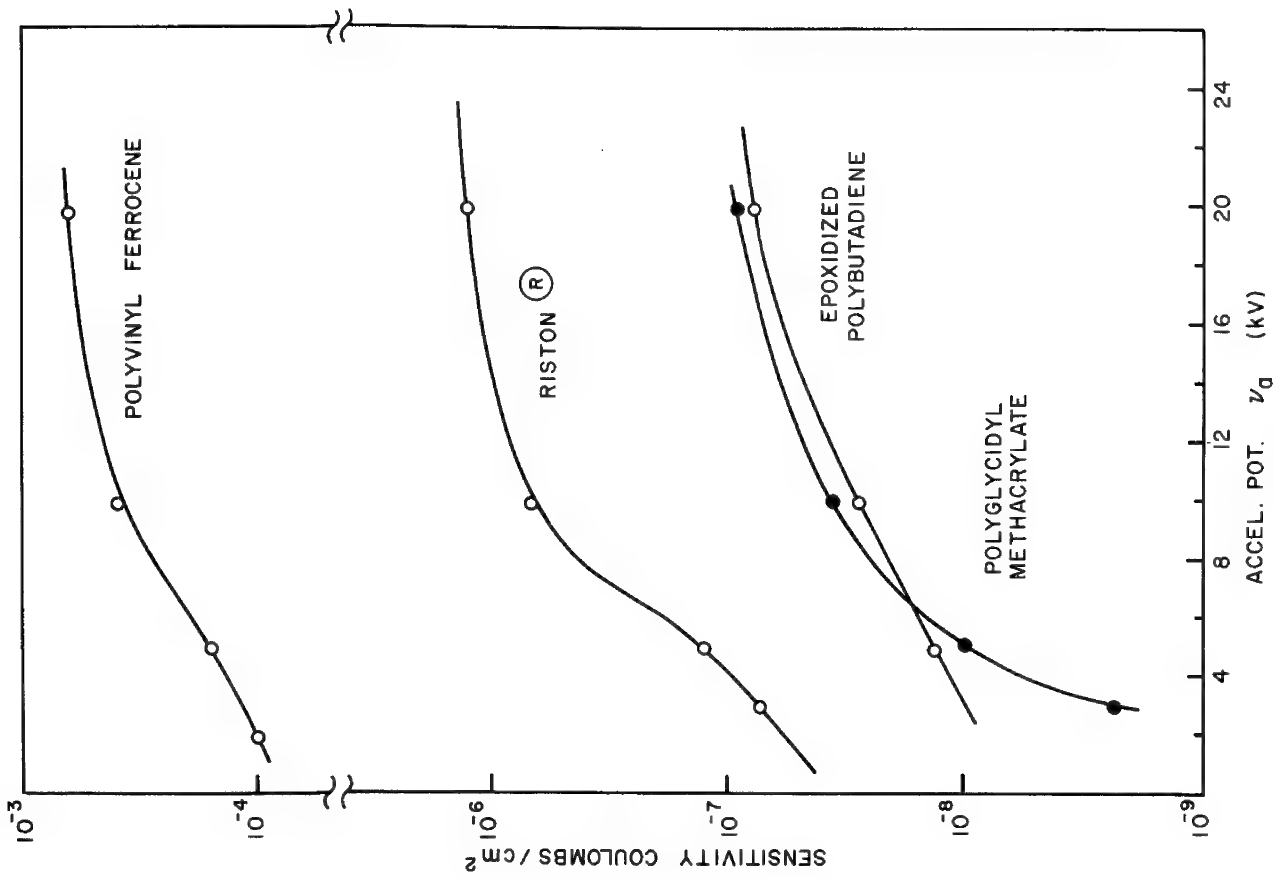


FIG. 1  
 SENSITIVITY AS A FUNCTION OF ACCELERATING  
 VOLTAGE FOR POLYVINYL FERROCENE®, RISTON®,  
 EPOXIDIZED POLYBUTADIENE & POLYGLYCIDYL METHACRYLATE  
 ® REGISTERED DUPONT TRADEMARK

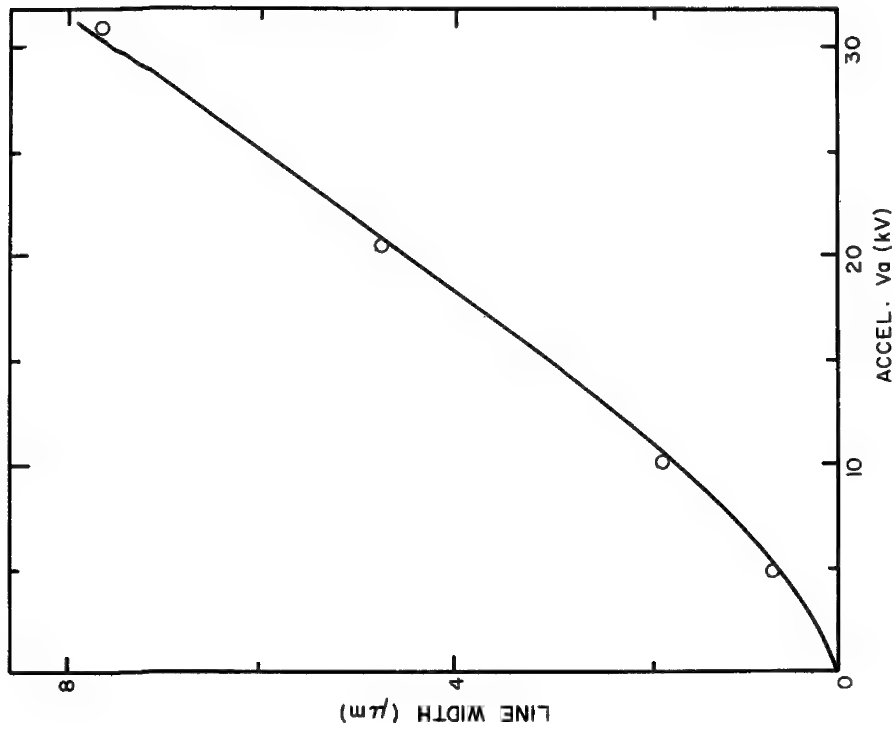


FIG. 2  
 MINIMUM EXPOSED RESIST LINE WIDTH AS A  
 FUNCTION OF ACCELERATING VOLTAGE USING  
 POLYVINYL FERROCENE.



# TEMPERATURE DEPENDENCE OF CATHODOLUMINESCENCE OF GaAs, GaP, AND $\text{GaAs}_x\text{P}_{1-x}$ \*

H.C. Marciniak and D.B. Wittry

Departments of Materials Science and Electrical Engineering  
University of Southern California, Los Angeles, California 90007

A clean vacuum electron beam column<sup>1,2</sup> in which samples can be irradiated without contamination over the temperature range of 27°-300°K was used in temperature dependence measurements of cathodoluminescence of GaAs, GaP, and  $\text{GaAs}_x\text{P}_{1-x}$ . A beam voltage of 50 kV was used in order to reduce the effects of surface recombination.

Figure 1 shows the peak of the cathodoluminescence spectrum of a lightly doped p-type ( $N_A = 7 \times 10^{16} \text{ cm}^{-3}$ ) GaAs sample as a function of temperature. The dashed curve is a plot of the absorption edge of GaAs versus temperature according to Casey and Panish.<sup>3</sup> At low temperatures two emission peaks separated by 11 meV are seen. Cusano<sup>4</sup> attributes the 1.487 eV peak to conduction band-isolated acceptors recombination. The 1.499 eV peak is probably due to conduction band-valence band recombination. At higher temperatures only one broad emission band is observed.

Figure 2 shows a cathodoluminescence spectrum of GaP taken at 27°K with an accelerating voltage of 50 kV, a beam current of 5nA and a spot size of 15 $\mu\text{m}$ . It was expected that donor-acceptor pair recombination between 2.2eV and 2.3eV as reported by Thomas, et al.<sup>5</sup> at 1.6°K could be observed. However, donor-acceptor pair recombination showing spectra of resolved peaks in GaP has not yet been reported at temperatures above 20°K. Shown in the figure is the "A" line due to the nitrogen bound exciton and the C bound-exciton line due to neutral sulfur donors.<sup>6</sup> The F line is due to recombination at pairs of isoelectronic nitrogen traps.<sup>6</sup> The other peaks could be phonon-replicas of the "A" line as discussed by Dean and Thomas.<sup>7</sup>

At the present time cathodoluminescence measurements are made as a function of temperature and beam current of  $\text{GaAs}_x\text{P}_{1-x}$  mixed crystals. It is expected that the nature of the various recombination mechanisms in these crystals can be determined through these studies.

The mixed crystals are first analyzed to determine the "x" value in  $\text{GaAs}_x\text{P}_{1-x}$  using electron probe X-ray microanalysis. The X-ray data is then processed using J. W. Colby's MAGIC<sup>8</sup> computer program for quantitative electron microprobe analysis. The cathodoluminescence measurements are made on the instrument described in references 1 and 2. Care is taken to analyze the same spot of the samples in both instruments because the samples are polycrystalline and may not be homogeneous.

The intensity of the main peaks as a function of current show first a linear dependence which changes to a square root dependence as the current is increased. This sublinear dependence results from the saturation of donor or acceptor levels at a certain beam current when other factors such as accelerating voltage and spot size are kept constant. This sublinear dependence has been observed previously in Zn-O doped GaP<sup>9</sup> and S-doped GaP.<sup>10</sup>

Measurements on these GaAs<sub>x</sub>P<sub>1-x</sub> crystals are being continued with special emphasis on those samples whose values of "x" are near the value at which the band structure changes from direct to indirect.

---

\* Research sponsored by the Air Force Office of Scientific Research, Office of Aerospace Research, United States Air Force, under Grant No. AF-AFOSR-68-1414; the National Science Foundation under Grant No. GK3904; and Advanced Research Projects Agency of the Department of Defense under Grant No. DAHC-15-70-G14.

<sup>1</sup>H.C. Marciniak and D.B. Wittry, "A Clean Vacuum Electron Beam Column for Cathodoluminescence Investigations", Fifth National Conference on Electron Probe Analysis; No. 44B, 1970.

<sup>2</sup>H.C. Marciniak and D.B. Wittry, Rev. of Sci. Instr. 42, 1810 (1971).

<sup>3</sup>M.B. Panish and H.C. Casey, Jr., Journal of Applied Physics, 40, 163 (1969).

<sup>4</sup>D.A. Cusano, Solid State Communication, 2, 353 (1964).

<sup>5</sup>D.G. Thomas, J.J. Hopfield and K. Colbow (1964)"Light from Distant Pairs." Radiative Recombination in Semiconductors (Paris), 67-77.

<sup>6</sup>M. Gershenzon (1966)"Electroluminescence from p-n Junctions." Luminescence of Inorganic Solids (New York), 625-627.

<sup>7</sup>P.J. Dean and D.G. Thomas, Physical Review, 150, 690-703 (1966).

<sup>8</sup>J.W. Colby, MAGIC - A Computer Program for Quantitative Electron Microprobe Analysis, Bell Telephone Laboratories, Inc., Allentown, Pennsylvania.

<sup>9</sup>H.C. Casey, Jr., and J.S. Jayson, Journal of Applied Physics, 42, 2774 (1971).

<sup>10</sup>S. Hosoki and H. Okano, "Scanning Cathodoluminescence Analysis of Compound Semiconductors", Pittsburg Conference on Analytical Chemistry and Applied Spectroscopy; Paper no. 161 (1971).

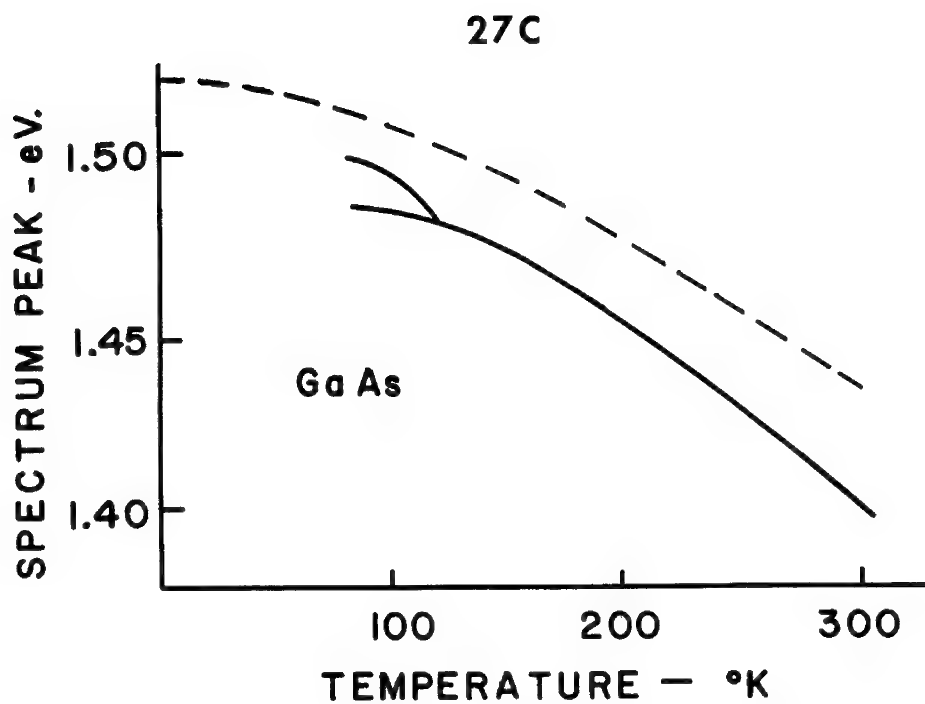


Figure 1

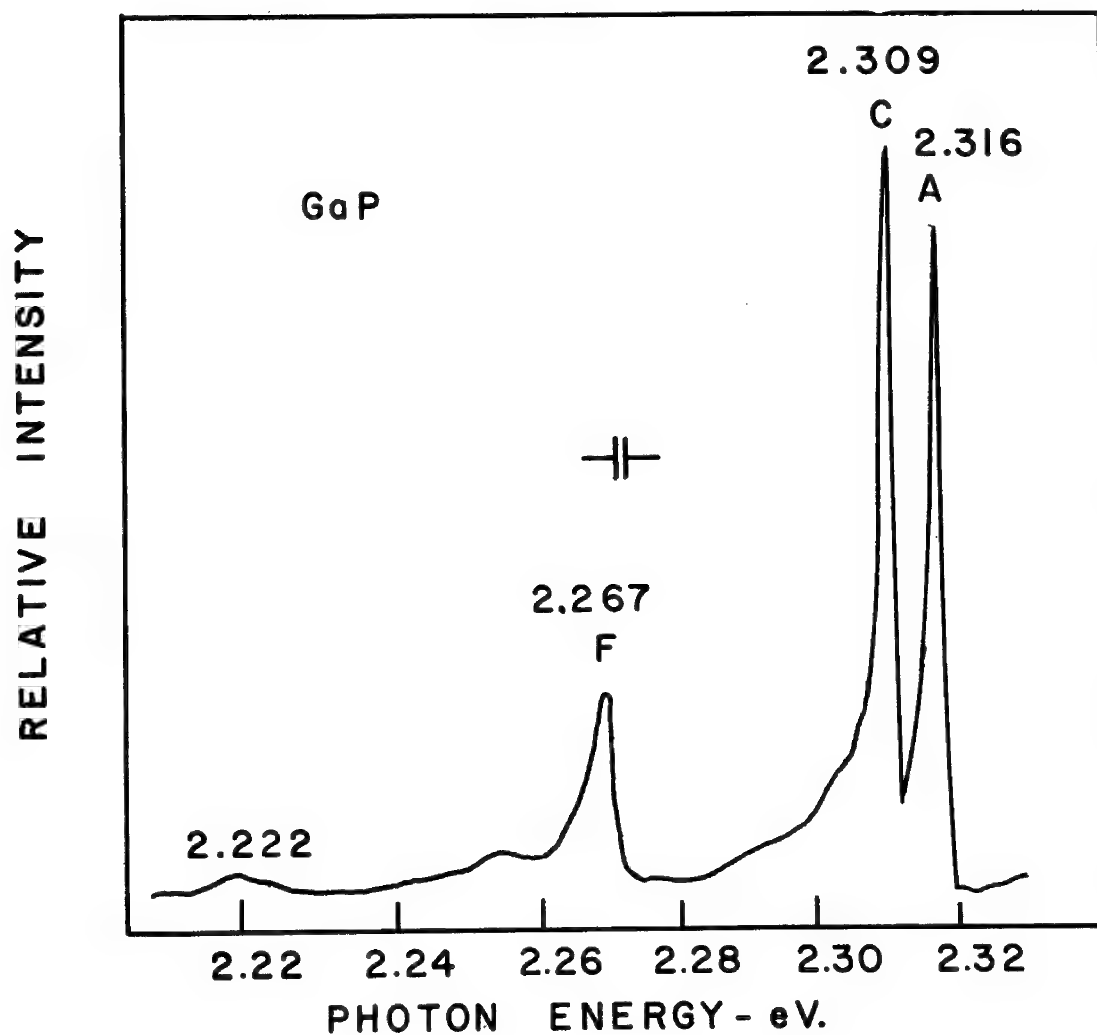


Figure 2

## ION NEUTRALIZATION AT INSULATOR SURFACES

by

Daniel V. Mc Caughan, R. A. Kushner and V. T. Murphy  
 Bell Laboratories Incorporated  
 Murray Hill, N. J.

The physics of the collision of ions with metal surfaces has been extensively studied over the past number of years. The aspects of ion neutralization spectroscopy, and ion scattering spectrometry for example, have received particular attention.<sup>(1,2)</sup> The effects of ion collisions on insulator surfaces have, by contrast, received little study. Various Soviet workers<sup>(3)</sup> have studied kinetic and potential neutralization effects on continuously deposited insulator films. They have shown that neutralizing electrons apparently come from up to several hundreds of Angstroms from the surface. Vance<sup>(4)</sup> has recently published results on ion bombardment of semi-insulating films of selenium at low energy. He has shown that charge builds up on the surface of these films during ion bombardment and has quantitatively evaluated the charge-up effects on these films. Mc Caughan and Murphy<sup>(5)</sup> have given detailed quantitative data on the charge-up effects observed in thin insulator films of insulator/semiconductor structures under low energy ion bombardment and shown these effects to be independent of whether the bombarding ion is  $\text{Ar}^+$ ,  $\text{N}_2^+$  or  $\text{N}^+$ . This work has led to a proposed mechanism for the neutralization effects observed when thin insulator films are bombarded by positive ions. This mechanism has important implications for ion neutralization spectroscopy, Auger spectroscopy, ion reflection spectrometry (or ion scattering spectrometry) and all processes of analysis in which low energy ions are used for analysis of insulator surfaces.

Consider a film of an insulator such as  $\text{SiO}_2$ . Its electron affinity is small, typically less than 2 eV; its band-gap is of the order of 9-10 eV. Consider an impurity in such an insulator. If we can use a band-type picture for the insulator we can assign levels in the insulator band-gap to impurities. Indications are that we can use such a band-structure picture for insulators - for example Eastman and DiStefan<sup>(6)</sup> have shown the valance band structure for films of  $\text{SiO}_2$  on Si, as being 11.6 eV wide, with detail structure. In addition to the impurity levels we will have surface states at the insulator surface, those surface states below the effective Fermi level being filled, those above being empty. Many insulators are in fact good conductors when electrons are introduced into their (normally empty) conduction band. Thus we have the situation shown in Fig. 1 at the insulator surface where the "surface atom" shown is an impurity atom bound at the surface. An ion approaching the insulator

surface will experience a reduction in its effective ionization potential due to the polarization of the dielectric as it approaches the surface. Its effective ionization energy at the time of neutralization will be determined by its velocity of approach to the surface. The time available for the (non-radiative) neutralizing collision will be of the order of  $2 \times 10^{-15}$  sec., and the neutralization would be expected to occur within  $10 \text{ \AA}$  of the surface. This has several important implications. Firstly, an ion of ionization potential less than the insulator bandgap plus the electron affinity may travel into the insulator un-neutralized provided it is not neutralized at an impurity site or a surface state. Secondly, an ion of ionization potential greater than the bandgap plus electron affinity will, at low energy, leave its charge on the surface, unless it is neutralized at an impurity site, provided its velocity is not so great as not to leave enough time for the transition. (For  $\text{Ar}^+$  ions, for example, this transition energy would be expected to be between 20 and 100 KeV.) Thirdly, any attempt to neutralize the surface of an insulator by flooding it with electrons is fraught with difficulty from the ion neutralization standpoint. What would be expected is that the flooding electrons would fill surface states and states in the insulator conduction band, therefore providing an additional source of neutralizing electrons for the primary beam ion. Thus the secondary reflected ion intensity in ion scattering spectrometry would be expected to drastically fall when flooding electrons are used to neutralize an insulator surface. Fourthly, we can explain charging effects deep in insulators in fast ion scattering experiments by the fact that the time available for neutralization at the surface is too short, therefore the scattering ion, whatever its ionization potential will carry its charge to its range in the insulator. A metal film on the surface, even a few  $\text{\AA}$  thick, will provide a large source of neutralizing electrons and will therefore prevent charge-up phenomena in this case. Finally, the neutralization at an impurity site of the bombarding ion can render that impurity mobile so that it can move from the surface during analysis and then give erroneous surface constituent measurements. The following paper will discuss this aspect in detail.

In summary the mechanism we have developed for ion neutralization at insulator surfaces not only explains our own results but has immediate relevance to the accuracy of Ion Scattering Spectrometry, secondary ion spectrometry etc.

REFERENCES

- (1) H. D. Hagstrum: P. Rev. 150, 495, (1966)
- (2) D. P. Smith: J. Appl. Phys. 38, 340, (1967)
- (3) U. A. Arifov: "Interaction of Atomic Particles with a Solid Surface" (Consultants Bureau, N. Y. 1969)
- (4) D. Vance: J. A. P. 42, 5430, (1971)
- (5) D. V. Mc Caughan and V. T. Murphy: J. Elec. Soc. (to be published), and talk presented at Fall 1971 Cleveland Meeting, (Abstr. 101)
- (6) Eastman and Di Stefano: P. Rev. Letters 27, 1560 (1971)

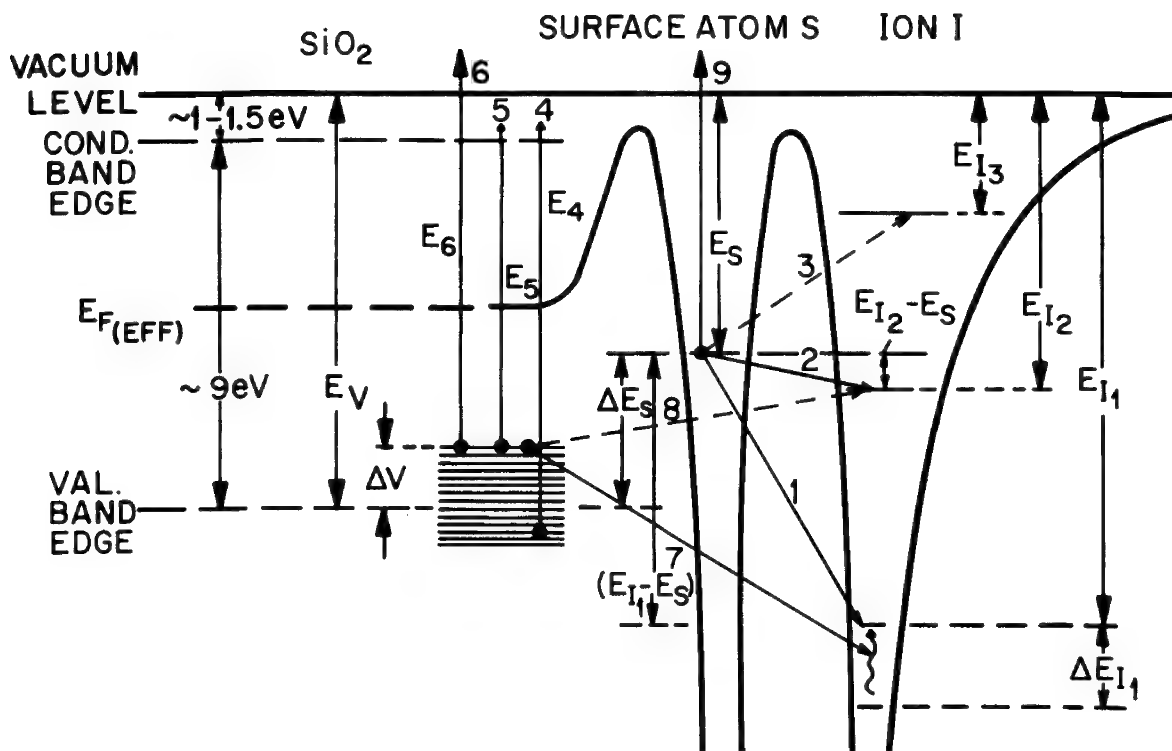


FIG. 1

## Ion Mobilization by Ion Bombardment

by

R. A. Kushner, D. V. McCaughan and V. T. Murphy  
 Bell Laboratories  
 Murray Hill, New Jersey 07974

ABSTRACT

The most striking observation to date from the investigation of the effects of ion bombardment on insulators is the mobilization and movement of sodium ions at room temperature as a direct result of the ion bombardment. This paper will describe this observation and its pertinence to analyses involving ion or electron bombardment of insulators.

The experimental apparatus for the bombardment is depicted in Fig. 1. The ions were generated in a plasma source, accelerated to the desired potential (500 eV) and directed to the target by the 60° magnet which also served to give a one-axis sweep of the ion beam across the sample.

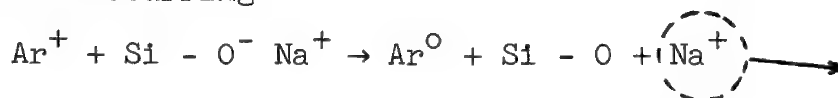
The samples for these experiments were 5000Å thermally grown silicon dioxide on silicon. Sodium containing 0.1% radioactive Sodium-22 was evaporated from a heated filament onto the surface of these oxides.

In counting the activity in the samples advantage was taken of the fact that Sodium-22 is a positron emitter. The products of the positron annihilation, two 0.51 MeV gamma rays emitted in coincidence, were detected. The Sodium-22 activity in the oxides was profiled by removing layers parallel to the surface with dilute HF and counting the etch solutions. The amount of oxide etched off was determined by color comparison with standard oxides. The total sodium per unit area or unit volume was then calculated from the known specific activity of the evaporated sodium.

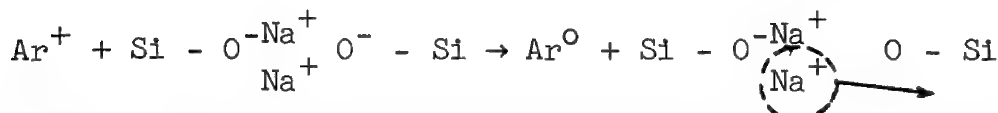
Figure 2 shows a typical profile. The ion energy was 500 eV and the dose was  $1 \times 10^{14}/\text{cm}^{-2}$ . Note:

1. No activity was lost from the sample as a result of the ion bombardment. The sodium used constitutes ~0.1 monolayers and the ion beam did not sputter off any measurable amount of this.
2. All sodium that moved at room temperature as a result of the ion bombardment reached the  $\text{SiO}_2/\text{Si}$  interface.
3. The efficiency for the activation of sodium is  $> 0.1$  per ion. Because of some nonuniformity in the beam sweep and location it is not possible at present to assign a more quantitative number.

As reported in the previous paper,<sup>(1)</sup> ion neutralization at the surface of  $\text{SiO}_2$  results in a large field across the oxide. What we have experimentally shown here is that, as a result of the ion neutralization, sodium moves away from the surface and to the  $\text{Si}/\text{SiO}_2$  interface at room temperature. A field alone, applied by a metal field plate at room temperature, causes no sodium movement. We envision the following reactions occurring



or



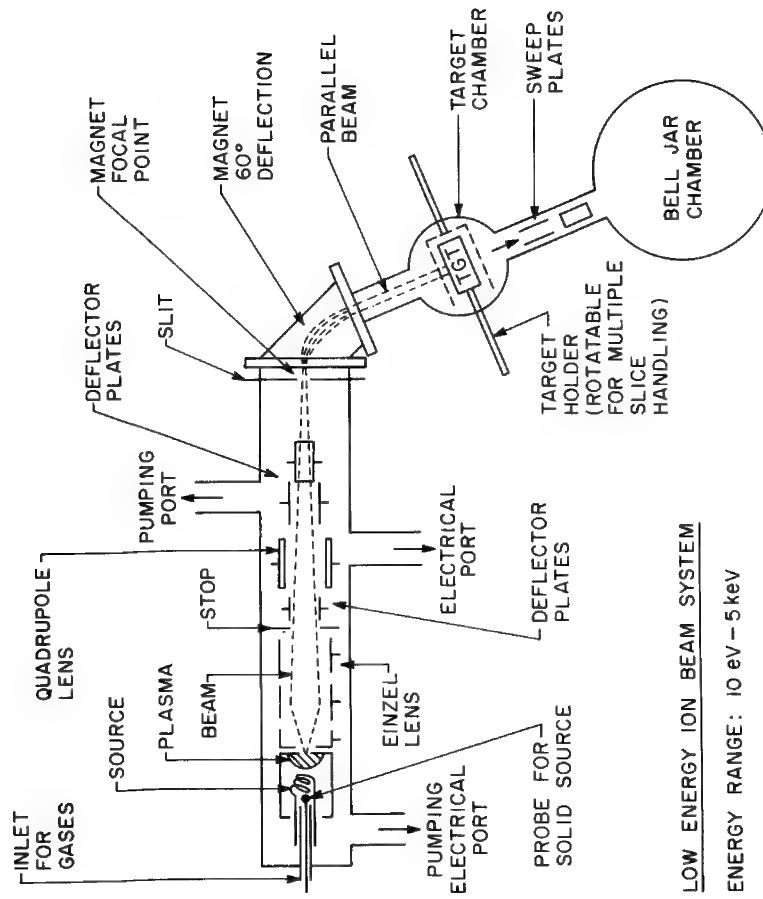
where the sodium is now free of its coulombic bond and can drift across the oxide due to the field set up by the neutralization of the bombarding ions near the surface at "bulk" centers.

What is equally important here is the pertinence to electron and ion probe microanalysis. There is already evidence in the literature for alkali ion movement under electron irradiation of alkali-silicate glasses which is amenable to a similar explanation.<sup>(2)</sup> Therefore, these observations have a direct bearing on all of the electron and ion probe analysis techniques. We can anticipate that, at least as far as alkali ions in insulators are concerned, the ion or electron beam may change the distribution of what it is trying to measure. For ion probe microanalysis the effect will depend on the ionization energy of the bombarding beam relative to the energy levels of impurities in the band gap of the material being measured.<sup>(1)</sup> For Auger electron spectroscopy the question becomes the effect of sputter cleaning of insulating materials prior to the actual measurement. For ion scattering and ion neutralization spectroscopy the same arguments hold and interpretation of the analyses of insulating samples must take into account the effect of surface charge build-up and ion neutralization induced impurity ion movement. We are at present extending these experiments to other common ions.

#### REFERENCES

1. D. V. McCaughan, R. A. Kushner and V. T. Murphy (previous paper, this conference).
2. Vassamillet and Caldwell J. A. P. 40, 1637 (1969).





#### LOW ENERGY ION BEAM SYSTEM

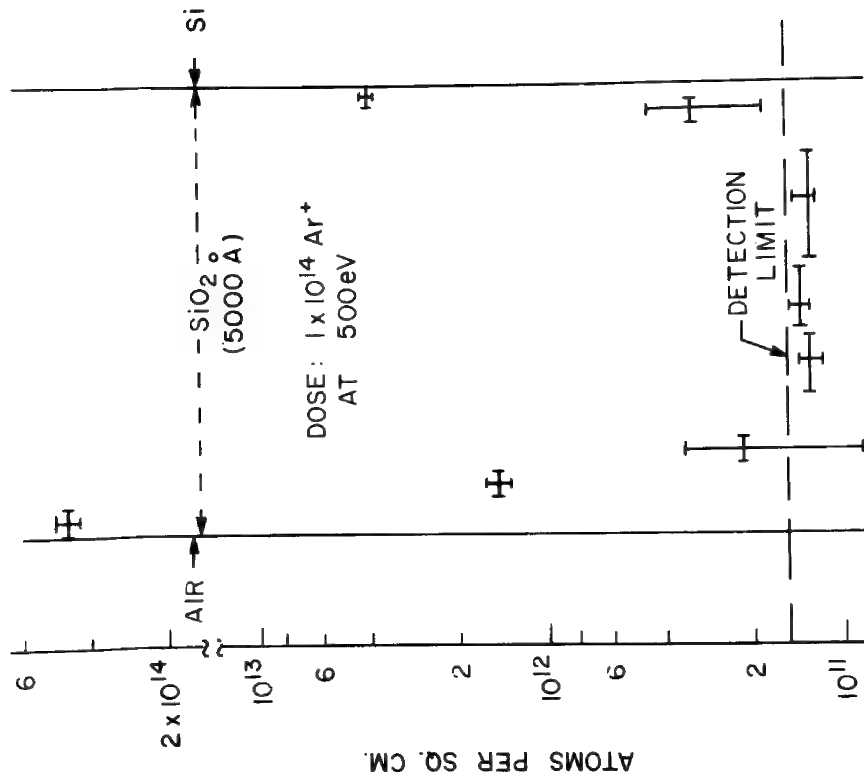
ENERGY RANGE: 10 eV - 5 keV

BEAM CURRENT:  $\begin{cases} 200 \times 10^{-9} \text{ A} @ 30 \text{ eV} \\ > 1 \mu\text{A} @ 2 \text{ keV} \end{cases}$

BEAM ENERGY SPREAD ~ 2-4 eV

MAGNET RESOLUTION ~ 3-4 amu @ 40 amu  
(VARIES WITH SLITS USED)

FIG. 1



SODIUM PROFILE IN BOMBARDED SiO<sub>2</sub>

FIG. 2

## Surface Composition by Analysis of Neutral Impact Radiation

by

C. W. White, D. L. Simms, and N. H. Tolk  
Bell Laboratories  
Whippany, New Jersey

ABSTRACT

A unique and sensitive technique for surface composition analysis has been developed. Called SCANIR, Surface Composition by Analysis of Neutral Impact Radiation, this technique evolved from experiments which show that visible, ultraviolet, and infrared radiation is produced when low energy (less than 4keV) ions<sup>1,2</sup> and neutrals<sup>3</sup> impact on a surface. The optical radiation produced in these low energy collision processes is characteristic of the surface constituents, including surface contaminants. In addition, comparing the radiation produced by ion and neutral impact reveals information on some of the fundamental electronic processes which result from the interaction of these atomic particles with solids.

The optical line radiation produced in collisions of low-energy ions and neutrals with solids arises from excited electronic states of atoms and molecules sputtered off the surface by the impinging beam<sup>1,2,3</sup>. The identity of the constituents of the solid in the first few monolayers can be established by analyzing the spectral distribution of radiation and identifying the prominent optical lines and bands. We find the neutral to be the more useful projectile since all problems associated with charge accumulation on non conducting surfaces are avoided. Low bombarding energies and currents are used to minimize damage to the solid. Application of the technique at these low energies results in a very sensitive probe of the surface region since the range of the incident projectile in the solid is limited at most to a few monolayers.

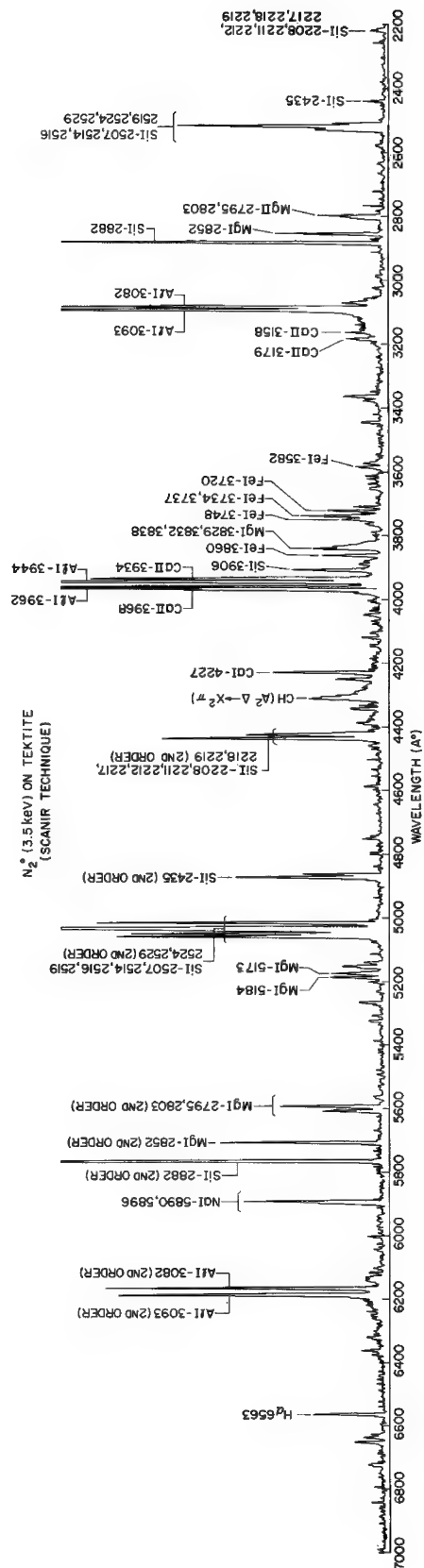
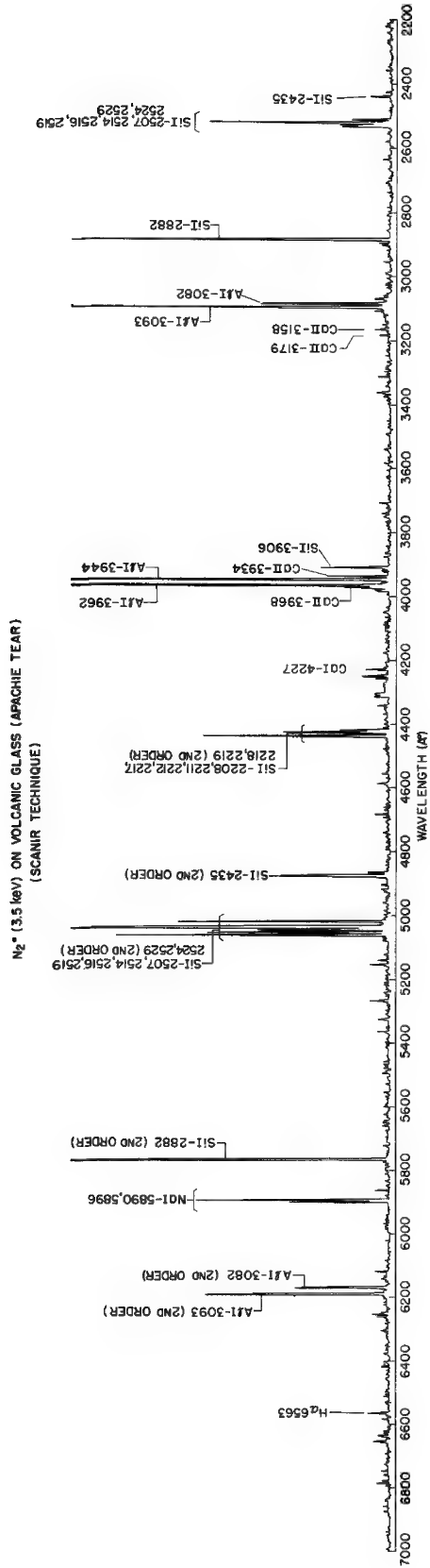
In the case of a metal or semiconductor target, ions (of large ionization energy) and neutrals of the same specie and energy are observed to produce photons from excited states of sputtered atoms with equal efficiency. This agrees with other results<sup>4</sup> which show that these ions impinging on a metal are neutralized by non-radiative processes several Angstroms in front of the surface before the sputtering encounter takes place. When wide bandgap insulators are impacted with neutrals we observe intense optical line radiation arising from excited states of sputtered atoms. Impacting low energy ions on these same insulators produces, in many cases, broad continuum of radiation similar to that produced by low energy electron impact, in addition to radiation from excited states of sputtered atoms.

We have applied the technique of analyzing the low-energy collision induced spectrum of radiation to various pure materials, to complex solids (Volcanic Glass and a Tektite), and to microliter quantities of liquids containing both organic and inorganic material (human blood). The spectrum of radiation produced in the impact of neutral  $N_2$  (3.5keV) on the Tektite<sup>5</sup> and Volcanic Glass<sup>5</sup> are shown in Figure 1. Prominent optical lines observed in the wavelength interval 2200Å - 7000Å are identified by element and wavelength. Radiation from common elements such as Si, Al, Ca, and Na are observed from both of these targets but the Tektite contains, in addition, Fe and Mg as evidenced by the optical lines characteristic of these two elements. These scans were obtained in a time period of 30 minutes each using an equivalent neutral current of  $3 \times 10^{-7}$  amps.

To obtain an indication of the sensitivity of the technique, we have recorded the collision induced spectrum of radiation from a silicate melt ( $SiO_2$ ) target<sup>6</sup> containing oxide impurities of Al, Fe, Ca, K, Mg, and Na at known concentrations. The observation of radiation from the impurities in this sample shows that detection capabilities range from 1 part in  $10^6$  (for Na) to 8 parts in  $10^4$  (for K) under present operating conditions. Substantial improvement is possible by increasing the photon collection efficiency, the integration time, and the incident projectile flux.

#### REFERENCES

1. H. Sporn, Z. Phys. 112, 278 (1939).
2. C. W. White and N. H. Tolk, Phys. Rev. Lett. 26, 486 (1971).
3. C. W. White, D. L. Simms, and N. H. Tolk, Thirty-Second Annual Conference on Physical Electronics, Albuquerque, New Mexico, March 20, 1972.
4. H. D. Hagstrum, Phys. Rev. 123, 758 (1961).
5. These samples were supplied by R. Preston Watts, Huntsville, Alabama.
6. The silicate melt was kindly loaned to us by Dr. Louis S. Walter, Geochemistry Laboratory Goddard Space Flight Center, Greenbelt, Maryland.



## HEMISPHERICAL TRIODE: A DEVICE AND TECHNIQUE FOR MEASURING ELECTRON EMISSION

A. R. Frederickson  
Air Force Cambridge Research Laboratories(AFSC)  
Bedford, Ma 01730

There are situations where it is important to measure the secondary electron emission yields of irradiated samples. This is usually accomplished by applying a variable retarding potential to one or more grids that lie in the path of the secondary electrons. In many cases the grid wires produce unwanted scattering of either the primary radiation or the secondary electrons, or both. The secondary yield is sometimes measured by applying a positive bias to the sample itself, but this technique is prone to error because low energy electrons emitted from the chamber walls cannot be easily separated from the electrons emitted by the sample. The hemispherical triode avoids these problems because the sample is kept at ground potential and the biased element is not in the path of the electrons. This device has the added advantage that the collecting element is also held at ground potential.

The use of the hemispherical triode is based on an analysis of the electrostatic potential inside a hemispherical conductive shell. The Dirichlet electrostatic Green's function has been determined for the hemispherical cavity<sup>(1)</sup>. If one specifies both the potential everywhere on the hemispherical surface and the charge density everywhere inside the hemispherical volume, then the potential everywhere inside the hemisphere can be determined. The potential function inside the hemisphere can be determined for any arrangement of potentials on the conducting surface. If the conducting surface is divided into three elements, then the flow of electrons between two elements can be modulated by a modulating potential applied to the third element. This modulation feature has application to experimental apparatus where low energy electron emission is being measured.

The particular apparatus that has been analyzed and used in experiments is shown in Figure 1. The apparatus consists of a hemispherical collector, a retarding potential bias ring, and an irradiated sample that emits secondary electrons. The analysis has been done only for the cases where the ring and the target are coplanar: but the ring and the target can be any size within this restriction. The effects of changing the relative sizes of the ring and the target have been analyzed and will be discussed.

The basic mode of operation can be understood by inspection of Figure 2. Figure 2 shows the constant potential lines in the vicinity of the sample for a collector and sample bias of zero volts and a ring bias of minus one statvolt. With this bias arrangement, an electron leaving the sample must overcome a potential barrier (due to the ring bias) in order to reach the collector. The height of the potential barrier depends on the direction of electron motion and in this case the height varies between approximately .40 and 1.0 statvolt. Thus, by applying, say, -50 volts to the ring (shown in Fig. 2) we retard all electrons with energies less than  $(.4)(50\text{eV}) = 20\text{eV}$  and collect all electrons with more

than 50eV energy. Electrons with energies between 20 and 50eV may be retarded depending on direction of emission. When zero volts is applied to the ring, there is no retarding potential and all emitted electrons are passed to the collector.

The angular dependence of the retarding potential can be lessened by changing the sizes of the target and ring. However, since high energy electron ( $\geq 10\text{KeV}$ ) bombardment produces relatively few emitted electrons with energies between 20eV and 50eV this angular dependence is of no consequence.

The advantages of the bias ring in an approximately hemispherical geometry are now clear:

- (a) Electron transmission is 100%.
- (b) Construction is relatively simple.
- (c) No grids need to be imposed in the primary beam path or secondary electron paths.
- (d) The retarding potential does not cause electrons emitted by both the chamber walls and the collector to flow to the target. For most geometries, only the flow of electrons emitted by the sample will be affected by the retarding potentials.

The device has been used to measure low energy and high energy electron yields from metals bombarded by 0.2 to 1.4 MeV electrons. Besides studying secondary electron yields the device has potential application in microprobe and SEM work:

- 1. Secondary electrons can be suppressed using this technique.
- 2. Secondary electron emission could be measured by rapidly varying the ring bias and concurrently measuring the in-phase sample emission current while holding the primary high energy beam current relatively constant.
- 3. For samples at high temperatures, the ring can be used to suppress thermionic emission while allowing secondary emission to pass<sup>(2)</sup>. This is done without requiring that a grid be placed in front of a sample.

#### References:

- (1) A. R. Frederickson, J. R. Jasperse, Neil Grossbard, "The Electrostatic Potential Inside a Hemisphere: Its Use as an Electron Energy Analyzer and as a Triode Electronic Device", AFCRL Report #71-0369, June 1971.
- (2) S. Kimoto, H. Hashimoto, T. Kosuge, and A. Mogami, "Specimen Heating Device for Scanning Electron Microscope". Proceedings Fourth National Conference on Electron Microprobe Analysis, Pasadena, Cal., July 1969.

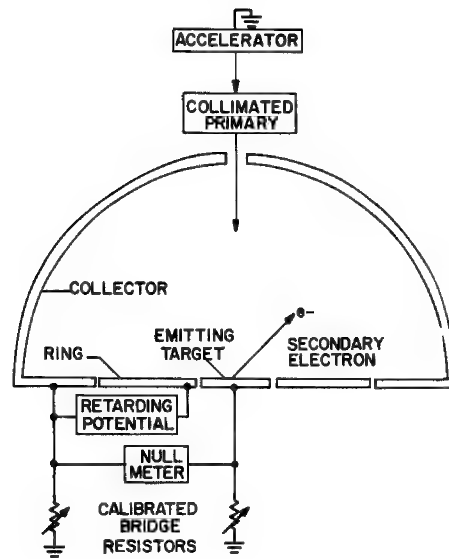


Fig. 1 Schematic of hemispherical triode and secondary emission measuring apparatus. A collimated or focused beam of high energy electrons passes through a hole in the spherical collector and bombards the target. A negative potential applied to the ring can retard target emission. The emission can be measured by many electronic techniques; in this case a bridge circuit is used to attain high accuracy.

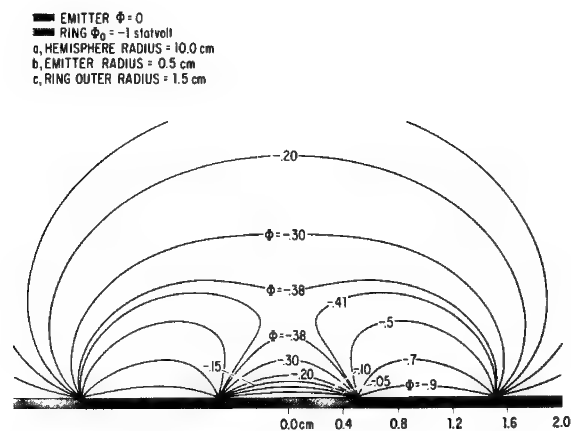


Fig. 2 Constant potential lines in the hemispherical triode. The entire hemisphere is not shown. The region around the emitting target and the ring are shown because it is the potentials in this region that retard secondary electrons.

THE APPLICATION OF SCANNING ELECTRON MICROSCOPY AND ELECTRON PROBE  
MICROANALYSIS TECHNIQUES TO THE FORENSIC SCIENCES

Gary Judd  
Materials Division  
Rensselaer Polytechnic Institute  
Troy, New York 12181

---

The potential for the application of electron optics techniques such as scanning electron microscopy (SEM) and electron probe microanalysis (EPM) to forensic sciences has been well recognized for several years. Basically the thought has been that the ease of photomicrograph interpretation, high resolution, high depth of field of the SEM and these similar properties coupled with the sensitive chemical composition capabilities of the EPM should make these instruments ideally suited for examination of physical evidence samples. However, this has not been the case primarily due to the fact that while the potential was realized the actual utilization required acceptance by the court system. As a prerequisite of that step, the study of various evidence material types by SEM in an effort to evaluate the reliability and reproducibility of this examination type was needed. In addition to a determination of the quality and precision of this application for SEM-EPM, the techniques required for handling and preparing physical evidence samples, the special technology and the analytical procedures that would be necessary in the application by forensic scientists had to be understood, well defined, and developed prior to any use in the field. Thus a research program of study in depth of each of several physical evidence sample types was necessary in order to ensure the most efficient and effective utilization of these techniques.

Paint chip samples were chosen for the initial study for several reasons; first, they are often found in such minute quantities that optical comparison analysis and gross chemical dissolution tests are difficult if not impossible; second, the reliance on color as a method for comparison is such that rarely can identification be made any more narrow in category than that of year, make and model, and when the colors are hard to differentiate from year to year, or car to car, e.g., blacks or whites, even identification of make or year may be impossible. Thus it was felt that the SEM could be used to analyze these types of samples directly and if there was any characteristic of the surface or cross section which could be found, the SEM with its excellent photomicrographic capabilities would be able to accomplish the identification.



Nearly one hundred paint samples from over fifty different vehicles were received from the New York State Police Scientific Laboratory. These were prepared for SEM observation and a total of 500 separate surface photomicrographs of the exterior (outside paint surface that one normally sees), cross section (edge), and interior (primer paint to metal side) surfaces were made.

The observations made could be divided into two categories. Firstly, those surface topographies which are so truly unique so as to present unequivocal data for use in a positive comparison of two samples from the same source; and secondly those surface topographies which while representative and characteristic of their source were less unusual in appearance and therefore were used for placing a sample in a class grouping for further evaluation. The second category of results were often used for a positive comparison of sample to source, but this required the use of more than one photograph view, for example edge and exterior photographs. In addition to use of topographical features, the energy dispersive analyzer has been employed to identify contaminant particles and to obtain spectra for the paint layers. This added analytical capability greatly facilitates comparison procedures.

A second group of evidence samples studied has been firing pin impressions. These analyses utilized the high depth of field capabilities of SEM and unequivocally established the fact that firing pin impressions over an extended number of firings can be used for characterization of the source weapons for most of the twenty weapons studied (semi automatic pistols, revolvers, and shotguns).

Another area of investigation has been whether the EPM can be used to determine the source ammunition of bullet fragments when any of several known ammunition sources were possibly used. In this study the antimony and sulfur content were found to vary significantly in certain batches of lead bullets. Using the antimony level as one criteria and the sulfur level as the second, sources of lead ammunition could be divided into categories, greatly aiding in the identification process of fragments.

A special imaging technique being developed for use in forensic samples in this program is a video taping method whereby an initial sample is taped and then the film played back while a second sample is viewed "live" in the SEM. The second sample can be oriented so as to present the exact same orientation to the camera as the first sample and therefore allow a view for comparison with no orientation shift or distortion. This development will minimize any possible misinterpretation in the photographs.

In summary, the SEM and EPM have been used as a basis for establishing a definite comparison between samples in several forensic evidence

category types. These comparisons have been performed based upon unique aspects of topography, overall class correlation, and/or composition analysis. The success of the SEM in paint sample analysis, bullet fragment studies and firing pin impression comparisons, predicts an extensive future application for these instrumentation techniques in the examination of physical evidence by forensic scientists.

## QUANTITATIVE ANALYSIS OF ULTRA-THIN SECTIONS: A MODEL EXPERIMENT

M. I. Corlett, Department of Geological Sciences, Queen's University, Kingston, Ontario, Canada; and R. S. Thomas, United States Department of Agriculture, Agricultural Research Service, Western Utilization Research and Development Division, Albany, California

Most quantitative electron probe microanalyses are carried out on sections whose thickness is greater than the depth of penetration of the exciting electron beam. When one is faced with the analysis of a thin section of materials -- a section whose thickness is less than the depth of penetration of the exciting electron beam -- at least three new problems arise:

A. What percentage of the thin-section X-ray production is absorbed, compared to a thick section of the same material?

B. What change is there in X-ray production because a supporting substratum (e.g. a glass slide) is encountered whose average atomic number differs from that of the thin section?

C. What percentage of the thick-section X-ray production is produced by the thin section?

A. The absorption correction. In a thick section the average absorption path is approximately  $0.5 \times \text{effective electron range} \times \text{cosec } \theta$ . In an ultra-thin section the average absorption path is approximately  $0.5 \times \text{thickness of section} \times \text{cosec } \theta$ . Therefore, for the thin section ( $\chi$ ) thick section is multiplied by (thickness of thin section/effective electron range for the radiation being considered) before  $f(\chi)$  is calculated.

B. The substratum effect. Consider a section of  $100 \text{ \AA}$  thickness. From our information on effective electron ranges (see C), the energy of the incident beam is virtually unchanged by its passage through this thickness of most materials. The beam is now incident on a supporting substratum; some electrons which are backscattered from this substratum will excite X-radiation in the thin section. But if this were a thick section there would also be electrons travelling back from the depths below  $100 \text{ \AA}$ , and exciting X-rays in the upper regions. The change in the number of electrons being backscattered because the depths below  $100 \text{ \AA}$  are of a different material is compensated for by multiplying the apparent thin-section concentrations by  $R_{\text{substratum}}/R_{\text{section}}$  where  $R$  is the Duncumb and Reed backscatter correction factor and an exciting voltage equal to the accelerating voltage is assumed, at least for ultra-thin sections.

C. Percentage yield. One can obtain data from Andersen's (1) effective electron range measurements and the Thomson-Whiddington full electron range; these ranges are given as mass depths. Andersen's measurements on  $\text{SiK}\alpha$  and  $\text{OK}\alpha$  may be separated; thus we have measurements available of mass depths at which electrons have the energies 0.0, 0.53 and 1.84 KV, as well as

the mass depth ( $0 \text{ mg/cm}^2$ ) at which the electrons have their incident energies. These mass depths can be translated into linear depths for any given density of materials; thus for a given incident electron energy, the energy of electrons at any depth in the specimen can be determined graphically, and the effective linear electron range for any radiation can be obtained. When Andersen's experimental results for depths corresponding to 50% of X-ray production are added to the effective electron range information, curves may be drawn relating thickness of section to percentage of thick-section X-ray yield.

While this approach is valid for thin sections in the 1-2 micron range it is difficult to define the percentage X-ray yield precisely enough for ultra-thin (ca.  $100 \text{ \AA}$ ) sections. Thus a model experiment was set up.  $\text{NaPO}_3$  layers of different thicknesses ( $40\text{--}350 \text{ \AA}$ ) were evaporated on  $\text{SiO}_2$  glass discs and analysed for Na and P. Since  $\text{SiO}_2$  and  $\text{NaPO}_3$  have similar atomic numbers the supporting substratum effect could be ignored. Absorption of X-rays by these thicknesses of  $\text{NaPO}_3$  is virtually nil; only the absorption of X-rays in the standards needed to be considered. Secondary fluorescence is negligible, and atomic number effects would be nearly identical in the specimens and the standards used ( $\text{NaAlSi}_3\text{O}_8$  and  $\text{Ca}_2\text{P}_2\text{O}_7$ ). Then for any section and radiation

$$\% \text{ yield} = \frac{k^1}{c} \times \frac{f(\lambda)_{\text{standard}}}{f(\lambda)_{\text{specimen}}} \times 100$$

where  $k^1$  is the apparent concentration in the ultra-thin section,  $c$  is the true concentration, and  $f(\lambda)$  is the modified Philibert absorption correction. Percentage yield can be plotted against thickness of the section to give the ultra-thin section continuation of the percentage yield curves derived from Andersen's work. These curves can then be used to calculate the percentage yield from thin sections for any radiation, provided only that the density of the material and the thickness of the section are known.

The results of the model experiment and calculation were applied to ashed thin sections of Tipula iridescent virus; no elements other than phosphorus could be detected, and the amount of phosphorus present is consistent with the composition  $\text{H}_3\text{PO}_4$ . Related electron microscope studies (2) on these ash patterns have pinpointed the location of DNA-phosphate in the virus.

#### References

- (1) C. A. Andersen, in *The Electron Microprobe*, pp. 58-74, J. Wiley & Sons, 1966.
- (2) R. S. Thomas and M. I. Corlett, Abstract, 3rd Int. Biophysics Congress, Cambridge, Mass., 1969.

## The Ionization Function and its Application to the Electronprobe Analysis of Thin Films

W. Reuter

IBM Watson Research Center

Yorktown Heights, New York

We developed an analytical expression for the depth distribution  $\phi(\rho z)$  of the x-ray production in electron probe microanalysis. In this expression the electron transmission in the multiple scattering region is represented by a linear fit to Cosslett's<sup>1</sup> experimental data (Fig. 1). In the region of random diffusion the transmission is expressed as  $\exp(-\sigma \rho z)$ . The surface ionization  $\phi(0)$  is given by an analytical expression, which is in good agreement with our experimental data (Fig. 2) and with the data calculated by Duncumb and Melford.<sup>2</sup> The effective path length in the diffusion region was calculated from Cosslett's<sup>1</sup> experimental data on the angular distribution of electrons transmitted through thick films. In the intermediate range Cosslett's expression for the depth dependence of the mean scattering angle was used. The depth distribution of the mean electron energy was approximated by Bethe's law and the corresponding ionization cross section was calculated from an equation fitted to the experimental data of Clark<sup>3</sup> and Green.<sup>4</sup> X-ray generation curves calculated by our expression are in good agreement with those experimentally determined by others (Fig. 3).

The x-ray generation function was applied to the analysis of thin films after appropriate changes have been made in  $\phi(0)$  as a function of the substrate composition and the film thickness. The mass deposition of the element in the film is found by numerical integration of the generation functions for the film and the bulk element standard respectively. The relative standard deviation is approximately  $\pm 10\%$ , based on the analysis of films of known thickness, using a wide range of substrate materials and primary energies (Table 1).

1. V. E. Cosslett, R. N. Thomas, Brit. J. Appl. Phys., 1964, Vol. 15, 883.
2. P. Duncumb, D. A. Melford, 1966, 1st Nat'l. Conf. on Electronprobe Microanalysis, College Park, Maryland.
3. J. C. Clark, Phys. Rev., 1935, 48, 30.
4. M. Green, Ph.D. Thesis, University of Cambridge, 1962.
5. A. Ya, Vyat-skin and A. F. Makhov, Zh. tekhn. Fiz., 28, No. 4, 740 (1958).
6. J. R. Young, J. Appl. Phys., 28, 524 (1957).
7. R. Castaing and J. Henoc, X-Ray Optics and Microanalysis (Herman, Paris, 1966) p. 120.

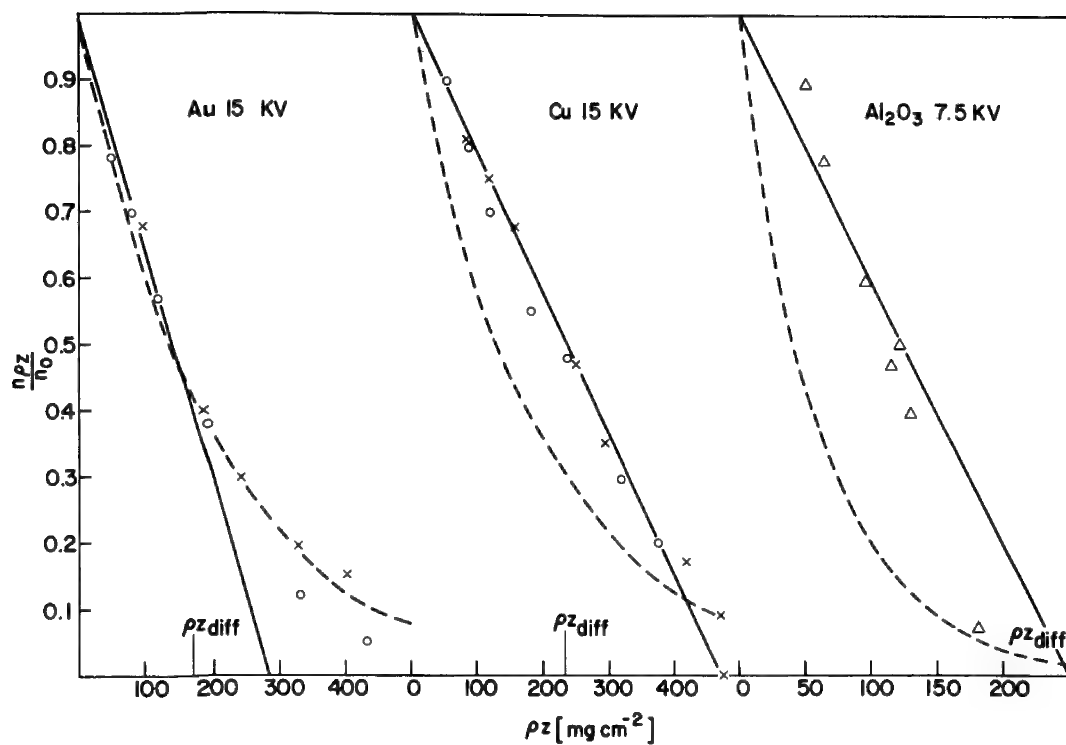


Figure 1: Electron transmission:

- x A. Ya et. al.  
 o V. E. Cosslett and R. N. Thomas  
 Δ J. R. Young  
 ---  $\exp(-\sigma \rho_z)$   
 —  $1 - 4 \cdot 10^4 Z^{0.5} \rho_z / E_0^{1.7}$

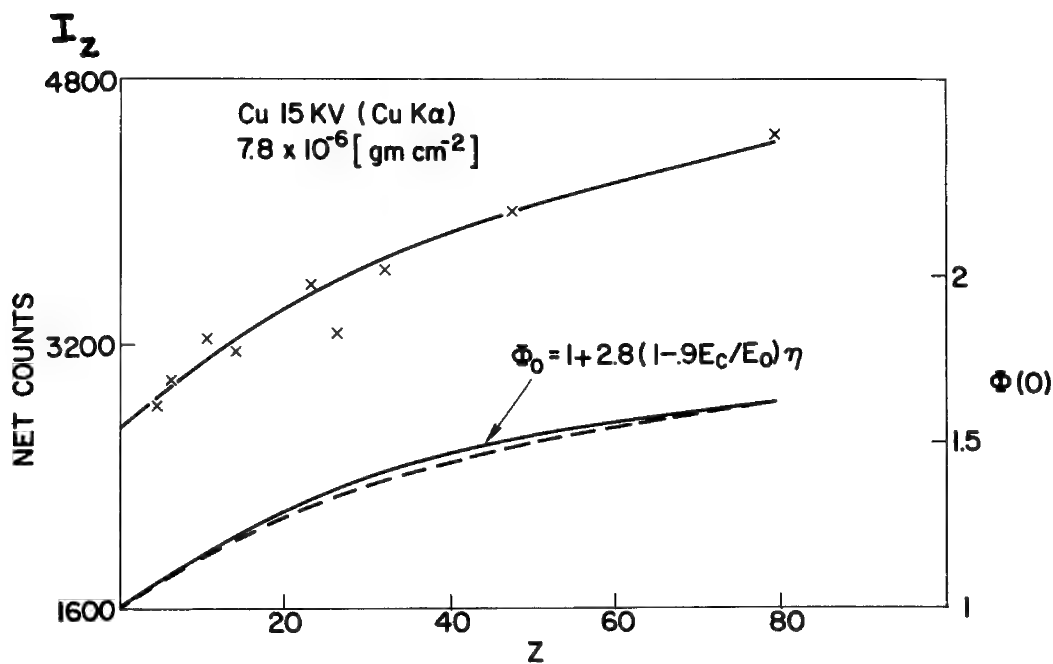


Figure 2: Upper curve: Background corrected Cu K $\alpha$  intensity emitted by a thin Cu-film on various substrates.  
 Lower broken curve: Normalized ( $I_z/I_{z=0}$ ) experimental curve.  
 Lower solid curve:  $\Phi_0 = 1 + 2.8(1 - 0.9 E_c/E_0) \eta_z$

TABLE I

El	Z <sub>sub</sub>	E <sub>0</sub> KV	E <sub>c</sub> KV	$\mu$ g <sup>-1</sup> cm <sup>-2</sup>	k	$\rho^Z_{\text{emp}}$ g cm <sup>-2</sup>	$\rho^Z_{\text{chem}}$ g cm <sup>-2</sup>
Al	5	12	1.56	426	.0324	14.2	14.5
					.0166	7.6	7.3
					.0098	4.6	4.4
					.0075	3.6	3.4
					.407	14.6	14.5
					.182	7.0	7.3
					.109	4.3	4.4
					.084	3.3	3.4
					.046	75	73
					.073	83	73
					.093	85	73
Cu	10	30	8.98	54	.063	72	83
	79				.104	85	83
					.433	71	83
					.590	82	83
					.612	45	48
Ni	10	6	.871	3500	.232	43	48
					.131	40	48
					.117	47	48
					.094	23	26
					.053	23	26
					.035	24	26
					.017	23	26
Au	78	30	11.9	128	.122	94	77
					.178	91	77
					.276	198	193
					.366	183	193

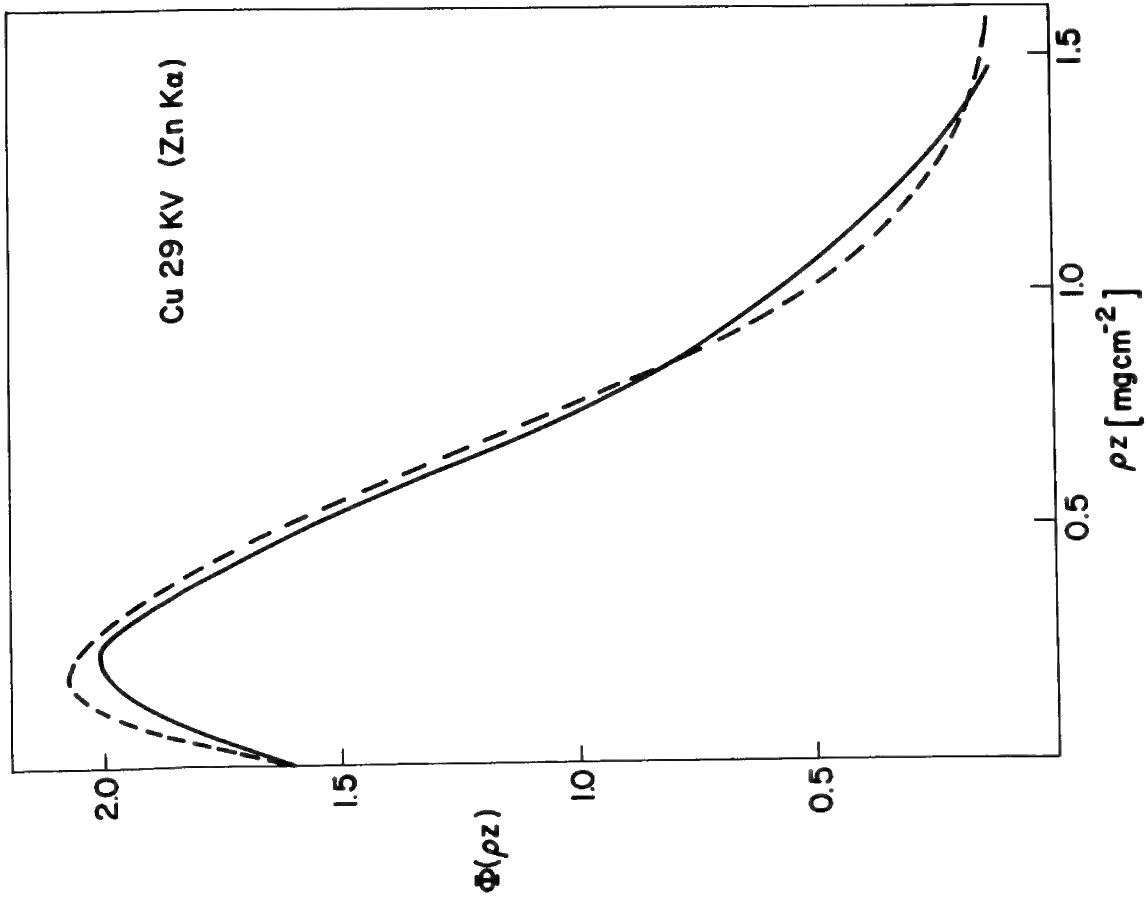


Figure 3: Ionization function  $\phi(\rho z)$  for Cu at 29 KeV using Zn as tracer:  
 — R. Castaing and J. Henoc<sup>7</sup>  
 --- our model

## AN ELECTRON MICROPROBE STUDY OF GOLD FILMS

by

R. B. Bolon and E. Lifshin

Materials Characterization Operation

General Electric Corporate Research and Development

The broad use of electron microprobes and scanning electron microscopes in the area of microelectronics has necessitated the development of quantitative correction procedures for the analysis of thin films. Although several models have been proposed<sup>1,2,3</sup> to describe X-ray generation for both pure elemental and alloy films, relatively little experimental data has been collected to test their validity. This is not too surprising because it is difficult to prepare uniform films of known thickness for pure elements, and additional complications arise in the case of alloys where the samples must be homogeneous and of known composition.

Although the present study is directed toward the analysis of thin films prepared from NBS Cu-Au microprobe standards, this paper is principally concerned with the results obtained from a preliminary study of pure gold films. Although some data has already been collected on gold films by other investigators<sup>1,5</sup>, it was necessary to collect additional data for a variety of substrates, operating voltages, and film thicknesses at the  $18^\circ$  takeoff angle of the Cameca microprobe used for this study. Furthermore, since it was felt that the accuracy of thin film data is often limited by film thickness measurements, a specially machined rotary shadowing mask was made to simultaneously deposit seven films varying in thickness by factors of two. Interference microscopy was then used to measure the thickest layers where the highest accuracy could be expected. Examples of data collected are presented in figures 1 and 2 which show the dependence of the  $AuM\alpha$  X-ray intensity on film thickness for a variety of substrates and operating voltages respectively. Measurements have also been made of the backscattered electron fraction as a function of substrate and the transmitted electron signal for carbon supported films. The various types of experimental data collected will be compared to that generated by Monte Carlo calculations using the method of Curgenven and Duncumb.<sup>6</sup>



## References

1. Cockett, G. H., and Davis, C. D., Brit. J. Appl. Phys., 14, 813 (1963).
2. Philibert, J. and Tixier, R., "Some Problems with Quantitative Electron Probe Microanalysis", Quantitative Electron Probe Microanalysis, Ed. by K. F. J. Heinrich, NBS Special Publ. 298, pp 13-33 (1968).
3. Colby, J. W., "Quantitative Microprobe Analysis of Thin Insulating Films", Advances in X-ray Analysis, Vol. 11, Plenum Press, New York, p 287 (1968).
4. Sweeney, W. E., Seebold, R. E., and Birks, L. S., J. Appl. Phys., 31, 1061 (1960).
5. Hutchins, G. A., "Thickness Determination of Thin Films by Electron Probe Microanalysis", The Electron Microprobe, ed. by T. D. McKinley, K. F. J. Heinrich, and D. B. Wittry, John Wiley & Sons, New York, p 390 (1966).
6. Curgenven, Mrs. L., and Duncumb, P., TI Research Laboratories Report #303, July 1971

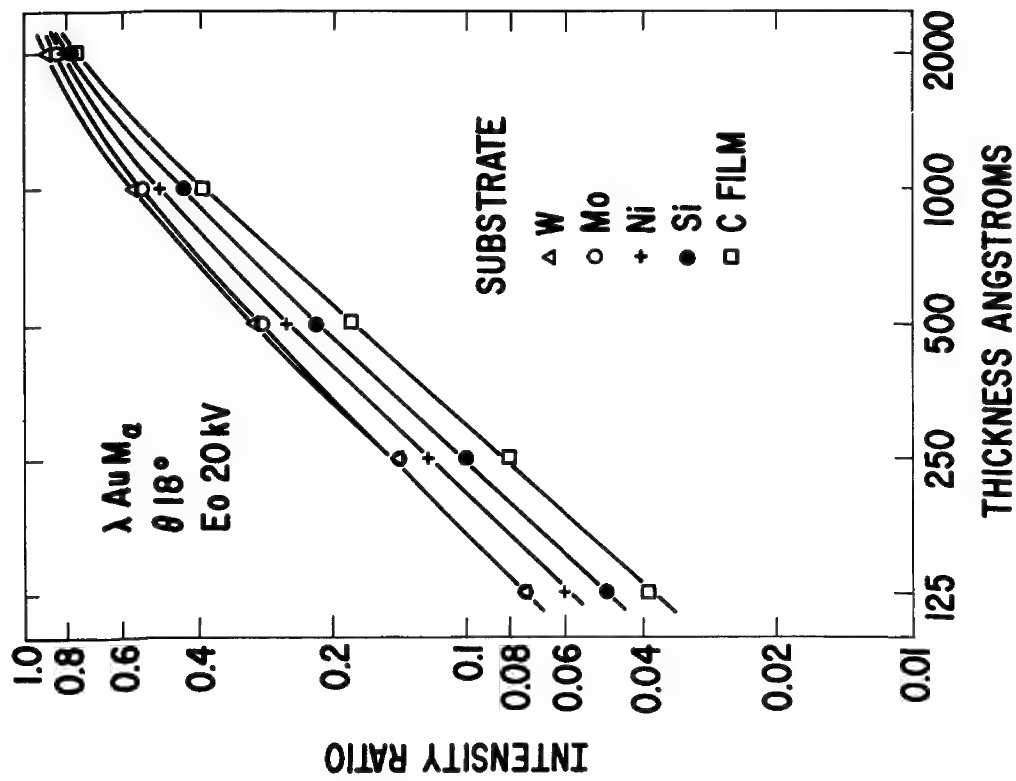


Figure 1 Variation of AuM $\alpha$  X-ray intensity ratio with film thickness at a fixed operating potential for various substrates. Data corrected for deadtime and backgrounds.

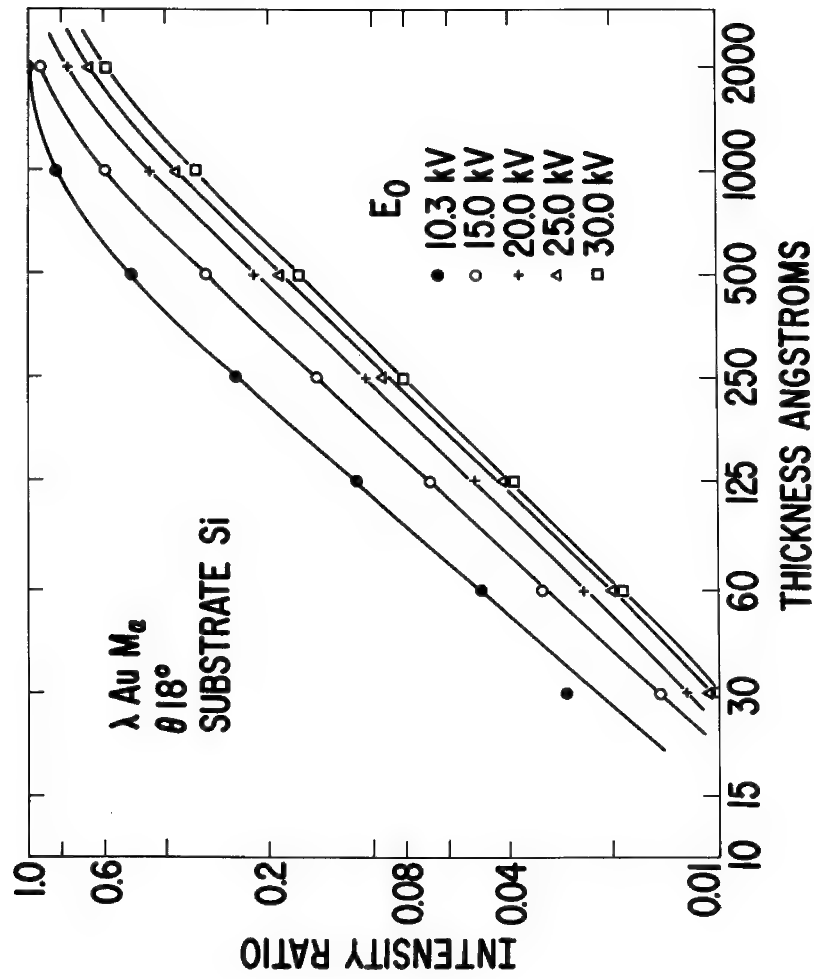


Figure 2 Variation of AuM $\alpha$  X-ray intensity ratio with film thickness for a given substrate at various operating potentials. Data corrected for deadtime and backgrounds.

The Effect of Take-Off Angle on Particle Analysis  
With the Electron Microprobe

J. T. Armstrong, P. R. Buseck, and E. F. Holdsworth  
Departments of Chemistry and Geology  
Arizona State University, Tempe, Arizona

Fine-grained particles (1-20  $\mu$  diameter) are widespread—for example, as airborne industrial and mineral pollutants, as ablation products from rockets and meteorites, as metal and insulator corrosion products, and as small inclusions in minerals and synthetic materials. Determination of their chemical composition presents major problems. The electron microprobe is, because of its small beam size, the best means for analyzing individual particles.

There are major difficulties connected with attempting to obtain quantitative or semi-quantitative analyses of small particles with the microprobe. The particles are too small to routinely imbed in a matrix and polish, and correction equations utilizing a fixed take-off angle for a flat surface are inappropriate. In addition, the volume excited by the electron beam generally exceeds the size of the smaller particles, thereby preventing the use of absolute count rates.

We have devised a series of experiments to determine whether these problems can be compensated for and reasonably accurate analyses of particles can be routinely performed.

White et al.<sup>1,2</sup> have suggested that approximate quantitative analyses of irregularly shaped particles may be obtained by comparing the ratios of intensities of two elements in a sample to a calibration curve obtained by determining similar ratios in a set of standards. They found that intensity ratios determined for two elements on an ARL-EMX microprobe for a variety of sets of zeolite particles of differing morphologies but identical compositions varied only by about 10-15% relative to the mean. We have confirmed these results for a variety of minerals on a Cameca MS-46 microprobe. This is encouraging, because theoretically if the take-off angles varied randomly from particle to particle and from spectrometer to spectrometer, the ratios would vary by several hundred percent in many instances.

There are several limitations to the ratio method. At best, it approximates a similar method used for analyzing flat surfaces while not correcting for absorption, fluorescence, and atomic number effects. Consequently, its use is restricted to the special case when a suite of standards very similar in composition to the particles being analyzed is available. Our experimental evidence shows that ratios measured from a set of particles of known composition are consistently different from those measured from a polished specimen of the same composition—clearly, the particle geometry is an important variable and cannot be assumed to be similar to that of a flat surface. Thus, in order to use this method for particle analysis, one would need a set of powdered standards. Such standards are difficult to prepare, are not always reuseable because they commonly degrade under electron bombardment especially if they contain volatile elements, and they are difficult, if not impossible, to recoat.

The ratio of intensities found in particles could be compared to those in polished standards if a useable mean take-off angle for the particles could be determined. We have analyzed both particles and polished sections of known compositions and determined their various intensity ratios for a variety of minerals. By reversing the conventional absorption and fluorescence correction equations (the atomic number correction cancels out when ratios are used) we solve for the take-off angle for each element. In order to obtain a unique solution for the take-off angles, it is necessary to take several different pairs of element intensity ratios on each particle and solve the equations simultaneously. In our case (Cameca MS-46 microprobe) we used ratios measured from four spectrometers—two pairs of spectrometers located at opposite sides of the specimen.

We have found that the range of calculated take-off angles for particles of a wide range of morphologies and sizes (1-20  $\mu$ ) is reasonably narrow. Moreover, it is measurably different from the  $18^\circ$  take-off angle of the Cameca microprobe for a flat surface. Thus it appears that a useful mean take-off angle for particles can be approximated for use in a modified correction program. We have designed such a computer program to correct intensity ratios for fluorescence and absorption.

#### References

1. White, E. W., Microprobe Technique for the Analysis of Multiphase Microcrystalline Powders, Amer. Min., 49, 196 (1964).
2. ———, Denny, P. J., and Irving, S. M., Quantitative Microprobe Analysis of Microcrystalline Powders. The Electron Microprobe (T. D. McKinley et al., eds.) p. 791, John Wiley and Sons, New York, 1966.

## ION MICROPROBE ANALYSIS OF SMALL PARTICLES

Michael A. Bayard

Walter C. McCrone Associates, Inc., Chicago, Illinois

The ion microprobe is perhaps one of the most useful tools for the all around analysis of particles. The basic operation of the machine is fairly simple. A beam of ions is generated in a duoplasmatron, accelerated to a suitable voltage and then passed through a primary mass filter in order to select a single species of ion for bombarding the sample. Any gas which will not corrode the source can be used. The single species is next focused by a pair of electrostatic lenses to form a spot on the order of  $1\text{ }\mu\text{m}$  on the surface of the sample. Secondary ions generated from the impact of the primaries are collected by an electrostatic collecting system, then passed through a mass spectrometer and analyzed. In addition, as in the electron microprobe, an optical microscope is provided for viewing the sample while under bombardment by the ion beam. Unfortunately, the present mass spectrometers used in ion probe microanalysis are of comparatively low resolution, the resolution being sacrificed in order to get a reasonable collection efficiency for the ions generated on the sample. Roughly 10% of the ions generated can be collected. All elements in the periodic table can be detected though the sensitivity varies by over two orders of magnitude.

In practical terms, the ion probe proves to be a very useful machine. Most of our applications to date have been in the area of small particle analysis where we are interested in determining the composition of both the outer layer of a particle, thus indicating its reactions with an environment, and the overall composition of the bulk material in the particle. In most cases considerable useful information can be gotten from the first 30-50 monolayers present in a particle as small as  $1\text{ }\mu\text{m}$ . There is one rather odd and fortunately useful property which occurs in the analysis of both thin films and small particles. This is the property of recondensation of material from the particle. The mass spectrometer is roughly 10% efficient and, of course, the sputtering process is also fairly inefficient at producing ions to be collected. However, in many cases material from a particle or thin film will condense to form a layer around the area of impact of the ion beam. This condensed layer can then be looked at with the beam as if it were the original material present in the sample, with the reservation that, in some cases, material will preferentially condense and unfortunately not have precisely the same composition as the particle. However, in many cases, it is better to try to attempt analysis of this condensation layer rather than the true surface of the particle. One reason for this is the fact that a reactive emission layer usually must be built up on the surface of the sample in order to get even reasonably quantitative analyses. For the first few tens of seconds to several minutes of ion bombardment, the intensity of emission fluctuates greatly. After a reactive layer is formed with the gas in the ion beam, usually oxygen, emission becomes steady and quantitative analysis can be attempted. With a small particle or thin film sample, although the first material sputtered off directly into the mass spec does not conform to this reactive layer, the condensed material does and, to a first approximation, can be analyzed quantitatively. Otherwise, at least 100 monolayers would have to be removed in order to approach the steady state conditions required for quantitative or semi-quantitative analyses.

The most critical limitation of the ion probe is the destruction of the sample. With particles on the order of half a micrometer or less this can be a real problem. Fortunately, the count rates and peak to background ratios are good. Particles of chromium oxide less than 500 Å across can readily be seen. The survival time of such a particle can be as long as 40 seconds. Also, because the condensation effect tends to enlarge the apparent ion source from the sample, a fairly large beam will still give a good signal on very small samples.

Many different particle systems have been analyzed. Lead particles from auto exhaust samples have been studied in some detail. There seems to be considerable difference between the composition of the outer layers of lead chlorobromide particles and the center of the particle. Tentative results indicate an almost pure  $\text{PbBr}_2$  species on the surface of particles in the 0.3–0.5  $\mu\text{m}$  size range, although more work is needed for verification.

Another facet, where the ion microprobe may prove very useful is organic analysis. At present the ion microprobe is thought of strictly as an inorganic tool and, for the most part, rightly so. However, many organic materials do give characteristic spectra when bombarded with very low voltage ions. Admittedly, the spectra are very difficult to interpret and, in most cases, the only thing that can be attempted is a fingerprint matching type of technique. In many cases though this is much better than no information at all as to the characteristics of the organic material.

TABLE 1

Composition of Lead Particles in Auto Exhaust,  
Outer Layer of Particle

Size ( $\mu\text{m}$ )	Pb	(%) Cl	Br
0.2	50	12	41
0.5	55	7	40
0.7	52	3	43
0.2	56	2	40
0.3	51	12	39
0.4	58	2	38
1.5	62	12	27
0.2	52	8	41
0.3	59	3	37
0.7	51	10	39
0.6	60	15	26
0.8	58	2	41

TABLE 2

Composition of Lead Particles in Auto Exhaust,  
Center of Particle

Size ( $\mu\text{m}$ )	Pb	(%) Cl	Br
0.8	63	11	22
0.7	65	13	18
0.5	59	10	33
0.7	68	15	17
0.3	59	16	24
0.5	62	14	21
0.2	61	10	25
0.5	67	11	20
0.8	65	13	22
0.3	63	10	29
0.9	65	9	25
1.8	59	11	29
1.7	68	14	19

SECONDARY ION EMISSION AND AUGER SPECTROSCOPY  
FOR THE SURFACE AND IN-DEPTH ANALYSIS  
OF SPUTTERED TANTALUM THIN FILMS

by

J. M. Morabito  
R. H. Minetti

BELL TELEPHONE LABORATORIES, INCORPORATED  
555 Union Blvd.  
Allentown, Pennsylvania  
and

R. L. Lewis  
Cameca Instruments  
Elmsford, New York

The Cameca\* Ion Microanalyzer has been used to analyze the surface and bulk of a number of sputtered tantalum thin films. This technique of chemical analysis has unique analytical capabilities which are based on the emission and subsequent mass analysis of characteristic secondary ions ejected by high energy (several KeV) ion bombardment.

Secondary ion mass spectra can be obtained which identify all impurity elements (including isotopes) present in the film with a sensitivity for most elements in the ppm range. Ion images with a lateral resolution of  $\sim 1\mu$  independent of primary beam size can provide a chemical distribution map of the impurities in the bulk and on the surface of the films. In-depth concentration profiles can also be obtained with a depth resolution in the 50 Å - 100 Å range which makes localized (i.e. small selected volume) analysis possible. The results obtained on sputtered tantalum films, reactively sputtered (Argon-oxygen mixtures) tantalum films, thermally oxidized tantalum and tantalum-aluminum films are presented to demonstrate these unique analytical capabilities.

In addition to these results, analytical results by Auger Spectroscopy and ESCA (Electron Spectroscopy for Chemical Analysis) on the same films have also been taken when complementary to ion emission analysis. The combination of both Auger Spectroscopy and Secondary Ion Emission analysis provided new insight into the surface chemistry of sputtered tantalum films and on the lateral and depth distribution of the impurities present in these films. Secondary ion emission was found to be more sensitive than the Auger technique.

---

\*Cameca Instruments, Elmford, N. Y.

The limitations of quantitative analysis based on a generalized model of secondary ion emission are also discussed. These limitations are mainly due to the existence of several mechanisms in the ion formation process and the possibility of the superposition of emission mechanisms, mass interferences, and to chemical and matrix effects which influence the yield of secondary ions. It is possible, however, to do quantitative analysis with the technique down to the ppm level with standards of known composition and structure. Quantitative analysis by this method is shown to depend on the accurate and reproducible measurement of characteristic parameters such as sputtering rate ( $\dot{z}$ ) and secondary ionization yield of the impurity relative to the matrix ( $K_{rel}$ ). The magnitude of  $K_{rel}$  is best determined by the use of standards. The equation which relates impurity concentration  $C$  (ppm at.) in a given matrix to these parameters is

$$C = \frac{i_{a_i} 10^6 \left( \frac{100}{a_i} \right) S(E, \alpha, M)}{K_{rel} K_m \sigma \dot{z} A (1.6 \times 10^{-19} \text{ C}^\circ/\text{ion}} \quad (\text{equation 1})$$

where,

1.  $C$  - Concentration (ppm Atomic)
  2.  $i_{a_i}$  - Secondary Ion Current of Impurity
  3.  $a_i$  - Isotopic Abundance
  4.  $S(E, \alpha, M)$  - Sputtering Efficiency of Matrix
  5.  $K_m$  - Secondary Ion Yield of Matrix
  6.  $\sigma$  - Surface Atom Density of Matrix
  7.  $\dot{z}$  - Sputtering Rate
  8.  $A$  - Area of Analysis
  9.  $K_{rel}$  - Secondary Ion Yield of Impurity  
Relative to the Matrix
  10.  $C^\circ$  - Coulombs
- Eq. 1 is applied to results on oxygen and nitrogen containing tantalum films, and for silicon in  $Ta_2O_5$ . The accuracy of these quantitative results is believed to be within  $\pm 10\%$ .

Qualitative surface analysis is possible with secondary ion emission, but the presence of hydrocarbon compounds and



adsorbed gases which cause mass interferences makes unambiguous surface impurity identification difficult. The Auger spectrum in the energy range from 0 eV to 975 eV obtained prior to in situ ion cleaning on a sputtered tantalum film is shown in Fig. 1. The major impurities on the surface of this film are sulphur, carbon, oxygen, nitrogen, iron, nickel, and copper. The significance and cause of these metallic impurities has been investigated. The secondary ion mass spectrum obtained on the same sample in the mass range from 50 to 72 is shown in Fig. 2. The spectrum was taken while sputtering through  $\sim 100$  Å of the tantalum film. The same metallic impurities detected by Auger Spectroscopy (Fig. 1) are present, but identification of these impurities is complicated by the presence of hydrocarbon  $C_xH_y$  parasite lines as shown in Fig. 2. This interference effect disappeared and did not return after the removal of approximately 40 Å from the tantalum surface. It is therefore not due to contamination of the tantalum film from residual gases in the sputtering chamber of the Cameca instrument. It is attributed to the presence of hydrocarbon compounds on the tantalum film prior to analysis.

FIGURE 1. Auger Spectrum of Sputtered Tantalum Film Prior to In Situ Ion Sputtering with Argon Ions

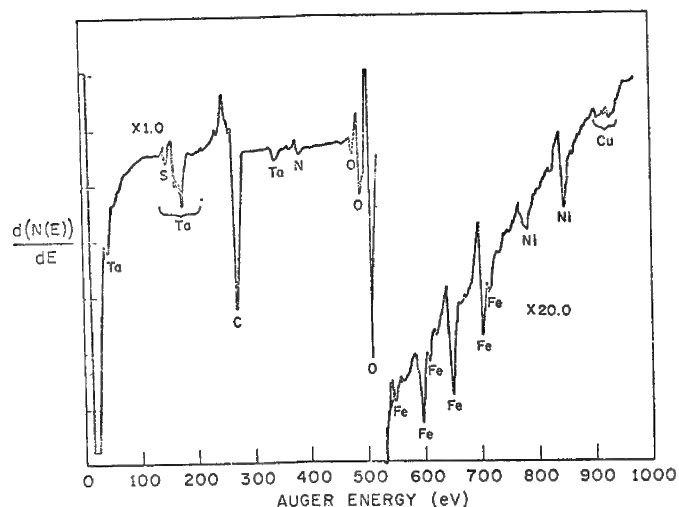
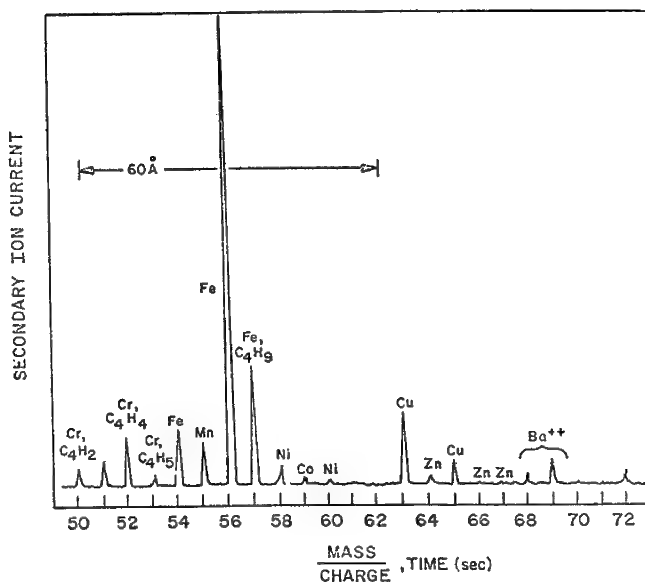


FIGURE 2. Secondary Ion Mass Spectrum of Sputtered Tantalum Film. This Spectrum was Recorded While Removing 100 Å from the Surface with Primary Argon Ions.



## CARISMA™ A QUANTITATIVE CORRECTION PROCEDURE

## FOR THE ION MICROPROBE MASS ANALYZER

C. A. Andersen  
and  
J. R. Hinthorne

Hasler Research Center  
Applied Research Laboratories

An analytic model has been developed (1) for the interpretation of sputtered ion emission from samples bombarded with high energy beams of reactive gases. This model states that the major factors that alter the relationship between the relative sputtered ion yields of the elements and their atomic concentrations in a given sample are those that are related to the excitation and ionization of the sample atoms in the atomic collisions caused by the ion bombardment. In this respect, our experiments have indicated that an equilibrium partitioning of energy exists between the atoms in the bombarded region, and that the ionization process can be written as a dissociation reaction:



Where the dissociation constant is given by:

$$K_n = \frac{n_M^+ n_{e^-}}{n_M}$$

where the n's represent the concentrations per unit volume of the singly charged positive ion and atoms of M and of the electrons. Under equilibrium conditions the energy states of all the particles within the excited volume can be described thermodynamically and the ion to atom ratio of each element calculated using the Saha-Eggert ionization equation:

$$K_n = \left( \frac{2\pi}{h^2} \cdot \frac{m_{M^+} m_{e^-}}{m_M} \cdot kT \right)^{3/2} \frac{B_{M^+} B_{e^-}}{B_M} \cdot e^{-E/kT}$$

where h is Planck's constant, k is Boltzman's constant; T is the absolute temperature, m represents mass, B represents the partition function, and E is the dissociation energy (in this case it is the first ionization potential of the atom M). It can be seen that if the partition functions and ionization potentials are known, the ratio of the number of singly charged ions to neutral atoms of an element is determined by the temperature and electron density of the assemblage.

This is the basis for a quantitative method since the singly charged ions are directly observed in the mass spectrum. Prediction of the singly charged to neutral atom ratio permits the calculation of the total number of atoms of an element present in the sputtering assemblage. If all the elements observed

in the mass spectrum are corrected in this way, the atomic composition of the sample is derived. A computer program entitled CARISMA™ (Corrections to Applied Research Laboratories Ion Sputtering Mass Analyzers) has been developed to perform these computations (2).

The accuracy of the correction procedure in trace element analysis is illustrated in figure 1 where well-characterized standard materials were analyzed. For each specimen CARISMA™ was used to search  $T-n_e$ -space to find a set of values for these two parameters which on the basis of the observed sputtered ion intensities gave an absolute atomic composition that best matched the known concentrations of two of the elements selected to be internal standards in that specimen. The observed intensities of all the other elements in the sample were then corrected at these same  $T$  and  $n_e$  - conditions to give the results illustrated. The elements used as internal standards are not shown and generally have an error of less than 5%. The vertical axis gives the average concentrations for the elements as determined by a variety of twelve common analytic techniques (3). A vertical bar illustrates laboratory spread. All values are in atomic percent. This type of comparison has been accomplished for over twenty elements to date with satisfactory results. CARISMA™ also contains provisions for using one or no internal standards but the accuracies of these procedures have not yet been fully evaluated.

The sputtering assemblage is basically a dense plasma of coexisting positive and negative atomic and molecular ions, of electrons, and of neutral atoms and molecules. The molecular and atomic species in an equilibrium assemblage are related through the dissociation reaction:



where the dissociation constant is given by:

$$K_n = \frac{n_M n_O}{n_{MO}}$$

where the  $n$ 's represent the concentrations per unit volume of the atoms and molecules. This dissociation constant can also be calculated with an appropriate Saha equation:

$$K_n = \left( \frac{2\pi}{h^2} \cdot \frac{m_M m_O}{m_{MO}} \cdot kT \right)^{3/2} \frac{B_{MO}}{B_M B_O} \cdot e^{-E/kT}$$

where the symbols are as before and  $E$  in this case is the dissociation energy of the diatomic gaseous molecule. At a given  $T$  and  $n_e$  - these relationships can be used, for example, to calculate the molecular monoxide to metal atom ratio if the concentration of free oxygen in the plasma is known. These equations are used in CARISMA™ to correct the data for atoms present in molecular form.

The accuracy of this approach is illustrated in figure 2 where data obtained from a mineral standard bombarded with a pure beam of  $^{18}O^-$  is shown. The observed positive atomic and molecular ion intensities of both  $M^{16}O$  and  $M^{18}O$  have been corrected for their degree of ionization and plotted as a function of the calculated dissociation constant and the average concentration of free

$^{16}\text{O}$  or  $^{18}\text{O}$  in the plasma as determined from the data. The fit of the data demonstrate that the molecular ions observed in the mass spectrum are the products of equilibrium reactions in the plasma phase and that their relative concentrations can be calculated from the above equations. The correlation of the data for molecules of the same atom with natural  $^{16}\text{O}$  from the sample and with implanted  $^{18}\text{O}$  demonstrates that the observed molecules are not directly related to the molecular structure of the solid. The concentration of implanted oxygen can also be calculated from these data.

#### REFERENCES

1. C.A. Andersen, Third, Fourth, Fifth and Sixth Natl. Electron Microprobe Conf., Chicago 1968; Pasadena 1969; New York 1970; Pittsburgh 1971; J. Mass Spect. and Ion Physics, 2 (1969) 61; 3 (1970) 413; Science, 175 (1972) 853.
2. C.A. Andersen and J.R. Hinthorne, Appl. Res. Labs. IMMA Manual, 1972.
3. M. Fleischer, Geochim. Cosmochim. Acta, 33 (1969) 65; F.J. Flanagan, *ibid*, 33 (1969) 81; J.C. Rucklidge et al, *ibid*, 34 (1970) 247; B.W. Evans, Contr. Min. Petr., 24 (1969) 293; D.M. Shaw, J. Petr., 1 (1960) 261; B. Mason and A.L. Graham, Smithsonian Contr. Earth Sci. 3; NBS Misc. Publ. 260, 1968; J. Stout, U. Minn. personal communication.

FIGURE #1

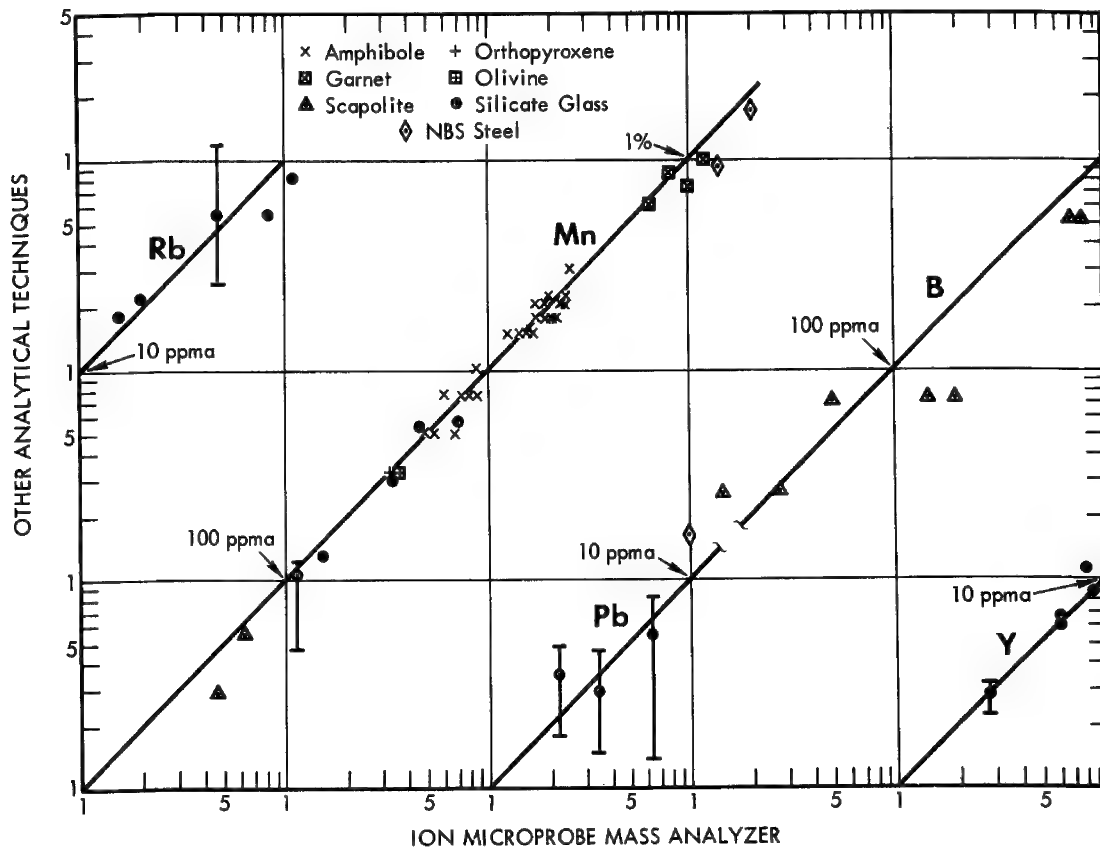
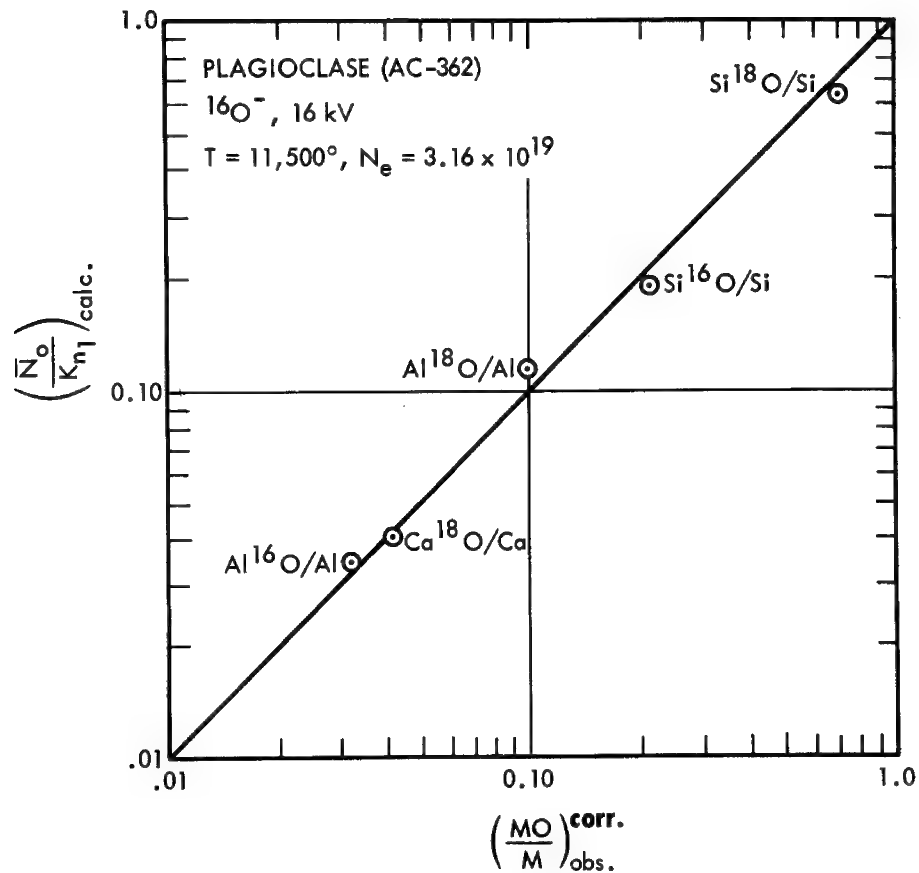


FIGURE #2



## PREPARATION AND EXAMINATION OF BIOLOGICAL SAMPLES

T. A. Hall

Cavendish and Biological Microprobe Laboratories, Cambridge, England

---

In this review paper we shall concentrate on two aspects of biological studies: the assessment and prevention of electron beam damage, and the preservation of the distribution of chemical elements during specimen preparation. We shall also consider the speed of microprobe analysis in relation to the requirements of biological studies.

Beam damage: Besides earlier studies of the removal or displacement of elements by electron probes in inorganic materials (1,2,3), there are now reports of effects in biological specimens (4,5). Höhling et al (5) carried out measurements on kidney homogenates and kidney sections 6  $\mu\text{m}$  thick, cut frozen and then dried in vacuum, and mounted on Nylon films 100-200 nm thick. Potassium, chlorine, sodium and continuum X-ray intensities were monitored during successive 6 or 10 sec counting intervals under a 30-kV probe. Effects were observed as a function of specimen current (10 vs. 60 nA specimen current as measured on a copper block), and as a function of coating (evaporated Al layer of approx. 30 nm, applied either to the top or to both faces of the preparation). The characteristic intensities did not show any clear change with time but large changes occurred in the continuum X-ray intensity, which is a measure of total mass. At 60 nA, for the singly coated specimens, the average mass during the initial counting period was approx. 15-20% higher than during subsequent counts. Smaller losses were observed for singly coated specimens at 10 nA and for doubly coated specimens at 60 nA, while no losses were manifest in doubly coated specimens at 10 nA.

Höhling et al also measured the mass fractions of K, Cl and Na in their sections (using thin stable mineral standards and the Marshall-Hall method (6,7) ), and compared their probe measurements with flame photometric assays of unprobed samples. For the singly coated specimens exposed to 60 nA, the average ratios of flame-photometric to electron-probe values were 0.59(K), 0.54(Cl) and 0.59(Na), suggesting a loss of approx. 40% of total mass under the electron beam.

At present we attribute the difference between probe and flame-photometric assay to beam damage, and we believe that the above "measure" of loss of 15-20% is not inconsistent with the apparent loss of 40%. According to Stenn and Bahr (8), the main cause of loss of organic mass is probably not thermal but is the escape of volatile molecules produced by the direct rupture of chemical bonds. The data of Bahr et al (9) indicate that the losses occur at extremely low exposure. They found that for a variety of organic films, 10-80% of mass is lost almost immediately and the remainder is thereafter relatively stable, the main loss occurring within an exposure of the order of 0.1 nanocoulomb/ $\mu\text{m}^2$ . Hence we cannot expect to see the full mass loss by means of sequential measurements with counting intervals of several sec, with currents of 10 nA or more; most of the loss of mass may occur entirely within the first counting interval.

Thus beam damage seems to raise serious obstacles to the measurement of elemental mass fractions in biological tissues. There<sub>2</sub> is no hope of doing X-ray microanalysis with integrated beams of 0.1 nanocoulomb/ $\mu\text{m}^2$  even with silicon energy-selective

X-ray detectors placed extremely close to the specimen. Also, we cannot hope to prevent the rupture of chemical bonds. We must seek preparative techniques which may prevent migration or loss after bond rupture has occurred, and we need monitoring methods which can establish the adequacy of these techniques.

At present we are setting up to monitor mass loss by means of continuum intensities with a silicon detector located approx. 15 mm from the specimen. The counting intervals will be of the order of 100 ms. With sections of  $500 \text{ ug/cm}^2$  (i.e.,  $5 \cdot \text{um} \cdot \text{g} \cdot \text{cm}^{-3}$ ) we expect 0.1 nanocoulomb to produce approx. 1000 continuum counts, so that this arrangement should suffice to follow mass loss directly under typical conditions of microanalysis. However the sensitivity of this method is probably too low for similar studies of the much thinner specimens (approx. 100 nm thick) which are used when the best spatial resolution is essential.

Specimen preparation: An important but difficult problem is the localization of readily diffusible substances, especially electrolytes. The preparative procedures for such studies all begin with very rapid freezing of a fresh tissue. This may be followed by the freeze-drying of a block, vacuum-embedding and then sectioning (10); or by freeze-substitution, embedding and sectioning (11); or by frozen sectioning and drying of the section (12,13,14). A more recent technique is frozen sectioning followed by study of the frozen section in the microprobe, always maintaining temperatures low enough to retain all water in the form of ice (15,16). In a 2-um section the ice can be preserved even locally under a 30-kV, 30-nA beam, if care is taken to provide good uninterrupted thermal conductivity back to the cold reservoir at liquid nitrogen temperature. In dried frozen sections there must be some migration of electrolytes, although Appleton (17) has shown that considerable localization can be maintained even intracellularly. In iced specimens localization is presumably better preserved and beam damage is perhaps reduced by better trapping of the volatile products of ruptured bonds; however the visualization of detail is a problem in such specimens, especially if they are not stained.

Speed of analysis: To achieve high spatial resolution and avoid beam damage, the trend is towards analysis of ultrathin specimens with fine, low-current probes and closely placed silicon detectors. X-ray intensity is reduced by a factor of 60 in going from a 60 to a 1 nA beam, and by a further factor of 20 in going from 2 um to 100 nm sections. Consequently it is not uncommon to see running times of 1000 sec quoted for assays in ultrathin sections. One thousand sec per point is too long for quantitative biological research projects. Hence for many studies thicker sections are preferable, and it is still urgent to establish ways to stabilize specimens under high beam currents.

- 
1. J.L. Lineweaver, JAP 34, 1786 (1963)
  2. M.P. Borom & R.E. Hanneman, JAP 38, 2406 (1967)
  3. L.F. Vassamillet & V.E. Caldwell, Proc. 3rd Nat. Conf. on Electron Microprobe Analysis, Chicago 1968, Paper No. 40
  4. S. Hodson & J. Marshall, J. Microscopy 93, 49 (1971)
  5. H.J. Hühling, T.A. Hall, W. Kriz, A.P. von Rosenstiel, J. Schnermann & U. Zessack, in press
  6. T.A. Hall & H.J. Hühling, In "X-Ray Optics and Microanalysis" (Eds. G.

- Möllenstedt & K.H. Gaukler), p. 582. Springer-Verlag, Heidelberg, 1969.
7. T.A. Hall & P. Werba, Proc. 25th Anniversary Meeting of the Electron Microscopy and Analysis Group of the Institute of Physics, p. 146. The Institute of Physics, London and Bristol, 1971.
  8. K. Stern & G.F. Bahr, J. Ultrastruc. Res. 31, 526 (1970)
  9. G.F. Bahr, F.B. Johnson & E. Zeitler, Lab. Invest. 14, 1115 (1965).
  10. M. J. Ingram & A.M. Hogben, In "Developments in Applied Spectroscopy", volume 6, p. 43. Plenum Press, New York, 1968
  11. A. Löffli, A.R. Spurr & R.W. Wittkopp, Planta (Berlin) 95, 341 (1970)
  12. T.C. Appleton, Proc. Royal Micr. Soc. 5, 190 (1970).
  13. K. Christensen, In "Autoradiography of Diffusible Substances" (Eds. L.J. Roth & W.J. Stumpf), p. 349. Academic Press, New York, 1969
  14. S. Hodson & J. Marshall, J. Microscopy 91, 105 (1970)
  15. T. Hutchinson, in press
  16. P. Echlin, In "Scanning Electron Microscopy/1971" (Part I), p. 225. Proc. 4th Annual Scanning Electron Microscope Symposium, IIT Research Institute, Chicago 1971
  17. T.C. Appleton, Micron, in press



A COMPUTER PROGRAM FOR QUANTITATIVE MICROANALYSIS OF THIN BIOLOGICAL MATERIAL

By

Ronald R. Warner and James R. Coleman

Department of Biophysics

University of Rochester, School of Medicine and Dentistry

Rochester, New York 14642

Frequently, the objective of quantitative microanalysis of biological material is the correlation of chemical composition with morphological structure. The material to be analyzed must be no greater than a few microns thick to achieve the desired morphological resolution. In addition, elements of physiological interest are usually present in low concentrations, requiring high voltages for detection. Under these conditions, quantitation becomes a thin film analysis.

The few available biological quantitation techniques have requirements that restrict their applicability and complicate their use. This paper describes a computer program, Basic, that is easy to use, requires no instrument modifications, no special techniques, no assumptions on matrix composition, density, or thickness, is not limited to ultrathin sections, and uses conventional metallurgical standards and specimen supports. Basic is based upon a previous computer program, Bicep (1), but uses the substrate intensity as internal compensation for changes in sample density and thickness.

Basic, like Bicep, corrects for atomic number and thin film effects as outlined by Colby (2):

$$K_A = C_A \frac{R_{AB} \left[ \int_{E_L}^{E_0} \frac{Q}{S_{AB}} dE + \eta_s \int_{E_L'}^{E_L} \frac{Q}{S_{AB}} dE \right]}{R_A \int_{E_C}^{E_0} \frac{Q}{S_A} dE} \quad (1)$$

where  $E_L$  is the average electron energy at the sample-substrate interface,  $\eta_s$  the backscattered electron coefficient, and  $E_L'$  the energy of backscattered electrons as they leave the film.  $E_L$  is calculated using the power law of generated characteristic radiation. From Green (3), characteristic radiation is generated according to the equation:

$$I = \eta (E_0 - E_c)^{1.63} \quad (2)$$

where  $\eta$  is the efficiency of x-ray production. However, Green observes a decrease in the exponent at higher overvoltages. For our operating conditions and low atomic number substrates, we estimate the exponent to be 1.2 from Green's data (Figure 1). Equation 2 is therefore:

$$I = \eta(E_o - E_c)^{1.2}$$

The ratio of substrate intensity generated below a film ( $I_1$ ) to that generated on uncovered substrate ( $I_2$ ) can be expressed as

$$E_L = E_c + \left(\frac{I_1}{I_2}\right)^{1/1.2} (E_o - E_c)$$

Fluorescence effects are taken into account in the conventional manner by using normalized concentrations and the appropriate values for the overvoltage.

The absorption correction in the film is identical to that in Bicep (1); however, intensities from the substrate must also be corrected for absorption. Absorption of substrate signal by the film is corrected using

$$I = I_o e^{-(\mu/\zeta)\zeta x \csc \theta} = I_o \exp \quad (5)$$

where  $\zeta x$  is calculated from Andersen's range equation (4),

$$\zeta x = .064 (E_o^{1.68} - E_L^{1.68}) \quad (6)$$

Self-absorption by the substrate under the film presents difficulties due to unusual geometry. Accordingly, a series of standards were prepared by evaporating aluminum onto silicon wafer fragments. Aluminum was chosen for its low atomic number and high absorption of silicon x-rays. The thickness of the coatings were roughly determined by weight differences. Several formulations for the absorption correction were tried on these standards. None gave any error worse than 30%. However, an empirical correction given by  $(1/\exp)^{0.8}$  gave the best fit and is shown in column 3 of Table 1.

A danger in fitting an empirical correction to a set of standards is the possibility that the result will apply to no other system. Accordingly, two other samples have been analyzed. A carbon film deposited by electron beam evaporation was analyzed and gives a value that is high. However, absorption in the film is 57%, a condition known to cause inaccuracies in an analysis (5). Parylene, a chlorinated hydrocarbon polymer obtained from Union Carbide and reported to be 4.4 microns thick and 25.6% chlorine, was also analyzed and gave remarkably good values.

For comparison, all films were also analyzed with Bicep, which requires knowledge of density and thickness. Results in column 4 were obtained using the experimental thickness values; results in column 6 used thickness values determined from Basic. The latter gave excellent results.

Basic must be refined and subjected to further tests. In particular, the exponent in the characteristic production of radiation must be determined as a function of high overvoltage, and a less empirical form for the absorption correction should be utilized. However, routine quantitation of biological material at the 10% accuracy level is clearly indicated.

The Basic program will handle up to 11 elements; a compound standard may contain 8 elements. One element may be determined by ratio, one by difference and any of the 11 may have assumed concentrations. Required inputs are the

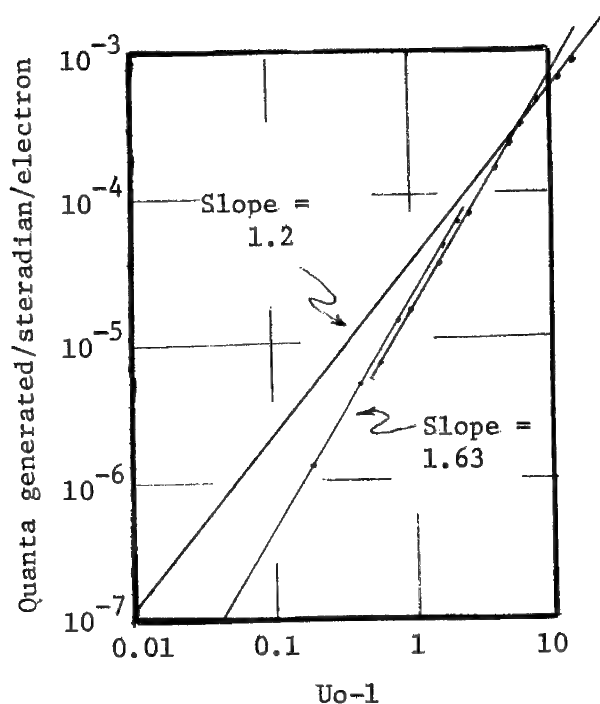


Figure 1. Characteristic production vs.  $(U_o-1)$ ; determination of exponent at high overvoltage.

accelerating potential, elements and lines analyzed, and the intensity ratios. The program is applicable to any film mounted on thick elemental substrates that gives a detectable substrate signal. The film must not contain the substrate element.

#### References

1. Warner, R. R., Proc. 6th Nat. Conf. EPASA, Pittsburgh, 1971.
2. Colby, J. W., Advances in X-ray Analysis 11, 287 (Plenum Press, New York, 1968).
3. Green, M., X-ray Optics and X-ray Microanalysis, Paltee, Cosslett and Engstrom, ed., Academic Press, New York (1963) 185-192.
4. Andersen, C. A. and Hasler, M. F., Congres International-L'Optique des Rayons X et la Microanalyse, Orsay, France, 1965.
5. Yakowitz, H., and Heinrich, K. F. J., Mikrochimica Acta 1 (1968) 182-200.

#### Acknowledgements

This paper is based on work performed partially on NIH Grant No. AM14272 and Biophysics Training Grant No. 5T1GM-1088 and partially under contract with the U. S. Atomic Energy Commission at the University of Rochester, Atomic Energy Project and has been assigned Report No. UR-3490-98.

TABLE 1

	<u>Depth</u> <u>(<sup>u</sup>)</u>	<u>K-Ratio</u> <u>(%)</u>	<u>Basic</u> <u>(wt. %)</u>	<u>Bicep</u> <u>(wt. %)</u>	<u>Basic</u> <u>Depth</u>	<u>Bicep</u> <u>Recalculated</u>
Aluminum						
	.025	.69	94.9	102.7	.03	94.4
	.171	4.92	96.6	104.3	.19	99.4
	.273	9.44	100.9	114.0	.34	102.9
	.538	17.28	105.5	110.3	.60	104.7
	.636	22.21	103.3	114.8	.79	103.6
	1.09	39.24	112.2	116.6	1.28	107.8
	1.14	42.00	109.9	117.7	1.38	107.4
	1.32	48.82	98.3	115.6	1.81	100.9
	1.35	50.88	109.1	118.9	1.67	107.1
	1.59	61.11	98.8	117.3	2.30	100.6
	1.67	64.31	105.0	119.5	2.25	105.4
	1.78	65.45	102.1	116.7	2.41	103.0
	2.12	78.54	103.2	120.1	3.05	104.2
	2.37	81.38	97.4	117.2	3.43	100.6
	2.88	90.27	97.5	106.7	3.85	101.0
Carbon						
	.132	6.94	117.6*	124.5*	.17	108.9*
Parylene <sup>†</sup> (Chlorine)	4.4	29.93	25.3	29.2	5.5	24.7

\* Absorption due to film is 57%, result inaccurate

† Parylene is 25.6% chlorine (Union Carbide)

# ENZYME LOCALIZATION IN MOUSE INTESTINE BY ELECTRON PROBE ANALYSIS

Richard B. Lyons, Robert Ruscica, Ann W. Cook & Robert Bundtzen

The enzyme, alkaline phosphatase was studied in the villi of the mouse duodenum to determine if electron probe analysis (EPA) could show localization of the enzyme comparable to that observed in the light microscope (LM).

The histochemical procedure used was a minor modification of the Gomori calcium-cobalt reaction which has several chemical steps, each of which may be followed analytically with the EPA. In the initial step, glycerophosphate (substrate) is hydrolyzed by the enzyme, thus releasing phosphate ions which are immediately precipitated by calcium ions (as calcium phosphate) at the enzyme location. In the next step a solution of cobalt sulfate is added to the tissue which causes a replacement of the calcium by cobalt. The final step is to create a precipitate of cobalt sulfide, which is then visible in the LM, by adding ammonium sulfide to the tissue sample. A control slide is prepared by thermal denaturation of the enzyme prior to the above reactions.

After the various incubation steps, tissue sections were air dried, photographed in the LM and surfaced with a thin (300-500Å) aluminum coating (since we desired to perform carbon analysis). The sections were then examined in the Materials Analysis Company Mac 5 combination EPA-SEM equipped with three energy dispersive spectrometers. Line scans, distribution patterns, back scattered (BSE) and secondary electron (SEM) images were obtained with accelerating voltages of 15-20 KV and beam currents of 0.005-0.01 µA.

After the complete series of reaction steps (Ca, Co and S), a single villus was utilized for LM (Figure 1,e) distribution of Co (Figure 1,c) and line scans for Ca, P, S and Co (arrows on the line scan position of the SEM in Figure 1,i indicate the position of the dotted line on the line scans shown in Figure 3,a). Figure 1,e shows the LM appearance of an adjacent section used as a control. Nearby villi presented better line scans and were utilized for SEM (Figure 1,d), BSE (Figure 1,h) distribution of S (Figure 1,a) and Co (Figure 1,b) and for line scans of Ca, P, S and Co (arrows of Figure 1,h correspond to dotted lines of Figure 3,b). Line scans and distributions of both villi show localization of S, Co and P at the absorptive border of microvilli (MVB) accompanied by a very low amount of Ca in the same region. When sections are removed after the first step of the reaction (Ca Cl<sub>2</sub> step), a Ca HPO<sub>4</sub> precipitate would be expected at the MVB without accompanying Co and S peaks. This can be seen in line scans for Ca, P and S (Co was not examined) in Figure 2 (the lower line in Figure 1,h was used for the scan). Note the very low S peak at the MVB compared to Figures 3,a and 3,b.

EPA allows elimination of some reaction steps since a visible precipitate is not required. Instead of carrying the reaction to the CoS precipitate, the EPA can detect the element, Ca, which is not visible with the LM, providing assurance that an element is or is not present. EPA clearly demonstrated the final reaction product (CoS) in the same location as observed in the LM as well as showing the

predicted localization of the elements at each step of the reaction sequences. The same tissue specimen, which is easily prepared and rapidly examined in the LM by conventional histochemical reactions, can also be used for EPA. Eventually, it may even be possible to obtain quantitative data.

Note: Mention of trade names or commercial products does not constitute an endorsement or recommendation for use by the U. S. Department of Health, Education and Welfare.

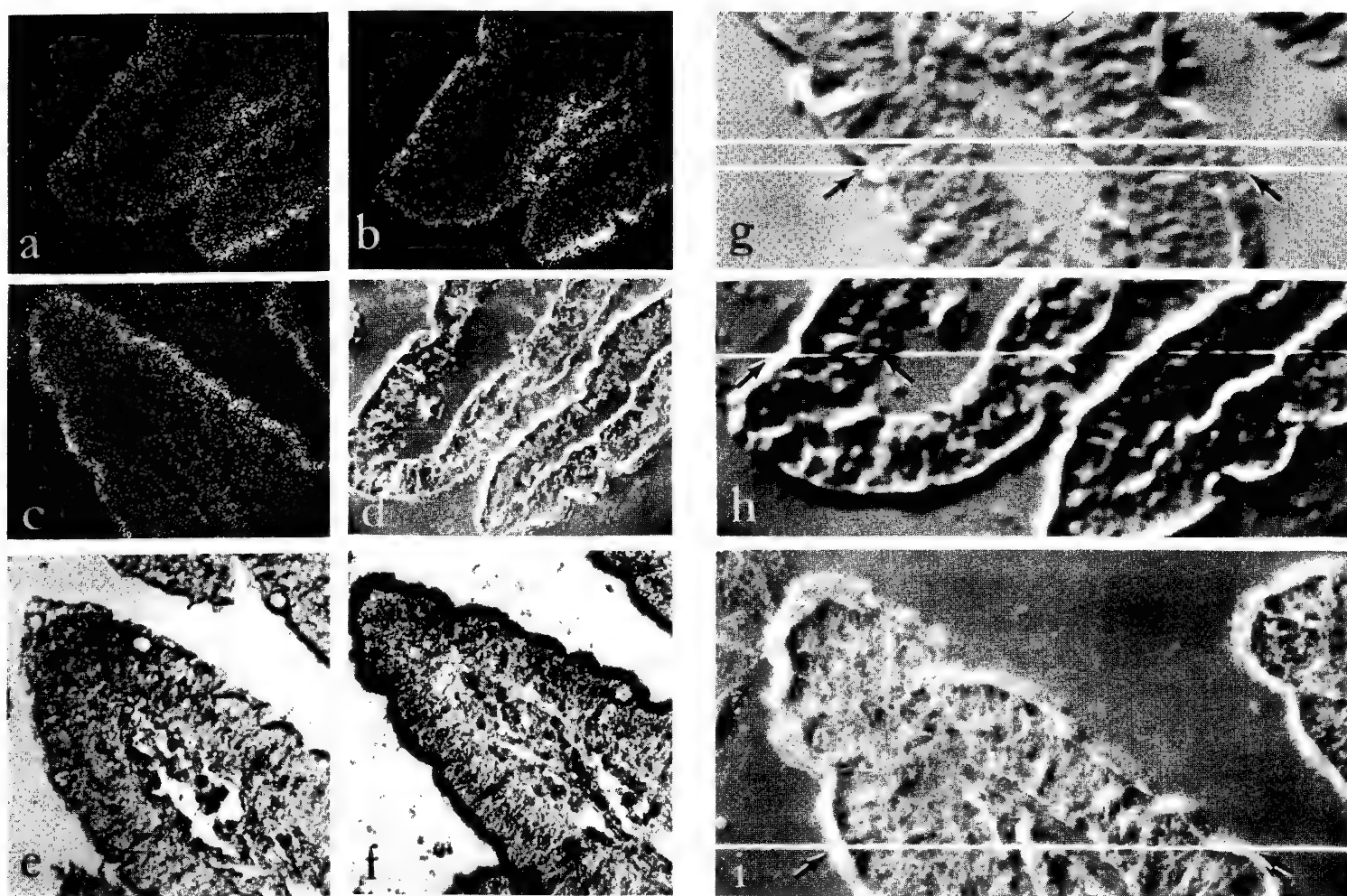


FIGURE #1

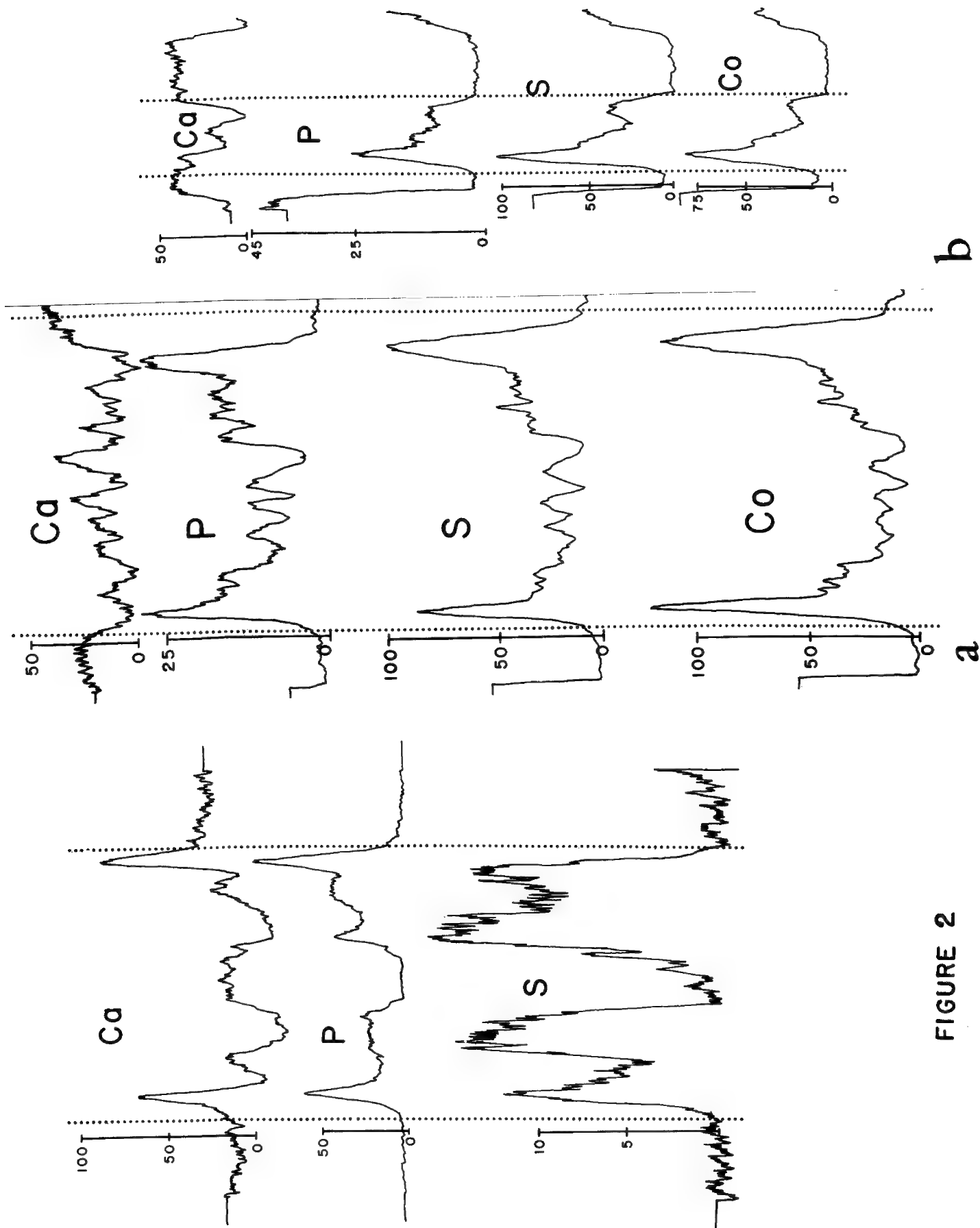


FIGURE 2

FIGURE 3

# THICKNESS AND MASS THICKNESS MEASUREMENTS WITHIN BIOLOGICAL SPECIMENS

by

John W. Edie and Ulf L. Karlsson  
Dental Research Laboratory (Oakdale)  
and Department of Anatomy  
University of Iowa, Iowa City, Iowa 52240

Section thickness is an important parameter in many biological investigations which employ electron optical instrumentation. In electron microscopy, an accurate estimate of section thickness is necessary (a) to estimate superposition effects, (b) for three dimensional reconstructions, (c) to estimate molecular masses, and (d) to observe radioactive concentrations in autoradiography. Similarly, some methods of quantitative electron probe analysis of thin sections requires knowledge of thickness, and mass thickness, such that absorption and fluorescent corrections are feasible.<sup>2</sup>

A means of estimating section thickness and mass thickness variations is available using electron beam attenuation through the specimen as a result of electron scattering. For thin specimens of mass thickness,  $\rho x$ , the transmitted intensity,  $I_t$ , of the electron beam of initial unimpeded intensity,  $I_0$ , follows the law

$$I_t = I_0 e^{-S_T \rho x}, \quad (1)$$

where  $S_T$  is the total mass scattering cross section.<sup>3</sup>  $S_T$  is thought to be primarily a function of electron energy with little, if any, atomic number variation.<sup>4</sup>

Using a transmission electron microscope, measurement of  $I_t$  requires the use of an objective aperture to prevent electrons scattered beyond prescribed angles from reaching a Faraday cage detector in the image plane. Obviously,  $S_T$  shows a critical dependence on this aperture's diameter and placement. The currents from the Faraday cage are proportional to incident electron beam intensities such that the ratio of electron beam intensities is measured as the ratio of detector currents. Therefore, for constant electron optical geometry,  $I_t/I_0 = i_t/i_0$ .

Many biological techniques require the use of embedding resins (e.g., Vestopal W or Epon 812) for physical support as sections are cut in ultramicrotomy. The local section thickness may be estimated by measuring the beam attenuation at points on the uniform plastic portion adjoining the specimen. Within the specimen, variations in transmitted beam intensity reflect local mass density variations if section thickness remains constant.



Absorption (or scattering) calibration data for plastics was acquired using standardized Formvar films whose thicknesses were measured using the method of multiple beam interferometry.<sup>5</sup> The films were subject to sublimation and contamination effects upon exposure to electron beams which were directly attributable to the current densities impinging on the film.<sup>6</sup> The effects can be controlled by slight movements of the plastic across the electron beam when the specimen current density is less than about  $10^{-4}$  Amp/cm<sup>2</sup>.

Figure 1 shows the beam attenuation on a logarithmic plot for differing electron energies and a 50 microns aperture. Multiple electron scattering cause these curves to leave the exponential relationship at mass thicknesses ranging from 20 to 40  $\mu\text{g}/\text{cm}^2$  for 40 and 80 KV, respectively--where the transmitted intensity is about 15% of the initial intensity.

Critical thickness,  $x_c$ , is defined as that thickness necessary to reduce the transmitted beam intensity to  $e^{-1}$  of its initial value. To at least the measurement accuracy of  $\pm 2\%$ ,  $x_c$  is proportional to accelerating voltage for constant aperture conditions. It is a simple matter to predict Formvar attenuation curves for a variety of operating conditions such that unknown film thicknesses may be determined from transmission measurements and equation (1). Within the exponential region, film thicknesses to 0.4 microns may be estimated with greater than 5% accuracy while thicker films, to 1-2 microns, may be estimated using empirical absorption curves.

The constancy of  $S_T$  for unchanged electron optical geometry was investigated by embedding small pieces of materials of known density (various plastics, pure metals and alloys) in Vestopal W. Thin sections of 300-1200 Å thickness were obtained using a diamond knife. A comparison was then made of the electron beam attenuation through the plastic and material portions of the section. A schematic of the experimental arrangement is shown in Figure 2. The transmitted intensities for mediums 1 and 2 are

$$I_1 = I_0 e^{-S_{T1}\rho_1 x_0}$$

and

$$I_2 = I_0 e^{-S_{T2}\rho_2 x_0}, \quad (2)$$

respectively. Eliminating the common section thickness,  $x_0$ , and introducing detector currents as measures of beam intensities yields the ratio

$$R = \frac{\ln(i_1/i_0)}{\ln(i_2/i_0)} = \left( \frac{S_{T1}}{S_{T2}} \right) \cdot \left( \frac{\rho_1}{\rho_2} \right) . \quad (3)$$

Figure 3 shows the results of the attenuation measurements for 80 KV electrons and a 50 microns aperture on a log-log scale. The ratio of current logarithms,  $R$ , is plotted versus the corresponding ratio of densities,  $\rho_1/\rho_2$ . To within measurement error, the slope of the trend line is unity. For constant  $S_T$ , a material's attenuation properties are deduced from knowledge of the material's density and the Formvar "standard" attenuation relations for the electron optical geometry and accelerating voltage employed.

Using this approach, thickness variations of uniform materials may be mapped or, knowing thickness, the local mass density (contrast) variations within the section may be quantified. Also, the high resolution of transmission electron microscopes suggest dry masses to be measurable from  $10^{-12}$  to  $10^{-18}$  grams.

#### REFERENCES

1. Zeitler, E. and Bahr, G., J. Appl. Phys. 33, 847 (1962).
2. Colby, J. in "Advances in X-ray Analysis", Vol. 11, 287 (1968).
3. Marton, L. and Schiff, L., J. Appl. Phys. 12, 759 (1941).
4. Hall, C., "Introduction to Electron Microscopy", McGraw-Hill, Chapter 8 (1966).
5. Tolansky, S., "Multiple Beam Interferometry of Surfaces and Films", Oxford Press (1948).
6. Edie, J. and Karlsson, U., J. Microscopie 13, 39 (1972).

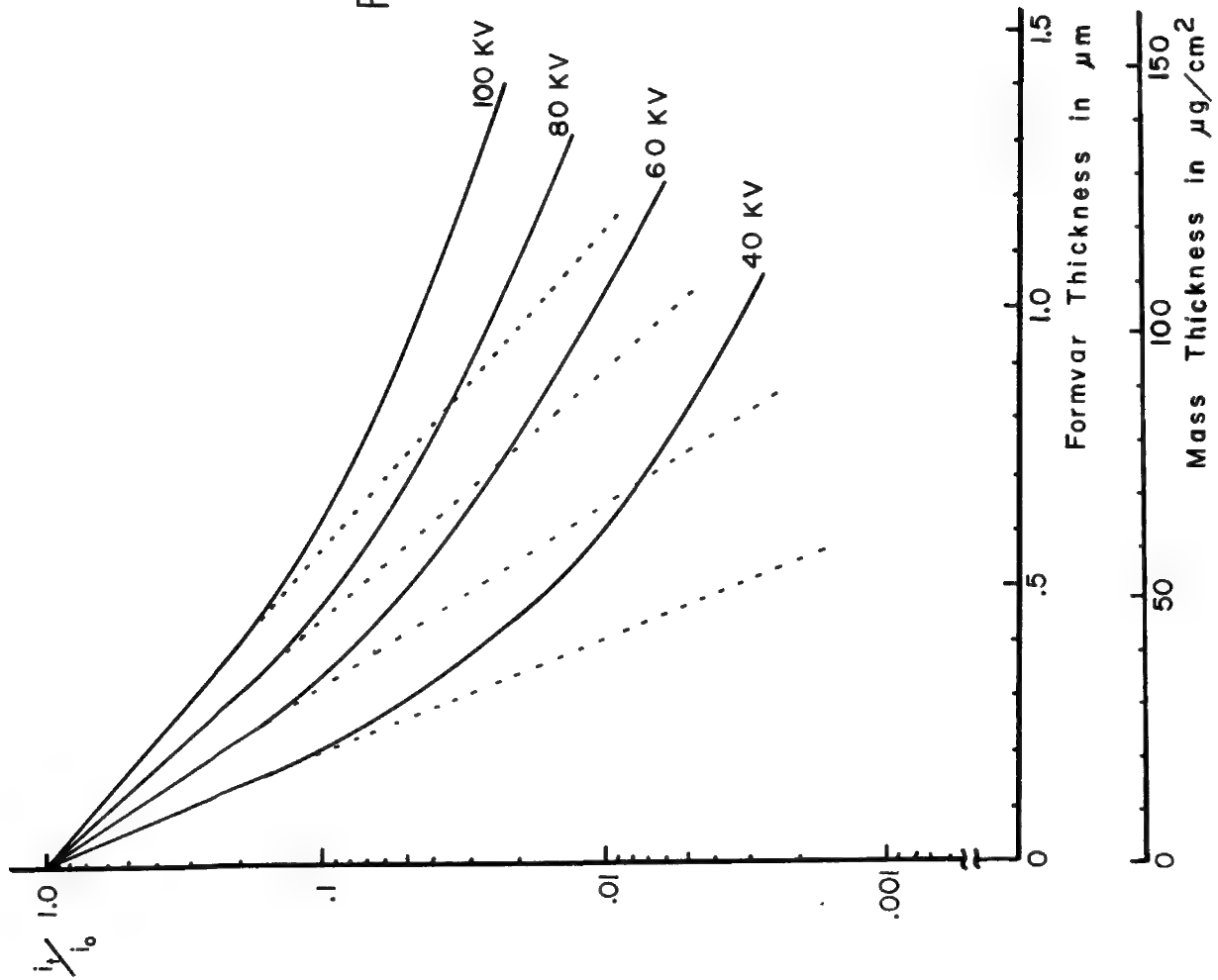


Figure 1

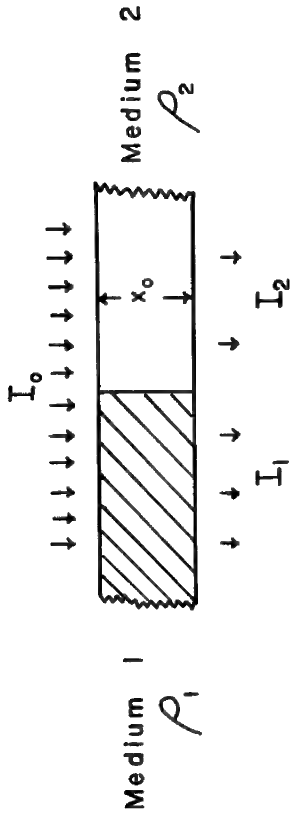


Figure 2

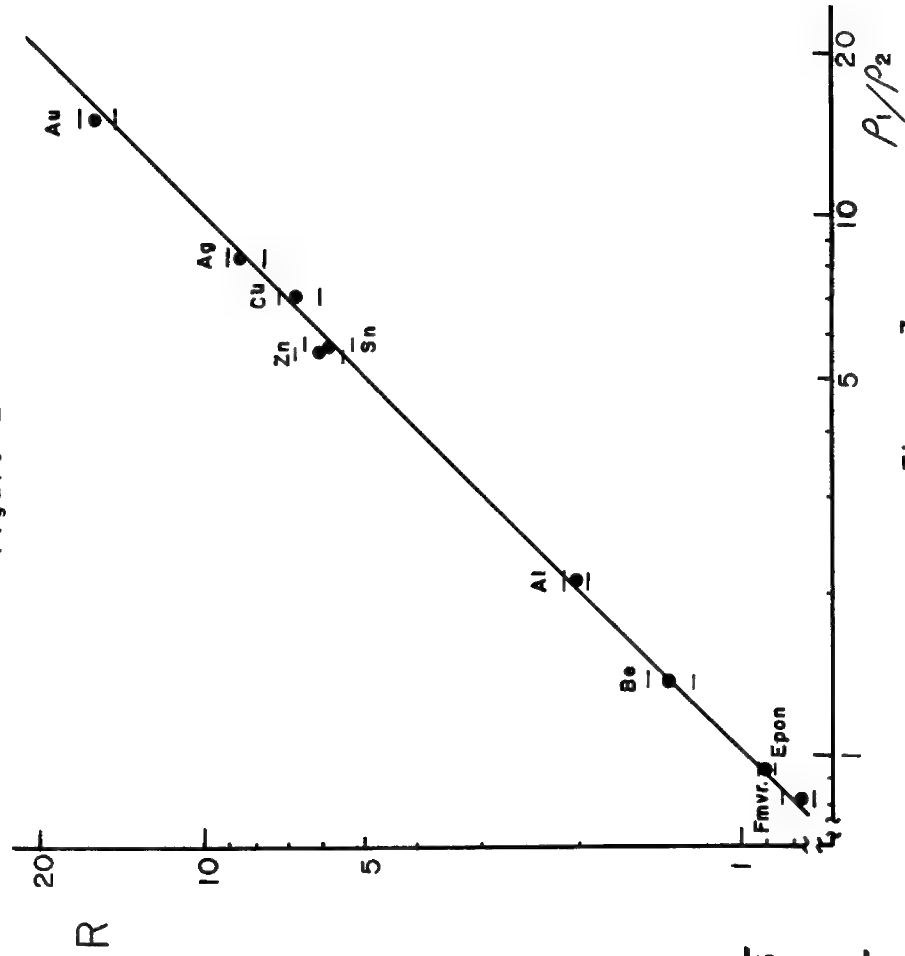


Figure 3

## CALCIUM TRANSPORT IN THE SMALL INTESTINE

by

Ronald R. Warner and James R. Coleman

Department of Biophysics

University of Rochester, School of Medicine and Dentistry

Rochester, New York 14642

The process of calcium absorption by the intestines has received considerable attention. Calcium must move across a layer of absorptive cells before entering the circulatory system. However, levels of intracellular calcium ion on the order of  $10^{-4}\text{M}$  can inhibit certain enzymes (1, 2) and uncouple oxidative phosphorylation (3); consequently, the concentration of calcium free in the cytoplasm is rigorously maintained at a level near  $10^{-6}\text{M}$  (4). The question then becomes, how do the absorptive cells transport large amounts of calcium without raising their own cytoplasmic calcium concentration?

Previous investigations of calcium transport using homogenization techniques indicate vitamin D increases the amount of a "calcium-binding protein" and enhances calcium translocation (5). From in vitro radioactive tracer studies, it is generally accepted that transport occurs both as an active, energy-requiring process and as a diffusional process (6, 7). However, results obtained from the tracer studies are frequently contradictory, being dependent upon the experimental conditions employed. With either technique the results are averages from a population containing many cell types, revealing little of the actual mechanism of transport in individual cells.

The present work utilizes an electron microprobe to analyze directly calcium in transport in individual absorptive cells. Intestines from rats and chickens were prepared following the procedure of Coleman, et al. (8) and Coleman and Terepka (9). Sections two microns thick were cut dry and mounted uncoated on solid substrates. Probe operating conditions were 22 KV and  $10^{-7}$  beam current.

The lumen of the intestines is surrounded by epithelium composed of two cell types, goblet cells and absorptive cells. These lie on supportive tissue composed of many cell types. Observations on the normal distribution of calcium in this tissue reveal the consistent presence of calcium in goblet cells throughout the small intestines irrespective of species, age and nutritional state. Calcium is confined to discrete localizations within the mucus-rich portions of this cell (Figure 1). This observation is consistent with fluorescent-antibody studies localizing calcium-binding protein in the goblet cells and brush border (10). We have detected calcium diffusely present in the brush border only occasionally in vitamin D replete animals.

In fasted animals, absorptive cells contain no detectable calcium. In animals fed ad libitum, absorptive cells vary from a state lacking detectable calcium to a state in which scattered localizations occur at the brush border, within cells,

and between or near lateral cell boundaries. Larger amounts of calcium are seen in localizations below absorptive cells.

In order to determine the sequential nature of calcium movements in absorptive cells, segments of intestines were incubated in a 2mM calcium solution for various times before fixation. Results show that calcium is initially localized in and below the brush border. At later times, calcium is observed localized in a supranuclear position and in or adjacent to intercellular spaces (Figure 2). Localizations below the nucleus are only seen near the cell periphery. Finally, calcium is observed, still localized, in the supportive tissue.

Effects of vitamin D are being investigated. Preliminary results indicate no calcium localizations occur in absorptive cells in animals deprived of this vitamin.

Our results indicate that calcium enters the cell in discrete localizations, is transported to a supranuclear position, and then to the lateral intercellular space. This pattern is similar to that believed to occur in the absorption of fat (11).

The localized nature of calcium in transport suggests that this material is being segregated from the cell interior where the calcium ion concentration must be kept around  $10^{-6}$ M. Since the calcium x-ray signal is not associated with phosphorus (or other inorganic elements), the active participation of mitochondria in the transport process, as has previously been suggested (12), is unlikely. It may be of significance that calcium localizations are observed in a supranuclear position, the site occupied by the Golgi apparatus.

#### References

1. Kachmar, J. F., and Boyer, P. D., J. Biol. Chem. 200 (1953) 669-682.
2. Kimmich, G. A. and Rasmussen, H., J. Biol. Chem. 244 (1969) 190-199.
3. Chance, B., Energy-Linked Functions of Mitochondria, Academic Press, New York, 1963.
4. Borle, A. B., Clin. Orthoped. and Rel. Res. 52 (1967) 267-291.
5. Wasserman, R. H. and Taylor, A. N., Science 152 (1966) 791.
6. Schachter, D., Dowdle, E. B. and Schenker, H., Am. J. Physiol. 198 (1960) 263-268.
7. Wasserman, R. H., Calc. Tiss. Res. 2 (1968) 301-313.
8. Coleman, J. R., DeWitt, S.M., Batt, P., and Terepka, A. R., Exptl. Cell Res. 63 (1970) 216-220.
9. Coleman, J. R. and Terepka, A. R., J. Histochem. Cytochem. (in press).
10. Taylor, A. N. and Wasserman, R. H., J. Histochem. Cytochem. 18 (1970) 107-115.
11. Friedman, H. I. and Cardell, R. R., J. Cell Biol. 52 (1972) 15-40.
12. Sampson, H. W., Mathews, J. L., Martin, J. H., and Kunin, A. S., Calc. Tiss. Res. 5 (1970) 305-316.

Acknowledgements

This paper is based on work performed partially on NIH Grant No. AM14272 and Biophysics Training Grant No. 5T1GM-1088 and partially under contract with the U. S. Atomic Energy Commission at the University of Rochester, Atomic Energy Project, and has been assigned Report No. UR-3490-97.

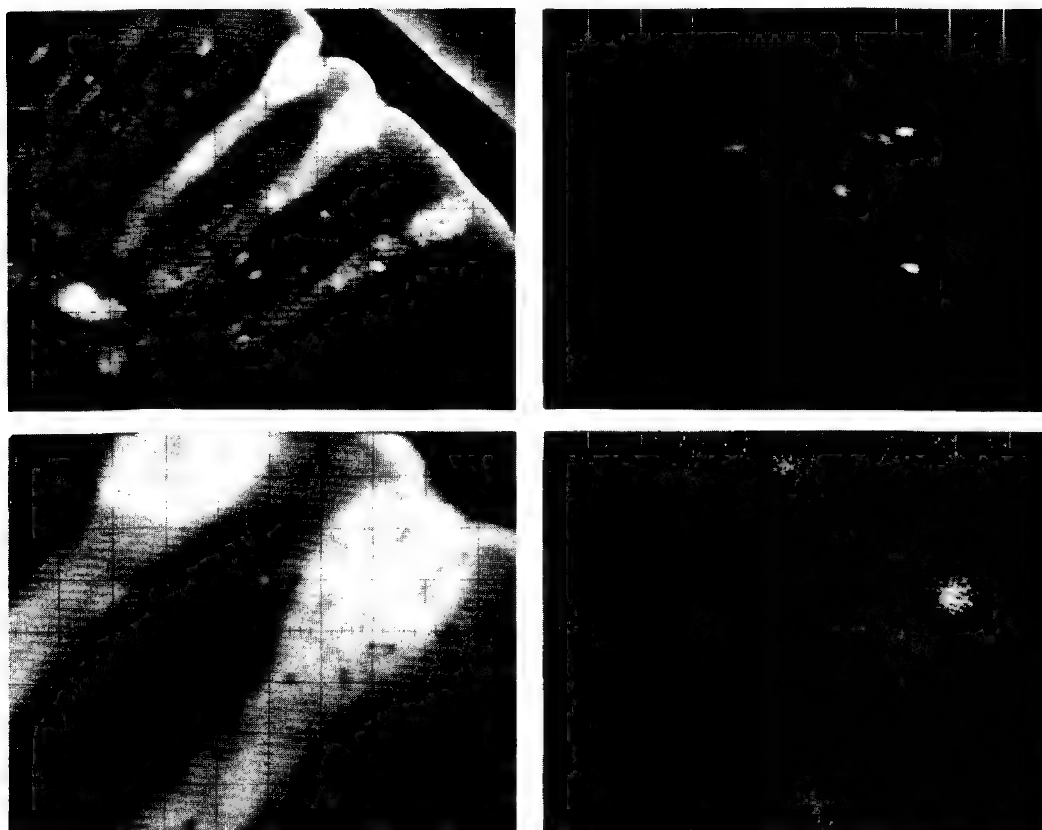


Figure 1. Sample current and CaK $\alpha$  images showing calcium distribution in goblet cells. Top 8 $\mu$ /grid square, bottom 2.5 $\mu$ .



Figure 2. Calcium distribution in absorptive cells after incubation. 7 $\mu$ /grid square.

SECONDARY ION AND ELECTRON PROBE  
MICROANALYSIS OF THE MINERALIZATION  
PROCESS IN BIOLOGICAL TISSUES\*

by

Dr. A. J. Tousimis  
 biodynamics Laboratory  
 6000 Executive Blvd.  
 Biodynamics Research Corporation  
 Rockville, MD. 20852

In animals, normal bone formation, growth and maintenance is directly dependent and related to the mineralization process. This takes place at the interface between an avascular tissue and a blood capillary network. Understanding this process is of great significance for normal bone growth and its maintenance during the entire life of the animal. Perhaps of more practical significance could be to learn more about pathologic mineralization. Among these are hardening of blood vessel walls--which accounts for most of heart attack deaths--mineral deposits in joints, some of the kidney stones, eye scleral hardening, and malignant tumor (cancer) calcification (retinoblastomas).



Fig. 1. Dark field photomicrograph of the mineralization interface, 50X.



Fig. 2. Electron probe result showing Calcium distribution, 750X.



Fig. 3. Same area as Fig. 2 showing Phosphorus, 750X.

For these studies, the epiphyseal plate of the proximal portion of the young (35 gm) hamster tibia was rapidly excised and frozen immediately in LN<sub>2</sub> cooled isopentane or fixed in paraformaldehyde, dehydrated and embedded in methyl-butyl methacrylate or epon araldite before sectioning. Sections 0.1 $\mu$  to 2.0 $\mu$  in thickness were mounted on quartz, aluminum, nickel, stainless steel or formvar thin films. The

---

\*Studies supported by a grant from the M. Tsonis Research Foundation to the Biodynamics Laboratory.

frozen dried and methacrylate removed sections were coated with gold or carbon in the SAMSPIN (1) respectively for secondary ion microanalysis (2) or scanning electron probe analysis and SEM (2).

Electron Probe Analysis (EPA): Figure 1 shows a photomicrograph of a 1u thick epiphyseal plate from the hamster depicting the interface where the capillary network from the diaphysis meets with the avascular cartilage displaying the columnar arrangement of chondrocytes. The calcium and phosphorus distribution at this interphase is shown

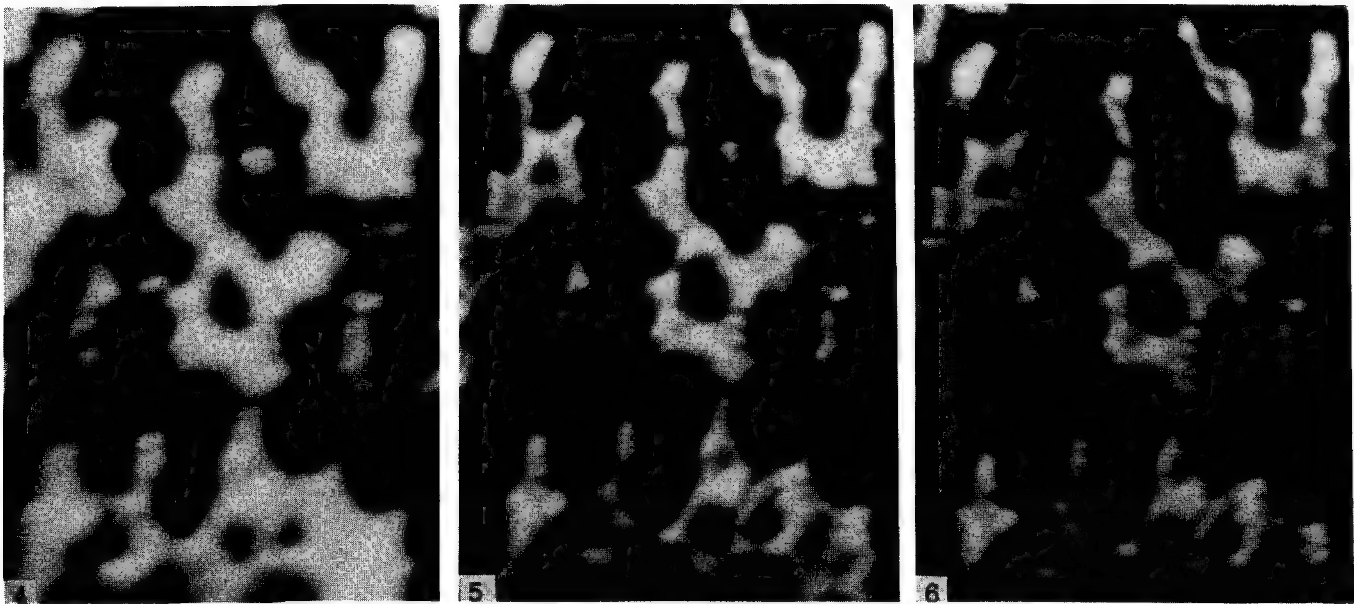


Fig. 4.  $^{40}\text{Ca}^+$  image  
 $t_0$ , 600 X.

Fig. 5.  $^{40}\text{Ca}^+$  image  
 $t_{10}$ , 600 X.

Fig. 6.  $^{40}\text{Ca}^+$  image  
 $t_{20}$ , 600 X.

in Figures 2 and 3. Point by point measurement and concentration calculation (3) for these two elements (wherever present together) are the same as that found for hydroapatite. Utilizing frozen dried sections (0.1u to 2.0u thickness) and measuring for the presence and distribution of Ca, P, S, K, Na, Cl, and Mg by electron probe analysis and electron microscopy (4) has enabled us to establish their relationship to ultrastructural features such as mitochondria, endoplasmic reticulum and cellular environmental matrix where the appearance of typical bone hydroxyapatite crystallites is clearly established (5).

Secondary Ion Microanalysis (SIMA): Similar preparations were also examined by Slodzian's secondary ion microanalysis procedure (6). The qualitative electron probe results have been confirmed utilizing either Argon or Oxygen positive primary ion sources. SIMA micrographs (Figures 4, 5, and 6) using the  $^{40}\text{Ca}^+$  ion show its distribution at the mineralization zone at 10 second time intervals of a carbon coated 1u thick methacrylate embedded epiphyseal plate section. Directly comparing Figures 2 and 6, the superiority in resolution of SIMA and EPA can be observed. The presence of electrolytes (Na, Mg, K, and Ca) in the maturation and proliferation zones by secondary ion analysis in the methacrylate embedded tissue, while not possible by electron probe analysis, suggests that these "ions" are



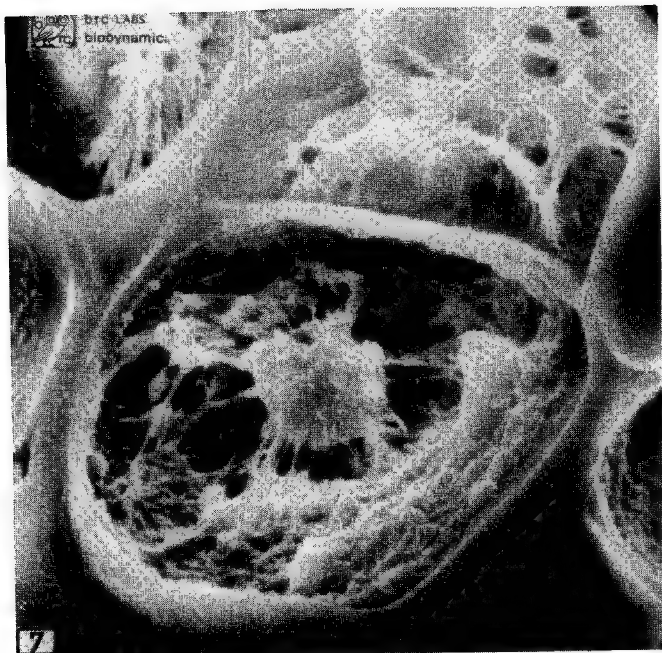


Fig. 7. Scanning Electron Micrograph of 1 $\mu$  thick epiphyseal chondrocytes and matrix before ion analysis. 2500 X.



Fig. 8. Scanning Electron Micrograph of 1 $\mu$  thick epiphyseal chondrocytes and matrix after ion analysis. 2500 X.

bound on the cellular and matrix organic components so that the various aqueous and organic solvents used during the tissue preparation do not remove them completely.

Scanning Electron Microscopy (SEM) was carried out on sections before and after their exposure to secondary ion microanalysis. Figures 7 and 8 show reflex secondary electron scanning micrographs of similar cells and their matrix of a 1 $\mu$  thick section of the epiphyseal plate before and after exposure to secondary ion analysis with Argon primary ions while the section is supported on a stainless steel substrate. The nonuniformity of etching of the specimen (Figure 8) is readily observable, a fact which could account for the distorted appearance of some structures in the ion micrographs and the difficulties in rendering the results quantitative.

1. Tousimis, A.J. and J.A. Nicolino, Proc. 6th Nat. Conf. EPA, pp. 61A-c, Pittsburgh, (1971).
2. Secondary ion microanalysis was carried out (1965) in collaboration with Georges Slodzian in R. Castaing's Laboratory for Solid State Physics, University of Paris, France; electron probe analysis with a V. G. Macres designed MAC electron probe and Scanning electron microscopy with a Nelson Yew designed Etec scanning electron microscope at the BRC-Laboratories, Rockville, MD.
3. Tousimis, A.J., Proc. 6th nat. Conf. EPA, pp. 36A-F, Pittsburgh, (1971).
4. Hagerty, J.C. and A.J. Tousimis, Biophys.J.8:193 (1968); Proc. 26th Ann. EMSA (1968), and; Proc. 27th Ann. EMSA (1969).
5. Tousimis, A.J., Symp. X-Ray and Electron Probe Analysis; Special Publ. No. 349, pp. 193-206, ASTM, Philadelphia (1963).
6. Castaing, R. and G. Slodzian, Proc. Reg. Conf. on Electron Microscopy. Delft, 1:169 (1960).

## TRACE METAL ANALYSES OF HUMAN SERUM WITH AN ELECTRON PROBE MICRO ANALYZER

P. S. Ong, P. K. Lund, and W. M. Conrad  
Department of Anatomic Pathology  
The University of Texas M. D. Anderson Hospital and  
Tumor Institute at Houston, Houston, Texas 77025

---

Trace elements play an important role in many biological processes. The serum Cu and Fe levels, for example, have been shown to reflect the clinical status of patients with Hodgkin's disease and untreated acute leukemia<sup>1,2</sup>. Therefore, these elements may prove useful for routine prognostic purposes.

The present work was aimed at obtaining a quantitative trace element profile at the routine clinical level. Two approaches are being followed, i.e., direct electron excitation and x-ray fluorescence excitation. This paper concerns methods developed for employing direct electron excitation.

Fig. 1 shows the order of magnitude of the various elements contained or present in 1 ml of human blood<sup>3</sup>. Cu and Zn are present at the  $\mu$  g levels, as is Fe in serum. These are within the sensitivities of x-ray fluorescence techniques. However, metals such as Ni, Co, and Au occur at levels below  $10^{-8}$  gram and require the more sensitive detection system provided by the microprobe. Utilizing this system requires the removal of the bulk of the matrix material which is composed primarily of organic substances and the elements Na, K, Ca, and Cl. This is done by first ashing the sample, followed by electrodepositing the trace metals on a Pt/Hg electrode. One ml serum yields an Fe/Cu/Zn/deposit of  $5 \mu$  thickness on a  $300 \mu$  diameter Pt wire. This is sufficiently thick to stop the electron beam and prevent intolerably high background. A miniature electrodeposition cell has been designed to handle 1 ml specimens. The metals are deposited on the cathode consisting of a small Pt wire coated with Hg. The anode is made of Pt wire. The solution is forced to pass between the electrode at a flow rate which allows efficient deposition of the significant material. After the process has been completed, the Hg is distilled off in vacuum.

Fig. 2 shows the spectrum obtained with a test solution containing 1 ppm of each of the elements Ni, Cu, and Zn. The various parameters are currently being studied, to establish a quantitative deposition rate for all of the elements of interest. The high signal for the elements in the ppm region allows the use of an energy dispersive system shown in Fig. 3, which is based on analysis of 1 ml serum. (This work was supported by NIH Grant GM 16229-04).

1. Hrgovcic, et al., "Serum Copper Levels in Lymphoma and Leukemia," *Cancer*, 22, 743-755 (1968).
2. N. Jaffe and M. M. Bishop, "Serum Iron Level, Hematocrit, Sedimentation Rate, and Leukocyte Alkaline Phosphatase Level in Pediatric Patients with Hodgkin's Disease," *Cancer*, 26, 332-337 (1970).
3. H.J.M. Bowen, "The Elementary Composition of Mammalian Blood," United Kingdom Atomic Energy Authority Research Group Report (1963).

## HUMAN BLOOD

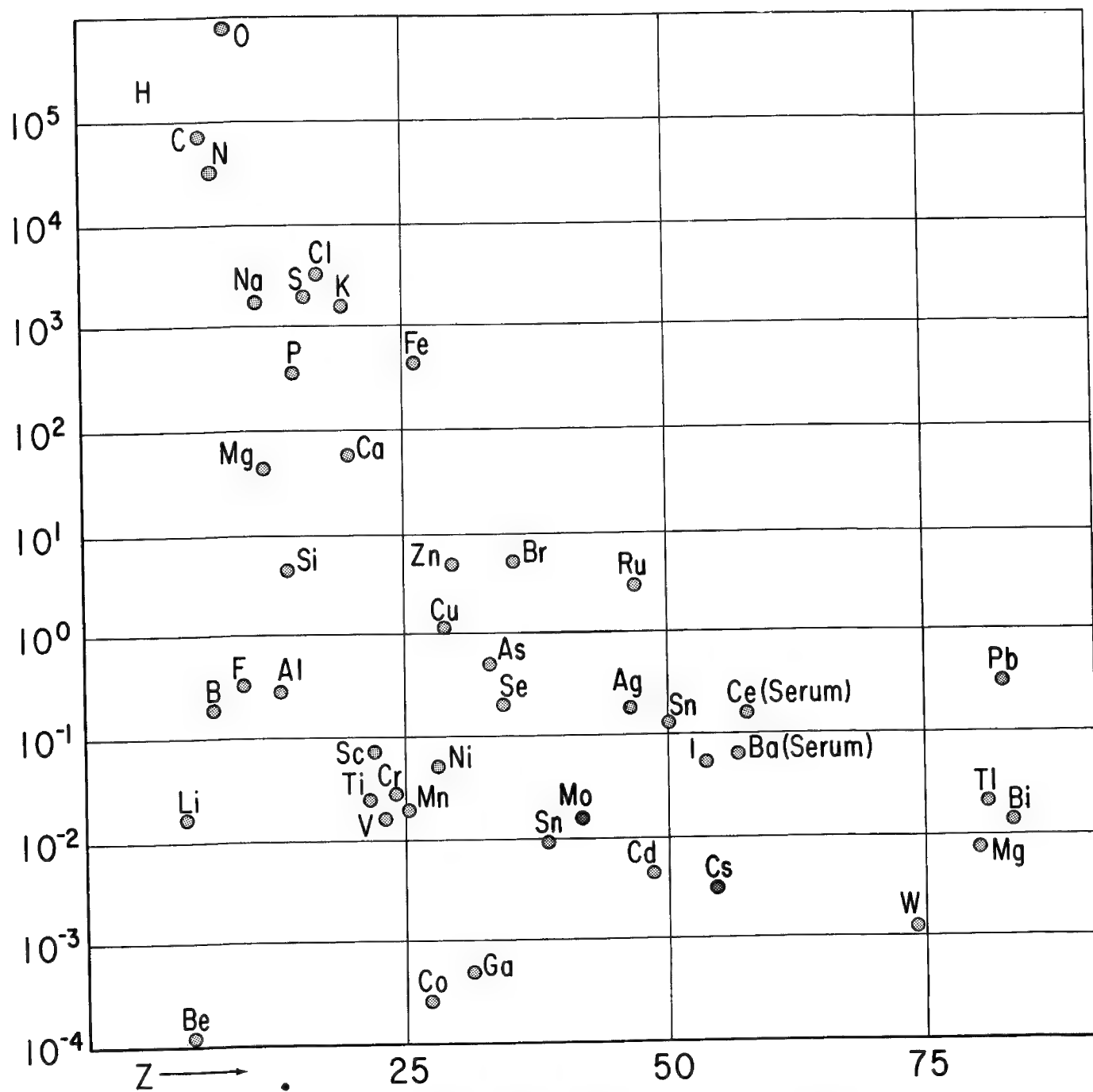


Fig. 1. Composition of human blood, from ref 3. The amounts are plotted in  $\mu\text{g}$  per ml sample, against atomic number  $Z$ . The value for Fe in serum is about  $1 \mu\text{g}$  per ml.

Standard Solution  
 3 hr, 3 1/2 Volt, 1m. A  
 500  $\mu$  Pt/Hg Cathode

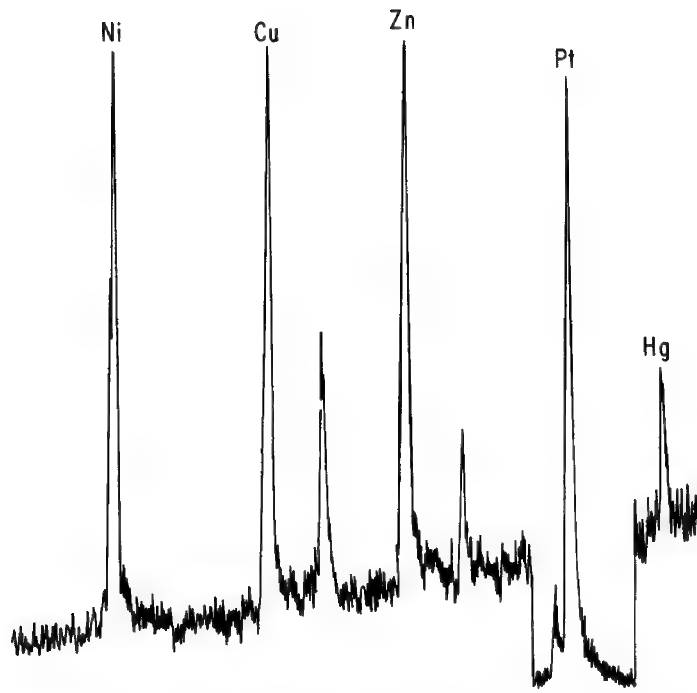


Fig. 2. Micro probe x ray spectrum of a Pt wire, after electro deposition out of a solution of Na. Cl containing 1 ppm of the elements Ni, Cu, and Zn.

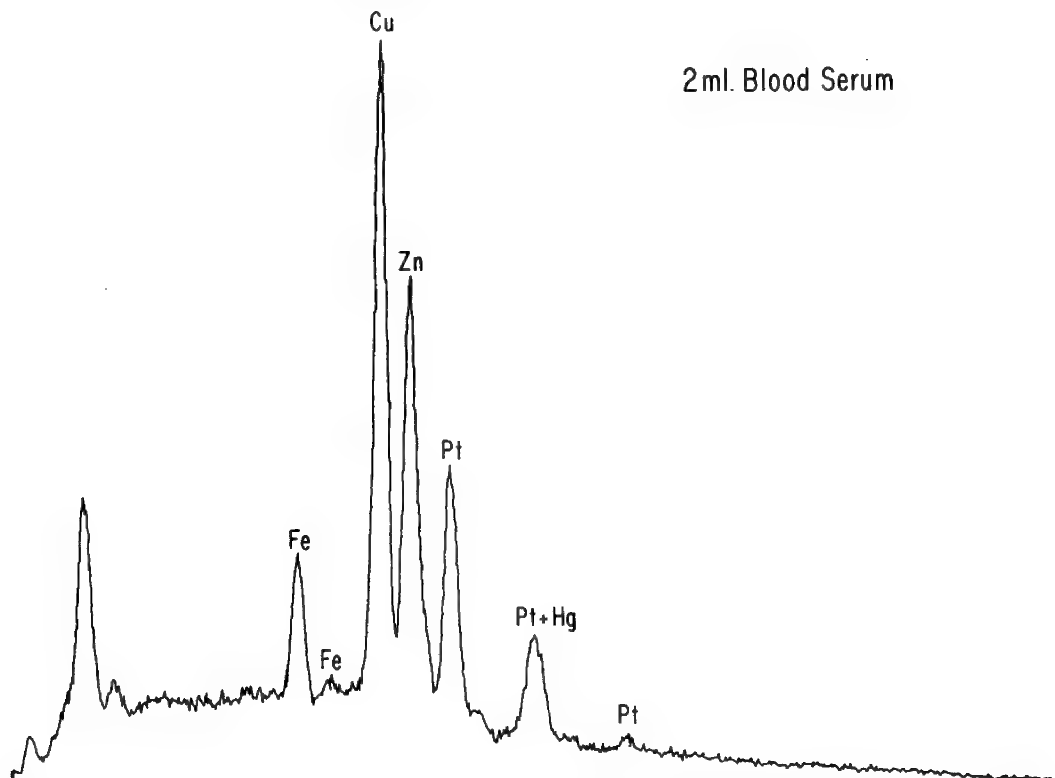


Fig. 3. Micro probe x ray spectrum of a Pt wire after electro deposition of 1 ml ashed human serum. The spectrum is obtained with an energy dispersive system.

ELECTROLYTES IN CELLS OF BIOLOGIC TISSUES\*

by

Dr. A. J. Tousimis  
 biodynamics Laboratory  
 6000 Executive Blvd.  
 Biodynamics Research Corporation  
 Rockville, MD. 20852

INTRODUCTION: The presence of electrolytes ( $\text{Ca}^{++}$ ,  $\text{PO}_4^{\equiv}$ ,  $\text{Cl}^-$ ,  $\text{CO}_3^{\equiv}$ ,  $\text{K}^+$ ,  $\text{Na}^+$ ,  $\text{Mg}^{++}$  and other) in biologic tissues (both plant and animal) has attracted the attention of many investigators. The intracellular and body fluid electrolyte concentrations reflect the biodynamic state of the cell and organism. In many cases these fluid measurements are of great clinical significance. The majority of their intracellular concentration and distribution measurements have been based on indirect procedures--electrochemical, microelectrode or cellular component isolation. Scanning electron probe analysis (1) offers a new approach to the study of electrolyte distribution in biologic cells (2) and calculation of their concentrations at the micron and submicron spatial resolution level (3). The subject of this paper is to report our results on three different methods of tissue preparation for scanning electron probe analysis of electrolytes.



Fig. 1. Backscattered scanning electron micrograph of small intestine cells 1 $\mu$  thick section on quartz substrate-method A, 600X.



Fig. 2. Backscattered scanning electron micrograph of small intestine cells 1 $\mu$  thick section quartz substrate-method B, 750X.



Fig. 3. Backscattered scanning electron micrograph of small intestine cells 1 $\mu$  thick section on quartz substrate-method C, 750X.

**METHODS:** Standard transmission electron microscopy methods now in use for ultrastructural studies of tissues subject the specimens to numerous aqueous and organic chemical fixatives and solvents which could alter the electrolyte spatial distribution before their examination in the electron probe. Therefore, the comparison methods we have chosen is all employee freezing of tissue specimen immediately in LN<sub>2</sub> cooled isopentane. Then either section it in the frozen state or freeze-dry en bloc. Method "A" consists of freeze-drying and embedding in a low viscosity epoxy resin (4) and then section at 1,000Å to 10,000Å in thickness and dry mount on either Silicon coated film or quartz substrates (3). Methods "B" and "C" utilize frozen sections of the same thicknesses as above (ultramicrotome) and dried at dry atmosphere (N<sub>2</sub>) or freeze-dried in vacuum on the substrate respectively. All preparations are finally coated with a 50Å layer of carbon before electron probe analysis.

**RESULTS AND DISCUSSION:** Figures 1, 2 and 3 show primary back-scattered electron scanning micrographs of the absorptive and secretory cells of the small intestinal epithelium prepared by methods described above. The differences in structural preservation is obvious (2). The method which gave the most consistent results both from ultrastructural and electrolyte distribution considerations was "C". Examples for the Silicon "shine-through" (3) and two electrolytes: Potassium and Chlorine are shown in figures 4-6, 7-9 and 10-12 for methods A, B and C in order. The electron beam damage on the epoxy embedded tissue was not consistent neither with ultrastructural features nor exposure times, thus resulting in SiK<sub>α</sub> x-ray micrographs (figure 4) that had no relation to the electrolyte (figure 5) distribution. The presence of chlorine in epoxys manifest itself into two difficulties: first one can confuse the normal chlorine distribution in the tissue section (figure 6) and second local losses of epoxy during electron exposure could introduce errors not only in the interpretations of scanning results but also in the

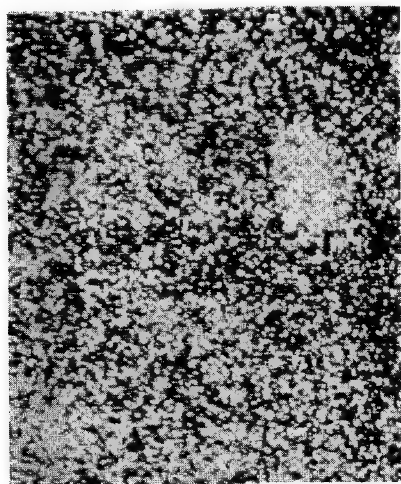


Fig. 4. EPA SiK<sub>α</sub>  
same area as Fig.  
1 SiO<sub>2</sub> substrate.  
Method A, 1000X.



Fig. 5. EPA KK<sub>α</sub>.  
Same area as Fig.  
1. Method A,  
1000X.

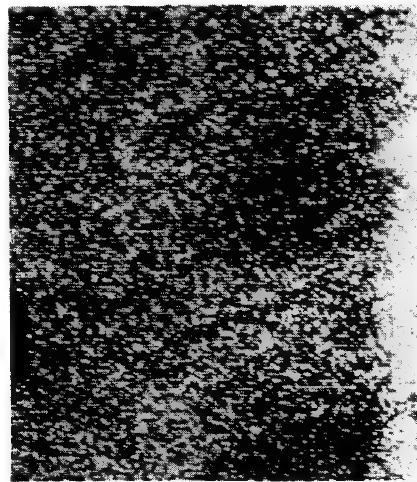


Fig. 6. EPA ClK<sub>α</sub>.  
Same area as Fig.  
1. Method A, 1000X.

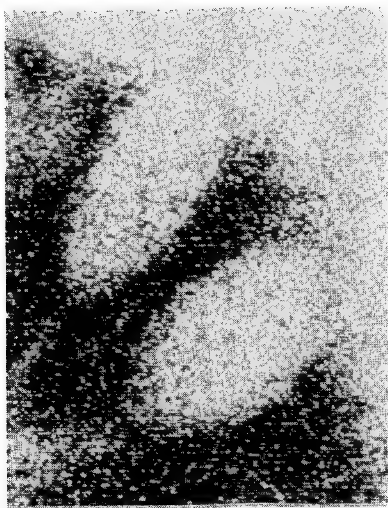


Fig. 7. EPA SiK $\alpha$ .  
Same area as Fig.  
2. SiO<sub>2</sub> substrate.  
Method B, 750X.

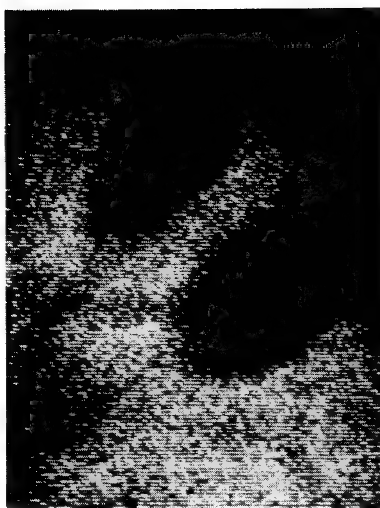


Fig. 8. EPA KK $\alpha$ .  
Same area as Fig.  
2. Method B, 750X.

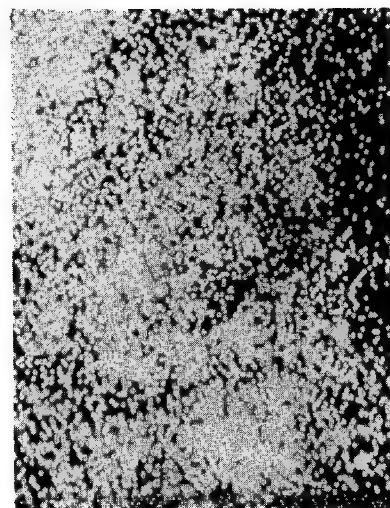


Fig. 9. EPA ClK $\alpha$ .  
Same area as  
Fig. 2. Method B,  
750X.

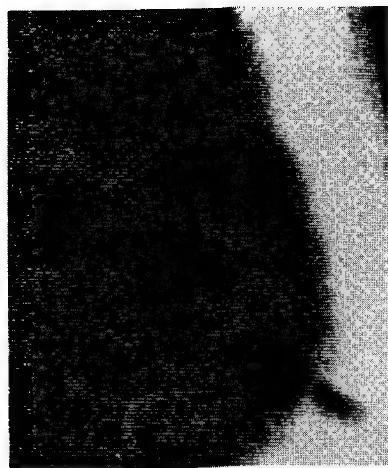


Fig.10. EPA SiK $\alpha$ .  
Same area as  
Fig. 3. SiO<sub>2</sub> sub-  
strate. Method C,  
750X.

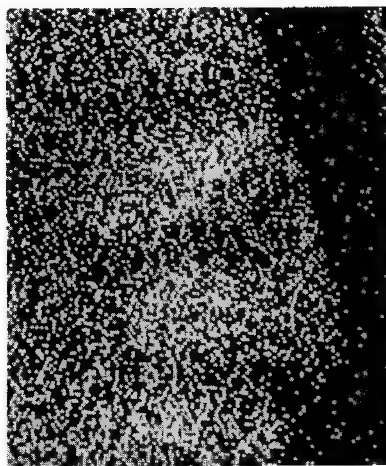


Fig.11. EPA KK $\alpha$ .  
Same area as  
Fig. 3. Method C,  
750X.

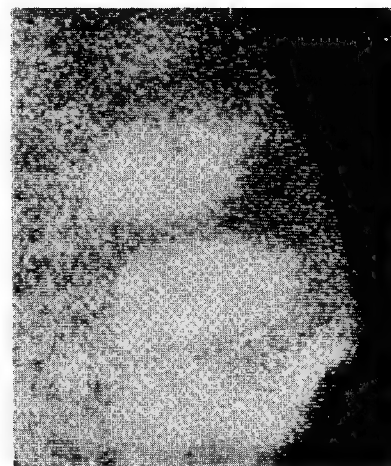


Fig.12. EPA ClK $\alpha$ .  
Same area as  
Fig. 3. Method C,  
750X.

calculation of the data to render it quantitative by any method (3). The potassium localization in both the absorptive and secretory cells of the small intestine is shown in figures 5, 8 and 11. It is of interest to note the similarity between methods "A" and "C" while in "B" the  $K^+$  has leaked out from goblet secretory granules but not from the remaining cytoplasm nor the adjacent absorptive cells. The spatial preservation not only of the K and Cl but also Na, Mg and Ca is more consistent and can be correlated with cellular ultrastructure and the quantitative results are in agreement with those of indirect, yet independent methods by method "C" than any of the other preparation methods utilized in our studies to date.

1. Castaing, R., Advances Electron Phys. Electron Optics, Academic Press, New York, (1960).
2. Tousimis, A.J., Proc. 2nd Ann. SEM Symp., pp. 219-230, Chicago, (1969).
3. Tousimis, A.J., Proc. 6th Nat. Ann. Conf. Electron Probe Analysis, pp. 36A-F, Pittsburgh, (1971).
4. Spurr, A.R., J. Ultrastruct. Res. 26:31 (1969).

\*Supported in part by NIH Contract #PH-43-66-10 and a grant from the M. Tsonis Research Foundation to the Biodynamics Laboratory. The cooperation and continuous encouragement by Drs. R. Lamont-Havers and Leonard Laster is gratefully acknowledged.



ELEMENTAL ANALYSIS OF REFRACTILE BODIES IN *AMOEBEA proteus*

James R. Coleman, Ronald R. Warner and Jytte R. Nilsson

Department of Radiation Biology and Biophysics  
University of Rochester School of Medicine and Dentistry

and

Biological Institute of the Carlsberg Foundation

Certain cytoplasmic organelles of *Amoeba proteus*, the "refractive bodies", are composed of phospholipid and contain substantial amounts of calcium and magnesium (2, 7, 9). It was suggested that the bodies might be stored food, but the question of why they contain relatively large amounts of calcium and magnesium has been ignored. It is known that intracellular calcium is of great importance and is carefully regulated (8, 10). There is evidence that excess calcium entering a cell is actively extruded from the cell, or is sequestered from the cytoplasm by being transported into mitochondria and other cell organelles (1). Thus, the concentration of free cytoplasmic calcium is maintained at about  $10^{-6}M$  even when the environment is  $10^{-3}M$  (1, 8). Our purpose was to test the hypothesis that the calcium-rich refractive bodies might function in the overall process of intracellular calcium regulation by sequestering intracellular calcium. Since the techniques used to establish the presence of calcium were not quantitative (7) and were also capable of removing or redistributing calcium (6), it was necessary as a first step to perform a qualitative and quantitative electron probe analysis of the refractile bodies. Individual organelles were analyzed *in situ* using preparative procedures and conditions previously described (5). This technique avoided loss of soluble materials by isolation procedures and permitted detection of variations among individual granules within a cell. Quantitative analysis was performed according to the BICEP program (11).

Refractile bodies are readily perceived in sample current images as well as x-ray images (Figure 1). They occur in three morphological classes: (1) 1.5 to  $7\mu$  or more in diameter, appearing as a lighter periphery surrounding a denser core of variable size; (2) smaller homogeneous bodies with an average size of about  $1.6\mu$  showing no evidence of a core; and (3) the smallest bodies, homogeneous and with no core, about  $0.8\mu$  in diameter.

All refractile bodies analyzed contained magnesium, calcium, potassium, phosphorus and carbon. Some bodies contained sodium and/or chlorine. Sulfur, iron and zinc were not detected. Quantitative analysis showed that the granules varied widely in composition. However, the atomic percent ratios of calcium/phosphorus, magnesium/phosphorus, potassium/phosphorus, and (calcium + magnesium + potassium)/phosphorus in individual granules were rather uniform (Table 1). Since the phosphorus signal from the granules is probably due to the phospholipids they contain, the relationship of calcium, magnesium and potassium to phosphorus is predictable. Phospholipids readily bind metallic cations, and in the case of calcium, the formation constant has been reported to be as high as  $10^4$  to  $10^6$  (3).

Thus, any metallic cations present in the cytoplasm would be expected to be associated with phospholipids in an equilibrium governed by the formation constant of the metal and phospholipid. This relationship suggests that such intracellular deposits of phospholipids may aid in controlling the cytoplasmic concentrations of minerals. In an organism with the characteristics and habitat of A. proteus, this process may have certain advantages.

This organism is a free living protozoon, whose only known source of minerals is from engulfed food organisms, or medium ingested through pinocytosis (4). Thus, minerals tend to appear in the cytoplasm as pulses. In order to control cytoplasmic concentrations and maintain them at constant levels, the minerals must be extruded or sequestered. If extruded, they are lost to the organism, a possible disadvantage for an organism which lives in a mineral-poor environment. Active transport of calcium into mitochondria for sequestration also entails disadvantages. First, oxidative phosphorylation is uncoupled until the cytoplasmic level of calcium is returned to its usual low value and, second, calcium transport requires substantial expenditure of energy in terms of electron transport (8). However, the use of phospholipid to sequester these minerals can eliminate these drawbacks. If the minerals were in association with phospholipid, then the concentration free in the cytoplasm would be largely a function of the formation constant for each element and the type of phospholipid present. Thus, the movement of an element from free to sequestered form would be governed by mass action considerations and would require little or no expenditure of metabolic energy.

#### Acknowledgements

This paper is based on work performed partially on NIH Grant No. AM14272 and Biophysics Training Grant No. 5T1GM-1088 and partially under contract with the U. S. Atomic Energy Commission at the University of Rochester Atomic Energy Project and has been assigned Report No. UR-3490-100.

#### References

1. Borle, A. B., 1971, in Cellular Mechanisms for Calcium Transfer and Homeostasis. G. Nichols and R. Wasserman, editors, Academic Press, New York, p. 151.
2. Byrne, J. M., 1963. Quart. J. Micro. Sci. 104: 445.
3. Carr, C. W. and Chang, K. Y., 1971, in Cellular Mechanisms for Calcium Transfer and Homeostasis. G. Nichols and R. Wasserman, editors, Academic Press, New York, p. 41.
4. Chapman-Andresen, C. 1971. Annual Rev. Microbiology 25: 27.
5. Coleman, J. R., Nilsson, J. R., Warner, R. R. and Batt, P. 1972. Exptl. Cell Res. (in press).
6. Coleman, J. R. and Terepka, A. R. 1972. J. Histochem. and Cytochem. (in press).
7. Heller, I. M. and Kopac, M. J. 1956. Exptl. Cell Res. 11: 206.
8. Lehninger, A. L. 1970. Biochem. J. 119: 129.
9. Mast, S. O. and Doyle, W. L. 1935. Arch. Protistenk. 86: 155 and 278.
10. Warner, R. R. 1971. Proc. VI Nat'l. Conf. Elec. Probe Analysis, Pittsburgh, Pa.

Table 1

Mean Ratios of Metals to Phosphorus in Atomic Percent in  
Refractile Bodies of Amoeba proteus

	<u>Large</u>		<u>Intermediate</u>	<u>Small</u>
	<u>Edge</u>	<u>Center</u>		
Ca/P	0.332(0.074)	0.375(0.065)	0.348(0.013)	0.250(0.054)
Mg/P	0.119(0.054)	0.096(0.060)	0.095(0.033)	0.132(0.050)
K/P	0.225(0.058)	0.117(0.041)	0.234(0.046)	0.250(0.057)
$\frac{\text{Ca} + \text{Mg}}{\text{P}}$	0.450(0.054)	0.471(0.051)	0.448(0.018)	0.383(0.038)
$\frac{\text{Ca} + \text{Mg} + \text{K}}{\text{P}}$	0.676(0.065)	0.647(0.072)	0.682(0.047)	0.632(0.041)

(Figures in parenthesis are standard deviations)

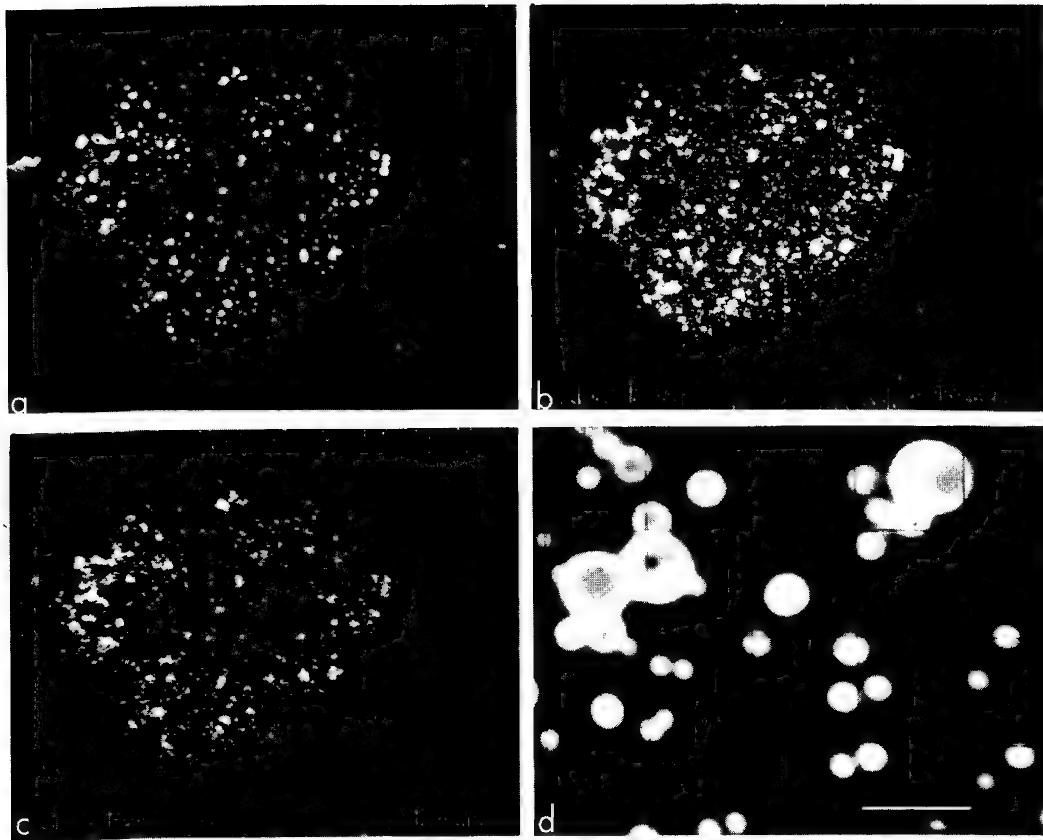


Figure 1. Sample current (a) image (22KV,  $3 \times 10^{-8}$  amp) of heat fixed Amoeba proteus, showing numerous refractile granules throughout the cell (40 $\mu$ /division). Phosphorus  $K_{\alpha}$  image (b) of same cell showing strong phosphorus signal from refractile granules and less intense signal from surrounding cytoplasm (15 min. integration). Calcium  $K_{\alpha}$  image (c) of same cell showing calcium signal largely restricted to refractive bodies (10 min. integration). Sample current image (d) showing large refractive bodies with dense cores and smaller homogeneous bodies (bar equals 5 $\mu$ ).

## Application of the electron microprobe in geology

Klaus Keil

Department of Geology and Institute of Meteoritics  
 The University of New Mexico  
 Albuquerque, New Mexico 87106

In the earlier days of electron microprobe analysis, only limited use was made of the instrument by geologists: in 1964, only about 60 papers had been published in this field, more than half of which were on meteorites. This situation has changed drastically and more than 700 papers have now appeared in the literature dealing with the electron microprobe and its application as a major research tool in mineralogy, petrology, geochemistry, oceanography, meteoritics, lunar sciences, and related disciplines [1]. Now, most major geology departments make extensive use of the instrument and several offer graduate courses on microprobe analysis.

The problems encountered in the application of the electron microprobe to geology, in many ways, are similar to those experienced in other fields. However, there are a number of specific problems which are enhanced when working with geological samples. First, most geological samples are poor electrical conductors and polished sections have to be vacuum coated with a thin conductive layer, preferably carbon. Second, most geological samples are poor thermal conductors and, hence, may vaporize under electron bombardment. Third, rocks are complex mineral assemblages of phases with often drastically different mechanical properties and, hence, preparation of polished sections is difficult. Fourth, most rocks consist of many different minerals that vary greatly in grain size and exhibit complex intergrowths. Hence, to identify these phases in the probe, polished thin sections that can be viewed in transmitted and reflected light (as opposed to polished sections for reflected light viewing) have to be used. Fifth, the dominant rock forming minerals in terrestrial, meteoritic, and lunar rocks are largely components of light elements (e.g. O, Si, Al, Fe, Mg, Ca, Na, K) whose relatively long K X-ray lines are somewhat more difficult to measure and are strongly absorbed.

Over the years, several different techniques have been worked out for the quantitative analysis of geological specimens. In mineral solid solution series, where essentially only two elements substitute for each other (e.g. olivine,  $\text{Mg}_2\text{SiO}_4$ - $\text{Fe}_2\text{SiO}_4$ ), all corrections except those for drift can be eliminated by the use of calibration curves, provided several homogeneous standards of well-known composition are available for the particular mineral group. Unfortunately, sets of well-analyzed, homogeneous mineral standards or synthetic phases are not always available and recourse has therefore to be taken to a single standard, hopefully of a composition and structure similar to the phase that is to be analyzed. This standard may be a mineral, a synthetic compound, or a synthetic glass, and X-ray intensities from unknown and standard should be corrected for drift, dead-time, background, mass absorption, secondary fluorescence, and atomic number, using theoretical correction procedures. Because of the similarity in composition between sample and standard, any errors inherent to the theoretical correction procedures will affect the analytical result much less than if a pure element standard were used.

A very convenient method of quantitative analysis of complex minerals is that of Bence and Albee [2]. Ziebold and Ogilvie [3] have shown that the calibration curve in a binary metal alloy system can be expressed by the linear function

$$C_{AB}^A / K_{AB}^A = \alpha_{AB}^A + (1 - \alpha_{AB}^A) \cdot C_{AB}^A \quad (1)$$

In this equation  $C_{AB}^A$  is the concentration of element A in the binary alloy AB relative to pure A;  $K_{AB}^A$  is the background-corrected intensity ratio of a characteristic line of element A in the binary alloy AB to that of pure A; and  $\alpha_{AB}^A$  is the parameter for A radiation in alloy AB that describes the shape of the curves (i.e. for  $\alpha_{AB}^A > 1$ , absorption dominates, and for  $\alpha_{AB}^A < 1$ , fluorescence dominates in the matrix effects). The parameter  $\alpha_{AB}^A$  can be determined as  $C_{AB}^A$  approaches zero:

$$\alpha_{AB}^A = \frac{C_{AB}^A}{K_{AB}^A} \quad (2)$$

Once  $\alpha_{AB}^A$  has been determined for a given system, the concentration of  $C_{AB}^A$  can be calculated from the measured  $K_{AB}^A$  for any concentration of A in AB:

$$C_{AB}^A = \alpha_{AB}^A \cdot K_{AB}^A \quad (3)$$

Bence and Albee [2] suggested that such empirical factors could be derived using oxides or well-characterized simple minerals and synthetic components as end members rather than pure elements, which would make electron microprobe analyses independent of complicated mineral standards of sometimes uncertain composition and homogeneity. They successfully extended this method to the analysis of multi-component systems, particularly complex minerals and water-bearing phases and reported empirical factors for the  $K_\alpha$  radiations of 10 elements (Na, Mg, Al, Si, K, Ca, Ti, Cr, Mn, Fe) in their respective oxides and  $H_2O$ . In a multi-component system, the concentration  $C_u^A$  of element A in the unknown (u) can be calculated as follows:

$$C_u^A = \beta_u^A \cdot K_u^A \quad (4)$$

$K_u^A$  is the measured background-corrected intensity of a characteristic line of element A in the unknown relative to the measured intensity of the same line in the oxide of A, and  $\beta_u^A$  is defined as follows:

$$\beta_u^A = \frac{K_u^A \cdot \alpha_{A\text{-oxide}}^A + K_u^B \cdot \alpha_{B\text{-oxide}}^A + K_u^C \cdot \alpha_{C\text{-oxide}}^A + \cdots K_u^N \cdot \alpha_{N\text{-oxide}}^A}{K_u^A + K_u^B + K_u^C + \cdots K_u^N} \quad (5)$$

Frazer et al. [4] have shown that as  $E_0$  (accelerating potential) decreases and approaches  $E_c$  (critical excitation potential) the effects of absorption, fluorescence, and electron backscatter (but not the electron stopping power  $S$ ) decrease and become negligible for  $E_0 = E_c$ . They suggest that intensity ratios of sample to standard could be obtained at different  $E_0$  as close as practically possible to  $E_c$ , and that

linear extrapolation to  $E_c$  would yield an intensity ratio for  $E_o = E_c$ . They also suggest a simple method for correcting for S and have successfully applied this technique for the quantitative analysis of minerals.

The electron microprobe has been applied to many different problems in geology. It has been of extreme importance in the quantitative characterization of more than 125 new minerals from earth, meteorites, and the moon. Mineral analyses and the study of the composition of coexisting minerals is probably the most important area of application of the probe in geology. Zonal structure of minerals, geochemistry of elements in individual mineral grains, bulk rock analyses with a broad electron beam, exsolution lamellae and fine inclusions, and rare gas contents have been studied with the probe. In addition, the instrument has been applied to the study of phase equilibria systems, luminescent properties of minerals under electron bombardment, modal analysis, wavelength shift studies and Kossel microdiffraction.

In conclusion it may be said that, in recent years, no other research tool has revolutionized geology as much as the electron microprobe, and its impact on earth sciences can only be compared to the introduction of the polarizing microscope to geology more than 125 years ago.

#### References

- [1] K. Keil, Application of the electron microprobe in geology; in "Microprobe Analysis" (ed. C. A. Andersen), John Wiley and Sons (in press).
- [2] A. E. Bence and A. L. Albee, J. Geol. 76, 382 (1968).
- [3] T. O. Ziebold and R. E. Ogilvie, Anal. Chem. 36, 322 (1964).
- [4] J. Z. Frazer, H. Fujita, and R. W. Fitzgerald, Scripps Institution of Oceanography, La Jolla, SIO-Report 71-11 (1971) (to be published in Materials Research Bulletin).

## MICROPROBE ANALYSES OF GLASSES IN LUNAR SOILS

R. W. Brown

Lockheed Electronics Company  
Houston, Texas 77058

W. I. Ridley, J. L. Warner and A. M. Reid

NASA Manned Spacecraft Center  
Houston, Texas 77058

Lunar missions to date have sampled six widely separated spots on the front side of the moon. The nature of the lunar surface geology at these sites has been deduced from detailed studies of the limited number of samples brought back from each site. Of these samples the soils contain the greatest amount of information in that they contain an assemblage of particles derived from a much larger area of the lunar surface than can be sampled directly. Repeated impacts have pulverized lunar surface material forming a soil consisting of both locally derived material and fragments thrown from distant regions of the moon by large impacts.

Microprobe analyses of glasses in the lunar soils can be used as a guide to the composition of the rocks from which the glasses were derived by impact melting. However, small impacts may not melt sufficient material to provide a representative sample of the parent rock and the nature of the impact process, with rapid heating and quenching, may allow element fractionation or incomplete melting. Impact glasses are commonly heterogeneous raising severe analytical problems; in addition, impact events melt not only homogeneous igneous rocks but soils and breccias that are themselves complex mixtures of several rock types.

We have found that if a large number of glasses are analyzed, the expected large amount of scatter in the data is observed. However, with sufficient number of analyses, preferred compositional groupings emerge from the data. We have made the logical assumption that these groupings reflect the composition of the parent rock types. To date we have completed 500 analyses of glasses in Apollo 14 soils, 350 analyses in Luna 16 soils, and 200 analyses in Apollo 15 soils. Each glass was analyzed for the elements Si, Ti, Al, Cr, Fe, Mg, Ca, Na, and K. All data were taken under identical conditions and monitored by including secondary standards with each run. Cluster analyses techniques were used to detect preferred compositions among each group of data.

This approach has allowed us to characterize the dominant rock types at each landing site. These data are of particular importance for the Apollo 14 and Luna 16 sites where few large crystalline rocks were sampled. At each site several components that are probably derived from more distant sources can be recognized. Some of these components are common to several sites and tentative conclusions can be drawn regarding regions of the moon not sampled directly. Correlations with Apollo 15 x-ray and  $\gamma$ -ray orbital data allow estimates of the major element composition of the lunar highlands.

Present data suggest that there are three major types of rock which have been sampled at the lunar surface: (1) Each mare basin contains basalts that are rich in Fe and Ti, low in Al and alkalis. Despite an overall similarity in composition among all mare



basalts each mare apparently contains basalts with some distinctive major element characteristics. (2) The Fra Mauro (Apollo 14) site and the regions around the Imbrium basin contain Fra Mauro basalts (KREEP) that resemble terrestrial high alumina tholeiites. Compared to the mare basalts these rocks are higher in Al and in K, REE and P. (3) The lunar highlands contain rocks that are very rich in Ca and Al and are highly feldspathic. The dominant rock type appears to be equivalent to anorthositic gabbro with 70 percent plagioclase feldspar and minor pyroxene and olivine.

Apollo 15 soils contain a major component of green glass that is rich in Fe and Mg, low in Al and Ti. This glass may derive from an ultrabasic lunar rock not previously sampled. One outstanding characteristic of the green glass is its remarkable homogeneity and constancy in composition despite the fact that it occurs in soils over a wide area of the Apollo 15 site. This glass should allow us to compare analyses among microprobe laboratories engaged in lunar studies as its variability, in the samples we have analyzed, is comparable to, or better than, our expected analytical precision.

INTRACRYSTALLINE VARIATIONS OF MAJOR AND  
MINOR ELEMENTS IN LUNAR PYROXENES

A. E. Bence

Department of Earth and Space Sciences  
State University of New York  
Stony Brook, New York 11790

Single crystal x-ray diffraction, transmission electron microscopy, and electron microprobe studies of pyroxenes from the lunar basalts have shown that these minerals, which are major constituents of most of the lunar rocks, are extremely complex both structurally and chemically (see, for example, 1-7). These complexities vary with the cooling histories of the host basalts, their bulk chemistry, and  $f_{O_2}$  during crystallization and, consequently, if properly evaluated, will provide a valuable tool for the understanding of lunar basalt petrogenesis. The nature of the lunar regolith precludes direct correlations between samples such as can be done on earth. For example, it is not possible to say immediately whether or not two lunar basalt samples are from the same flow unit and, if so, what their positions are in that flow. However, correlations of bulk chemistry, mineralogy, textures, and pyroxene crystallization trends may make it possible to make such determinations. Furthermore, as the American Apollo program winds down, the only new samples that we might expect to obtain will be soil samples from unmanned missions such as have been returned by Luna's 16 and 20. Examination of pyroxenes from lithic fragments in the 2-4 mm fraction may provide sufficient data to determine the nature of the parent rock and its emplacement history.

Quantitative electron microprobe investigations of the major and minor element crystallization trends in pyroxenes from a number of lunar basalts reveal significant differences between the various basalt textural and chemical types (8). These trends (Figs. 1-4) reflect the changing composition of the liquid phase with respect to major and minor components as crystallization proceeds and, although equilibrium conditions did not prevail, may be best understood in terms of a partitioning of components between the liquid and crystalline phases. The appearance of a new crystalline phase establishes further competitions for the components in the melt and if the competition is severe, will result in abrupt changes in the crystallization trends for crystals previously growing the melt. Such discontinuities observed in the pyroxene crystallization trends for Fe-Ca-Mg (Fig. 1), Ti-Al (Fig. 2), Ti-Cr-Al<sup>VI</sup> (Fig. 3), and Al/Si-Fe/Mg (Fig. 4) are consistent (and correlate texturally) with the onset of plagioclase crystallization and, in one case, with the late-stage appearance of an aluminous spinel. For basalts of similar bulk chemistry and mineral paragenesis, but different textures, variations in crystallization trends are most easily explained by different cooling histories. In general, the late-stage crystallization histories appear to be rapid, near-surface events for all the basalts; however, the initial stages, as inferred from the pyroxene chemistry, differ for a number of basalt types. The primary difference for the initial stages is the position of plagioclase in the paragenetic sequence.

The compositional discontinuities occur over sub-micron to several micron intervals, represent relatively minor changes in the concentrations of Ti, Al, and Cr, and are not generally visible optically. Further complexities are introduced by the fact

that sectoral control within a single pyroxene crystal results in very different compositional trends in the (010), (110), and (100) directions. As a consequence great care must be taken in obtaining and interpreting quantitative electron microprobe data for these trends. In the present investigation, quantitative determinations for Fe, Ca, Mg, Si, Ti, Cr, Al, Mn, and Na were obtained by running successive four-element step scans across the crystals and matching profiles. Selected points along these profiles were then analyzed for statistical determinations. Data were reduced to oxide weight concentration according to a modification of the scheme of Bence and Albee (9) and pyroxene formulas were determined by normalizations to 6 oxygens.

#### References

1. Bence, A. E., Papike, J. J., and Prewitt, C. T., *Earth Planet. Sci. Lett.*, 8, 393-399 (1970).
2. Bence, A. E., Papike, J. J., and Lindsley, D. H., *Proc. Second Lunar Sci. Conference, Geochim. Cosmochim. Acta Suppl. 2*, Vol. 1, 559-574. The M.I.T. Press (1971).
3. Boyd, F. R. and Smith, D., *J. Petrology*, 12, 439-464 (1971).
4. Hollister, L. S., Trzcinski, W. E., Jr., Hargraves, R. B., and Kulick, C. G., *Proc. Second Lunar Sci. Conference, Geochim. Cosmochim. Acta Suppl. 2*, Vol. 1, 529-557. The M.I.T. Press (1971).
5. Papike, J. J., Bence, A. E., Brown, G. E., Prewitt, C. T., and Wu, C. H., *Earth Planet. Sci. Lett.*, 10, 307-315 (1971).
6. Champness, P. E. and Lorimer, G. W., *Contrib. Min. Pet.*, 33, 171-183 (1971).
7. Radcliffe, S. V., Heuer, A. H., Fisher, R. M., Christie, J. M., and Griggs, D. T., *Proc. Apollo 11 Lunar Sci. Conference, Geochim. Cosmochim. Acta Suppl. 1*, Vol. 1, 731-748 (1970).
8. Bence, A. E. and Papike, J. J. (in press).
9. Bence, A. E. and Albee, A. L., *J. Geol.*, 76, 382-403 (1968).

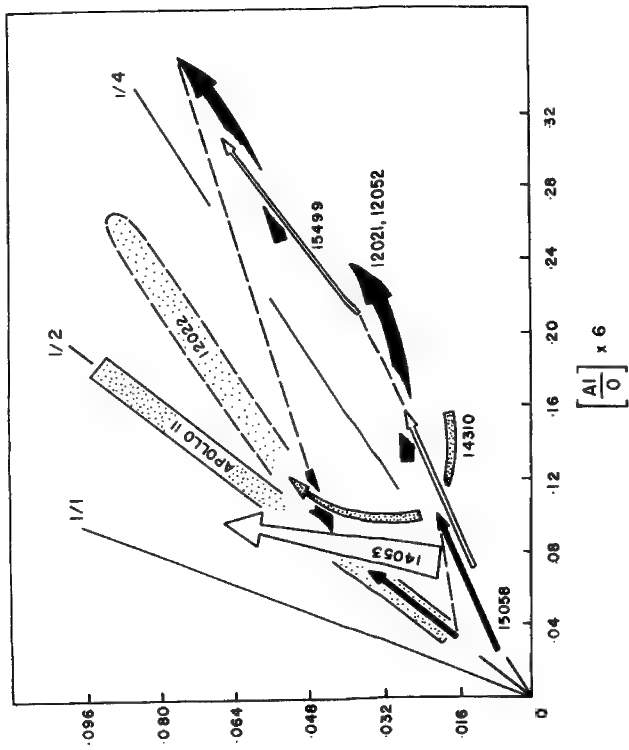


Fig. 1

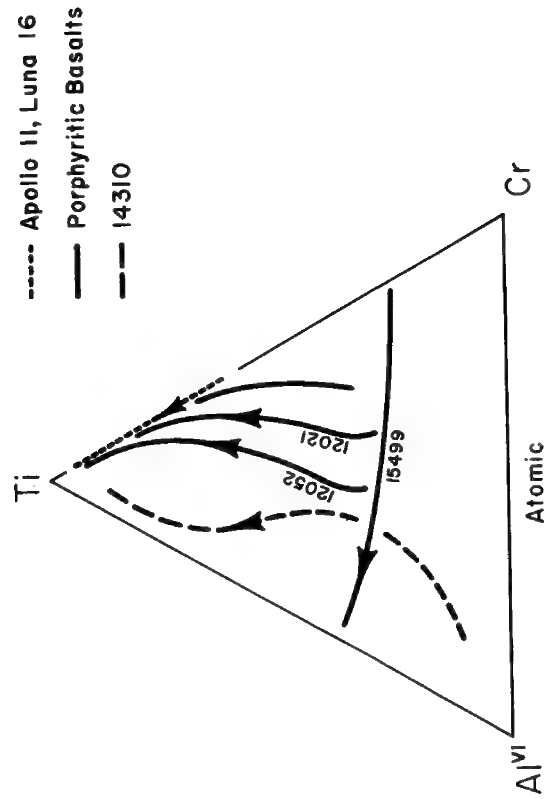


Fig. 2

Fig. 3

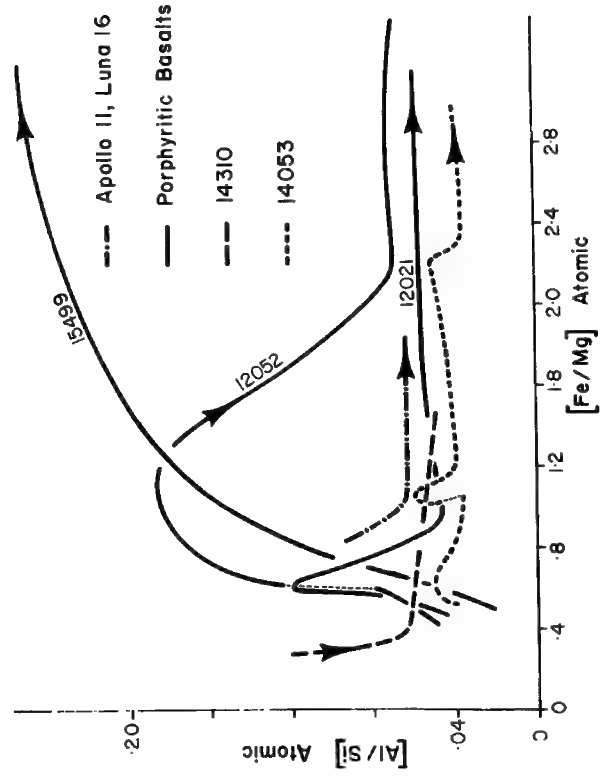


Fig. 4

## Vapor-Phase Crystallization in Lunar Breccias

D. S. McKay, U. S. Clanton, and G. H. Ladle

## Summary

Many of the highly recrystallized breccias from Apollo 14 contain crystal lined cavities or vugs. The mineralogy of the vugs based on Scanning Electron Microscope (SEM) and Energy Dispersive X-Ray (EDX) analysis consists of well developed crystals of plagioclase, pyroxene, ilmenite, apatite, whitlockite, iron, nickel-iron, and troilite. Plagioclase and pyroxene appear to form a substrate on which all other crystals grow. Iron, nickel-iron and apatite crystals appear to be late forming crystals; the most perfectly developed crystals are apatite. The growth of crystals in interior vugs, the development of detailed and complete crystal faces, the abundance of growth steps, and the delicate network of crystals separated by open spaces strongly suggests that growth was from a vapor phase.

The crystals are interpreted as having formed from a hot vapor containing oxides, halides, sulfides, alkali metals, iron and possibly other chemical species. The vapor was associated with the thermal metamorphism and subsequent cooling of the Fra Mauro Formation after it had been deposited as an ejecta blanket by the Imbrian impact. An analogy may be made with the zone of vapor-phase crystallization of terrestrial ash flows. Terrestrial ash flows typically display vapor-phase alkali exchange, loss of volatile gases, and the development of fumaroles and sublimates. Lacking H<sub>2</sub>O as a major vapor component, cooling lunar ejecta blankets would not be expected to duplicate in detail features seen in terrestrial ash flows. However, a vapor phase would be expected and the cooling history would be analogous. The redistribution of volatile species in a vapor phase appears to be a significant feature of large lunar ejecta blankets, and may have been more important in early lunar history when late stage accretion and mare basin excavation provided large ejecta blankets.

## Figure Captions

## Figure 1

- a. SEM photograph of a doubly terminated hexagonal apatite crystal in a breccia vug. This apatite contains about 2 percent chlorine based on EDX analysis. (14261).
- b. SEM photograph of a nest of apatite crystals. First and second order prisms; first, second, and third order hexagonal dipyrramids; and basal pinacoid faces are present on the apatite crystals in Figure 1, a, b, and c. (14161).
- c. SEM photograph of a stubby apatite partially filling a small vug; this crystal is twinned. Apatite crystals are found only on substrates of plagioclase and pyroxene crystals. (14143).
- d. SEM photograph of a stubby discoidal crystal of whitlockite (center). A tabular rhombohedral habit is suggested but rounded faces make indexing uncertain. (14261).

## Figure 2

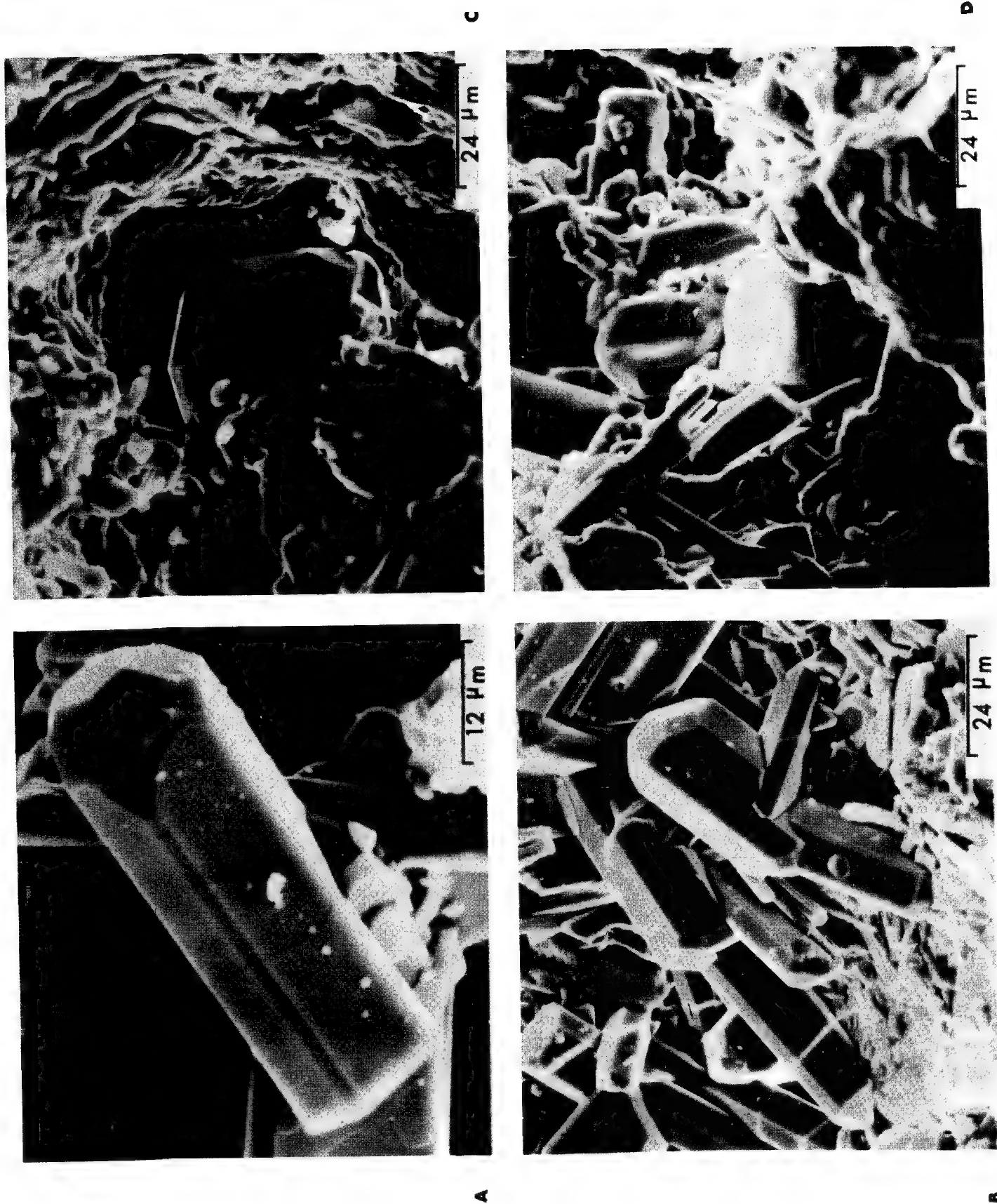
- a. SEM photograph of a host of small, mostly tabular plagioclase crystals which have grown on the growth steps of a pyroxene crystal. (14261).

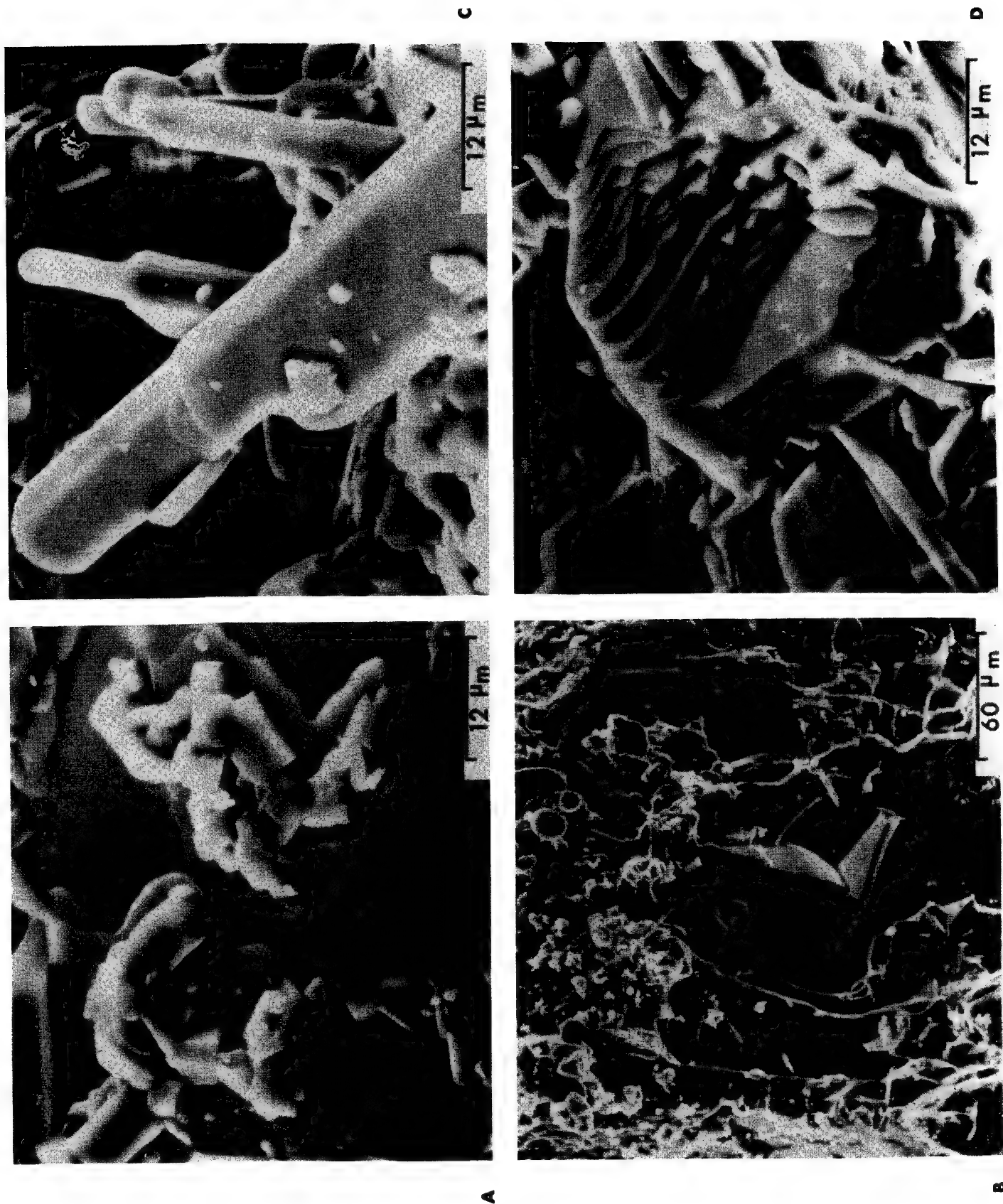
- b. SEM photograph of tabular plagioclase crystals in a small vug in a recrystallized breccia. (14001).
- c. SEM photograph of low calcium, prismatic pyroxene crystals. Pyroxene needles smaller than about 2 micrometers in diameter are rounded and have hemispherical terminations; larger crystals have regular faces. A tabular crystal of ilmenite clings near the free end of the largest pyroxene crystal; an iron crystal is partially visible in the background behind the ilmenite crystal. (14261).
- d. SEM photograph of growth steps on a calcium pyroxene crystal; this linear bunching of growth lines is characteristic of many of the vug pyroxene crystals. (14161).

Figure 3

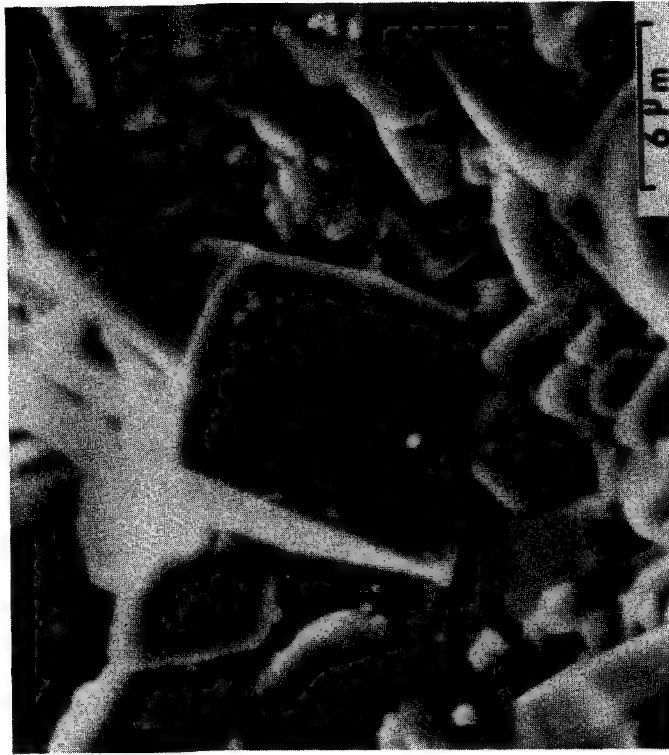
- a. SEM photograph of pseudo octahedron of ilmenite with basal pinacoid, rhombohedron and prism faces. Ilmenite crystals are relatively uncommon in vugs; most tend to be small and tabular as shown in Figure 2c. (14262).
- b. SEM photograph of a euhedral iron crystal. This tetrahexahedron has an axis of four-fold symmetry projecting toward the upper right of the photograph. The crystal contains no detectable nickel (less than 1 percent). (14161).
- c. SEM photograph of an iron crystal with well developed faces and bunched growth lines. The three large faces form part of an octahedron; the smaller rectangular form is one face of a dodecahedron. (14262).
- d. SEM photograph of a nickel-iron crystal with a partial coating of iron sulfide, presumably troilite. The tetrahexahedron has been photographed along an axis of three-fold symmetry resulting in the pseudo-hexagonal outline. The crystal contains about 12 percent nickel. (14258).

NASA  
S-72-30019 Figure 1.

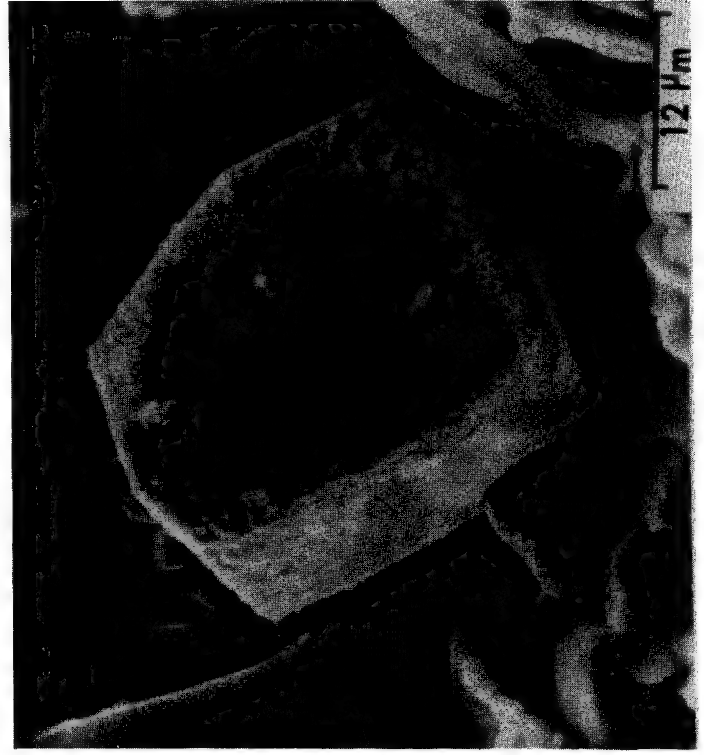




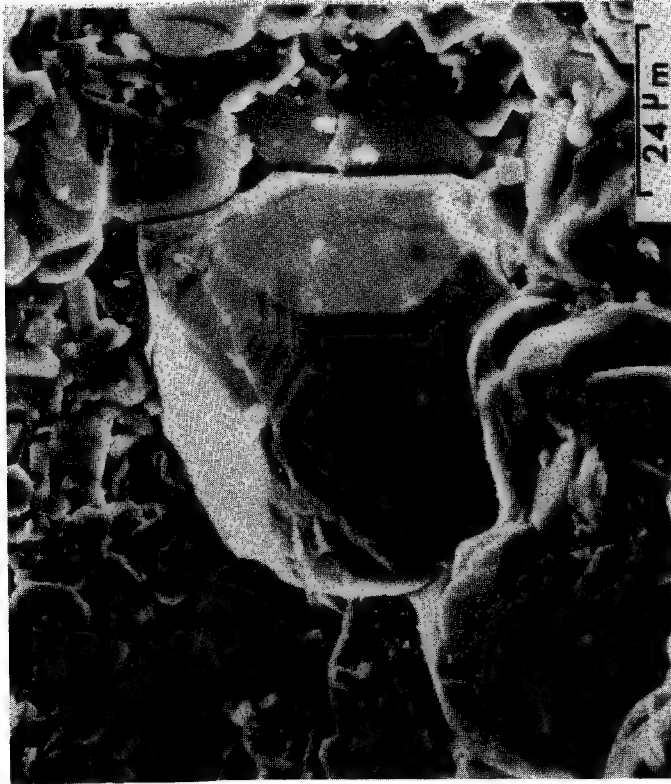




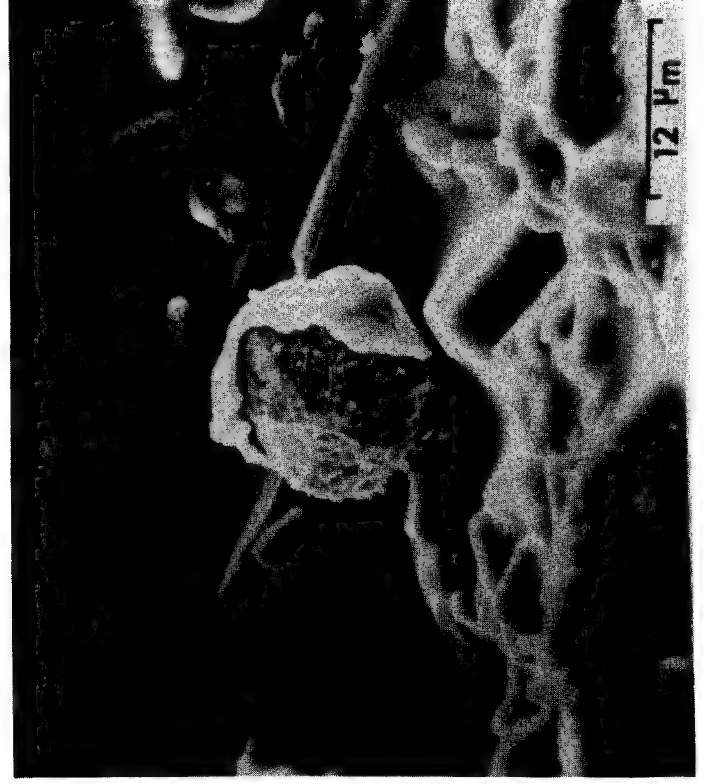
A



B



C



D

## LOW KeV ANALYSIS OF SILICATE MINERALS USING PURE ELEMENT STANDARDS

G. Cunningham, T. Palmer,

K. Snetsinger and M. Blanchard

NASA-Ames Research Center

Moffett Field, Calif. 94035

INTRODUCTION

The elements Mg, Al, and Si, common in rock forming minerals, generally require large matrix corrections which reduce the accuracy of electron microprobe analysis. Desborough and Heidel (1971) have demonstrated that 6 KeV analysis of these elements using mineral standards can eliminate the need for matrix corrections. This paper presents results of electron microprobe analysis at 6 KeV for Mg, Al, and Si in well analyzed silicate minerals using pure elements as standards. The data show this approach is acceptable in certain instances and no matrix corrections are required. These results indicate it is not necessary for the standard and sample to have similar amounts of the same elements. Hence, pure elements and other simple compounds may be used as standards whenever the conditions are met.

PROCEDURE

Analyses were performed using the MAC model 400 electron microprobe. The elements Mg, Al, and Si were analyzed at 6 KeV with an ADP crystal and a gas flow proportional detector and a specimen current of 0.0100 microamp on the pure element standard. The electron beam diameter was about 5 microns. Count rates were low; ranging from 50 to 200 cps on the standards and from 10 to 100 cps on the samples. For each sample three 50 second counts were made on 10 different grains (when fewer grains were available, widely separated spots were used) so that sample inhomogeneity would be eliminated. Data were corrected for wavelength shift, deadtime, instrument drift and background. Mineral samples were selected so a large range of compositions and mass absorptions would occur.

RESULTS

Data shown in Table I indicate the measured values of Mg, Al, and Si, are within experimental error of the chemical values whenever the atomic number (Z) of the standard was near the Z of the sample. This appears typical for those analyses when the Z of the standard is within  $\pm 1$  of the sample. A progressively larger error is introduced as the Z of the sample gets farther away from the standard. At 6 KeV the electron beam penetration is very shallow so the absorption is at a minimum, and the principle matrix correction should be atomic number. The data support this.

Table II shows results of 6 and 25 KeV analysis for Mg, Si, and Fe in a meteoritic olivine (Marjalahti) using pure elements as standards. As would be expected Mg and Si results at 6 KeV without corrections were superior to the 25 KeV

analyses with matrix corrections. Only for Fe are the corrected values (25 KeV) better than the uncorrected values (6 KeV). The atomic number correction was much greater than absorption or fluorescence corrections for Fe.

### CONCLUSIONS

Low KeV analysis for Mg, Al, and Si using pure element standards can be effective in those applications where the Z of the standard is near that of the mineral sample to be analyzed. Advantages of low KeV analysis include: (a) elimination of matrix corrections; (b) only elements of interest need be analyzed in a sample; (c) time is saved; and (d) the need is reduced for many costly chemically analyzed standards. Problems with low KeV analysis include: (a) lower count rates, which means poorer precision and longer count times; and (b) a smaller volume is analyzed, which suggests surface contamination and sample inhomogeneity will produce larger errors.

### REFERENCES

Bence, A. E., and Albee, A. L., 1968, Empirical Correction Factors for the Electron Microanalysis of Silicates and Oxides, *Journal of Geology*, Vol. 76, pp. 382-403.

Desborough, G. A., and Heidel, R. N., 1971, Improved Electron Microprobe Analysis at Low Operating Voltage: I Silicon, Magnesium, and Aluminum, *American Mineralogist*, Vol. 56, pp. 2129-2135.

Table I: Six KeV Analysis of Minerals for Mg, Al & Si using Pure Element Standards. Data in weight percent.

Element	Corundum	Quartz	Cordierite	Marjalahti Olivine	Wilburforce Hornblende	Suzimaki Olivine	Chromite
(1) Z=10.65	Z=10.80	Z=10.97	Z=11.90	Z=13.80	Z=14.98	Z=16.95	
Mg (Z=12)							
Chemical <sup>(2)</sup>	-- <sup>(4)</sup>	--	7.27	28.60	5.02	15.40	6.94
MicroProbe <sup>(3)</sup>	--	--	7.1±.3	28.5±.8	4.8±.3	14.5±.5	6.3±.4
Al (Z=13)							
Chemical	52.92	--	17.71	--	5.11	--	10.27
MicroProbe	52.7±.6	--	17.6±.3	--	5.1±.4	--	9.8±.3
Si (Z=14)							
Chemical	--	46.76	23.07	18.83	19.15	16.50	--
MicroProbe	--	44.9±.6	19.4±.4	18.6±.2	19.0±.3	16.9±.5	--

(1)  $Z = \text{Effective atomic number} = \sum C_i Z_i$ ; where C = weight fraction, Z = atomic number.

(2) Chemical = Wet chemical values.

(3) MicroProbe = Microprobe results not corrected for matrix effects

(4) Horizontal lines indicate elements not determined or below 0.2% weight percent.

Table II: 25 KeV Analysis vs 6 KeV Analysis  
of Mg, Si and Fe in Marjalahti  
Olivine using Pure Element Standards.  
Data in weight percent.

Elements	Chemical Analysis	6 KeV Microprobe Analysis(1)	25 KeV Microprobe Analysis(1)	25 KeV Bence & Albee(1968) Correction Program(2)
Mg	28.60	28.51	15.49	30.03
Si	18.83	18.54	9.76	18.19
Fe	8.85	7.41 <sup>(3)</sup>	7.73	8.95

(1) Corrected for wavelength shift, detector deadtime, instrument drift and background, no matrix effect corrections.

(2) Corrected for mass absorption, fluorescence and atomic number

(3) Fe analysis done at 10 KeV.

Acknowledgment - These analyses were performed by Trapelo/West (Contract NAS2-6006) under the supervision of Mr. H. D. Shade.

ELECTRON PROBE INVESTIGATION OF HYDROGEN-INDUCED  
BLISTERS AND INTERNAL CRACKS IN IRON

J. L. Bomback and I. M. Bernstein\*

United States Steel Corporation  
Research Laboratory  
Monroeville, Pennsylvania 15146

It is well known that hydrogen can have an extremely deleterious effect on the mechanical properties of iron-base materials. Nucleation and growth of hydrogen-induced surface blisters and internal cracks lead to macroscopic size defects. The characterization of these defects including their morphology, distribution and effects on the surrounding lattice is of great value in the study of hydrogen embrittlement. This can be accomplished with various electron probe techniques. In particular, the morphology of internal cracks can be observed on stereo projection microradiographs and the distortion of the surrounding lattice estimated from the superimposed Kossel absorption conics. Surface blisters are easily imaged in the SEM while selected area channeling patterns reveal the deformation around the blisters.

The geometry of the microradiograph/Kossel arrangement is shown schematically in Fig. 1. The Kossel absorption conics are used since they and the radiographic image are gnomonic projections from the point defined by the x-ray source whereas the apices of the diffraction conics are not well defined. Figure 2 shows several internal cracks in a pure iron crystal which had been cathodically charged at room temperature for 1 hr. at a current density of 30mA/cm<sup>2</sup> and in the absence of applied stress. The black and white lines are the Kossel absorption and diffraction conics respectively.

The micrographs were taken in an Acton Kossel camera on Kodak No. Screen Medical film using an iron foil target. The specimen to film distance was 12.5 cm. Exposure time was 10 min. at 30 kv and 100 na. Figure 3a is an enlargement of the region around crack A and Fig. 3b shows the corresponding Kossel pattern from a perfect iron crystal.

The crystal orientation was such that the crack region coincided with the intersection of 3(110) type conics. The severe deformation near the crack manifests itself as a smearing of the (110)<sub>g</sub> conic. This can be visualized as regions with lattice misorientations of  $\pm 1^\circ$  20  $\mu$ m from the crack edge, and decreasing to  $\pm 0.1^\circ$  at 50  $\mu$ m. Usually the distortion is localized to within 100  $\mu$ m of the defect and does not appear generally throughout the crystal. As more cracks nucleate and grow, the regions of high plastic deformation surrounding the cracks begin to overlap and the lattice distortion is more pronounced.

---

\* Now with the Dept. of Met. & Mat'l Science, Carnegie-Mellon University, Pittsburgh, Pa. 15213.

The surface blister on a  $\langle 110 \rangle$  face is shown in Fig. 4. The steps up the side of the blister indicate a discontinuous slip process. Selected area channeling patterns were taken to determine the crystallographic relationship governing the directional morphology of the blister and the degree of lattice perfection around it.

The authors acknowledge the help of Mr. Howard Wagenblast who took the micrographs.

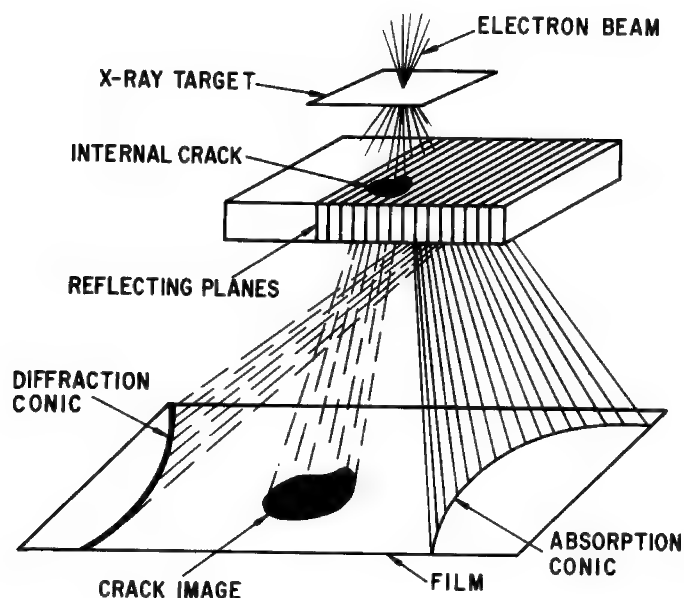


Fig. 1 - X-ray Projection Radiography and Kossel Geometry.

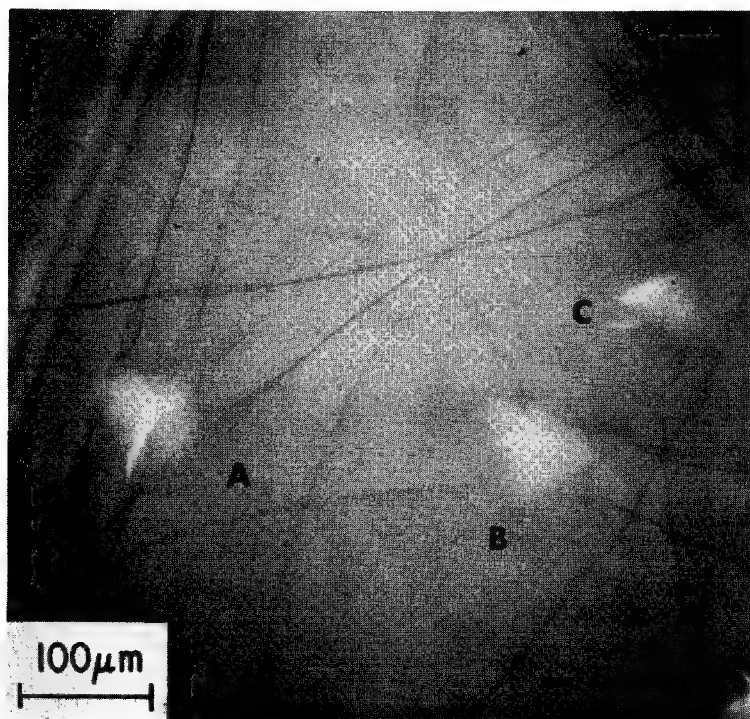


Fig. 2 - Several Hydrogen Induced Cracks.

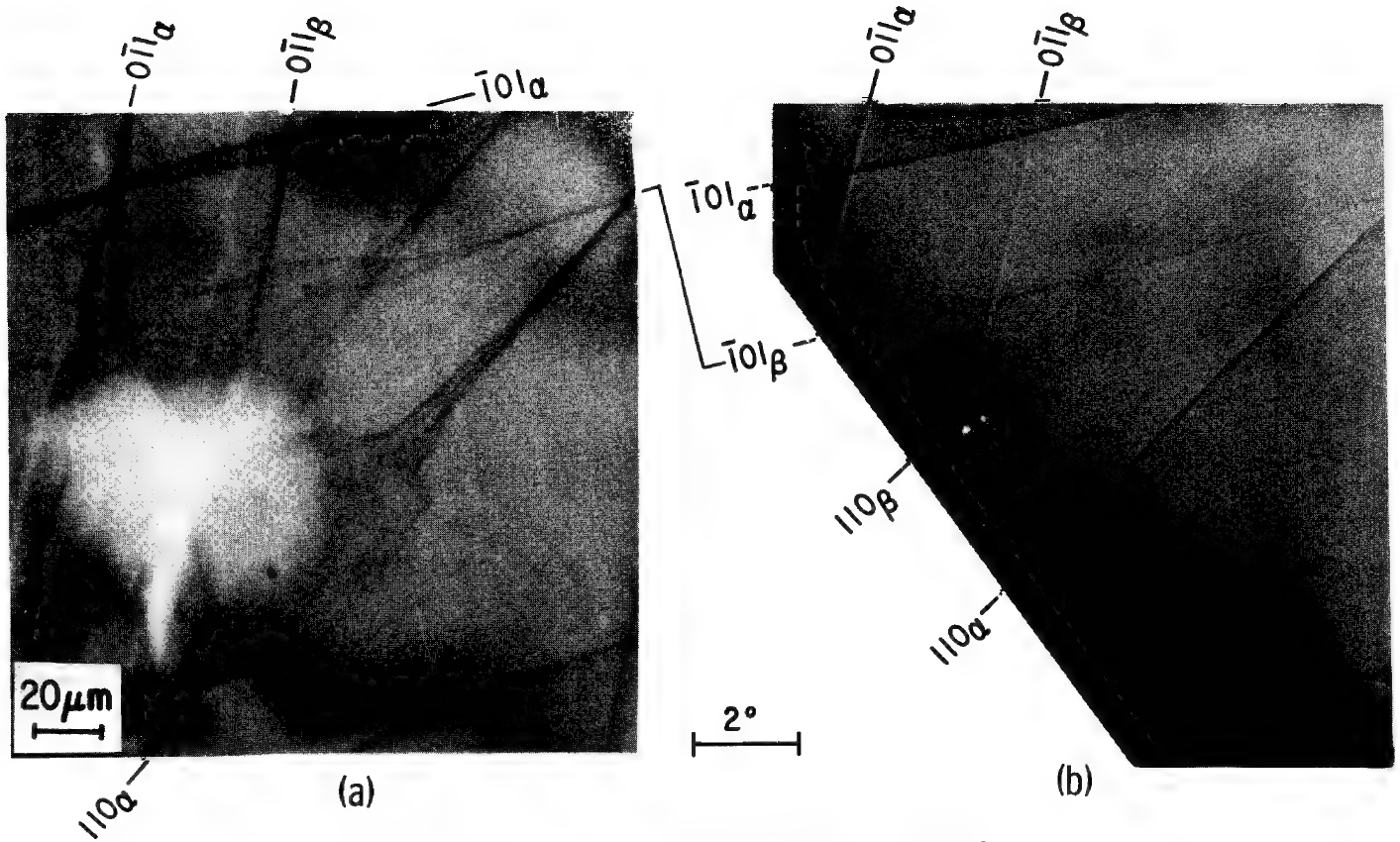


Fig. 3 - Enlargement of Crack A in Fig. 2.

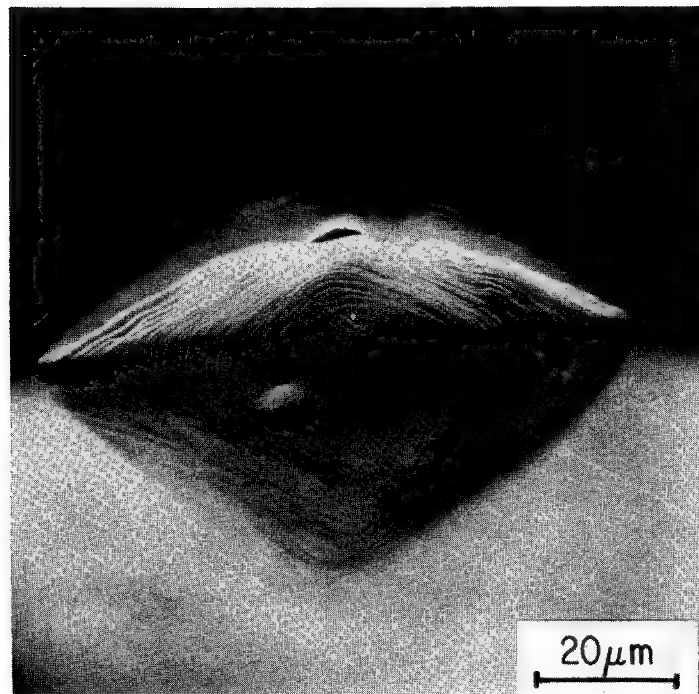


Fig. 4 - Hydrogen-Induced Blister on  $110$  Iron Crystal.

## EXAMINATION OF MEDIUM RANK COALS BY SEM

L. F. Vassamillet, Carnegie-Mellon University, Pittsburgh, Pa.

In a study of the Mössbauer spectra of iron in several samples of coal (1) it was observed that a hitherto unobserved Mössbauer spectrum was obtained in addition to the well-known pyrite spectrum. The non-pyrite iron is Fe(II), in a high-spin configuration, in octahedral symmetry, and apparently in a rather well-defined state. The identification of minerals present in many coals does not account quantitatively for several of the metallic elements present (such as Fe) and it has been postulated that some sort of "organic" bonding with the coal is involved. However, little was known about the structures of the "organically bound" metallic elements. The Mössbauer study established the valence state of the iron and as well cast some doubt on this "organic" form of its presence.

Early microprobe results (2) showed the iron to be present in varying amounts throughout the matrix of the coal samples investigated, and often associated with other elements such as Si, Al and Mg. Although such elements as Ca, Na, Ti and K were also found in the coals, the correlation with Fe was rather poor, especially on the larger mineral inclusions. Of the possible Fe containing minerals based on known minerals associated with bituminous coals (3) prochlorite ( $2\text{FeO} \cdot 2\text{MgO} \cdot \text{Al}_2\text{O}_3 \cdot 2\text{SiO}_2 \cdot 2\text{H}_2\text{O}$ ), satisfied the two sets of criteria required by the microprobe results and the parameters of the Mössbauer spectra (1).

X-ray micrographs showed a very high correlation of Fe with Si and in several instances gave good correlation with Mg and Al. However, the ratios of Si, Mg and Al to Fe were highly variable. This of course could be due to variations in mineral grain size as well as compositional differences.

Prochlorite is a member of the chlorite family of minerals (3),  $(\text{Mg}, \text{Al}, \text{Fe})_{12}[(\text{Si}, \text{Al})_8]_{20}(\text{OH})_{16}$ . These minerals form an extensive isomorphous series with considerable atomic substitution. Limiting forms may contain no iron, no aluminum, or no magnesium. They possess a layer structure, resembling micas. The location of the Fe in the layers does conform to the octahedral symmetry required by the Mössbauer spectrum (5). Another mineral group, the amphiboles, also forms an extensive isomorphous series with atom exchange between Al and Si, Mg and Al and Mg and Fe (6). Hornblende, a member of this group, is an occasional mineral in bituminous coals. Current studies (5) indicate that Fe(III) is always observed in the several mineral specimens examined by the Mössbauer technique, and no similar spectral form has been observed in any of the coals.

Using the SEM the small mineral grains are easily seen due to the large atomic number difference between the matrix and the mineral. X-ray spectra have been obtained from these grains by an energy dispersive detector. For semi-quantitative analysis, standards of  $\text{SiO}_2$ ,  $\text{MgO}$ ,  $\text{Al}_2\text{O}_3$  and an olivine were used.

Although unambiguous identification is not possible on mineral grains of the sizes common to the coals investigated, the evidence is very strong that a large fraction of the iron present in coal but not associated with sulfur is widely distributed throughout the matrix in very small particles (10 microns and less) of a high density mineral. It appears likely on the basis of the Mössbauer and SEM studies that the concept of "organically bound" iron is neither required nor experimentally substantiated.

## References

1. Lefelhoez, J. F., Friedel, R. A. & Kohman, T. P., *Geochemica et Cosmochimica Acta*, 31, 2261 (1967).



2. Dutcher, R. R., White, E. W. & Spaekman, W., Proc. 22nd Ironmaking Conf., Iron and Steel Div., Met. Soc. of AIMME. p. 463 (1964); Vassamillet, L. F. unpublished (1968).
3. Nelson, J. B., BCURA, Bull. 17, 43 (1953)
4. Deer, W. A., Howie, R. A. & Zussman, J., Rock Forium, Minerals, Vol. 3, p. 131, J. Wiley & Sons, New York (1962).
5. Kamarchik, Peter, Kohman, T. P. and Friedel, P. A., private communication.
6. Berry, L. G. & Mason, B.; Mineralogy, W. H. Freeman Co., San Francisco (1959).

EXAMINATION OF LOW GRADE URANIUM ORES BY  
ELECTRON BEAM TECHNIQUES

Gregory S. Maurer, Oberlin College, Oberlin, Ohio  
L. F. Vassamillet and T. B. Massalski  
Mellon Institute of Science, Carnegie-Mellon University  
Pittsburgh, Pa.

Present methods of uranium extraction from low-yield ores are relatively inefficient. For example, the point of diminishing returns on the processing of granitic uranium and thorium ores occurs at about 60 per cent efficiency (1). Variation of processing parameters (e.g. leaching time, acid strength, temperature, ore mesh size) results in significantly higher yields, but always at the expense of production costs. It is known, at least for the case of the granitic ores, that this difference in "recoverability" is due in large part to mineralogical differences.

Given that higher extraction efficiency is desirable, and assuming that microstructure plays an important role in the extraction of uranium from all ores, it seems natural to begin with suitable characterization of those ores now being mined commercially. Such ores have already been well-characterized by traditional mineralogical techniques (e.g. optical properties, x-ray diffraction pattern); a new look from a different point of view could be most enlightening.

Six different ores from the western and midwestern United States were examined. Secondary electron micrographs were taken of representative areas; x-ray micrographs were taken of the same areas so that microstructure could be correlated to chemical composition. X-ray wavelengths with which area scans were made were determined by multichannel analysis. The ores may be separated into two distinct classes on the basis of uranium distribution characteristics. In one category all detectable uranium-bearing matter is found in the interstices among the principal and distinguishable grains of the ore; in the ores of the second category, the uranium-bearing material is found as a primary constituent of a number of distinguishable grains.

The ore from the Mineral Jo mine is typical of ores in the first category; the uranium is found in interstices among the quartz and pyrite crystals which constitute the bulk of the ore. Calcium and vanadium are associated with the uranium. The uranium-bearing mineral in this ore had tentatively been identified as carnotite (2); the sample examined had no trace of potassium, and could therefore not have contained carnotite. Moreover, while the ore contains vanadium, the x-ray micrographs show that the uranium and vanadium concentrations are inversely related - wherever uranium concentration increases, vanadium concentration decreases.

Ore from the Lucky Mc mine is representative of the second category of ores. The uranium-rich regions in the ore are very small and their structure rather difficult to distinguish by optical methods. Use of the scanning microscope reveals a two-phase structure of alternating light and dark bands. The width of the bands is variable, but of the order of 0.1 - 1.0 micron. The uranium is located in the light bands and is combined with phosphorus, arsenic, magnesium, aluminum, and iodine. The dark bands are primarily carbon. This mineral does not agree in composition with any minerals reported to be present in the area (3). The chemical composition closely resembles that of novacekite and saleéite, both of which are very rare. One possible conclusion is that these minerals are not so rare as previously thought; rather, they are rarely found in crystals large enough to be identified by optical and x-ray diffraction techniques.

It would be presumptuous, on the basis of this work, to draw any specific conclusions concerning uranium extraction processes; however, a case has been made for a methodology of mineral characterization which utilizes SEM and multichannel analysis. In this instance such a methodology has resulting in:

- 1) a fast way of limiting the field of possibilities during the process of mineralogical identification.
- 2) a simplification of interpretation of x-ray diffraction patterns.
- 3) the detection and possible identification of minerals which are present in quantities too small to be detected by traditional mineralogical techniques.

References:

1. Hurst, F. J., Crouse, D. J., and Brown, K. B., Recovery of Thorium (and Uranium) From Granitic Rocks, Oak Ridge National Laboratory: ORNL 3987.
2. U. S. Bureau of Mines Assay
3. Heinrich, E. W., The Geology and Mineralogy of Radioactive Raw Materials (New York: McGraw Hill, 1958).

ELECTRON MICROPROBE TECHNIQUES FOR DETERMINATION OF THE  
OXYGEN POTENTIAL IN IRRADIATED MIXED OXIDE FUELS

by

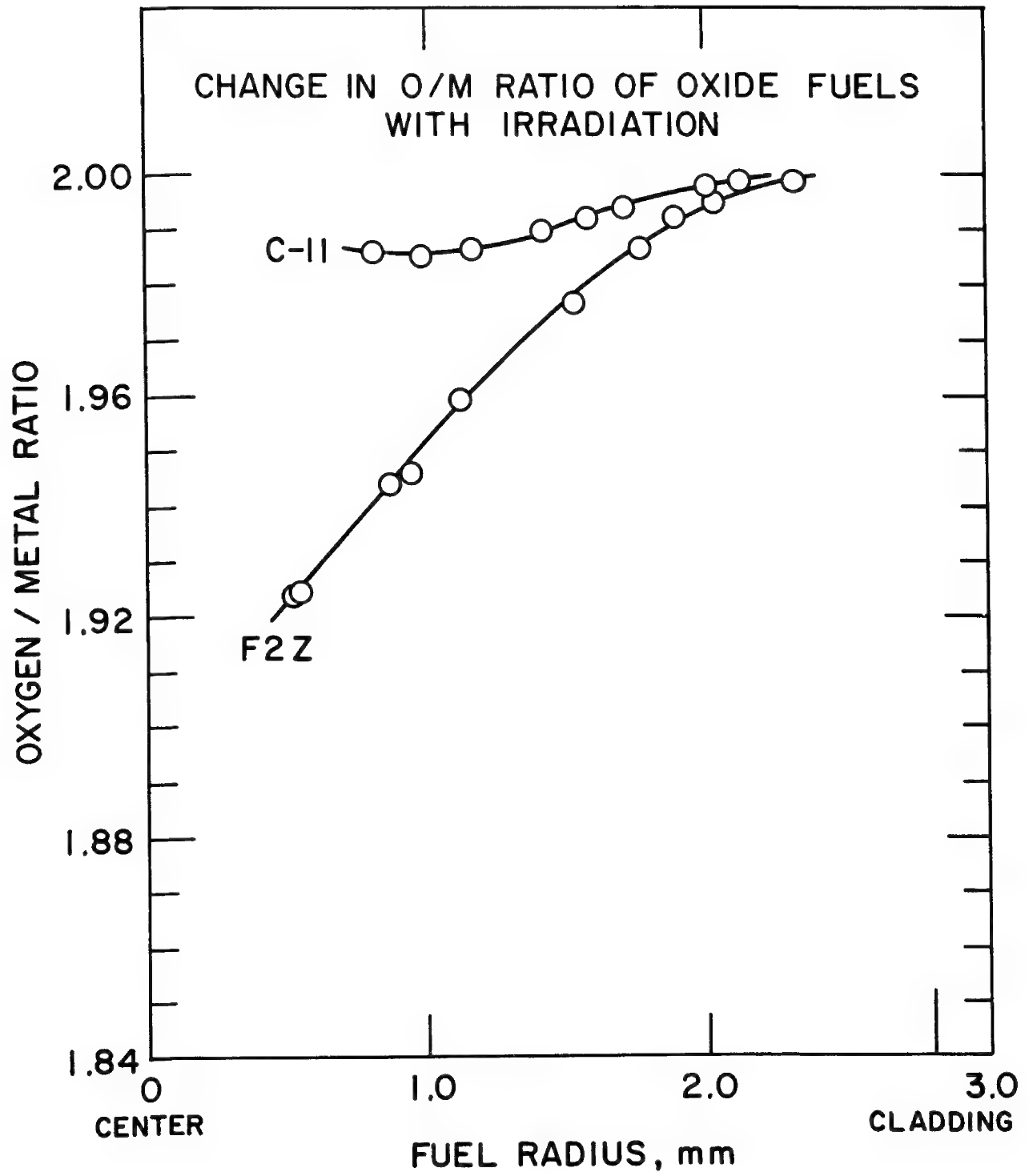
Carl E. Johnson, Charles A. Seils, and Melvin S. Foster  
Argonne National Laboratory, 9700 South Cass Avenue,  
Argonne, Illinois 60439

The migration of fission products in mixed (U,Pu) oxide fuel elements during irradiation at high temperatures has significant importance on the thermodynamic characteristics of the fuel. Electron microprobe analyses<sup>1,2,3</sup> of the characteristic metal inclusions found in irradiated fuels have reported these inclusions to be alloys of Mo, Te, Ru, Rh, Pd. Compositional data indicate that in many cases the molybdenum content is less than predicted from fission yield data. Fission of the fuel releases oxygen to the system. Thermodynamic data indicates that as a fuel becomes increasingly oxidized with fission, molybdenum will be oxidized and may in fact "buffer" the oxygen potential of the fuel while undergoing irradiation. If equilibrium conditions are assumed to exist in the fuel during irradiation between the molybdenum in the alloy and oxide phases then molybdenum may serve as a redox indicator and together with appropriate thermodynamic equations, be used to indicate the oxygen potential across the fuel radius.

The determination of low levels of fission product molybdenum in the mixed oxide fuel matrix by electron microprobe examination is a difficult task. The most reliable method involves a closely spaced point by point counting procedure across the Mo  $L_{\alpha}$  spectral peak to determine the maximum peak height and suitable background corrections. To perform such a task on a significant number of experimental data points by a manual procedure would be extremely tedious and inefficient of operator time. However, just such an approach is ideally suited to computer control of the microprobe. Our EPM utilizes a Canberra system interfaced to an 8K Varian 620/i computer with additional 123 K of disc storage. Spectrometer movement, data acquisition, and readout onto punched paper tape are controlled through a simple set of instructions entered through the teletype keyboard. Data reduction to net counting rate complete with an estimate of the standard deviation is accomplished by a "DISCOM" program which accepts as input the paper tape generated by the automated electron microprobe. Thus, a significant quantity of data may be accumulated and processed without resort to manual control.

This approach has been successfully applied to a series of fast reactor mixed oxide fuels. Typical of the type of data obtained are shown in Figure 1 where the oxygen to metal (O/M) ratio has been plotted as a function of fuel radius for two of the fuels studied. For a fuel which had a start of life O/M = 2.00 it is seen that a significant redistribution of oxygen has occurred. The effect of this oxygen migration on fission product redistribution, fuel swelling, and on cladding attack will be explored in greater detail.

1. Bramman, J. J., Sharpe, R. M., Thom, D., and Yates, C., J. Nuclear Materials **25**, 201 (1968).
2. O'Boyle, D. R., Brown, F. L., and Sanecki, J. E., Ibid. **29**, 27 (1969).
3. Stalica, N. R., and Seils, C. A., Proceedings American Ceramic Society, p. 215 (1969).



# INTERDIFFUSION BETWEEN URANIUM DIOXIDE AND URANIUM-PLUTONIUM DIOXIDE DURING IRRADIATION

by

*E. M. Butler, R. O. Meyer, and D. R. O'Boyle*

Argonne National Laboratory  
Argonne, Illinois 60439

Diffusion rates of uranium and plutonium in mixed-oxide fuels have a major influence on important processes in operating fuels such as restructuring, plasticity, and migration phenomena. Some diffusion measurements in  $(\text{U,Pu})\text{O}_2$  have been made,<sup>1-3</sup> but no systematic measurements of diffusion coefficients in irradiated mixed-oxide fuels have been reported. To understand and predict the in-pile behavior of fast-breeder-reactor nuclear fuels, irradiation-enhanced diffusion rates for uranium and plutonium in  $(\text{U,Pu})\text{O}_2$  fuels have been measured using a shielded electron microprobe.

The two fuel rods examined were irradiated in the Experimental Breeder Reactor II (EBR-II) at moderate power levels ( $\approx 13$  kW/ft) for 120 days (3.5 at.% burnup) and for 370 days (10.0 at.% burnup), respectively. These fuel rods were unique in that the upper half of each was fabricated from mixed-oxide  $(\text{U}_{0.8}\text{Pu}_{0.2})\text{O}_2$  fuel pellets and the lower half from  $\text{UO}_2$  fuel pellets. Since the uranium used in both types of pellets was fully enriched, the heat-generation rate was uniform in the region of the dissimilar oxide-fuel interface. This interface region thus formed an ideal diffusion couple, which was analyzed with the electron microprobe after irradiation. Moreover, since heat was removed from the surface of the fuel during irradiation, a steep radial temperature gradient existed in the fuel rod. Thus, in a single experiment, diffusion rates between  $\text{UO}_2$  and  $(\text{U,Pu})\text{O}_2$  were determined over a wide temperature range. The fuel-rod geometry, sectioning scheme, and range of temperatures for the samples analyzed are illustrated in Fig. 1. Numerous microprobe traces were taken perpendicular to the pellet interface, as indicated in the figure where two schematic traces are shown.

The sections analyzed were highly radioactive ( $\approx 50$  R/hr at 9 in.), and the examination was performed in a shielded electron microprobe (MAC-450).<sup>4</sup> The sample surface was polished with diamond abrasive in an alpha-gamma hot cell without further surface preparation prior to microprobe examination. The sufficiently

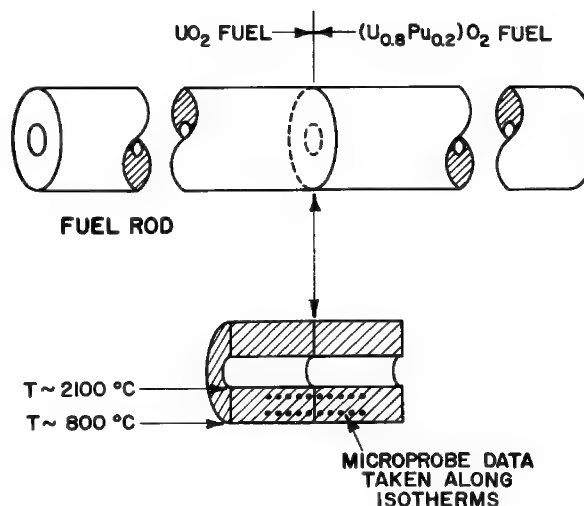


Fig. 1. Diagram of irradiated fuel rod, fabricated from  $\text{UO}_2$  and  $(\text{U,Pu})\text{O}_2$  fuel pellets, showing section examined by microprobe analysis.

high conductivities of the heavy metal oxides make conductive coating unnecessary, provided the specimen current was limited to 0.03  $\mu$ A. The width of the diffusion zones was large enough ( $>10 \mu$ ) so that no correction for the size of the X-ray volume was required. Intensities of the uranium  $M_{\alpha}$  and plutonium  $M_{\beta}$  X-rays were measured at 20 to 50 points along each isotherm. These intensities were compared with the intensities from pure  $UO_2$  and  $PuO_2$  standards, and ZAF and radioactive background corrections were made by means of the MAGRAM computer code.<sup>5</sup> Two concentration profiles across a specimen interface taken at different radial locations, which correspond to 1430 and 1865°C, are shown in Fig. 2.

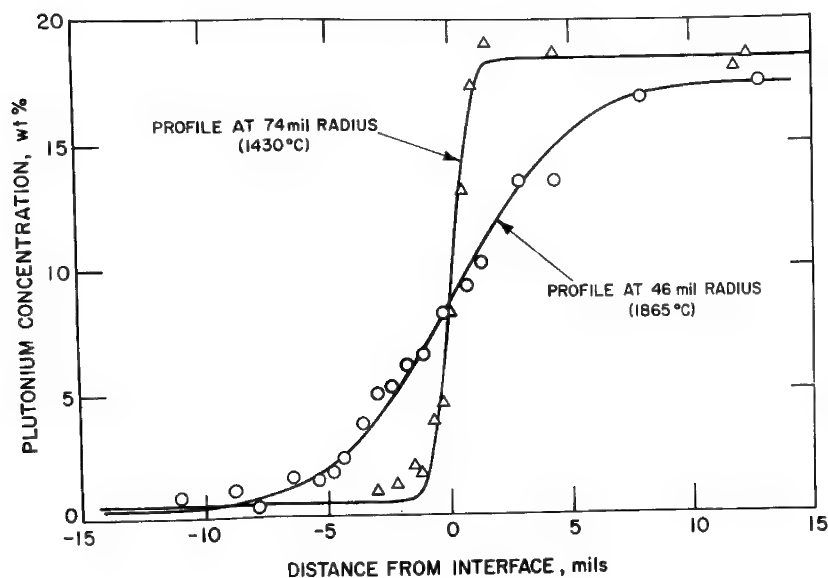


Fig. 2. Plutonium-concentration profiles measured perpendicular to the pellet interface at 1430 and 1865°C. Both profiles were measured on the same fuel rod that had been irradiated in a fast-neutron flux for 120 days.

An analysis of the concentration profiles for the diffusion-couple geometry indicated in Fig. 1 results in an interdiffusion coefficient,  $\tilde{D}$ . If this coefficient is independent of composition in the range from 0 to 20 wt % plutonia, the diffusion equations can be solved in closed form to yield the concentration in terms of a complementary error function.<sup>6</sup> Thus by plotting the concentration data on arithmetic probability paper, the data form a straight line.<sup>7</sup> The data shown in Fig. 2 have been replotted in this manner in Fig. 3, and the diffusion coefficients were calculated from the slopes of the straight lines. The annealing times and temperatures required to calculate the diffusion coefficients were

obtained by recording the reactor operating history and by using standard warm-up procedures<sup>6</sup> to account for temperature changes during irradiation. Temperatures as a function of radial position in the fuel were calculated by a method discussed previously.<sup>8</sup> For the concentration profiles shown in Figs. 2 and 3, the diffusion coefficients are

$$\tilde{D} = 4.9 \times 10^{-12} \text{ cm}^2/\text{sec} \quad T = 1865^\circ\text{C}$$

$$\tilde{D} = 1.3 \times 10^{-13} \text{ cm}^2/\text{sec} \quad T = 1430^\circ\text{C}.$$

The effects of temperature, general actinide redistribution,<sup>9</sup> radial diffusion, and temperature changes during restructuring will be discussed.

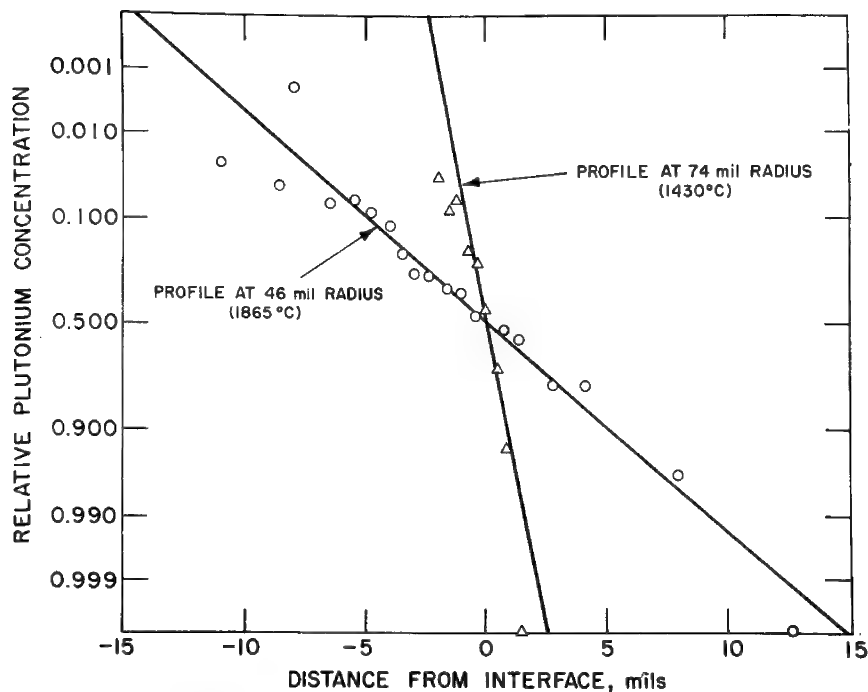


Fig. 3. Probability plots of the data presented in Fig. 2 showing relative plutonium concentrations as a function of distance from the dissimilar pellet interface.

#### REFERENCES

1. G. Riemer and H. L. Scherff, "Plutonium Diffusion in Hyperstoichiometric Mixed Uranium-Plutonium Dioxides," *J. Nucl. Mater.* **39**, 183 (1971).
2. R. Theisen and D. Vollath, "Plutonium Distribution and Diffusion in  $\text{UO}_2\text{-PuO}_2$  Ceramics" in *Plutonium as a Reactor Fuel* (IAEA, Vienna, 1967), p. 253.
3. R. Lindner, D. Reimann, and F. Schmitz, "Diffusion in Mixed U/Pu Oxides," in *Plutonium as a Reactor Fuel* (IAEA, Vienna, 1967), p. 265.
4. V. G. Macres, O. Preston, N. C. Yew, and R. Buchanan, "A Shielded X-Ray Microprobe for the Analysis of Radioactive Samples," *Vth Intern. Congress on X-ray Optics and Microanalysis* (Springer-Verlag, Berlin, 1969), p. 248.
5. R. Natesh, E. M. Butler, and D. R. O'Boyle, *MAGRAM--A Computer Code for Quantitative Electron-microprobe Analysis of Radioactive Materials*, USAEC Report ANL-7794 (Oct. 1971).
6. P. G. Shewmon, *Diffusion in Solids* (McGraw-Hill Book Co., N. Y., 1963).
7. W. A. Johnson, "Diffusion Experiments on a Gold-silver Alloy by Chemical and Radioactive Tracer Methods," *Trans. AIME* **174**, 331 (1942).
8. R. O. Meyer and B. J. Buescher, "A Simple Method of Calculating the Radial Temperature Distribution in a Mixed-oxide Fuel Element," *Nucl. Tech.* (to be published).
9. R. O. Meyer, E. M. Butler and D. R. O'Boyle, *Actinide Redistribution in Mixed-oxide Fuels Irradiated in a Fast Flux*, USAEC Report ANL-7929 (to be published).



MICROANALYSIS OF FISSION PRODUCTS  
IN URANIUM OR URANIUM-PLUTONIUM  
IRRADIATED OXIDES FUELS

by J. BAZIN M. PERROT  
N. VIGNESOULT  
C. CONTY and J. GUERNET

---

## 1 - Introduction

The COMMISSARIAT à l'ENERGIE ATOMIQUE uses microanalysis techniques for the examination of post-irradiated experimental fuels to be used in french industrial reactors. A shielded microprobe has been developed with the collaboration of the CAMECA Company and is in operation since January 1971.

From this date, several analysis have been completed on fuels consisting of Zircalloy clad enriched Uranium as well as on stainless-steel clad  $UO_2$  - Pu  $O_2$  mixed oxide.

We shall quickly describe below the instrument and the specimen preparation and then we shall give some results obtained on both above fuels.

## 2 - Specifications of the shielded probe

As the instrument has been already described in full details (1), we only give here its main features.

### 2.1 X-ray optics

X-rays are analysed by using 4 spectrometers with 7 monochromators allowing a wavelength range from 1.3 Å to 80 Å. All elements from B to Pu can then be analysed. Counting is achieved by 4 gas-flow proportional counters.

### 2.2 Design and efficiency of the biologic shielding

The shielding design allows a full protection of operators during analysis as well as during the insertion of specimens.

This shielding is made of 10 centimeter thick wall of lead or of an equivalent thickness of tungsten alloy as shown on fig. 1 and 2. The transfer cask, located at bottom, contains the specimen stage. This cask allows the specimen to be inserted in the probe after preparation in a preparation cell.

The circled numbers which can be seen on fig.2 are corresponding to estimations of radioactive intensity expressed in mRad per hour for a specimen of 4 Curies of .75 MeV located in the heart of the protection, all other parts of the probe being supposed removed.

During experiments it has been found out that, for a specimen of 10 Curies at . 75 MeV, the irradiation intensity on the shielding surface was less than 2.5 mRad/hour and was in the order of . 2 mRad/hour at the operator place.

With this specimen the radioactive background measured without electronic discrimination varies from 1,000 c/s with the counter as close as possible to the specimen to 70 c/s with the counter as far as possible of it.

### 3 - Specimen preparation

The specimens can be  $\alpha$   $\beta$   $\gamma$  emitters. First, they undergo a metallographic preparation, during which the specimen is impregnated and embodied in a heavy metal alloy which obstructs all open cracks. Then, it is mechanically polished by using liquids which do not dissolve fission products. After this preparation, which is followed by an observation with a microscope, the decontamination begins. This operation is made easier due to the impregnation with a metallic alloy which strengthens the specimen and allows ultra-sonic cleaning. Then, the cleaned specimen is placed on the Microprobe specimen stage. In case the specimen shows porosity it can be coated with a thin metallic film evaporated under vacuum. All the tests completed so far have shown that the above method is really effective and avoids specimen destruction or probe contamination.

### 4 - Examples of recent applications

#### 4.1 Molten fuels specimens

Several experimental irradiations have allowed Zircalloy clad  $\text{UO}_2$  fuels to be operated until burnup of about 60,000 MW day per ton with permanent central melting of the oxide (2).

We have studied, in these fuels :

- the repartition of the fission products insoluble in the matrix (alloys such as Rh-Ru-Mo-Pd-Tc in white metallic inclusions and U-Ba-Ce or Ba-Zr in grey phase).
- The nature of the layers touching each other between oxide and cladding material (a Zr-Cs layer close to the cladding material, then a layer consisting of Pd, Ba and Te, which is not an association of these 3 elements, and finally, close to the oxide, a layer which contains chiefly Ba).

The radial repartition of fission products, insoluble in the matrix, such as Zr and Mo, has been also investigated.

#### 4.2 Study of a clad failure ( $\text{UO}_2$ - Zircalloy)

One Zircalloy clad  $\text{UO}_2$  fuel has been irradiated one year long in a pressurized light water reactor with a fissure in the clad. The burnup reached is about 8,000 MW day per ton. The analysis of a zone close to the fissure has shown the local increase of oxygen in the oxide.

The curve on fig.3 shows the radial variation of the O/U ratio in this element as compared with the O/U ratio in a non-irradiated  $\text{UO}_2$  fuel. This investigation has shown the existence of Zirconium coming from both fission and corrosion on the fissure edge.

#### 4.3 High irradiation rates simulation in $UO_2$ - $PuO_2$ fuels

Fuels doped with fission products have been irradiated in order to simulate the thermic conditions in the reactor. The variation of fission products (Zr, Ce, Ba, Mo) has been investigated.

#### 4.4 Analysis of oxide-cladding material reactions in fuels for fast neutron reactors

Slices of steel clad  $UO_2$  -  $PuO_2$  fuels irradiated in the experimental reactor "SILOE" until burnup far higher than 100,000 MW day per ton have been investigated in order to determine the nature of the layers of reaction existing between oxide and cladding material.

Results are used when trying to understand the mechanism of these reactions.

### 5- Conclusion

After more than one year of experimentation, it can be said that our "hot" probe system works quite well. After very little improvements, the operation of our equipment is from the beginning troublefree and very easy, particularly from the standpoint of the maintenance as the way of preparing the specimens has allowed full elimination of all microprobe contamination.

Highly active fuels has been investigated. The analytical sensitivity is very close to the sensitivity which can be reached without radioactive background, and above application examples allow to appreciate the quality of the results.

### - BIBLIOGRAPHY

- (1) "Design and Experimental Results of a shielded electron probe Microanalyzer for highly radioactive specimens".  
by J. BAZIN, C. CONTY, J. GUERNET, E. ROUSSEL and N. VIGNESOULT.  
OSAKA X-Ray Optic and Microanalysis Conference - September 1971.
- (2) "Comportement des crayons Eau ordinaire en régime fondu".  
by G. de CONTENSON, N. VIGNESOULT and J. BAZIN.  
C.E.A. Report to be published.

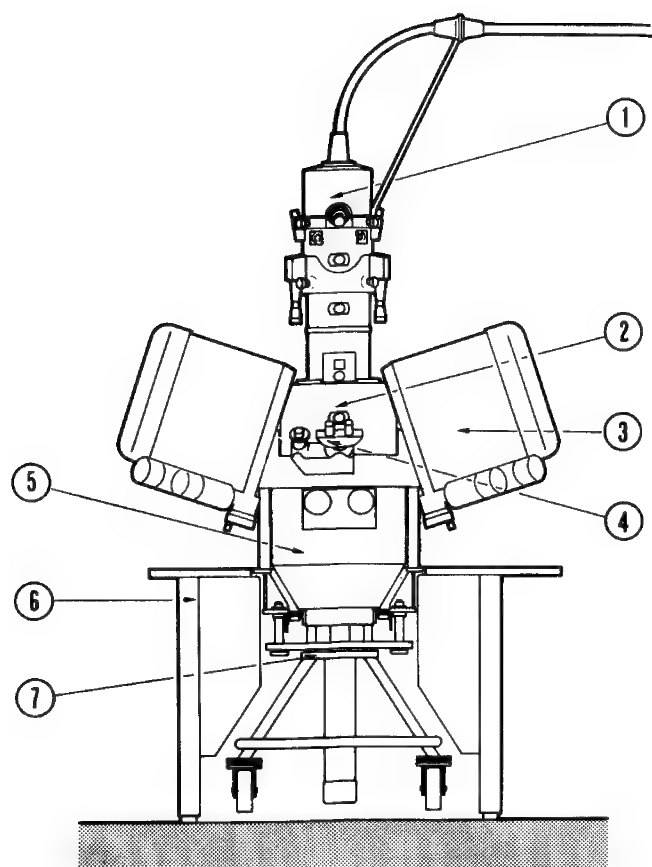


fig. 1

Front view of instrument

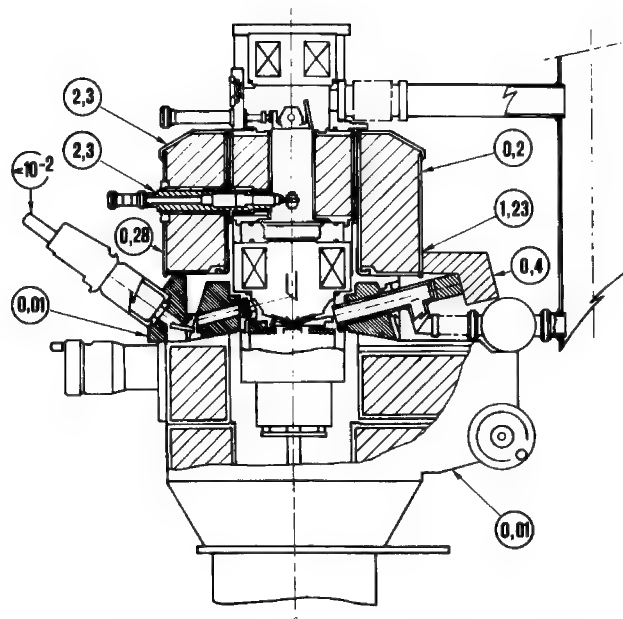
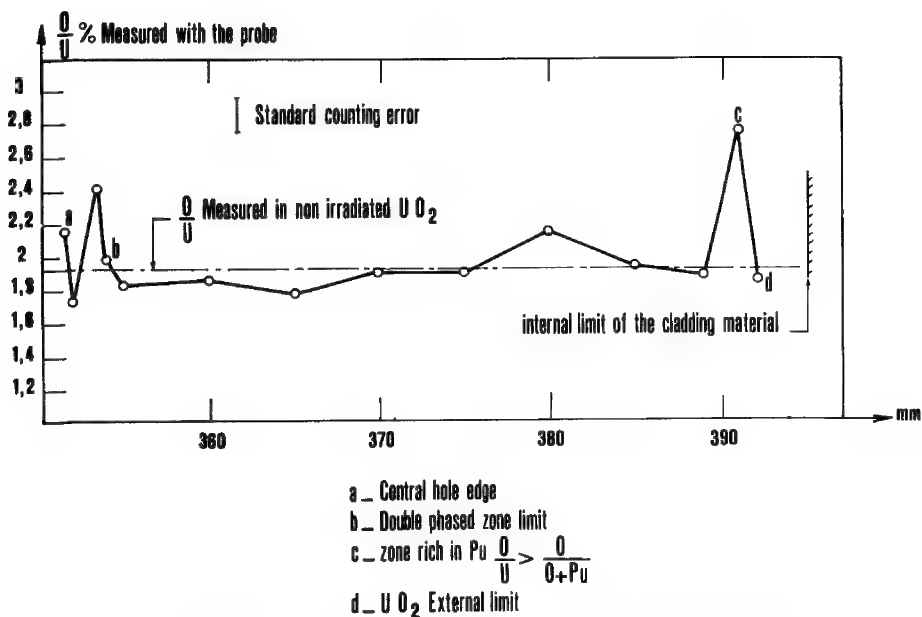


fig. 2 Cross section showing the accessories arrangement in the column and the sliding cover of the transfer cask.

fig. 3 Radial variation of O/U ratio in a zircalloy clad  $UO_2$  nuclear fuel broken during irradiation.

ELECTRON PROBE ANALYSIS OF CORRODED Cr-Ni ALLOYS IN COMBINATION  
WITH A LIGHT OPTICAL ZnSe INTERFERENCE METHOD.

A.P. von Rosenstiel      Metaalinstituut TNO, Delft / Holland  
A.G. van Zuilichem      Koninklijke/Shell-Laboratorium, Amsterdam,  
Holland

Severe corrosion was found in Incoloy 800 parts after having been in service in not combustion gas. According to the service conditions mentioned, sulphur was not involved in the corrosion process.

Preliminary investigation by microprobe analysis indicated a very complex structure. The phases present could neither be distinguished by chemical etching nor by backscatter electron imaging.

Instead of an elaborate and time consuming probe analysis for a great number of structure elements possibly present, the evaporized ZnSe interference layer (Pepperhoff method) was used revealing clearly all phases present.

Characteristic areas (interference colours) of the phases present could easily be recognized under the light optics of the microprobe which were subsequently analysed.

In the heavily corroded Incoloy large corrosion attacked areas within the base material as well as intercrystalline corrosion products were observed. In total more than 9 different phases were identified in the corrosion layer.

In the completely corroded outer parts of the sample (fig. 1) only oxides (Cr-Fe-oxides) were analysed. In a zone between oxide layer and the base material more or less irregularly shaped Ni-(Fe)-sulphides are present. Besides very complex oxides and oxisulphides, containing Cr, Ti, Mn and Si in varying quantities were detected in this zone.

From the corrosion zone penetrating into the base metal similar corrosion products were detected on the grain boundaries: Ni-(Fe)-sulphides at the tip of the grain boundaries, Cr-Fe-oxides and complex oxides and oxisulphides. In front of this corrosion zone along the grain boundaries, decarburisation of the base metal was observed. At the tip of the corroded grain boundaries within the non-affected base material only sulphides were analysed.

In the corroded base material (see fig. 2 and 3) a more complex composition of corrosion products can be recognized. The colour photographs show two colour groups: in all the bluish phases Ni is more or less dominating, in the purple phases Cr is the main component. Except for the bright blue Ni-Fe-matrix all these phases were sulphides.

The Pepperhoff technique in this case greatly contributed to the microprobe analysis, firstly by an indication of the number of phases present in the corrosion layer, and secondly in facilitating the area to be analysed for the identification of each phase.

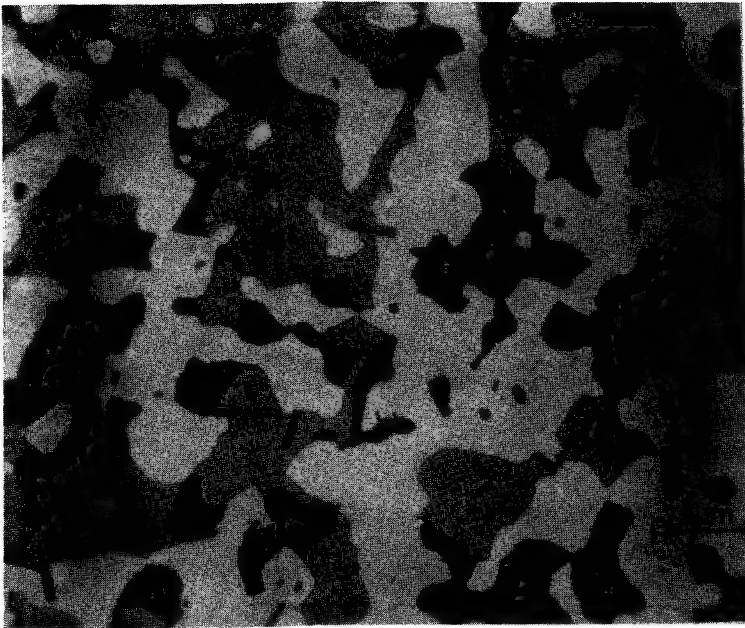


Fig. 1

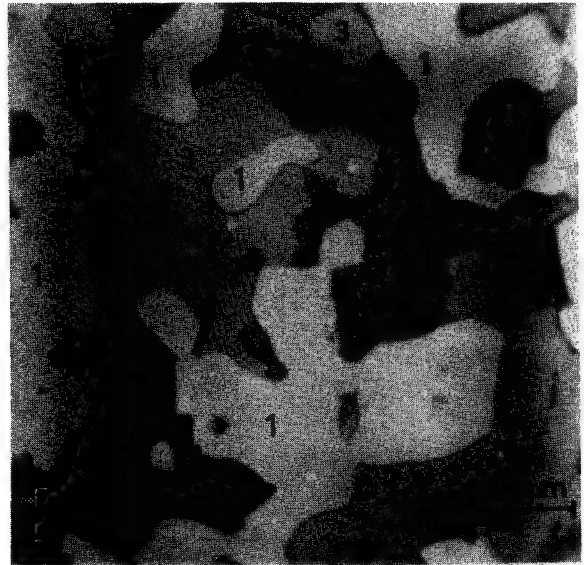


Fig. 1a

- 1 = Ni-Fe-matrix
- 2 = Cr-(Ni)-Ti-S
- 3 = Cr<sub>2</sub>Mn-(Fe)-S
- 4 = Nb-Ni-(Cr)-S

Fig. 1a



EL+



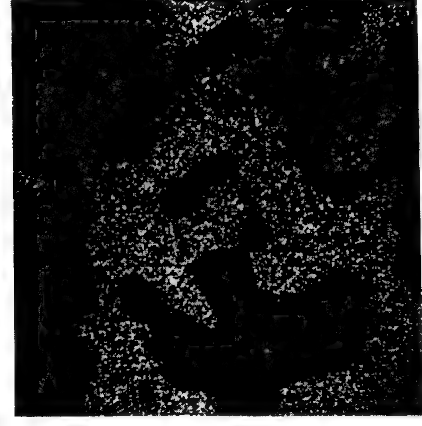
Cr



Ni



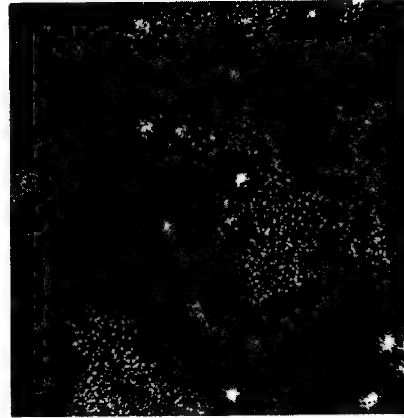
Mn



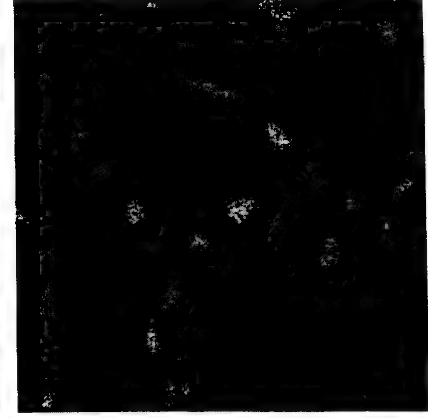
S



Fe



Ti



Nb

Fig. 2

- 1 = Ni-Fe
- 2 = Cr-Fe-Mn-S
- 3 = Ni-S-(Ni<sub>2</sub>S<sub>3</sub>)
- 4 = Ni-Fe-S
- 5 = Ni-Ti-Fe-(Cr)-S

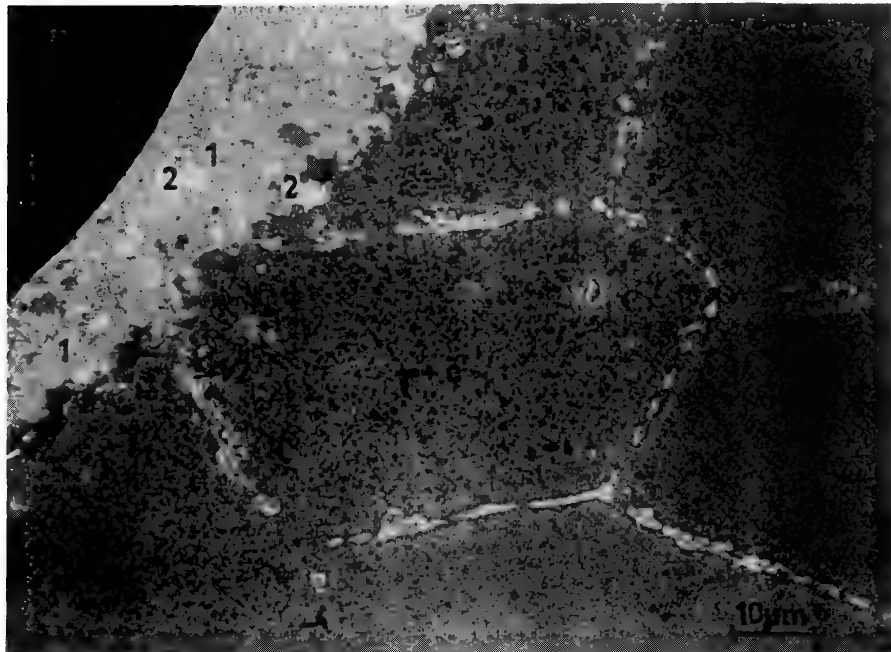
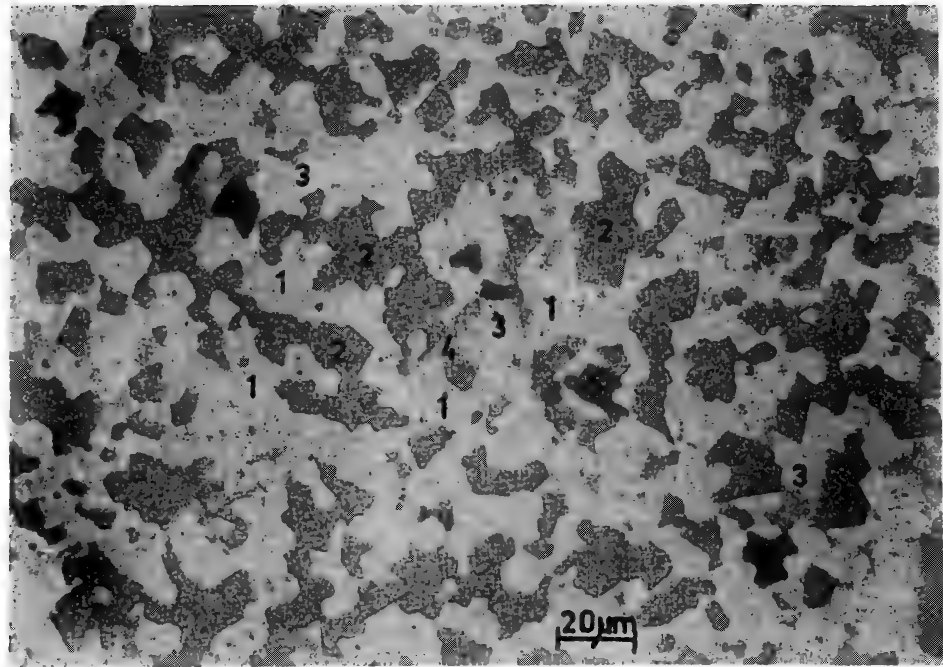
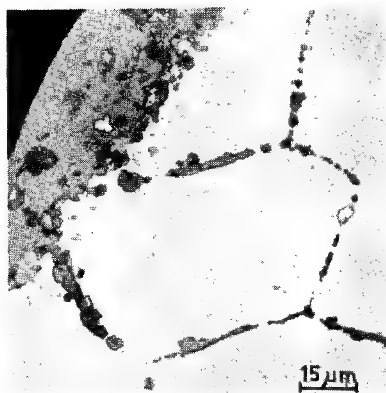


Fig. 3

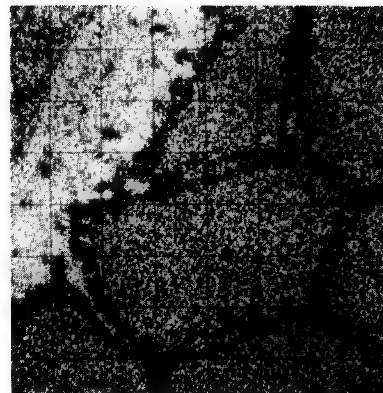
- 1 = Cr-Fe-O
- 2 = Ni-Fe-S
- 3 = Ni-S (Ni<sub>2</sub>S<sub>3</sub>)
- 4 = Cr-S
- γ + c = austenite + carbides



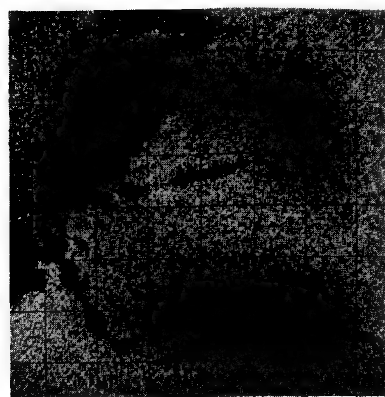
Fig. 3a



EL-



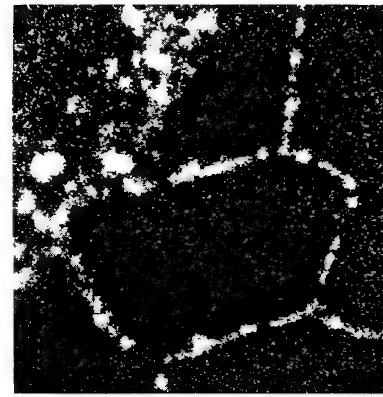
Cr



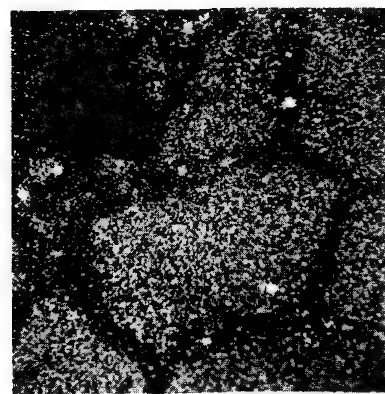
Fe



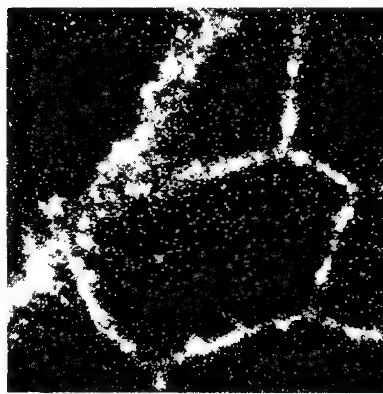
Ni



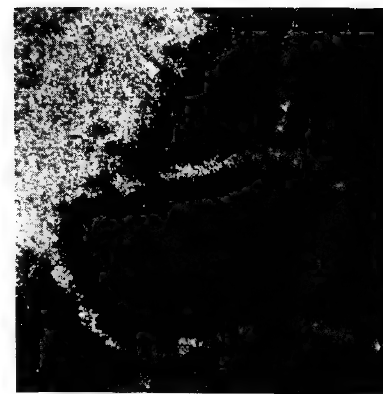
Al



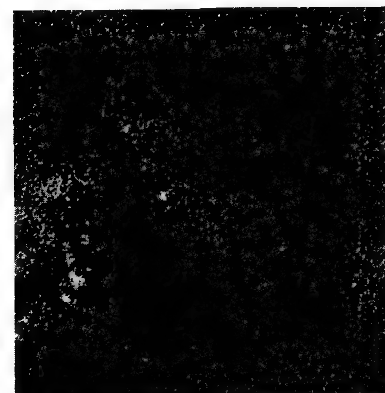
C



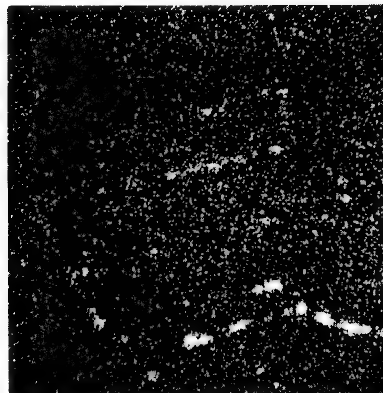
S



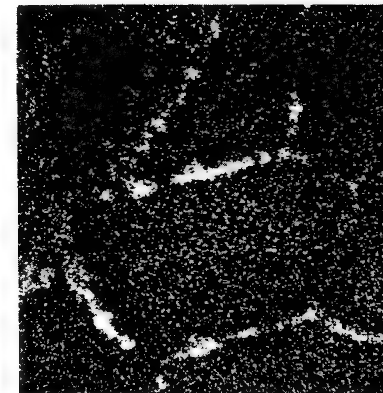
O



Mn



Ti



Si

## BONDING IN PORCELAIN ENAMEL-METAL SYSTEMS\*

J. B. Woodhouse and A. I. Nedeljkovic

Materials Research Laboratory  
University of Illinois, Urbana, Illinois 61801

Porcelain enamels containing CoO, NiO and some other oxides develop good bonds when applied to a Ni-flashed low carbon steel, while the enamels without these oxides and steels without the Ni-flash perform poorly. Although these systems have been the subject of extensive microscopic and x-ray diffraction studies, the bonding mechanism is not well understood. In general, it is agreed that an intermediate layer, formed during firing, is of great significance and studies of its microstructure and microchemistry are essential to the understanding of the adhesion of the enamel to the metal.

Boron and Pask (1) studied the bonding of CoO containing enamel to Armco iron and attributed the good adhesion found in that system to the concentration of cobalt occurring in a dendritic growth at the interface, a discovery made by means of the electron probe microanalyser. Microanalysis was the tool again, in the study of the adhesion of enamels to aluminum by Gugeler (2) and Baker (3). These latter authors pointed out that Al plated with Cr was strongly bonded to the enamel, while aluminum alloys containing magnesium exhibited poor adhesion due to the formation of a magnesium rich layer at or near the interface.

In the present work, porcelain enamels containing NiO, CoO, TiO<sub>2</sub> and MoO<sub>3</sub> were applied to low carbon steel and to such steel coated with a flash of nickel (about 1 gm per m<sup>2</sup>) and fired for 5 minutes at temperatures in the range of 1100°F to 1700°F. The percentages of the oxides added to the "base composition" (Na<sub>2</sub>O, B<sub>2</sub>O<sub>3</sub>, 3SiO<sub>2</sub>) were those commonly used in the production of commercial enamels. After firing, the adhesion was tested by a standard falling weight test. The microstructures were then examined in a scanning electron microscope, equipped with an energy dispersive spectrometer, by electron probe microanalysis, optical microscopy and x-ray diffraction.

Enamels containing 2% NiO gave poor adhesion to low carbon steel when the firing temperature was 1500°F or below. At 1600°F, the adhesion improved and at this temperature, evidence was found from microanalysis for a nickel rich layer at the interface between the enamel and the metal. Nickel has a lower oxidation potential than iron and the reduction of NiO during firing and precipitation of nickel at the interface are thermodynamically possible and, in fact demonstrated here. X-ray diffraction of the interface material revealed that a portion of the nickel was precipitated out to form a nickel - iron alloy.

---

\*This research was supported in part by the U. S. Atomic Energy Commission under Contract AT(11-1)-1198.

A flash of metallic nickel, deposited on the steel prior to its enameling, improved the adhesion considerably, and was a more effective promoter of adhesion than the oxide additive to the enamel. The techniques used in this study showed that the nickel in sample fired at temperatures from 1100°F to 1700°F remains at the interface and does not diffuse away, although, it does tend to alloy with the iron at the higher firing temperatures. A decrease in the adhesion at these higher temperatures seems to accompany this alloying.

In all these firings it was noticed that iron diffuses out into the enamel, the higher the temperature the longer the range of the diffusion. However, this diffusion was greater by about 50% in the specimens with the nickel flash. The nickel layer acts as a barrier to the diffusion of iron resulting in the preferential formation of the higher oxides of iron at the interface which higher oxides dissolve at a higher rate in the enamel than FeO. The diffusion profiles for iron in the samples having good adhesion are characterised by their ranges (20 to 40 microns) and by the relatively high concentration of iron found at the interface. Iron diffuses into the enamel in an ionic form and it is essential to a good bond to have it in the form of the  $\text{Fe}^{++}$  ion. In samples fired at temperatures higher than 1600°F diffusion of iron increased, the maximum value at the interface decreased and the adhesion deteriorated.

In the case of the enamel with additions of  $\text{TiO}_2$  fired onto nickel flashed steels, it recrystallised at temperatures in excess of 1400°F, at 1300°F titanium was uniformly distributed through the enamel without any indication of diffusion towards the interface. At 1500°F, microanalysis revealed a build up of titanium at the interface as well as the formation of titanium rich particles in the enamel due to the recrystallisation of the enamel. The concentration at the interface was found to be associated with the formation of a needle like crystalline structure of iron titanate ( $\text{FeO} \cdot \text{TiO}_2$ ). The recrystallised zone in the enamel contained  $\text{TiO}_2$  in the form of anatase at temperatures around 1500°F and rutile at 1700°F. The amount of iron titanate at 1700°F seemed to decrease and this was accompanied by a loss of adhesion.

#### References

1. Borom, M. P., Pask, J. A. J. Am. Ceram. Soc. 49, 1-6 (1966)
2. Gugeler, A. L., Proc. of P.E.I. Forum 29, 202-8 (1967)
3. Baker, M. A., Proc. of P.E.I. Forum 32, 48-51 (1970)

## LOCATION AND IDENTIFICATION OF SMALL PARTICLES WITHIN LARGE SAMPLES

J. Gavrilovic

Walter C. McCrone Associates, Inc., Chicago, Ill.

Air pollution samples, which are usually collected on a Millipore type filter, consist of large numbers of particles in the 20-30  $\mu\text{m}$  size range but range to submicrometer size particles. A majority of the particles present are common dusts consisting of particles such as calcium carbonate, quartz, other numerous silicates, various combustion products, and a variety of organic fragments of biological origin. In such samples, both location and analysis of a specific phase is often necessary, for example, lead compounds, asbestos, and fragments of various metals.

The finding and/or location of such particles is usually performed, using optical techniques, by scanning large numbers of particles under an optical microscope and identifying a specific particle or phase by its optical characteristics. However, optical techniques are limited and in two cases, inadequate: first, when a phase is optically indistinguishable from the other phases and second, when the phase is not optically distinct and is present in very low quantities. In both of these cases, techniques other than optical microscopy have to be applied. Among these, the electron microprobe is the most powerful analytical tool.

The three methods used in our laboratory for locating and analyzing such particles are: one, the manual scanning of an area with the electron beam; two, the photographic technique; and three, a completely automated electron microprobe. One of the steps essential to locating a specific phase within a large sample is sample preparation. It is necessary to insure the presence of the desired phase in the sample presented for probe analysis. One of the best methods is by spreading a large number of small particles on a low-atomic number substrate such as polished beryllium. The sample, on the beryllium, must be well enough dispersed so that no clustering or overlapping of particles occurs; but the particle density per unit surface area must be high enough to insure that the amount of time required to locate a specific phase is kept to a minimum.

Manual scanning - If the desired phase is present within the sample in quantities of the order of 0.2 - 0.5%, then the fastest way to locate them is to preset the spectrometer or spectrometers for a particular element or elements and scan an area with the electron beam to observe when the signal (x-ray intensity) from the spectrometer becomes very intense.

Photographic method - If the desired phase is present in quantities, which are well below the 0.5 - 0.2% range, down to a few hundred parts per million, then the manual approach becomes too laborious and the photographic technique is used to more efficiently produce the same results. This technique is based on a prolonged exposure (15 to 30 minutes) picture of an area with a large number of particles. The resulting x-ray photograph will reveal a concentration of a specific element within a single particle or sample. For example, in an area where the population density is one particle per every 36 square micrometers, an area of 300 x 300 micrometers will contain 2,500 particles. Therefore, a single exposure of 20 minutes will be in effect equal to the analysis of 2,500 particles for one element.

Automated electron microprobe - If the proportion of a phase within a sample is below 100 parts per million, the photographic approach becomes inefficient since the probability of one particle being in a photographed area becomes remote. Therefore a computer-operated probe becomes a necessity. Within our laboratories we have a completely automated electron microprobe. This has been accomplished by interfacing the probe to a Digital Equipment Corporation PDP-15/30 computer. Programs have been developed by which a beryllium substrate, dispersed with small particles, is traversed under the stationary electron beam while the x-ray spectrometers are set for specific combinations of elements. Every time a particle which contains this specific combination of elements comes under the beam, the stage stops and the x-ray spectrometers are automatically moved to cover the entire range of elements, ultimately producing a complete analysis of a desired particle. To insure that the particle of a specific phase is in a sample, an equation, based on a 98% probability, following a Poisson distribution, can be applied:

$$N_{\min} = \frac{400}{K_A}$$

where  $N_{\min}$  is the minimum number of particles in a sample which will contain one particle of phase A,

$K_A$  is the number of particles of phase A per every 100 or % of phase A.

As an example, in an air pollution sample, an automated search was performed for lead compounds with a sample which had only 50 parts per million of lead. After 48 hours, 15 lead-containing particles were found and analyzed. In another case, a sample of small particles containing a small proportion of asbestos fibers was analyzed. The x-ray photographic technique revealed magnesium silicate fibers, some of which were subsequently identified by optical methods as asbestos fibers.

MEASUREMENT AND ANALYSIS OF SCANNING  
ELECTRON MICROSCOPE IMAGES

Roger R.A. Morton  
Bausch & Lomb Incorporated  
Rochester, N.Y.

Instrumentation to measure and analyze the images generated by optical microscopes has been available for some years. However, it is only recently that it has been possible to perform the image analysis directly from images generated by electron scanning microscopes and electron probes.

In general image analysis systems detect features having a predetermined density or gray level in the image, determine the boundaries of these features, and perform a variety of counts and measurements on the detected features. Some of the measurements which may be performed are shown in figure 1 and figure 2 shows some of the types of counts which may be performed. In addition, area measurements such as total area, area including holes, area excluding holes are available, as well as intercept distribution, free path distributions, and number of features larger than a given size.

Consequently, image analysis of electron beam microscope generated images adds a variety of new measurements and capabilities to these already versatile instruments. For example, it is possible to perform measurements of the number of features larger than a given size, or the longest dimension of any feature in 100 milliseconds using the Bausch & Lomb QMS system.

Most of the available measurements are either count, length, or area measurements on a two-dimensional image. These results may be processed using one of a number of different types of data processing techniques available with the QMS to provide derived information which may relate more directly to the specimen characteristics. Examples of these derived results are surface area of embedded features, volume of specific constituents, the isometry of the material, and size distributions of embedded grains, and so on.

The basic technique used to generate these measurements is real time digital analysis of the binary signal which defines the boundaries of the features. This signal is derived by processing a video signal generated repeatedly by reading at high speed a stored image derived from the image created by the electron beam microscope.

The storage step is employed because the scan rate of the electron beam microscope is substantially slower than the speed at which the image analysis system can process the image. This discrepancy in the speed of the two systems is very large in the case of X-ray analysis. However, even for secondary electron images a considerable discrepancy may arise if the electron beam microscope is to generate video signals having the high signal-to-noise ratio required for accurate image analysis.

The scan rate of an electron probe may vary over an exceptionally wide range. The extreme values being from 60 frames per second to 1 frame every 30 minutes, and with a number of lines varying from 250 to 1500. To store an image generated within this wide range formats involves a number of novel techniques.

The image is stored by sampling approximately 1-million points over the field. Depending on the frame rate, these sampling points may occur from 30-million per second to 50 per second. The sampling process therefore requires that the noise bandwidth of the signal in excess of the sampling rate be restricted to be compatible with the sampling bandwidth. The bandwidth reduction is implemented using a digitally controlled wide bandwidth filter prior to the sampling operation necessary for storage. Virtually no signal information is lost in this filtering process because the large number of sampling points ensures that the signal bandwidth does not exceed the sampling bandwidth.

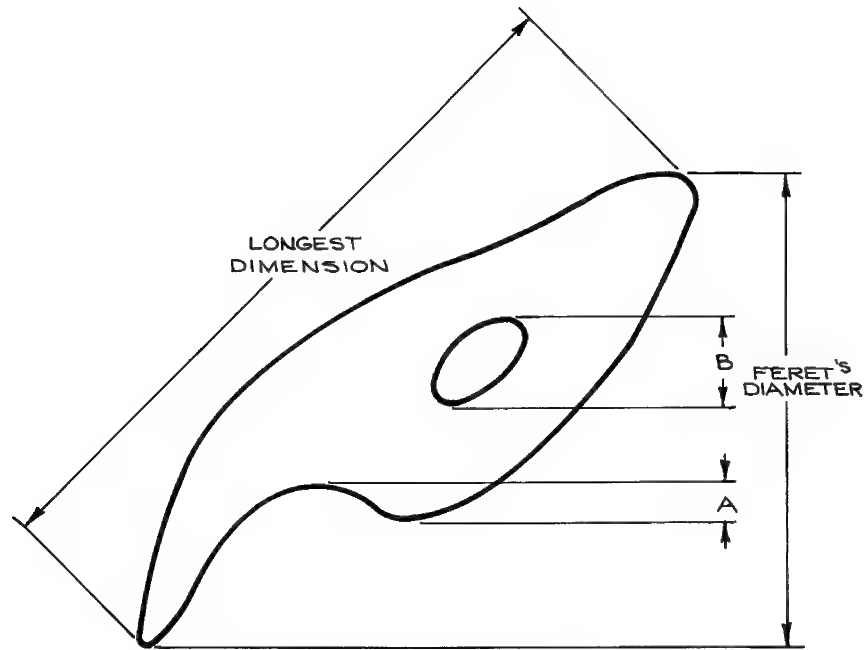
Another requirement in storing the image is that the storage system be able to compensate for non-linearities which may be inherent in the sweep generators and amplifiers of the electron probe. The image storage system compensates for these non-linearities by storing the video signal of each sampling point, at a location determined by the amplitude of the X and Y sweep.

To operate the storage system, the operator presses a button and the next vertical sweep of the electron probe is stored. Immediately the storage is completed, the storage system goes into the read mode and an image appears on the QMS display at a high scan rate. This image is now available for image analysis by the operator, independent of the electron probe. Successive images may also be laid on top of each other and added or subtracted from each other.

#### FIGURE CAPTIONS

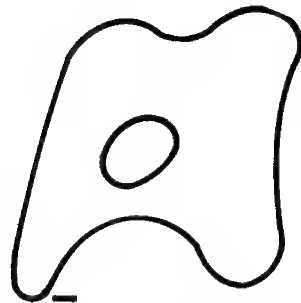
Figure 1. Examples of linear measurements available with the Bausch & Lomb QMS.

Figure 2. Some of the types of counts available.

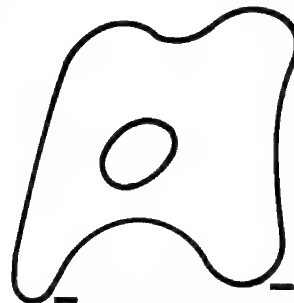


$$\text{PROJECTED LENGTH} = A + B + \text{FERET'S DIAMETER}$$

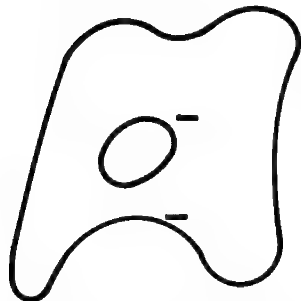
FIGURE #1



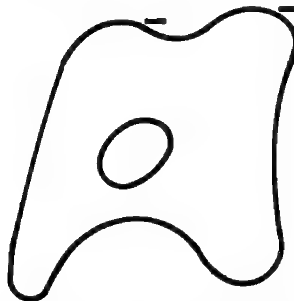
(a) PARTICLE COUNT



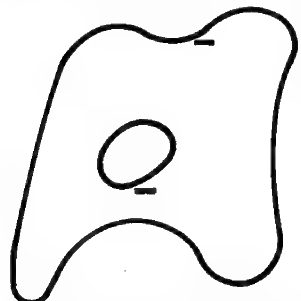
(b) LOWER POSITIVE TANGENT OR ENDPOINT COUNT



(c) LOWER NEGATIVE TANGENT



(d) UPPER POSITIVE TANGENT



(e) UPPER NEGATIVE TANGENT

FIGURE #2



Quantitation of SEM and Electron Probe Images  
with the Quantimet 720

R.A. Swenson, B.C. Partridge and  
R.H. Heil

Quantitative image analysis techniques which were developed for optical microscope images have since been applied to many other fields. One of the most recent applications has been in the field of Electron Probe images. At the same time, new techniques have been introduced which permit methods of feature classification to be performed which are not possible for other types of image producing devices. The electron probe makes good use of image analysis since the techniques allow simultaneous processing of many probe signals, including X-ray signals for which processing rates may be used up to 1000 times faster than the usual photon limit suggests.

The image analysis system utilizes digital scan drive circuitry to orthogonally scan the specimen. Precise differential and integral linearity is maintained throughout the resulting matrix of over 600,000 data prints. This factor lends itself ideally to SEM and microprobe image analysis, since this circuitry feeds from an image, requiring successive scans. It is essential to have positional reproducibility to accurately relate all data to respective features.

One important recent Quantimet innovation in feature counting is the separation of the signal which defines the outline of the feature and the signal which defines the parameters by which it is to be classified. These signals may be derived from one video signal, e.g. cells whose outline is defined by a detected grey level and characterized by the area of their nuclei defined by another grey level. If an SEM is being used, the two signals may be derived from two video signals which are obtained from the specimen simultaneously. It is this technique which is the basis of the pattern recognition facilities now being developed. As a feature is scanned, associated parameters (A.P.'s) are computed and carried down the A.P. locus which follows the feature outline to the counting point (Fig. 1). The accumulated A.P.'s are released at the counting point and the feature may be identified by these parameters.

Typical parameters which may be used for classification are area, perimeter, height and width. They may be used either in themselves, e.g. for a size distribution in terms of feature area, or in combination as form factors, e.g.  $\text{Area/Perimeter}^2$  for segregating different shapes (Fig. 3).

An important development of density classification is for x-ray signals on SEM's and micro-analysers, where the third dimension is the number of x-ray pulses per picture point and the classifying parameter is X-ray density. The signal defining the feature outline is a video signal obtained simultaneously, e.g. a specimen current signal. Features may be classified according to their composition, identified by characteristic X-radiation at speeds much higher than those normally associated with X-ray images. This is because if an X-ray image is being analysed alone, it must be used as a video signal where different

features are characterized by grey levels. This means that the scan speed must be slow enough to give typically one hundred pulses per picture point to build up a sensibly noise-free image. If, however, the feature outline is defined by another video signal, it may be classified by the X-ray density over the whole feature, (Figs. 1 and 2), and since the feature area will normally be thousands of picture points less than one pulse per picture point will be enough to give statistically the "correct" density over the whole feature giving a potential speed increase of 1000 times.

#### References

1. Roberts, F. & Young, J.Z. Proc. Inst. Elect. Engrs. 1956, 99, III A, 747.
2. Braggins, D.W., Gibbard, D.W., Gardner, G.M. "The Application of Image Analysis Techniques to Scanning Electron Microscopy". SEM/1971 Proc. 4th Annual SEM Symposium, I.I.T. Research Inst. 1971.
3. Fischer, C. "The New Quantimet 720". The Microscope, Vol. 19, Jan. 1971, 1-20.
4. Fischer, C. "The Quantimet, Setting the Threshold and the Correction of Offset Threshold Errors". Practical Metallography, Vol. 6, 11, 1969, 659-671.
5. Cole, M. "Instrument Errors in Quantitative Image Analysis", The Microscope, Vol. 19, Jan. 1971, 87-103.

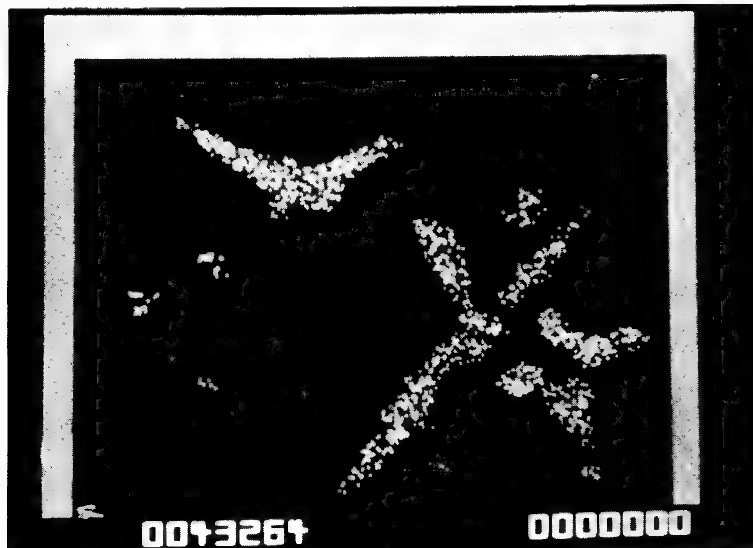


Figure 1

Gated X-ray counts for copper inclusions in a copper silver composition showing copper rich areas. The specimen current signal is used to define the features of interest and in which the X-ray count is desired. This photograph obtained directly from a microprobe analyser shows how background can be eliminated since only X-ray counts occurring within the boundaries of the features are considered. Each picture point can contain up to 7 X-ray counts. The total count is shown in the digital display.



Figure 2

The same specimens as shown in Figure 1. The matrix background area in this case has been defined as the "region of interest" and only x-ray counts not occurring within the boundaries of the features are considered. Note the X-ray count.

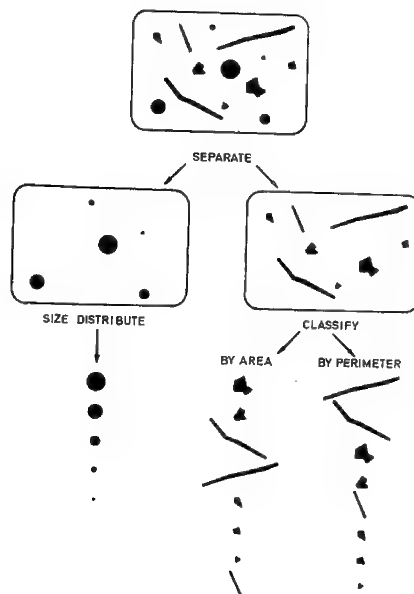


Figure 3

In a field containing a mixture of feature shapes, pattern recognition criteria may be used to select features on basis of their form. Area/Perimeter<sup>2</sup> has been used in this example to select only circles. A size distribution can then be performed on the separated features.

## ELECTRON MICROPROBE AUTOMATION: X-ray Peak Location

by

F. Kunz and E. Eichen  
 Ford Motor Company, Dearborn, Michigan

With the exception of X-ray spectra studies pertaining to peak shifts due to chemical bonding effects(1-2), the general shape of the electron microprobe X-ray peaks has been of little concern to the analyst. However, recent advances in electron microprobe automation has brought about the need for algorithms so on-line computers can be programmed to automatically detect and position the spectrometers to the wavelengths of maximum intensity. As previously reported(3-4), X-ray peaks have been automatically located by retrieving the theoretical wavelength from a stored table of wavelengths (K $\alpha$ , L $\alpha$ , M $\alpha$ ) or calculating the theoretical wavelength, correcting for spectrometer mechanical backlash, and moving the spectrometer 0.02 angstroms above the theoretical value. The spectrometer is then moved in 0.0002 angstrom steps across the peak recording the intensity and wavelength at each step. The maximum intensity is determined by the computer and its corresponding wavelength is assumed to be the peak location. Although this method is suitable for peak location, in actual practice computer core memory is used inefficiently and too much time is required (normally, 100 seconds for 200 steps). This paper describes an alternate method which reduces the total time from 100 seconds to just under 10 seconds without any appreciable loss in accuracy.

The method consists of obtaining X-ray intensities at three equally spaced wavelengths as shown in Figure 1 which are used to form three lorentzian(5) equations (Equations 1, 2 and 3) and solved simultaneously for the peak wavelength (Equation 4).

$$I_1 = I_p \left[ 1 + \frac{4(\lambda_1 - \lambda_p)^2}{W^2} \right]^{-1} \quad (1)$$

$$I_2 = I_p \left[ 1 + \frac{4(\lambda_1 - \Delta\lambda - \lambda_p)^2}{W^2} \right]^{-1} \quad (2)$$

$$I_3 = I_p \left[ 1 + \frac{4(\lambda_1 - 2\Delta\lambda - \lambda_p)^2}{W^2} \right]^{-1} \quad (3)$$

$$\lambda_p = \lambda_1 - \frac{\Delta\lambda}{2} - \frac{\Delta\lambda}{\frac{I_1(I_3 - I_2)}{1 + \frac{I_3(I_1 - I_2)}{I_1(I_3 - I_2)}}} \quad (4)$$

where

$I_p$  = peak intensity

$\lambda_p$  = peak wavelength

W = full width half maximum

The use of the lorentzian to describe electron microprobe X-ray peaks has been reported previously by Colby(6). Alternate methods employing the three point parabola or gaussian can also be applied. The initial calculation uses the stored or calculated theoretical wavelength as the second wavelength, whereas, in subsequent iterations the calculated peak wavelength is used as the second value. In practice, three iterations (9 X-ray intensities) are sufficient to locate the peak. During the first iteration,  $\Delta\lambda$  is set equal to  $0.5 \times \text{FWHM}$  (75% maximum intensity) where FWHM (full width half maximum) was determined empirically prior to the calculation. The method of using the calculated peak wavelength in successive iterations has been previously applied by Wilson(7).  $\Delta\lambda$  is reduced by one-half in each iteration. Appropriate safeguards are written into the computer program so that if spurious counts are recorded and the peak is calculated erroneously, the program will be resequenced. The statistical error due to random counting statistics can be calculated, however, comparison of the calculated peak and the peak obtained by stepping indicates reproducibility to within  $\pm 0.0002$  angstroms.

- 
1. Baun, W. and Solomon, J., "Characterization of SiO Using Fine Features of X-ray K Emission Spectra", in Proceedings Sixth National Conference on Electron Probe Analysis, Pittsburgh, Penn., 1971.
  2. Baun, W. and Solomon, J., "Chemical Bonding Studies on Boron Interstitial Compounds", in Proceedings Sixth National Conference on Electron Probe Analysis, Pittsburgh, Penn., 1971.
  3. Kunz, F., Eichen, E., Matthews, G., and Piner, S., "Electron Microprobe Automation", in Proceedings Sixth National Conference on Electron Probe Analysis, Pittsburgh, Penn., 1971.
  4. Kunz, F., Eichen, E., Matthews, G., and Francis, J., "An Automated Electron Microprobe System", to be published in Vol 15, Advances in X-ray Analysis, 1972.
  5. Yap, F. Y., "Statistical Error Analysis of Wavelength Criteria for X-ray and Gamma Ray Spectra", Ph.D. thesis, John Hopkins University, Baltimore, 1967.
  6. Colby, J., presented during tutorial session at Sixth National Conference on Electron Probe Analysis, Pittsburgh, Penn., 1972.
  7. Wilson, A.J.C., "The Location of Peaks", Brit. J. Appl. Phys. 16, p. 667.

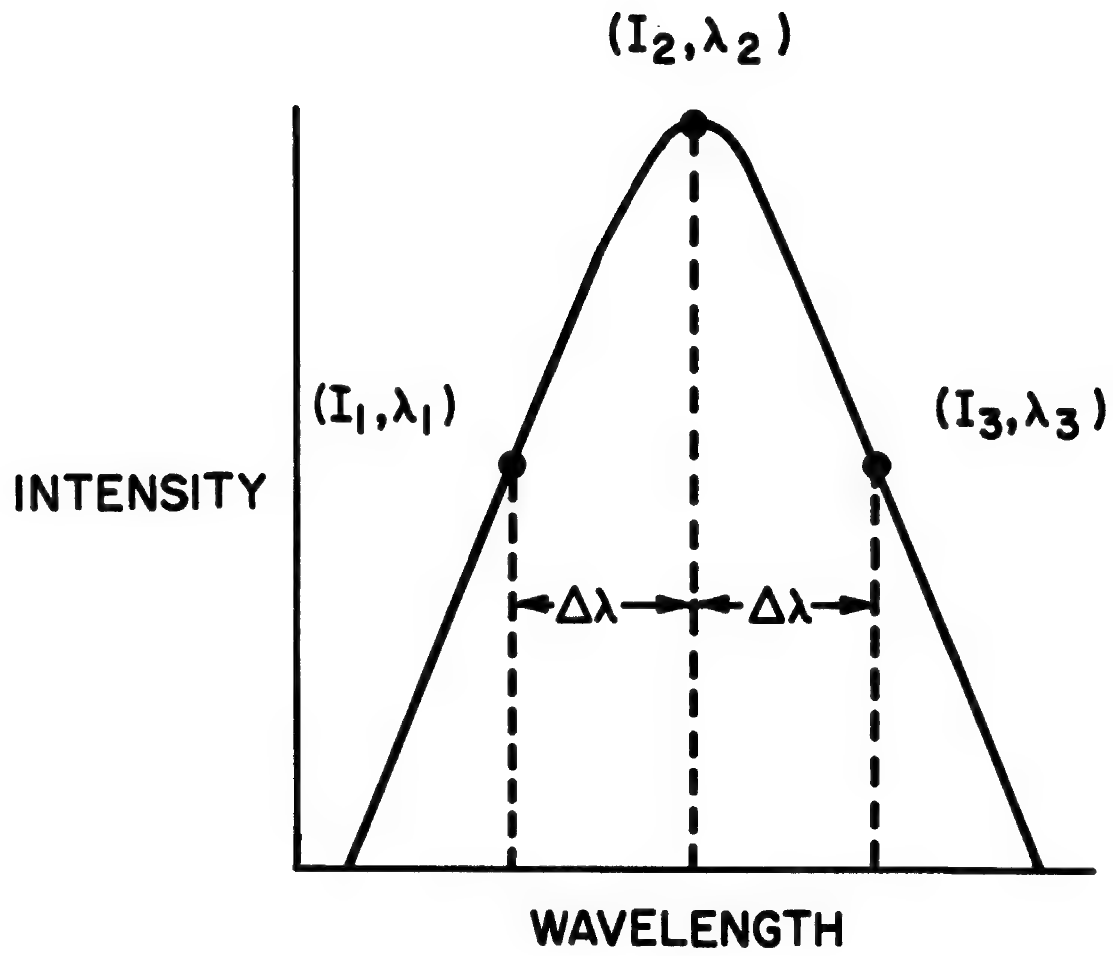


Fig. 1

## AN AUTOMATED CRYSTAL SPECTROMETER SYSTEM FOR QUALITATIVE MICROPROBE ANALYSIS

by  
Eric Lifshin

Materials Characterization Operation  
General Electric Corporate Research and Development

During the past few years considerable emphasis has been placed on the use of solid-state X-ray detectors for rapid qualitative X-ray analysis in electron microprobes and scanning electron microscopes. Although their success is well deserved, it is clear to most instrument users that energy dispersion analysis complements rather than replaces conventional crystal spectrometers, which remain essential for the analysis of light elements, low concentration levels, chemical bonding effects, and most quantitative problems. In order to more effectively accomplish these tasks, the need for automated microprobe systems has been well recognized.<sup>1-5</sup> This paper describes a crystal spectrometer automation system which couples a Cameca electron microprobe, Canberra Datanim electronics, a GEPAC 30-2E minicomputer, and related software.

As shown in Figure 1, a special multiterminal switching device, TRICOM, is used to interconnect the GEPAC 30-2E to either a teletype, a GE600 timeshared computer system,<sup>6</sup> or a Canberra model 6726 telecomputer interface. Programs written in GEPAC 30 assembly language can be stored, edited, assembled, partially debugged, and loaded into the GEPAC 30 using available software in the timesharing system. Once loaded, final debugging is done in the GEPAC 30 where working programs can be stored in core or on a 54K byte (8 bits) disc.

The factors considered to be desirable in setting up an automated spectrometer system include:

1. Optimization of the time spent collecting useful data by scanning only those wavelength ranges containing specific peak or background information.
2. The development of a simple interactive procedure between the operator and the system.
3. High reproducibility of results.
4. Minimizing the operator interaction with the system.

5. Increased flexibility of qualitative analysis through digital step scanning and data recording, along with the development of associated programs for spectral analysis.

6. Clear and concise methods of presenting the result.

Figure 2 illustrates a typical interaction of the operator and the system. The computer first requests specific information, including spectrometer option, step scan range, increment size, and counting time. Elements to be analyzed can then be specified by entering their chemical symbols separated by commas. Ranges of elements can be specified by entering the chemical symbols of the extremes separated by a hyphen. In case of errors, specific control characters can be used to delete characters or lines. Incorrect element symbols are noted as such. Once the element table is entered, the computer sequentially looks up the appropriate spectrometer setting of each element, step scans through the peak starting at one half the range below the peak to one half the range above the peak using the selected increment size and counting time. The data is presented in digital form and can be plotted with labelled intensity and wavelength scales on a Calcomp plotter as shown in Figure 3. Simple procedures are available for spectrum stripping and evaluating whether or not a peak is statistically significant.

#### References:

1. E. Davidson, A. J. Hartwick, and J. M. Taylor, Fifth National Conference on Electron Microprobe Analysis, New York, 1970.
2. E. Eichen and F. Kunz, Fifth National Conference on Electron Microprobe Analysis, New York, 1970.
3. T. D. Kirkendall and P. F. Varadi, Sixth National Conference on Electron Microprobe Analysis, Pittsburgh, 1971.
4. A. A. Chodos and A. L. Albee, Sixth National Conference on Electron Microprobe Analysis, Pittsburgh, 1971.
5. J. J. Colby, Lecture Notes, Summer Course on Electron Microprobe Analysis and Scanning Electron Microscopy, Lehigh University, June 21-25, 1971.
6. P. R. Kennicott, V. P. Scavullo, J. S. Sicko, and E. Lifshin, Proceedings Fall Joint Computer Conference, 1971, AFIPS Press, Montvale, New Jersey, p. 423.



## QUALITATIVE MICROPROBE ANALYSIS PROGRAM

## SELECT SPECTROMETER OPTION

= 2 (C)

THE PRESENT SPECTROMETER RANGE IS 04.00 MM.  
WITH A STEP SIZE OF 0.05 MM.  
AND A COUNTING TIME OF .1X10+3 SECONDS.

ARE THERE ANY MODIFICATIONS? = YES (C)

RANGE = 02.00 (C)  
INCREMENT = 0.02 (C)

TIME:

DIGIT = 1 (C)DECADE = 3 (C)

SUPPLY ELEMENT SYMBOLS

= FE, TI, NI - ZN (C)

PRESENT SPECTROMETER SETTING IS:

11 814678

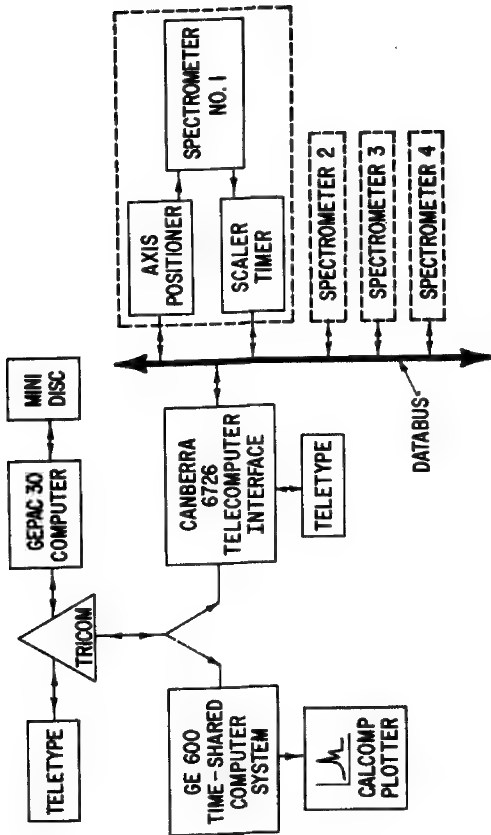
## SPECTROMETER SCAN FOR FE

POSITION	TIME	COUNTS
11 814380	41 001000	43 000245
11 814382	41 001000	43 000218
11 814384	41 001000	43 000257
11 814386	41 001000	43 000213
11 "	41 001000	43 000213

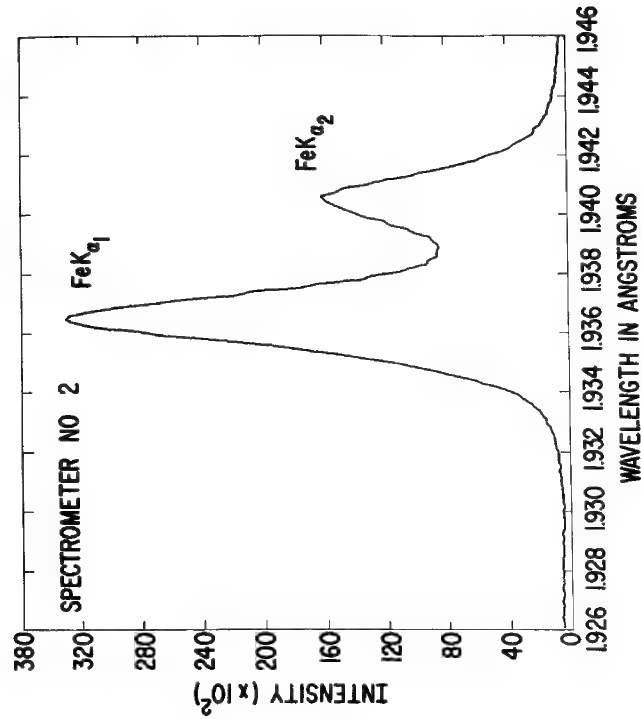
## 2. Typical System-Operator Interactions

a. (C) denotes carriage return.

b. Underlining denotes information supplied by the operator.



1. Schematic Representation of Automated Spectrometer System.



3. Computer Plot of Iron Scan in a Steel Standard (redrawn for clearer reproduction).

MICROPROBE ANALYSIS INTEGRATED  
AUTOMATION COMPUTER SYSTEM

By

J. W. Colby

At previous meetings, systems have been described for automating microprobes, usually to do specific tasks. The system described here differs from many of its predecessors by virtue of being far more complete and being more generally applicable to routine microprobe analysis of many different types of samples. We have not only automated the spectrometer drives and readouts, and the stage, but also the baseline and windows of the pulse height analyzers, the accelerating potential, the grid bias, the filament control, and the condenser and objective lenses. We are also in the process of automating and controlling the vacuum system and the detector high voltage.

The block diagram of the system is shown in the accompanying figure. At the heart of the system is a PDP-11 with 12K words (16 bit) of core, backed by a high speed disk having a capacity of 256K words. There are other peripherals also, such as a high speed paper tape reader and punch, a write-only magnetic tape drive which is IBM compatible, a high speed line printer and a calcomp plotter. These are interfaced through a Canberra computer interface to Canberra electronics which drive and control the various operations on the microprobe. We have replaced our high voltage power supply with a CPS, 0-30 kV power supply which is remotely programmable, and which was modified by CPS for us to also provide bias control. Our two lens supplies were replaced with KEPCO power supplies, which are also remotely programmable in a constant current mode. The detector supplies are being replaced with CPS supplies to be also controlled by the computer.

Algorithms have been derived for completely controlling the gun and lens supplies, providing a stable beam current to the sample. Programs have been written which direct the operator through filament exchange and alignment. Once that is done, the high voltage is set, the bias is set, and the filament is saturated. The bias is then continually adjusted, if necessary, to keep the emission current constant. The condenser lens is similarly adjusted, if necessary, to keep the aperture (beam) current constant. Equations were derived and programmed to allow the computer to set any emission, beam or sample current desired for a given analysis, within the operating capabilities of the components. Each time the filament is saturated, the voltage required for saturation is sampled by the computer, and compared to the voltage required to saturate a new filament. From the percentage change in saturation voltage, the computer is able to determine the approximate remaining filament life, and suggest corrective action if warranted. As the computer changes accelerating potential, the beam

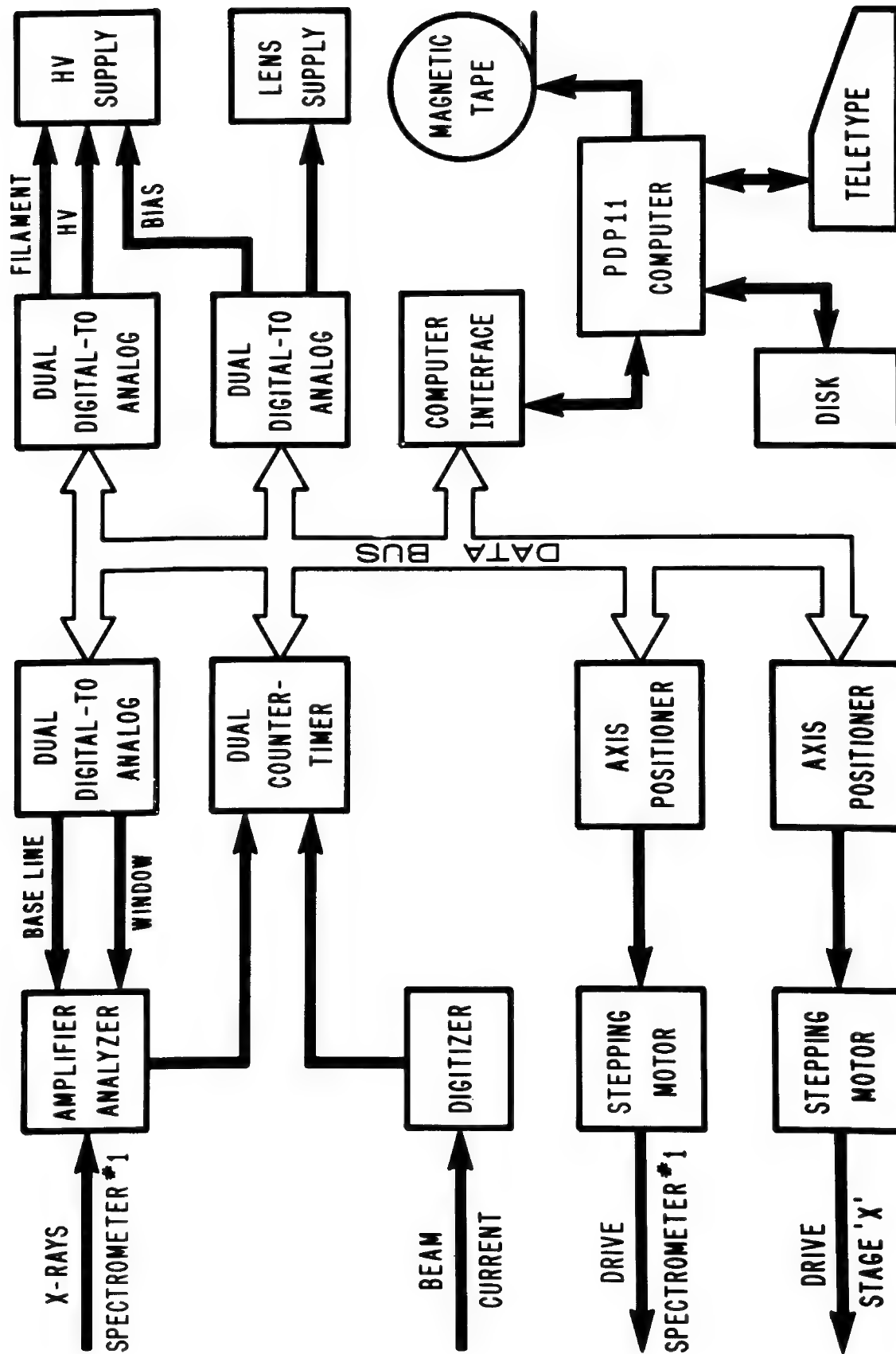
is automatically focussed, thus maintaining not only a stable beam current, but also a well focussed beam, providing, then, the ability to precisely control analytical conditions.

Algorithms have also been developed for peaking spectrometers and for precisely controlling the stage. The pulse height analyzers have been programmed to sweep the baseline and window in synchronism with the spectrometers, thus precluding higher order interferences.

Each function has been individually programmed as a sub-program, which may be invoked separately, or called by large programs. The large programs do specific tasks, such as qualitative scans, quantitative analysis, diffusion profile, wavelength step scans for chemical bond studies, etc. These large programs are, in turn, called by a supervisor program, which has the capability, then, to perform any type of analysis on any number of samples, or on the same sample.

In use, the supervisor is invoked, and it interrogates the operator questions pertinent to subsequent analyses, and instructs him to locate the samples and standards under the cross hairs of the light microscope. The coordinates of each are read in and stored. This process is continued for the remaining samples, and finally, the computer is told to "GO". Whereupon it finds the first sample, invokes the programs necessary to do whatever type of analysis it was instructed to do, and analyzes the data for significance. This process is continued for the remaining samples. Hence, it is obvious that the operation after the initial dialogue with the computer is completely automatic, and may be unattended. Hence, the reason for monitoring filament life, is to allow the computer to suggest that the filament should be changed if its predicted life is shorter than the total analysis time required for the unattended operation. Most of the decision making is done by the computer. Some of these algorithms will be described in more detail.

Finally, it has been said by some that their particular operation does not lend itself to automation, because the samples and analyses that they do are all different. However, within the Bell System, we have analyzed all shapes and sizes of specimens from dust particles and wire to mounted metallurgical samples, and probably more elements than most other laboratories; yet, the automation is able to handle all of it with the exception of x-ray and electron current imaging, and we are working on that.



## COMPUTER AUTOMATION OF AN ELECTRON MICROPROBE

L. W. Finger and C. Hadidiacos

Serious errors may result if an electron microprobe is used for quantitative analyses of chemically inhomogeneous materials. If the spectrometers are manually repositioned so that counts for all elements may be collected for a given stage location, it is extremely likely that spectrometer setting errors will result. Alternatively, the spectrometer positions may be held constant during the analysis, making it necessary to reposition the stage and measure the elements in sets. With an inhomogeneous specimen, the compositional errors introduced by the uncertainties in stage repositioning could seriously affect the results. A computer may be used to overcome these difficulties since it may perform error-free manipulation of the spectrometers; consequently, all elements may be measured without moving the stage. As an additional benefit, the computer can be programmed to perform nearly instantaneous data reduction and correction procedures.

We have automated our M.A.C. Model 400 electron microprobe using Canberra Industries interface and operational modules and a Digital Equipment Corporation PDP 11/20 computer. This system controls a drive motor and scaler/timer pair for each of three spectrometers. The addition of stage drive electronics is planned for the immediate future.

One of the major difficulties associated with automated analysis lies in the control of the electron beam. The computer must be able to interrupt the beam upon command, yet the location at which the beam strikes the sample must be reproducible within a fraction of a micron. Manually operated probes use mechanical shutters that may or may not affect the beam position; in any event they are not easily converted to automatic operation. We have overcome this difficulty by inserting a motor driven shutter assembly into the path of the electron beam. This device is used as a beam current monitor as well as a beam-stop and its operation does not affect the position of the beam. Whenever the beam is interrupted, the current flowing from the graphite stop to ground is measured by a digital voltmeter which may be read by the computer. Since both this current and the counting rate are proportional to the electron beam current, it is possible to correct the data for beam current drift. This technique is somewhat more versatile than conventional beam-integrators because the entire electron beam is sampled - not just the currents at the edge of the beam. Although seldom necessary except for demonstrations, the data may be properly corrected for beam current changes as large as a factor of 10.

The usefulness of any computer-controlled instrument is largely determined by the software. We have provided a set of routines which will allow the operator to perform quantitative analysis as well as service functions, such as spectrometer manipulation.

We have designed our analysis routine to measure the complete chemical analysis of a single spot with the capability of calculating the average and standard deviation of the points measured for a single grain. The analyses are corrected using the method of Bence and Albee (1968) and the coefficients of Albee and Ray (1970). In addition, the program will calculate a chemical formula normalized either for a

given number of cations or oxygen atoms. To minimize the destructive effects caused by long exposure to the beam, several features unique to our system have been incorporated into the program: (a) the scaler/timer units are operated in the fixed-count mode with a maximum time override for low count rates, (b) the spectrometer channels are operated asynchronously, i.e. one unit may be driving to a new position while another is counting, etc., (c) the shutter is open only when at least one channel is counting and (d) the operator selects only the elements that he wishes to analyze. Operation in this fashion has imposed constraints on the hardware employed since each channel must have a separate timer and scaler. However, the software is much more affected by the independent operations of the channels since this requires a time-sharing monitor system. If a great deal of computer resources were available, a general purpose routine could be implemented; however, we use a limited capability system which unfortunately prevents the coding of programs in a high-level language - only machine language routines may be used. The disadvantage caused by the relative inflexibility of such a system has been partially overcome by preparing a routine which allows a program written in the BASIC language to communicate with the microprobe interface. This scheme is beneficial when special purpose measurements are to be made or new techniques are tested.

The ultimate test for any computer-controlled instrument is its ability to provide results. For example, in an analysis of a clinopyroxene for nine elements, the time between the positioning of the stage and the completion of the printing of the corrected results (with mineral formula) was roughly 2-1/2 minutes. For this particular experiment, the scaler/timer presets were set at 20,000 counts or 30 seconds. During a recent four-week period, our system was used approximately 200 hours by 14 different operators, most of whom have extremely limited computer experience. The number of elements in their analyses ranged from 3 to 10; approximately 10,000 elemental concentrations were measured.

#### References

- Albee, A. L. and L. Ray (1970). Analytical Chemistry, 42, 1408-1414.  
 Bence, A. E. and A. L. Albee (1968). J. Geol., 76, 382-403.

THE PROGRAM CYCLOPS FOR THE QUANTITATIVE ANALYSIS  
OF ELECTRON MICROPROBE X-RAY DATA

Henry R. Thresh<sup>\*</sup>  
Chase Brass & Copper Company

Ted E. Keller  
Case Western Reserve University  
Department of Computer Engineering

The immense versatility of the electron microprobe analyzer confronts the analyst with developing the most reliable and rapid procedures in striving for an efficient instrument operation. This is particularly relevant for quantitative analysis where the means of proceeding from data collection to the final corrected data can be arduous and time consuming. Specifically, the minimum requirements for the evolution of an analytical method at the Casting Laboratory were considered to be, (i) alternative approaches of collecting machine data, (ii) the use of programmed spectrometers for multi-element coverage, (iii) means of identifying blocks of data at the collection source, (iv) a pre-correction scheme for raw data to derive corrected K ratios, (v) submit these intensity ratios to one of the many major correction programs now available [1], (vi) format verification to prevent computation being jeopardized, (vii) plotting routines to allow immediate evaluation of some types of output data.

This problem has been pursued by, (i) embodying an encoder switch into the data output device to permit the operator to identify blocks of data at the teletype terminal, (ii) constructing the software CYCLOPS to handle data from several modes of analysis, utilize tagged data and and present pre-corrected K ratios to a major correction procedure, (iii) use of Calcomp plot routines to plot data such as step scan analysis into a meaningful format for rapid evaluation. Previous attempts at using the encoder switch concept for automated data acquisition have been made by Frazer et al. [2]; Fisher and Wickersty [3].

A code number is generated at the end of each line of data by incorporating an encoder switch into the last collection position of the data translator on an ARL EMX-SM Microprobe. By using the three digits labeled NPROC (program procedure code), NEL (element number) and IND, control is exercised over the processing of the data by the program. Format verification and the use of certain values of NPROC permits the program to remove erroneous data.

<sup>\*</sup>This author is now associated with the Argonne National Laboratory

Computation procedures are divided into two sections (i) a preliminary correction routine for converting raw data into K ratios by allowing for the usual data collection factors such as dead-time, background and drift, (ii) a major correction scheme to remove the effects of absorption, fluorescence and atomic number due to the matrix. At this time a version of the program MAGIC III [4] is used for this purpose. By reducing data handling to the routine collection of raw data on paper tape and accessing this information to the computer with only a few cards to be punched, which describe the data and control the program, a greater utility of a microprobe operation can be established.

The program CYCLOPS is written in Fortran V for the UNIVAC 1108 Multiprocessor system and requires approximately 24,000 decimal words of core storage. It can analyze up to eight elements and a ninth by difference. It will accept up to 300 data points in either the point or stepscan analysis modes. As an alternative to the use of an encoder switch, the above procedures are sufficiently flexible to permit a user to insert a special control character at the teletype prior to the collection of a set of lines of data, to simulate an encoder switch setting for these lines. Documentation of this program, including listings and two extensive analytical test problems for the point analysis stepscan modes, is now available[5].

#### REFERENCES

- [1] D.R. Beaman and J.A. Isasi ; "A Critical Examination of Computer Programs used in Quantitative Electron Microprobe Analysis", Anal. Chem., Vol. 42, p. 1540, 1970.
- [2] J. Frazer, R.W. Fitzgerald and A.M. Reid ; " Computer Programs EMX and EMX2 for the Electron Microprobe Data Processing ", SIO Ref. No. 66-14, 1966, Inst. for the Study of Matter, Univ. of Cal., LA Jolla.
- [3] G.L. Fisher and W.G. Wickersty ; " Manip ; A Computer Program for Processing X-Ray Data taken directly from the Electron Probe Microanalyzer ", Tech. Paper 643 T-OP, Inter. Nickel Co., Suffern.
- [4] J.W. Colby ; " Quantitative Microprobe Analysis of Thin Insulating Films "; Adv. in X-ray Anal., Vol. 11, p. 287, 1968.
- [5] T. Keller and H.R. Thresh ; " A Description of the Program Cyclops for the Quantitative Analysis of Electron Microprobe X-Ray data ", Casting Laboratory Rep. No. 71-30, Chase Brass & Copper Co., Cleveland.



# IMPROVED DECONVOLUTION TECHNIQUE TO STUDY ELECTRON MICROPROBE CONCENTRATION PROFILES

by

Z. Mencik

Ford Motor Company, Dearborn, Michigan

The resolution with which concentration profiles can be determined using an electron microprobe is limited by the finite dimension of the volume taking part in the emission of the characteristic X-ray radiation. Knowing the size and shape of this volume through a determination of the so-called beam function (which is a trace across a sharp boundary of two dissimilar materials) makes it possible under certain conditions to derive the true concentration profile using a procedure known as deconvolution. This process, which is carried out mostly by Fourier analysis, has an operational limit given by the presence of noise in any real data. This need not be a serious obstacle if the width of the profile to be deconvoluted is much greater than the width of the beam profile. However, when these two become of comparable width serious difficulties are encountered. In the latter case the noise component becomes of greater importance with every increasing order of the Fourier coefficients which are operated upon in the Stokes(1) method, and the series has to be terminated when the level of the noise becomes significant compared to the signal. This termination will in turn result in serious oscillations. A procedure had been proposed, the sigma termination(2), which can remove the worst of the oscillations, but this happens at the expense of loss of detail, as is acknowledged in the literature(3).

A procedure is proposed here which will improve the deconvolution of such profiles if properly applied. It consists in supplying by extrapolation the converging tails of the series of Fourier coefficients, the extrapolation being based on the trends observed in that portion of the series which is still relatively free of the noise signal. The assumption is used that the profiles to be scanned conform to profiles generated by diffusion from sharp junction profiles and as such do not contain periodic fluctuations of a period similar to those resulting from series termination. While the sigma termination removes the oscillations by damping the Fourier coefficients at the expense of loss of detail, recovery of the higher terms by extrapolation on the contrary adds such terms as are necessary to remove the oscillations without loss of detail. This procedure consists of the following:

1. Generating Fourier coefficients of an artificial sharp step profile placed with the discontinuity in the center of the period (also the experimental specimen scan is placed with its mid-point in the center of the period).
2. Forming logarithms of ratios of the Fourier coefficients of the real profile to the coefficients of the step profile.
3. Finding the first and second derivatives of this logarithm profile as a function of the length coordinate.

4. Extrapolating the missing terms using the Taylor series and converting to the profile itself.

The procedure is limited by certain provisos. For instance, the real profile to be deconvoluted must contain only one diffusion step; if more than one are present, each step has to be dealt with separately. Again, the first and second derivatives must be either negative or zero.

Another procedure which can improve the performance of any deconvolution technique, if properly applied, is the use of an iterative procedure consisting of following steps:

1. Convolution of a preliminary result of deconvolution back with the beam function.
2. Subtraction of the convoluted profile from the measured profile.
3. Deconvolution of the difference profile generated in step 2 with the beam profile.
4. Adding this to the preliminary result as correction.

In this way the inaccuracies of the deconvolution step are improved by iteration.

Taking this procedure one step further, we can omit the first deconvolution by substituting for the preliminary result an assumed concentration profile complying with whatever physical and chemical data are available about the specimen and the diffusion process which generated the specimen. Any inaccuracy in the choice of the assumed profile will be corrected in the iteration cycle. This procedure is especially suitable if we have to handle a system having a discontinuity in the true concentration profile such as the asymmetric profile resulting from the diffusion of a component from a fluid bath of constant composition into a solid.

Both techniques mentioned here have been tested using computer generated model data. Deconvolution was carried out using the Fourier method; convolution needed in the above iterative process proceeded either through the Fourier method or directly using the equation for convolution

$$z(x) = \int_{-\infty}^{\infty} f(t) \cdot b(t-x) dt$$

where  $z(x)$  is the convoluted profile,  $f(t)$  is the assumed profile and  $b(t-x)$  is the beam function. Integration was replaced by summation. The latter method is especially suited for situations in which the beam function has to be assumed as changing in the close neighborhood of a composition discontinuity, due to the effect of the discontinuity on the X-ray volume. This would essentially permit us to deconvolute with a variable beam function.

Programs for the described techniques have been written in Fortran IV.

- 
1. Stokes A.R.: Proc. Phys. Soc. 61, 382 (1948)
  2. Moore L.: Brit. J. Appl. Phys. 2, 237 (1968)
  3. Gupta P.K.: J. Phys. D.: Appl. Phys. 3, 1919 (1970)

# NONPARAMETRIC ANALYSIS APPLIED TO THE SEM AND MICROPROBE STUDY OF INDUCED-ARC AND RESISTIVE WELDS

Arthur J. Saffir  
University of the Pacific  
2155 Webster St.  
San Francisco, Calif. 94115

Donald I. Zenobia  
Precision Metallurgical Co.  
Millis, Mass. 02054

Composite materials, such as precious metals bonded to base metal substrates, have wide application in the biomedical and electronic fields. These materials not only offer substantial economy compared to devices fabricated entirely from precious metals but also possess unique, desirable properties. However, the properties of the precious metal must not be impaired by a defective weld. This report concerns our studies of the two processes, currently used to fabricate composite electrical contacts, in which precious metal (Au, Ag, Ag-CdO) is welded to a base metal substrate by either an induced-arc weld or a resistive weld.

In the induced-arc weld process, the components are held at a relative potential of 10 to 100 volts. The components are allowed to contact briefly, 50 to 500  $\mu$ sec, permitting current to flow. They are then drawn apart in order to strike an arc. After arcing for 300 to 3000  $\mu$ sec, the components are forcefully driven together while the current continues to flow. In the resistive process, the components are brought in contact, a voltage is applied, and the current passing through the junction provides heat to form a weld. The service life of the induced-arc devices, exceeds 5x in certain applications. Contacts obtained from 5 manufacturers, were mounted, sectioned and prepared for electron microprobe analysis. The electron microprobe revealed regions of diffusion ranging from 10 to 80  $\mu$ m in width, by 20 to 200  $\mu$ m long at the weld interfaces of all specimens studied, Fig. 1 and 2.

Quantitative analysis of the composition of diffusion zones was difficult to interpret because of the variety of precious metal components studied. On the other hand, because the location of the diffusion zones appeared to be sample dependent, the distributions were studied statistically by means of Kruskal-Wallis analysis. This nonparametric analogue of one-way analysis of variance is widely applicable to nonparametric microprobe and SEM data. This technique, an extension of the Mann-Whitney test for two independent samples, tests several random nonparametric samples with the null hypothesis that all of the samples are derived from the same population. The requirement that the observations have rank order was met by assigning: a value of 1 to welds with no observed diffusion zones; a value of 2 to welds with diffusion zones observed only at the periphery; a value of 3 to welds with diffusion zones observed at the center as well as the periphery. No welds were observed to have diffusion zones at the center without peripheral diffusion zones also. Analysis indicated that: diffusion regions were distributed throughout the weld interface in the induced-arc welds but were confined near the periphery of the resistive welds,  $p = .99$  (about 30 times more diffusion zones were found in the central regions of induced-arc welds); significant differences did not result from differences among materials (Au, Ag-CdO welded to Cu) or differences among manufacturers (except differences related to which welding process was used).

Studies of failed resistive welded contacts (none lasted more than 40,000 cycles)

proved informative despite the unavailability of comparative data on the induced-arc welded contacts (none failed during testing which was terminated after 209,000 cycles). Low magnification examination of failed contacts shows cracks propagating circumferentially with little evidence of bonding except at the periphery, Fig. 3. It is likely that failure initiated at the periphery of the weld and then propagated centrally and circumferentially. Higher magnification SEM and microprobe studies reveal microscopic silver-rich masses clinging to the copper substrate near the periphery of failed resistive welds, Fig. 4. Identified as diffusion zones, these masses are apparently responsible for bonding.

It is concluded that:

1. nonparametric analysis has wide applicability in SEM and microprobe studies
2. diffusion zones are responsible for bonding
3. resistive welds are bonded only peripherally
4. under certain conditions, peripheral bonding is inadequate
5. induced-arc welds have diffusion zones distributed throughout the weld area
6. it is likely that these widely distributed diffusion zones convey the characteristic ruggedness of the induced-arc weld contact
7. the severe performance requirement of electrical contacts and certain biomedical applications necessitate induced-arc welds

Accordingly, our continuing studies of biomedical applications are leaning heavily toward the induced-arc process. The results of this work will be reported in a later communication.

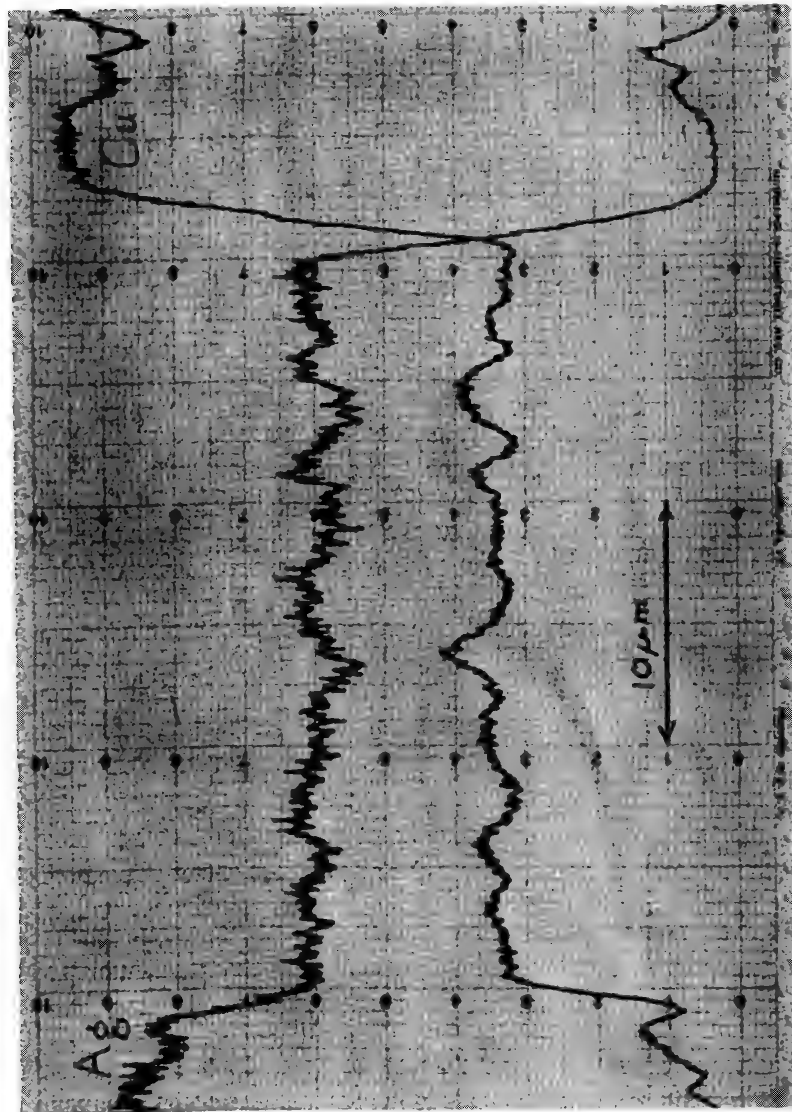


Figure 1. This diffusion zone of a composite contact consisting of a silver contacting region welded to a copper substrate. Regions of constant composition, suggestive of intermetallic phases were frequently observed, but they varied considerably in size, composition and distribution among specimens. They were widely distributed throughout the weld interfaces of the induced-arc specimens and localized to the periphery of the resistive weld specimens.

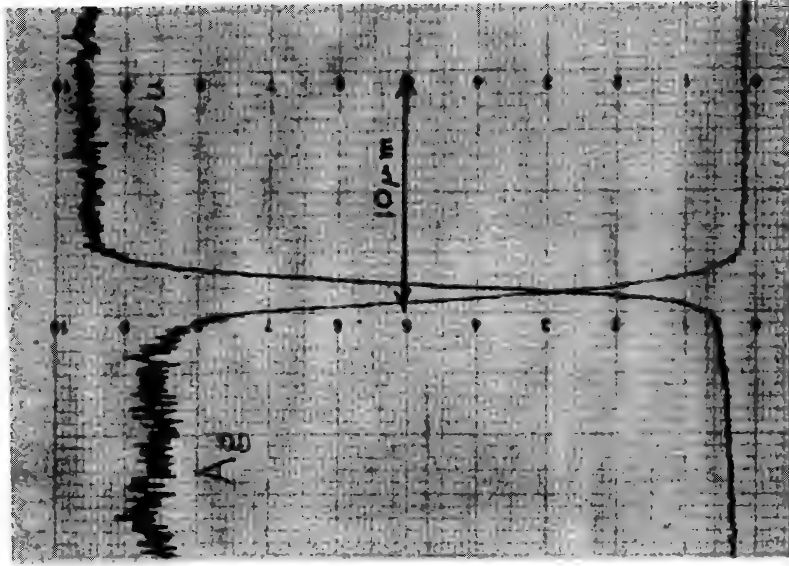


Figure 2. The central portions of resistive welds show little evidence of diffusion except at the periphery of the welds. The clean separation between silver and copper components seen in Figure 2 suggests the absence of diffusion zones.



Figure 3. The silver component of this resistive weld contact is seen to separate cleanly from the copper substrate below. The regions of adhesion seem to be limited to the peripheral parts of the welds. Note the small mass of material clinging to the copper near the edge (arrow).

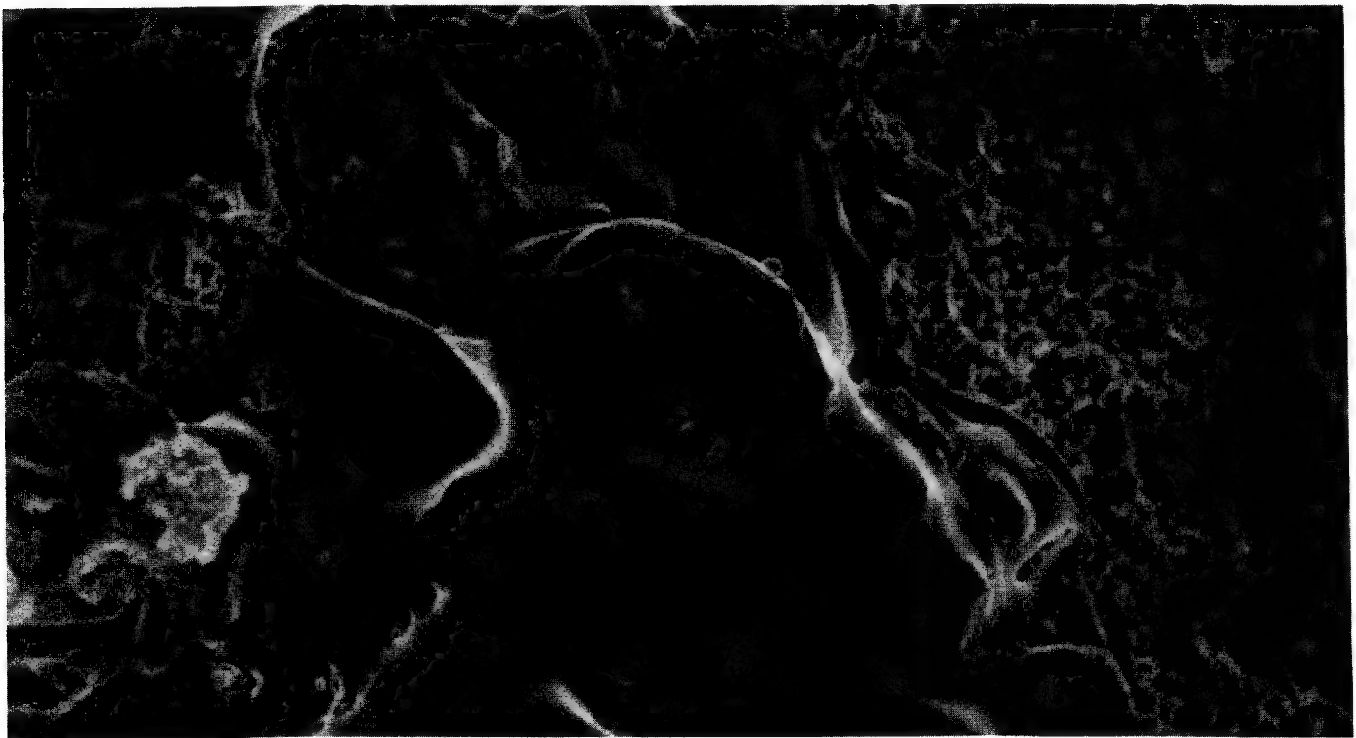


Figure 4. A small mass of material clinging to the periphery of a failed resistive weld is seen in more detail.

THE EFFECT OF CARBON FILM THICKNESS ON THE INTENSITY OF  
SELECTED K $\alpha$  RADIATION

James F. Villaume, Derrill M. Kerrick and  
Leland B. Eminhizer  
Mineral Constitution Laboratories  
The Pennsylvania State University  
University Park, Pennsylvania 16802

A possible error in quantitative electron microprobe analysis arising from variations in the thickness of conducting films has been the foreboding of several workers. To date the only quantitative estimate of the effect such variations would have on characteristic x-ray intensities is provided by Sweatman and Long (1), who have developed an equation which expresses the loss of x-ray intensity in terms of electron and x-ray absorption by the conducting film. The present study was undertaken to provide experimental data on carbon as a conducting film in microprobe analysis which could then be applied directly to practical situations and to the evaluation of theoretical considerations of carbon as an absorber of electron and x-ray energy.

Carbon film thickness was determined during evaporation using a Sloan Instrument Company thickness monitoring system, which is designed to measure film thickness as a change in the frequency of a crystal oscillator. With this instrument film thicknesses could be measured to an accuracy of  $\pm 3\%$  of the actual film thickness. By comparing several mounts of the same material with a constant film thickness, compositional variation was nearly eliminated as a possible interfering effect. Each mount was then coated with the desired carbon film thickness and the x-ray intensities of the various mounts compared to those of the same material with a reference carbon film thickness of 200 Å, which was found to be the lower limit at which the carbon film would still conduct. The results of this study are presented in Figure 1.

For each element shown on the graph the percent intensity loss for a particular carbon film thickness is given as

$$100 - \left( 100 \times \frac{\text{ave. intensity for film thickness } x}{\text{ave. intensity for a 200 Å film thickness}} \right).$$

Each data point in the figure represents the average of some 90 intensity measurements; counting statistics suggest a reasonable error of 1% from the average intensity values given. Data points for a given radiation closely approximate a straight line relationship between the two variables as the linear correlation coefficients for all the lines are consistently above .95. Intensity loss at a particular carbon film thickness is independent of the concentration of the element being analyzed and with the exception of fluorine is given by the equation of Sweatman and Long (1).

The data clearly show that in quantitative microprobe analysis as much as a 5% error will be introduced for certain elements as a radiation intensity loss when the difference between the carbon film thicknesses of sample and standard is between 200 and 400 Å. For the purpose of monitoring carbon film thickness and

thereby avoiding such errors the darkening of glazed porcelain and the identification of interference colors on a suitable substrate such as gold (see Table 1) are probably satisfactory when expensive electronic equipment is not available.

### References

1. Sweatman, T. R. and Long, J. V. P., 1969, Quantitative electron-probe micro-analysis of rock-forming minerals: Journal of Petrology, v. 10, pp. 332-379.
2. Böhler, S., "Electron Microscopical Specimen Preparation Techniques," Balzers Aktiengesellschaft Für Hochvakuumtechnik und Dünne Schichten, Balzers.

TABLE 1

## INTERFERENCE COLORS OF CARBON FILMS ON GOLD SUBSTRATE

<u>Approx. Thickness</u>	<u>Color</u>
150 Å	Orange
200 Å	Indigo red
240 Å	Blue
350 Å	Blue-green
430 Å	Green-silver

From Böhler (2)

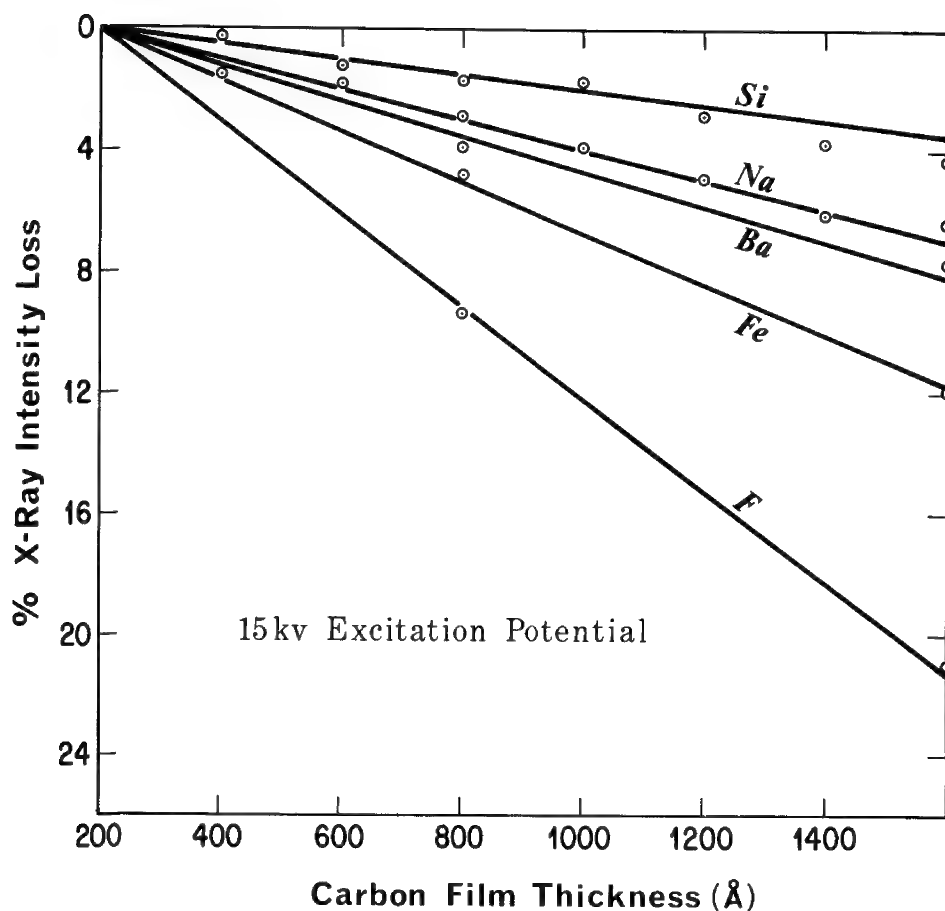


Figure 1



## MIRROR-MODE ELECTRON PROBE MICROANALYSIS

J. Ordonez and E. Brandis

IBM Components Division  
East Fishkill Facility  
Hopewell Junction, New York 12533

Subsurface chemical analysis, using the microprobe, is done by varying the accelerating potential of the electrons in the electron beam (1). The higher the accelerating potential, the deeper the electron penetration in the specimen. If this accelerating potential is varied, a concentration profile of a particular element in the specimen as a function of depth can be obtained. To do this, however, one has to realign the instrument to maintain the same beam current, specimen current, and beam size, every time the accelerating potential is changed. An alternate approach to this method is presented here. A negative potential is applied to the sample. This potential can then be varied while, at the same time, a potential on the anode plate and through the column is kept constant. Thus, one can obtain any desired 'net' potential on the specimen. Furthermore, since no adjustments in the gun and column are needed, the beam and specimen current remain constant for a given net potential.

A special specimen holder is used. This holder is completely insulated from the rest of the instrument (Fig. 1).

Using this setup, x-ray intensities of copper from a standard were obtained at various 'net' potentials. Similar x-ray measurements were made by varying the anode plate potential. The results of these two measurements are shown in Table I. The difference in copper x-ray intensity obtained with those two approaches is negligible.

Figure 2 shows the results obtained with phosphorus, from a sample containing a phosphorus-rich layer, in which these two techniques were compared. Varying the anode potential and the sample potential, the phosphorus x-ray intensity difference is insignificant. The decrease in x-ray intensity at about 8kV is due to the fact that beyond this accelerating potential the electron beam has penetrated the phosphorus-rich layer.

To minimize the effect of sample topography on the electric field distribution between the sample and the objective lens, a metal diaphragm is placed on the holder which exposes to the electron beam only the area of interest in the sample. Primary beam deflections at various 'net' potentials were measured. Results are indicated in Table II. Since the x-ray optical setup in the microprobe allows a beam deflection of about  $100\mu$  from the center point still remaining in the Rowland Circle, the beam deflections measured using this technique are within allowable tolerances.

For a sub-surface chemical analysis the specimen bias technique yields the same results as that of varying the anode potential. The technique is fast, requiring only a change in potential at the sample, and everything else remaining constant. If quantitative analysis is needed, standard correction factors can also be applied to this technique.

#### REFERENCE

- (1) N. Koopman and J. Gniewek, Fourth National Conference, "Electron Probe Micro-analysis," Chicago, Ill., 1969.

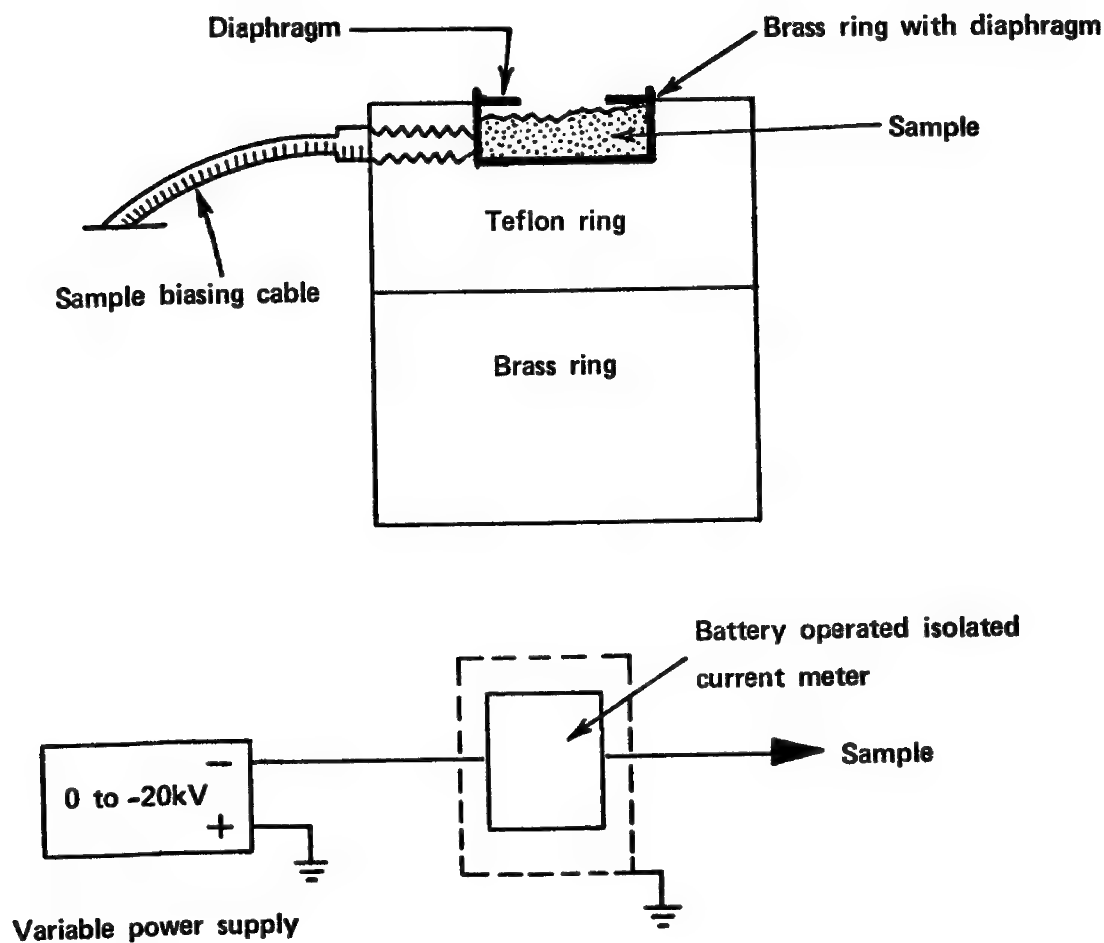


Fig. 1. Sample holder and circuit used.

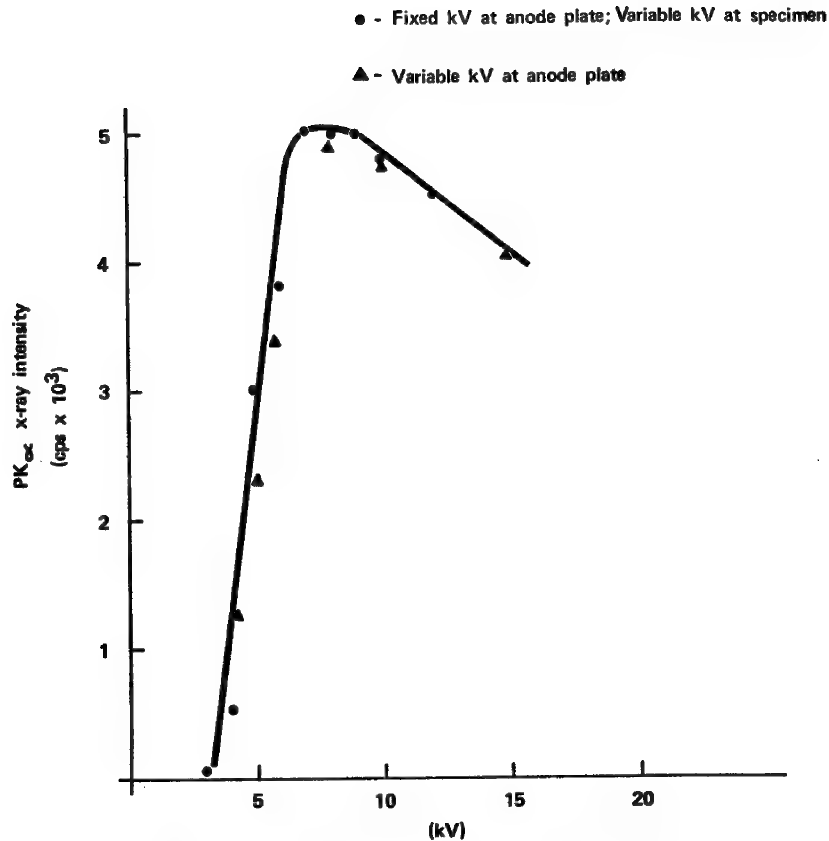


Fig. 2. Phosphorus x-ray intensity vs anode and sample potentials.

TABLE I. X-ray intensities of copper at various potentials.

Anode Potential [kV]	Specimen Current [A]	X-ray Intensity (cps.)	Anode Potential [kV]	Specimen Potential [kV]	Specimen Current [A]	Net Potential [kV]	X-ray Intensity (cps.)
15	$10^{-8}$	475	20	5	$10^{-8}$	15	480
20	$10^{-8}$	2200	30	10	$10^{-8}$	20	2250
30	$10^{-8}$	10150	35	5	$10^{-8}$	30	10200

TABLE II. Electron beam deflection as a function of 'net' potential (anode potential minus sample potential).

Anode Potential [kV]	Sample Potential [kV]	Net Potential [kV]	Specimen Current [A]	Beam Deflection [ $\mu$ m]	
				X	Y
20	0	20	$10^{-8}$	0	0
20	5	15	$10^{-8}$	5	0
20	10	10	$10^{-8}$	5	0
15	0	15	$10^{-8}$	0	0
15	5	10	$10^{-8}$	5	2
15	10	5	$10^{-8}$	5	2
10	0	10	$10^{-8}$	0	0
10	5	5	$10^{-8}$	15	10
10	6	4	$10^{-8}$	20	10
10	8	2	$10^{-8}$	20	15

## Microprobe Technique for Determination of Thickness and Phosphorous Concentration of Gate Oxide Phosphosilicate Glass in FET Devices

Giulio DiGiacomo

IBM Components Division  
East Fishkill Facility  
Hopewell Junction, New York 12533

This microprobe technique is capable of determining the thickness and phosphorous concentration of the phosphosilicate glass in FET gate oxide. The technique is equally applicable to wafers and devices. The latter application is unique since there is no other way, at present, to obtain this information on actual FET gates. In addition to the extended capability to real devices, this technique yields the phosphorous concentration with a precision of  $\pm 0.1$  mole%, about one order of magnitude better than that obtainable by the etch rate method. The oxide and phosphosilicate thickness are determined with a precision of  $\pm 5 \text{ \AA}$ , comparable to that achieved by ellipsometry, with the advantage of applicability to actual devices.

The full characterization of the phosphosilicate glass (PSG) in terms of phosphorous concentration and thickness requires the measurements of both phosphorous and oxygen characteristic radiations before and after a layer of the PSG is removed by etching. The removal produces X-ray intensity decrements of both elements proportional to the thickness of the layer removed and makes it possible, with the original intensity values, the calculation of thickness and phosphorous concentration of the PSG and the total thickness of the gate oxide.

An illustration of the principle of the microprobe approach appears in Fig. 1 which also defines the X-ray values measured and shows the thickness and concentration quantities. The proportionality constants between these quantities and the X-ray intensities have been determined experimentally utilizing samples of known phosphorus content and oxide thickness. When X-ray intensities are plotted versus phosphorous content and oxide thickness, straight lines result. For thin films, these relationships are linear at sufficiently high voltage.

Figure 1 also shows that the electron beam penetration is about twice the thickness of the silicon oxide. The acceleration voltage of 5kv was found to give optimum sensitivity for both elements. At lower potential, the method becomes less sensitive to  $\text{SiO}_2$  removals while attenuation due to carbon contamination becomes significant for both elements. Higher voltages curtail the sensitivity of  $\text{P}_2\text{O}_5$  as a result of peak/background ratio. Figure 1 exhibits the initial X-ray measurements of both elements  $I_{\text{O}}^i$  and  $I_{\text{P}}^i$ . These two intensity values

when used in Figs. 2 and 3, respectively, yield the initial oxide plus PSG thickness,  $t_{\text{SiO}_2 + \text{PSG}}^i$ , and the initial phosphorous content in terms of thickness X concentration units,  $t_{\text{PSG}}^i \cdot C_p$ .

After the X-ray measurement is completed, the wafers are etched to remove a layer of the PSG. Having removed parts of the PSG, a second microprobe measurement is made for both elements. The intensities  $I_o^f$  and  $I_p^f$  thus obtained are again used in Figs. 2 and 3 to determine the new oxide thickness,  $t_{\text{SiO}_2 + \text{PSG}}^f$ , and the new phosphorous content,  $t_{\text{PSG}}^f \cdot C_p$ .

From the above measured values, the thickness and phosphorous concentration of the PSG are determined by:

$$t_{\text{SiO}_2 + \text{PSG}}^i - t_{\text{SiO}_2 + \text{PSG}}^f = \Delta t_{\text{SiO}_2 + \text{PSG}} = \Delta t_{\text{PSG}}, \quad (1)$$

$$t_{\text{PSG}}^i \cdot C_p - t_{\text{PSG}}^f \cdot C_p = \Delta t_{\text{PSG}} \cdot C_p, \quad (2)$$

$$I_p^i - I_p^f = \Delta I_p \propto \Delta t_{\text{PSG}} \cdot C_p, \text{ and} \quad (3)$$

$$I_o^i - I_o^f = \Delta I_o \propto \Delta t_{\text{PSG}} (C_o \text{ known}), \quad (4)$$

where  $C_p$  = phosphorous concentration and  
 $C_o$  = oxygen concentration.

Dividing Eq. (3) by Eq. (4)

$$\frac{I_p}{I_o} = C_p, \quad (5)$$

$$\frac{I_p^i}{C_p} = t_{\text{PSG}}^i, \text{ and} \quad (6)$$

$$\frac{t_{\text{PSG}}^i}{t_{\text{SiO}_2 + \text{PSG}}^i} = \text{Thickness ratio.} \quad (7)$$

Thus, measurement of both PSG thickness and composition are obtained with two microprobe measurements and only one etching operation.

Figures 4 and 5 are the calibration curves used for the analysis of oxygen and phosphorous, respectively. As shown in the figures, ellipsometry and neutron activation are used to calibrate the X-ray intensities of oxygen and phosphorous, respectively,

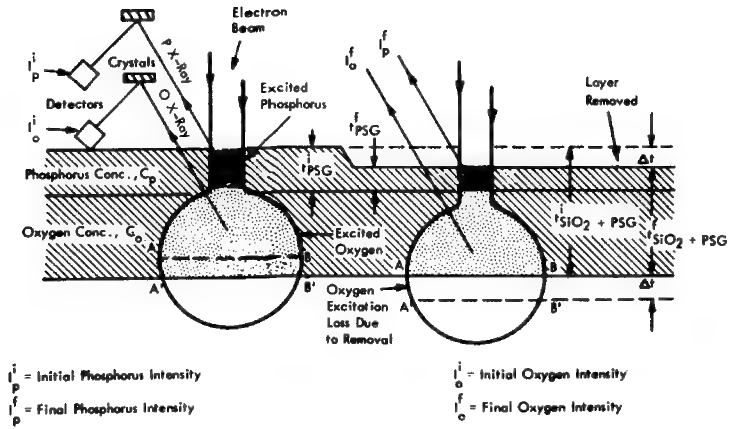


Fig. 1. Principle of microprobe technique.

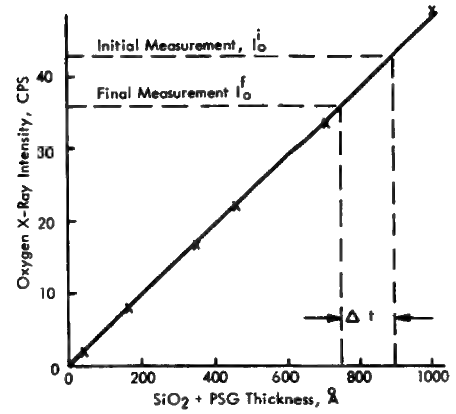


Fig. 2. Determination of PSG layer removed.

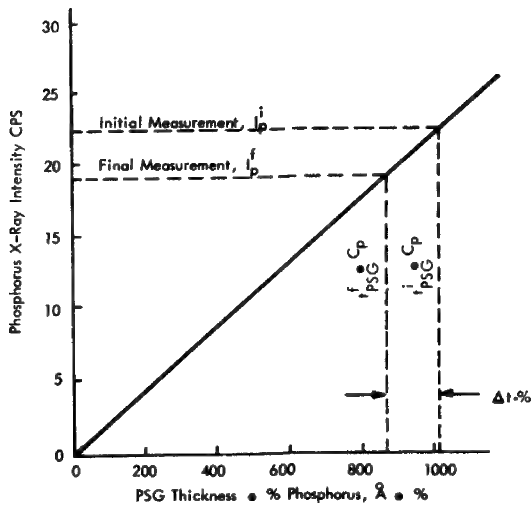


Fig. 3. Determination of phosphorous content in Å % units.

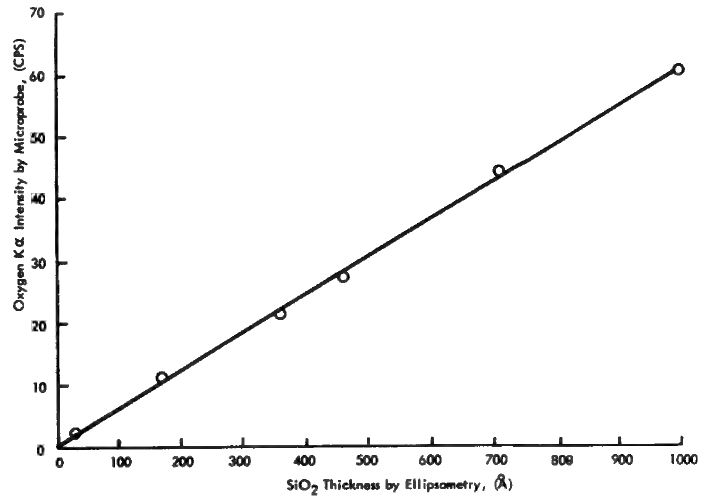
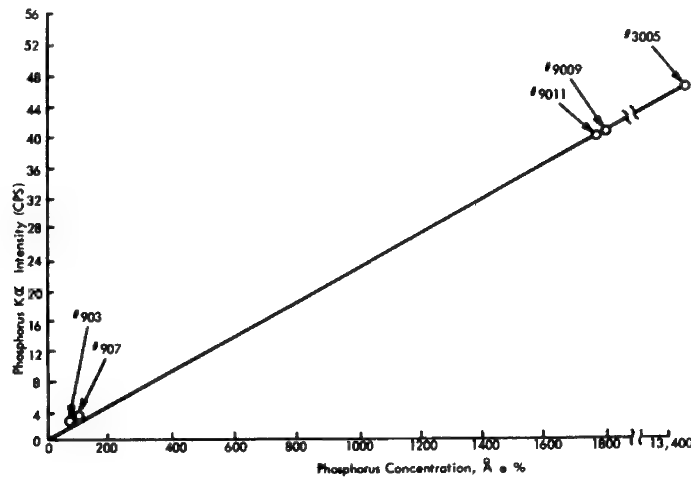
Fig. 4. SiO<sub>2</sub> thickness calibration curve.

Fig. 5. Calibration curve for PSG phosphorous content.

## NON-DISPERSIVE X-RAY DATA ANALYSIS BY COMPUTER

William G. Miller, Illinois State Geological  
Survey, Urbana, Illinois 61801

Data derived from a non-dispersive X-ray analyzer attached to a scanning electron microscope are processed by a series of routines written in Fortran IV (level G) for an IBM System 360/75. The program is equally well suited for any spectral type of data produced by a multichannel analyzer or other equipment whose output is in a digital format giving occurrences against a constant interval (x-y plot).

The output of the X-ray unit is the number of secondarily-emitted X-ray photons counted in each channel of a 1024-channel analyzer. Each channel represents a photon energy of 20 eV. These data are read into a Teletype machine, which produces a punched paper tape and a printed listing of the digital data. The paper tape is converted to punched cards on an IBM 047 keypunch. These cards are the input to the program. The wiring diagram for the 047 program board designed to accept USAC II teletype code is available on request.

The program provides elucidation of peak positions, as well as the maximum number of events for that channel and the integrated area under individual peaks. It also provides curve smoothing and background subtraction. The background due to both the randomness of the X-rays and that due to noise in the Si detector and associated electronics are removed. Up to six pre-determined spectra can be stored and later subtracted from the input data in order to remove unwanted peaks.

The program is designed for batch processing of many spectra to provide the most efficient use of computer time. However, as few as one spectrum can be processed, if so desired. The control within the program is determined by a control card, which conforms as closely as possible to the OS/360 Job Control Language in order to eliminate confusion in the usage of the program. This type of control allows each individual spectrum to be treated in a different manner during batch processing.

As written, this program will run equally well with on-line and off-line Calcomp plotters. User modifications are made easier through the extensive use of comments and the segregation of each function into well-labelled logical blocks. Common statements are used in order to conserve memory and to facilitate the transfer of data between the different sub-routines.

The program produces Calcomp plots of the spectra, identifying each peak as to the element it represents and providing a camera-ready copy for reproduction or publication (Fig. 1).

The length of the plot is automatically scaled to the number of points (channels) on the X-axis. The Y axis is normally eight inches long. The length of the plot can be set to any desired value for increased resolution by the use of a control card parameter. Through the use of another specified parameter, the plot can be scaled to fit a Xerox 7000 series reducing copier, which can then produce a handy 8½ x 11 inch copy. The entire plot can be enlarged or reduced by any amount within the limits of the plotter by the use of a third control parameter. The plotting format allows the interchangeable use of 12-inch and 30-inch plotter paper. An easily-read printed output is also produced, which lists the input data, the control statements, and their resulting flag values, along with the integration and peak determination results.



3/15/72 JUGO BAUX STUB #21 O.L. #2 PHOTO #2 1000 CTS

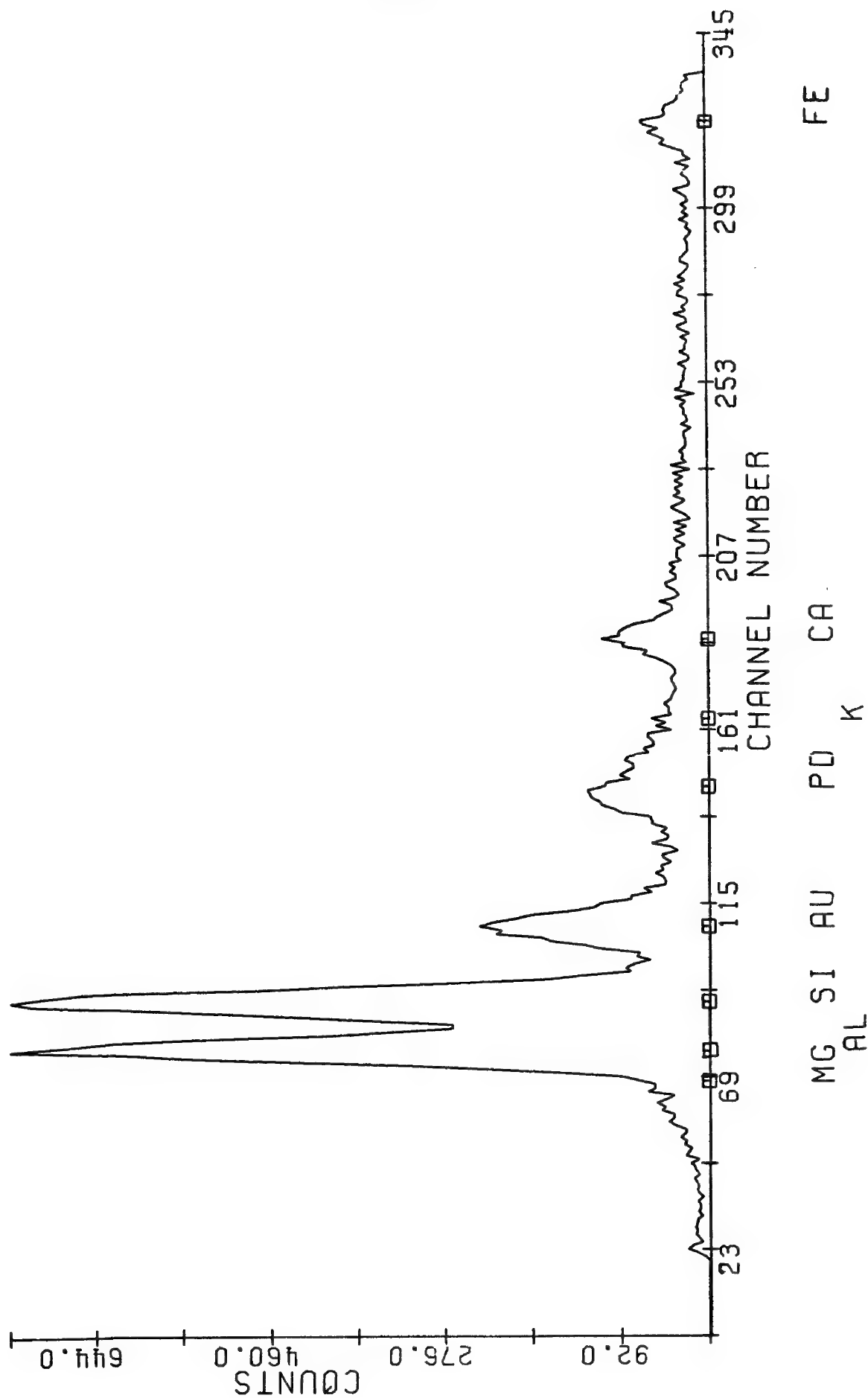


Fig. 1. A representative plot of the X-ray data from a Bauxite sample.

BACKGROUND SUBTRACTION FOR  
ENERGY DISPERSIVE XRAY SPECTRA

J. C. Russ  
EDAX Laboratories  
div. of Nuclear Diodes, Inc.  
4509 Lindsey Drive  
Raleigh, North Carolina

Spectra obtained by Energy Dispersive Analysis of Xrays (EDAX) with electron excitation contain background in addition to the peaks from characteristic photons emitted by the elements in the specimen. This background includes negligible contributions from such sources as cosmic radiation and spurious electronic noise pulses, but for the most part is due to photons of Bremsstrahlung from the specimen. This is the non-characteristic ("white") radiation generated by the deceleration of electrons deflected by the electrostatic fields surrounding the atoms in the target. The general shape of the energy distribution of Bremsstrahlung is a function of electron energy, and the total intensity increases proportional to beam current and the average atomic number of the target. However, the energy distribution is modified significantly by absorption within the sample and thus becomes dependent on takeoff angle and target composition. Since the mass absorption coefficients of different elements vary non-linearly with energy and change abruptly at the respective absorption edges, there is no way to use a general analytical expression for the shape of Bremsstrahlung. In fact, this is not generally possible even between absorption edges.

For quantitative analysis it is necessary to use the total counts for the element(s) of interest, subtracting the background underlying the peak. This is even more important for EDAX spectra than for conventional wavelength-dispersive spectra because the broader peaks cover a greater amount of background, often including an absorption edge either of the element itself or another element in the sample. The use of conventional background subtraction methods used in other fields (eg. gamma-ray or chromatographic spectra) is not satisfactory since these rely on interpolation or extrapolation of the background on one or both sides of the peak. These methods can rarely accomodate the non-linear shape of Bremsstrahlung and can never handle the discontinuities associated with absorption edges. It is the inaccuracy of these methods that has been primarily responsible for the cases of poor accuracy (especially at low concentrations) reported when using EDAX spectra for quantitative calculations.

This paper reports a new and unique method of background subtraction that avoids this limitation and is therefore particularly well suited to EDAX spectra. It can also be used for other types of spectra having background resulting from other physical processes. Understanding the method is facilitated by considering the EDAX spectra

in the frequency domain, in which it consists of four relatively distinct components: 1) the very low frequency continuously but non-linearly varying "overall" background; 2) intermediate frequencies from the characteristic xray peaks; 3) high frequency channel-to-channel fluctuations that result from the normal statistics of xray detection; and 4) ultra-high frequencies that result from the discontinuous steps in background at absorption edges. Not all of the information on edges is at these ultra-high frequencies, but enough to adequately model the effect on peak intensities remains. Techniques using single windows to discriminate against high frequencies to eliminate noise are fairly common. Instead we selectively preserve components 2 and 4. As a fringe benefit this filtering technique also provides some smoothing of the spectrum, although not as much as can be obtained with different frequency filters or by a least-squares averaging method. There is also a modest but useful improvement in the resolution of overlapping peaks. These two factors enable the method to reveal peaks that are often not obvious in the original spectrum as shown in Figure 1.

The accuracy of the background subtraction is critical to obtaining accuracy in any subsequent calculations. To evaluate the precision and reproducibility we measured 20 spectra from an alloy steel and calculated the coefficient of variation (standard deviation expressed as a percentage of the mean) for the total number of counts integrated in a window on the chromium peak before and after background subtraction. The table below also lists the coefficient of variation expected simply on the basis of counting statistics. The increase in actual variation is not significantly greater than that expected.

	MEAN	C.V.(%)	STAT. C.V.(%)
Before subtraction	173,393	0.65	0.24
After subtraction	141,684	0.87	0.42

To evaluate accuracy we measured a series of specimens with silicon in aluminum oxide in concentrations varying from 0.5 to 3.0%. The resulting plot of concentration vs. intensity (after background subtraction) is linear and intersects the origin within 0.01% which is less than the detection limit in this matrix. By comparison the use of a linear interpolation method using the background below the Al peak and above the Si peak overestimates the peak area; the I vs. C curve shows a residual error of 0.11% Al and also gives a poorer fit to a straight line.

This background subtraction method is well suited to use in an on-line minicomputer, requiring about 10 seconds for a typical 400 channel spectrum. The same unit can perform the other necessary operations including spectrum stripping, peak integration and mathematical calculation of quantitative correction factors using a ZAF type model.

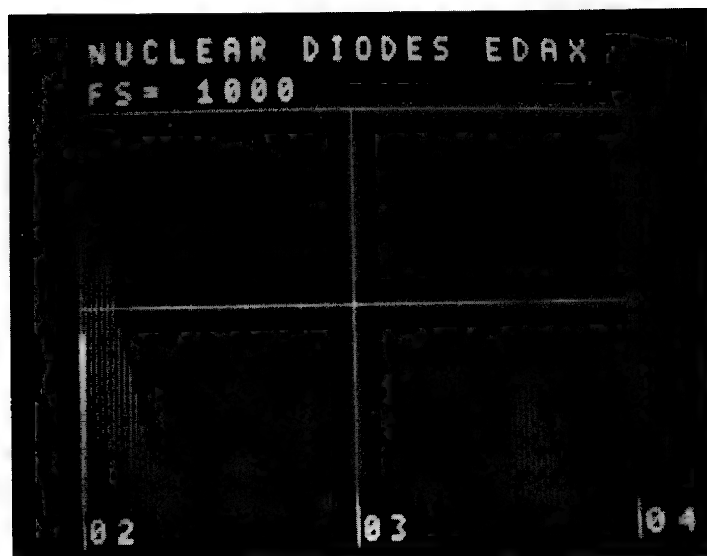


Figure 1. Spectrum before (dots) and after (bars) background subtraction.

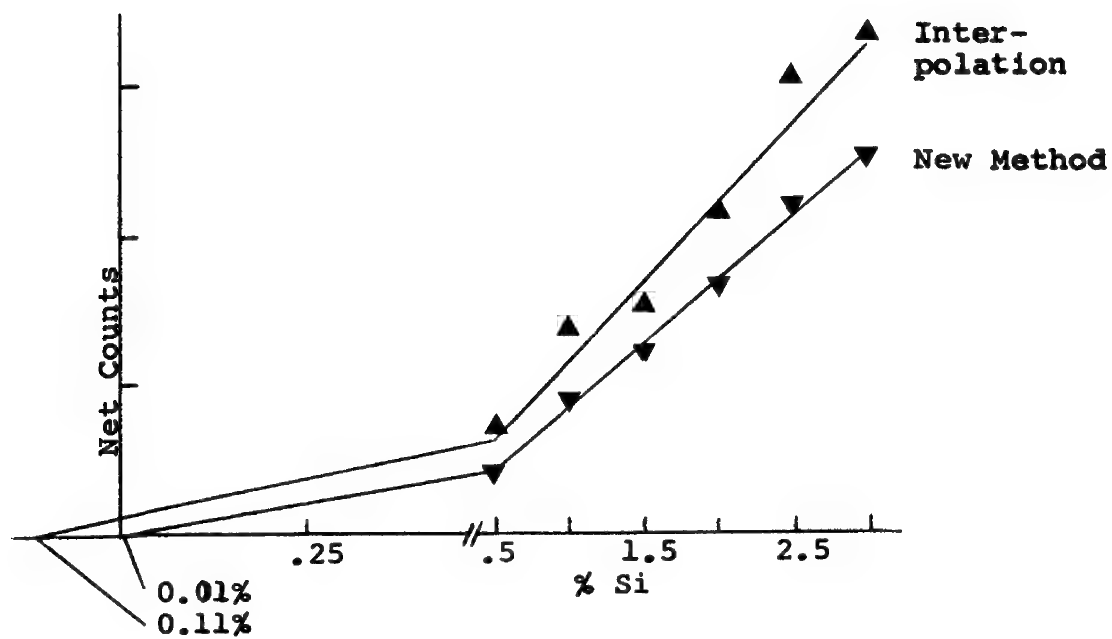


Figure 2. Intensity vs. Concentration plots using conventional linear interpolation and new background subtraction methods.

MATHEMATICAL SMOOTHING OF X-RAY SPECTRA  
OBTAINED WITH SEMICONDUCTOR DETECTORS

Michael W. Vannier and Lloyd V. Sutfin

Children's Hospital Medical Center  
Orthopedic Research Laboratories  
Boston, Massachusetts 02115

There are two sources of noise in x-ray energy analysis spectra: the statistical nature of x-ray production and ionization fluctuations within the detector. This noise manifests itself as channel-to-channel variations when the spectra are accumulated in multichannel analysers. The effects of the channel-to-channel variation are particularly pronounced in spectra obtained at low counting rates resulting in relatively few counts per channel, as in the microanalysis of thin biological specimens.

The removal of this statistical noise component simplifies later processing and improves the limitations on the degree of resolution enhancement that is possible. The first and higher derivatives are very sensitive to noise fluctuations present in the raw spectrum, and small peaks may be indiscernable in the presence of noise if the peak locations are found by inspecting the first derivative.

Several methods have been used to smooth gamma ray spectra prior to spectrum decomposition. The least squares fitting of a polynomial to the spectrum and recalculation of the spectrum by weighted averages has been used extensively in data smoothing (1,2). More recently, Grosswendt (3,4) introduced a modification to this procedure which takes into consideration the behavior of the spectrum between the sampled points. Inouye, et al. (5) have used digital band pass-filtering of the Fourier transform of the spectrum to remove the frequencies most associated with noise. The value of these frequencies is determined by the energy calibration of the spectrometer. Golay (6) has shown the equivalence of data smoothing by least squares procedures and by digital filtering in the limiting case.

According to the central limit theorem (8), the distribution of the sum of  $n$  independent random variables approaches the Gaussian distribution for  $n$  sufficiently large. Applying this theorem to the generation of x-ray fluorescence spectra, we would expect the noise intensities to have a normal distribution centered at zero (7). In order to quantitatively estimate the effectiveness of the various smoothing techniques, we have obtained the mean, standard deviation and probability distribution of noise intensities removed from the raw spectra. (Noise removed is found by subtracting the smoothed result from the original spectrum.) In addition, the centers and areas of peaks as well as the total number of counts in the spectra were monitored to detect changes due to the various smoothing techniques. Also, the first difference for each spectrum and its smoothed counterpart were calculated and the number of maxima and minima in the spectrum (noted as points where the first difference changes sign) were determined. Excluding the presence of peaks due to sample composition, the

number of such points is directly related to the noise content of the spectrum.

The results of this study indicate that for noisy spectra the Fourier transform technique for statistical noise removal may be superior. However, the proper smoothing filter function must be chosen. Significant losses in resolution can occur using the least squares techniques, especially if the raw spectrum is very noisy, and the amount of noise left in the spectrum is usually greater. However, for spectra which are relatively noise free, i.e., when count rates are high and peak and peak/background values are favorable, both techniques approach each other and the least squares technique may be preferable since it is more easily implemented and is suitable for use with the small dedicated computers being used more and more frequently in microanalysis.

#### REFERENCES

1. Savitzky, A. and Golay, M.J.E., Anal. Chem. 36,1627 (1964).
2. Yule, H.P., Nucl. Instr. Meth. 54,61 (1967).
3. Grosswendt, B., Nucl. Instr. Meth. 93,461 (1971).
4. Grosswendt, B., PTB-Mitteilungen 2/71, 83-89 (1971).
5. Inouye, T., Harper, T. and Rasmussen, N.C., Nucl. Instr. Meth. 67,125 (1969).
6. Golay, M.J.E., IEEE Trans. Computers C-21,299 (1972).
7. Schwartz, M., Information Transmission, Modulation and Noise, p. 373 ff, (McGraw Hill, New York, 1959).
8. Panter, P.F., Modulation, Noise and Spectral Analysis, p. 127, (McGraw Hill, New York, 1965).

AN APPROACH TO QUANTITATIVE SEM ANALYSIS

H.P. Hotz

Qanta/Metrix Division  
Finnigan Corporation  
Sunnyvale, California.

When an energetic electron within a scanning electron microscope (SEM) or microprobe enters a sample of matter a number of processes can take place in order for it to slow down and stop. The more important of these are bremsstrahlung, the loss of energy by radiation as a result of acceleration, and electron ejection resulting in the production of x-rays. If only these primary events took place, the emitted intensity of characteristic x-rays would be exactly proportional to the concentrations of the elements present. However, secondary processes are important and the resulting interrelations are mathematically multiply connected. Consequently a description of the probability of the radiation of a photon of a given energy into a detector in terms of fundamental processes is possible only by means of models or by a Monte Carlo calculation scheme. Either way, the result is that the intensity of characteristic x-rays is given as a complicated function of the concentrations and the flux in the incident electron beam. A large number of computer programs have been developed for calculating these intensities. In application, one measures the intensities and wishes to calculate the concentrations. This is done by iteration; a set of concentrations are chosen and intensities calculated, which are then compared with the experimental ones and the trial concentrations corrected and the whole process repeated until one is satisfied with the result. A successful procedure converges to the correct answer.

Present reduction programs have generally been written for use with electron microprobes and goniometer-diffraction-spectrometers. As long as a line unambiguously belonging to each element is resolved by a solid state detector, these programs should be equally applicable to data obtained with a solid state detector and an SEM. The solid state detector makes possible a great reduction in the required electron beam current and more rapid data accumulation. The geometry in a SEM - solid state system is different from that in a microprobe.

It has become common to use small dedicated digital computers to process and store the photon spectrum as it is acquired by a solid state detector attached to a SEM. One naturally expects that it may be possible to use this same computer to make the concentration calculations. A little arithmetic quickly shows that this expectation is not as likely as one might expect due to the large size of existing microprobe reductions programs. However, further examination shows that by elimination of data relating to elements not presently under consideration and by efficient programming, the reduction is possible and the Qanta/Metrix KOREX program is a successful result.

The KOREX program is another example of fluorescence, absorption, atomic number correction schemes. The iteration scheme suggested by Criss and Birks<sup>1</sup> is used. Backscatter is determined by a polynomial fit to the values of Duncomb and Reed.<sup>2</sup> The primary radiation is calculated by the method of Philibert and Tixier.<sup>3</sup> Absorption is taken into account using the model of Philibert<sup>4</sup> except that the geometry is adapted to the SEM situation. This point will be discussed in more detail. Fluorescence by characteristic lines makes use of Castaing's<sup>5</sup> equation except that for programming convenience a weight factor is added to allow use of any characteristic line in the analysis. No correction is made for fluorescence caused by continuous radiation since this is expected to be small.

One notes that the resultant mathematical structure is quite complex and since approximate models are used in deriving it, its success can be regarded as an empirical fit to the experimental situation. Thus additional corrections having a similar mathematical form or effect are not needed if the calculation is standardized against a known sample. For this reason KOREX is designed to use a standard. This procedure avoids any uncertainties in absolute detector efficiency, additional absorbers in the x-ray path, and absolute beam current. In addition the method can result in higher precision since standards close in composition to the unknowns may be used. Reproducibility is determined by counting statistics in taking the data and not by the reduction method. Experimental tests of the KOREX program will be presented.

#### References:

1. J.W.Criss and L.S.Birks, "The Electron Microprobe", T.D.McKinley, K.F.J.Heinrich and D.B.Wittry, Ed., John Wiley & Sons, Inc., New York, New York. 1966 p.217.
2. P.Duncumb and S.J.B.Reed, "Quantitative Electron Probe Microanalysis, National Bureau of Standards (U.S.) Special Publication 298", K.F.J.Heinrich, Ed. p.133.
3. J.Philibert and R. Tixier, *ibid.*, p.13.
4. J.Philibert, "X-Ray Optics and X-Ray Microanalysis", Academic Press, New York, New York, p. 379.
5. K.F.J.Heinrich, "Analytical Chemistry," Vol 44, p. 353 (1972).



Escape Peaks in Si(Li) Detectors\*

John B. Woodhouse

Materials Research Laboratory  
University of Illinois, Urbana, Illinois 61801

Calculation and experiment indicate that the escape peak associated with any monochromatic radiation detected in a lithium drifted silicon detector is never greater than 1.5% of the main peak intensity. The relation between the counts recorded in the escape peak,  $I_e$ , the main counts,  $I_o$ , the K-shell fluorescence yield,  $\omega_K$ , the K absorption edge jump ratio for Si,  $r$ , the absorption coefficient for the monochromatic radiation in Si,  $\mu_o$ , and that for Si  $K\alpha$  radiation in Si,  $\mu_e$ , is

$$I_e = \frac{1}{2} I_o \cdot \omega_K \cdot \frac{(r-1)}{r} \left\{ 1 - \frac{1}{a} \log(1 + a) \right\}$$

where  $a = \mu_o / \mu_e$ .

Experiments with a commercial Energy Dispersive Spectrometer, having a lithium drifted silicon detector, mounted on a scanning electron microscope and using a series of pure element samples to produce a range of monochromatic wavelengths, gave data in fair agreement with the calculated curve.

Low energy lines were difficult to use in these experiments because of the rapidity with which the background varies at energies below about 3 keV.

The calculated expression should also be applicable to lithium drifted germanium detectors in which the escape peaks are expected to be much greater than those found in Si(Li) detectors because of the higher value of the fluorescence yield of that element.

The accompanying figure gives the curve for Si(Li) detectors calculated from absorption data due to Heinrich (1) and using 0.035 for the fluorescence yield of Si, a value derived from Fink et al. (2).

References

1. Heinrich, K. F. J., "X-ray Absorption Uncertainty," The Electron Microprobe, 296-377, John Wiley, New York, 1966.
2. Fink, R. W., Jopson, R. C., Mark, H., Swift, C. D., "Atomic Fluorescence Yields," Rev. Mod. Phys. 38, 513, 1966.

\*This research was supported in part by the U. S. Atomic Energy Commission under Contract AT(11-1)-1198.

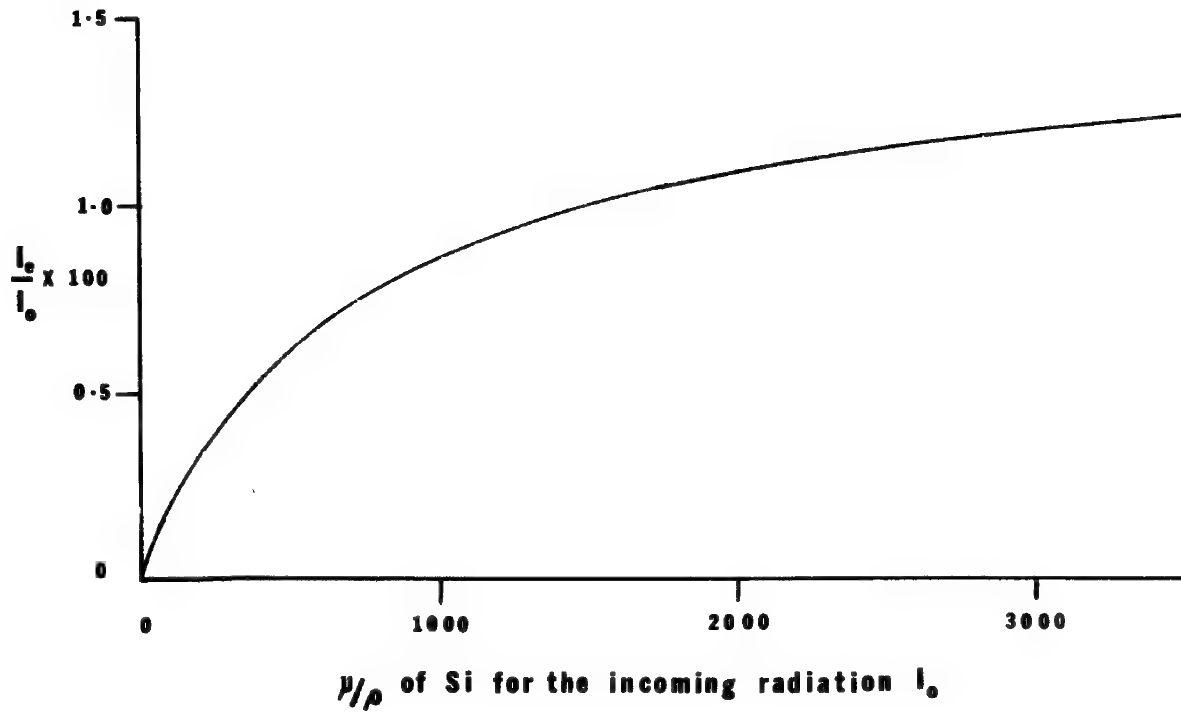


Figure 1.

# A METHOD FOR THE AUTOMATIC LOCATION AND IDENTIFICATION OF PEAKS OBSERVED IN ENERGY DISPERSIVE X-RAY SPECTRA

Ted E. Keller  
Case Western Reserve University  
Department of Computer Engineering

Henry R. Thresh\*  
Chase Brass & Copper Company

## I. INTRODUCTION

The rapid development of Si (Li) detectors has provided the microprobe analyst with the capability of collecting large quantities of spectral data in comparison with the output of wave length spectrometers. This situation creates an imbalance between data collection and interpretation, if manual inspection of recorded spectra is used in conjunction with an energy table of selected X-ray emission lines. Therefore an automated approach is often desirable.

The initial part of spectra interpretation is concerned with peak location. Several algorithms are available in the literature which can be applied to this problem. In this work we considered three basic algorithms which are (i) determining the peak positions by the changes in slopes between data points accounting for the statistical uncertainty of the background as related to an emerging peak [1], (ii) mathematical smoothing of the spectra and interrogation of the smoothed data for changes in slope [2], [3] and (iii) a cross-correlation technique which finds an assumed structure, such as a peak, within the spectra [4],[5]. Once this peak position is found, irrespective of the method used, an energy equivalent is derived from a calibration routine used in conjunction with an appropriate energy table. We selected the cross correlation technique for application to this problem.

## II. MATHEMATICAL CONCEPT

The correlation function can be defined [4],[5] as follows;

$$C(\tau) = \lim_{T \rightarrow \infty} (2T)^{-1} \int_{-T}^T f(t)g(t+\tau)dt$$

\*This author is now associated with the Argonne National Laboratory

where  $f(t)$  is the functional form of the structure to be isolated,  $g(t)$  is the spectra detected and is assumed to be of the form  $g(t) = a f(t) + b$  where  $a$  and  $b$  are constants. In a practical situation one realizes (i) the data collected is discrete rather than continuous, (ii) the limit condition will have to be relaxed, and (iii) the integration must be approximated by a summation. The correlation function can now be approximated by:

$$C(\tau) = \sum_{t=0}^{n-1} f(t)g(t+\tau)$$

such that  $n$  defines the number of data points i.e. channels. In general,  $f(t)$  will only be significant over a few channels therefore it is convenient to define a 'window' width  $M$  to encompass the significant channels. To correctly apply this technique to energy peaks,  $f(t)$  must assume the functional form of the structure it is to locate in the spectra (a gaussian) and a background must be subtracted from the data. As suggested by Black [4], this background can be approximated by:

$$A(\tau) = M^{-1} \sum_{i=t}^{t+M-1} g(i)$$

To permit one standard deviation ( $1\sigma$ ) of statistical fluctuation, the background to be subtracted will be  $B(\tau) = A(\tau) + \sqrt{A(\tau)}$ . The correlation function then becomes in its final form:

$$C(\tau) = \sum_{t=0}^{M-1} f(t)[g(t+\tau) - B(\tau)]$$

This function will produce a positive correlation only in those areas where a peak exists, and negative correlation elsewhere. The peak positions may then be determined by examining the maxima of the positively correlated spectra and converted to an energy equivalent to be compared with suitable energy table.

### III. PROGRAM DESCRIPTION

The program is written in FORTRAN V for the UNIVAC 1108 multi processor system. At the present time, the program requires approximately 4K core storage. The program can handle spectra containing up to 50 peaks, returning a list of elements which occur within a specified energy width of the peak position. Energy library of the elements is sufficiently flexible to permit revisions to suit users needs. The program is controlled by a set of instructions allowing for, (i) automatic calibration, (ii) in-line documentation, (iii) processing with optional table listing and plot of the original spectra.

### IV. CONCLUSIONS

This program has been found to be a powerful procedure in the rapid interpretation of large volumes of spectral data. However, the analyst should exercise caution in the area of trace elements and completely overlapping peaks.

## V. REFERENCES

- [1] R. Gunnink and J.B. Niday; " Quantitative Analysis of Unknown Mixtures by Computer Reduction of Ge(Li) Spectra ", Mod. Tr. in Act. Anal., Vol 2, p. 1244, 1969.
- [2] A. Savitzky and M.J.E. Golay; " Smoothing and Differentiation of Data by Simplified Least Squares Procedures ", Anal. Chem., Vol. 36, p. 1627, 1964.
- [3] H.P.Yule; " Mathematical Smoothing of Gamma Ray Spectra ". Nuc. Instr. and Meth., Vol. 54, p. 61, 1967.
- [4] W.W. Black; " Application of Correlation Techniques to Isolate Structure in Experimental Data ", Nuc. Instr. and Meth., Vol. 71, p. 317, 1969.
- [5] A.L. Connelly and W.W. Black; "Automatic Location and Area Determination of Photopeaks ", Nuc. Instr. and Meth., Vol. 82, p. 141, 1970.

## THE RAPID IDENTIFICATION OF MICROCONSTITUENT PHASES IN COMMERCIAL SILICON

Arnold F. Kolb, Microscopy Laboratory, Dow Corning Corporation  
Donald R. Beaman, Microscopy Laboratory, The Dow Chemical Company

The synthesis of methyl chlorosilanes is based on the direct process fluid bed reaction of powdered silicon with methyl chloride vapor above 300°C. (1) Some elements present as impurities catalytically affect the nature and extent of reaction. (2) The purpose of this study was to learn how these elements may be recognized, and to determine how they are associated with each other as intermetallic compounds in the solid silicon.

### Optical Identification of Phases

Microconstituent phases in silicon were characterized microscopically by their reflected polarization colors and extinction angles using tungsten illumination. The color and intensity of the intermetallic compounds were observed with and without crossed polars at various positions during microscope stage rotation. Tentative classification into four principal groups of intermetallic compounds was made. The inclusions in the silicon matrix were photographed to provide a record of their location and appearance for subsequent electron probe examination.

Figure 1 illustrates, as an example, one of the inclusions analyzed with 15 phases identified as to their location in the inclusion. Using reflected light with slightly uncrossed polars, the various crystalline phases present are shown. Color photomicrographs illustrating the appearance of these phases under reflected polarized light will be shown. The characteristic polarization colors and optical features of the phases found in silicon are sometimes appreciably dependent on the presence of minor constituent elements. The electron probe was utilized to ascertain this dependence. The optical characteristics upon which this classification was based, and the elements contained in each compound determined with the aid of an energy dispersive spectrometer, are shown in Table I.

### Qualitative Identification of Phases

To establish with certainty the chemical identity of the optically recognized phases in these inclusions, the optically analyzed samples, with their inclusions, were subsequently analyzed in the electron probe. Using Nomarski interference contrast microscopy, the phases are visible by their polishing relief features, as shown in Figure 2; and phases representative of the four component groups of Table I are indicated. For each optically identified phase in each inclusion, a photograph was made of the x-ray energy spectrum of that phase, using an energy dispersive spectrometer (EDS). Some phases not subjected to optical analysis were identified with the EDS. There were 13

general phase compositions found, and they contained the following combinations of elements:

AlSiFe*	SiFe*	AlSiFeMn	AlSiCa	SiTiVCrFeMn	AlSiFeNi
AlSiFeCa*	SiTiVFeCr*	SiTiVFe	TiSiFe	AlSiFeCaNi	AlSiFeNiTi
*Denotes optically characterized phases.					AlTiFeNiCu

From the energy spectrum data it was observed that two phases, which by optical data appeared only slightly different, did vary in their chemical composition. Qualitative energy data indicated that one of these phases consisted of AlSiFeMn and the other was AlSiFeCa, indicating Ca and Mn substitution in this compound are not distinguishable from each other optically with sufficient reliability.

### Quantitative Analysis of Phases

The largest and most representative phases were quantitatively analyzed with the wavelength dispersive spectrometer. The exact location of the probe spot is shown in Figures 1 and 2 by the carbon contamination spot on the inclusion phases. The quantitative data shown in Table II were obtained from the x-ray intensity ratios using the Duncumb and Reed atomic number correction, (4) Duncumb and Shield's absorption correction (5) Heinrich's  $\sigma$  value, (6) and the Reed characteristic fluorescence correction. (7) Only one of the compounds, SiFe, did not meet the normal standards for quantitative reliability. The quantitative results are satisfactory in view of the small size of some of the particles. The combination of optical polarized light characteristics and the photomicrographs of the inclusions, together with the energy spectrum data and quantitative probe results, has made possible an accurate correlation between optical appearance and chemical composition. Thus rapid visual identification of the principal microconstituent phases in commercial silicon is now possible.

### References

1. R. O. H. Voorhoeve, Organosilanes: Precursors of Silicones, Elsevier, New York, 1967.
2. M. N. Short, Microscopic Determination of the Ore Minerals, U.S. Geological Survey Bulletin No. 914, 1940.
3. E. N. Cameron, "The Study of Opaque Minerals in Reflected Light," ASTM Symposium on Microscopy (1959), pp. 39-73.
4. P. Duncumb and S. J. B. Reed in Quantitative Electron Probe Microanalysis, K. F. J. Heinrich, Ed., NBS Special Publ. 298, 1968, p. 133.
5. P. Duncumb and P. K. Shields, in The Electron Microprobe, T. D. McKinley, K. F. J. Heinrich and D. B. Wittry, Eds., Wiley N.Y., 1966, p. 284.
6. K. F. J. Heinrich, in Advances in X-ray Analysis, J. Newkirk, G. Mallett and H. Pfeiffer, Eds., Plenum Press, N.Y., Vol. 11, 1968, p. 40.
7. S. J. B. Reed, Brit. J. Appl. Phys., 16, 1965, p. 913.

TABLE I. OPTICAL CHARACTERIZATION OF PHASES IN SILICON

Component Group	Phases	Polarization Colors*				Compound**
		Plane Light	Intensity	Nicols Crossed	Nicols Off 5°	
I	5,6,8,9,12,14	Pinkish cream. Changes to gray on stage rotation.	Strong	Yellow in 2 positions. Medium yellow-brown in 2 positions. 4-ZnC positions.	Orange-yellow and brilliant blue.	SiFe
II	1,3,7,10	Pale yellow.	Very weak	Nearly constant dark brownish-gray.	Nearly constant lighter brownish gray.	AlSiFeCa
III	2,11	Pale yellow.	Weak	Medium dark gray in 2 positions. Dark orange-brown in 2 positions. 4-ZnC positions.	Light gray and dark orange-brown.	AlSiFe
IV	4,15	Cream	Moderate	Light gray. 2-ZnC positions.	Slate gray at extinction. Pale gray-orange at 45° positions.	SiFeTiCrVMn
V	Matrix	Light grayish-yellow.	None	Gray-black	Dark gray.	Si

\*Tungsten illumination, 3050°F

\*\*Qualitative designation - based on optical and EDS data



TABLE II. QUANTITATIVE ANALYSIS OF INCLUSIONS BY ELECTRON PROBE\*

<u>Inclusion</u>	<u>Al**</u>	<u>Si</u>	<u>Ca</u>	<u>Ti</u>	<u>V</u>	<u>Cr</u>	<u>Mn</u>	<u>Fe</u>	<u>Ni</u>	<u>Total</u>
A	26.9	31.5						39.2		97.6
B	23.1	32.2	6.2					34.8		96.3
C		41.6						49.5		91.1
D		46.0		30.8	1.1	4.3	0.3	16.5		99.0
E		33.8		0.1	1.5	31.1	0.7	30.7		97.9
F		51.3		7.6	18.3	20.3		3.2		100.7
G		51.1		10.4	35.4			1.8		98.7
H	33.4	35.0	25.8							94.2
I	24.1	32.9	6.2					35.2	2.0	100.4
J	44.2	17.4					0.5	32.2	4.2	98.5

\* $E_0 = 15$  KV,  $\psi = 18^\circ$ 

\*\*Weight %, corrected

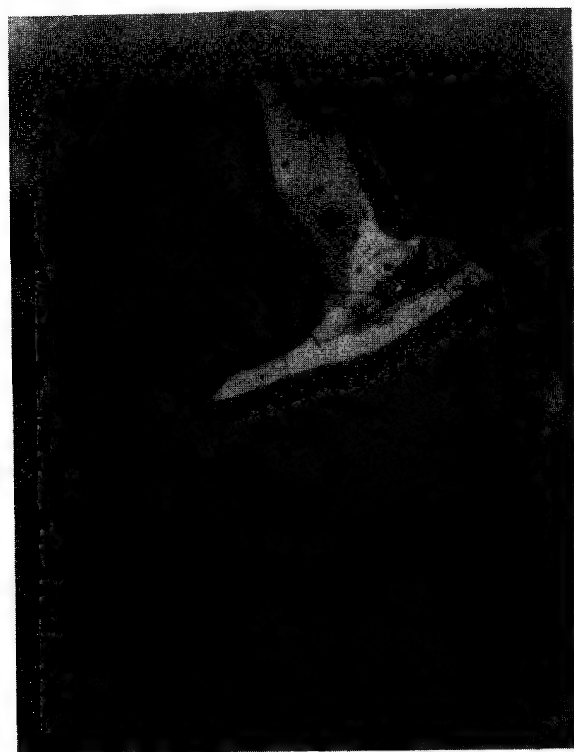


Figure 1  
Inclusion in Silicon - 250X  
Differentiation of Phases with  
Reflected Polarized Light



Figure 2  
Inclusion as in Figure 1 - 400X  
Location of Analysis Points and  
Principal Phases

## Retrospective Identification- The Analysis of Microspheres

H. Edward Mishmash  
3M Company, Saint Paul, Minnesota

A long existing problem that has confronted anyone who desired to tag a material is that there has not existed a satisfactory non-radiotracer type method. In some specific cases, addition of small amounts of a non-contaminating material, such as a metal oxide, to a product has worked to a degree. However, in most applications this has been extremely limited because the level of the tracer needed was either prohibitively high or ruined the product. Also, this type of coding is quite limited with respect to changing of tagging elements and their concentration limits.

A system of tagging has been developed, using the analytical capabilities of the electron probe, that can be useful for a great many applications and avoid the above mentioned problems. The technique is based on the fact that microspheres can be made and coded with varying known compositions and concentrations of several elements; and small amounts of these beads can be added to a material or product. By changing the bead composition, the material can be identified, by analysis of the spheres, as to its source and time of manufacture.

The entire system is hinged on the ability to perform a satisfactory analysis on perhaps a single spherical particle in the 30-100 $\mu$  size range. It is obvious that the instrument of choice is the electron probe; a MAC 400 was used in this work. One of the preliminary areas of possible application that was studied was that of explosive tagging. For the system to be useful for this, the microspheres had to be able to survive a blast and be recoverable without an excess of tedious preparation.

Figure 1 is a scanning electron photomicrograph of a typical ceramic microsphere that has been recovered from a test explosion. There has been a slight amount of injury to the sphere, but it is still in good shape for analysis.

The technique for recovery and isolation of the microspheres is relatively simple. In the case of the explosive study, a large amount (up to several pounds) of debris is taken from the blast site. This is first sieved through screens and the material in the appropriate size range is saved. The beads are made of high density materials so that after washing with water and drying, the remainder of the residue is floated away with methylene diiodide, which is a liquid having a specific gravity high enough to float most silicious material. From the remaining material, which is then dried, the spheres can be removed and mounted on an adhesive coated slide for analysis.

Figure 2 shows how these appear under the microscope in relation to other particles of similar density. Microspheres from ten test explosions have been examined and identified according to the coding elements, with the bead concentration of 1 part per 1000 in the explosive. The exact concentration of the spheres in the debris is not known of course, but it has to be extremely low. This points out the advantage of this system in other applications which can only tolerate a slight tagging addition.

There are two alternatives available with regard to the electron probe analysis, those being the choice of a strict quantitative analysis or a comparative semiquantitative method. The comparative method, with corrections only being made for background, was chosen for several reasons, one of them being the ease of analysis. There are several million different combinations available by varying the minor percentage coding elements in the bead matrix in steps of a factor of two and under these circumstances a semiquantitative or comparative analysis only are needed. Other problems such as those associated with standards, any manufacturing inconsistencies, and different electron probe variations would also be minimized.

Three additional possible problem areas had to be studied to be certain of the validity of this system; homogeneity, concentration gradients among lots necessary for no possible inconsistencies, and the reproducibility or accuracy of analyzing a spherical particle. The major concern was over the last problem and Table I shows the results of these studies. In brief, the homogeneity of the beads appears to be satisfactory for good analysis, concentration gradients of a factor of two are more than adequate, and the reproducibility is essentially the same as that obtainable with mounted and polished samples which provide a flat surface normally required for electron microprobe analysis.

Although this study mentions the results from the explosive investigation, the applications of this technique are certainly not limited to just that problem. A few other areas that might have possible use include drugs, paint, tax stamp adhesive, gun powder, synthetic base materials and other "self-detective" applications. This technique utilizing the electron probe can provide a manufacturer or government agency with a way to tag a material and have positive proof of its origin or use.

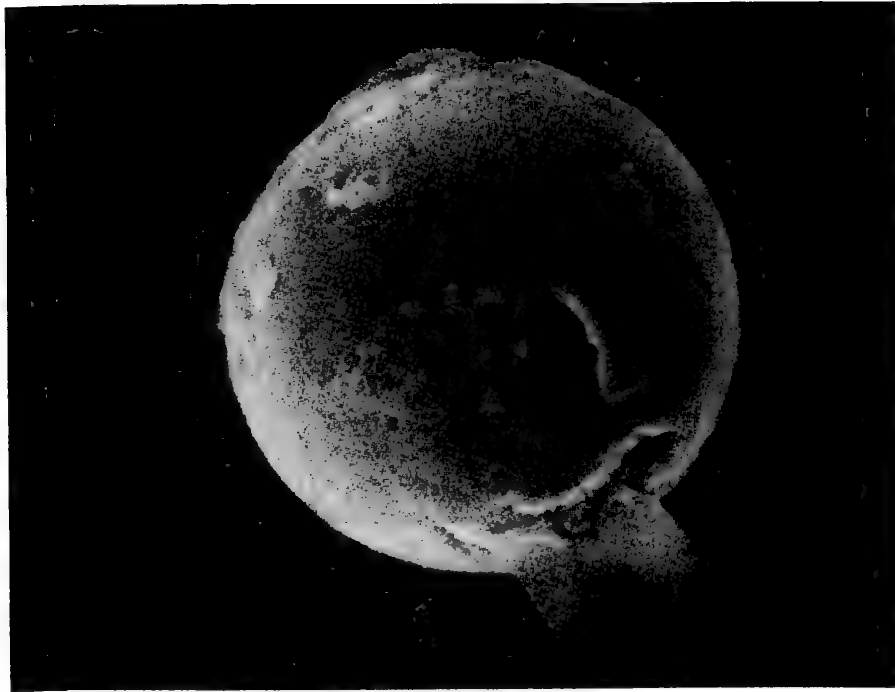


Figure 1. Scanning electron micrograph of microsphere recovered from explosion. 900X

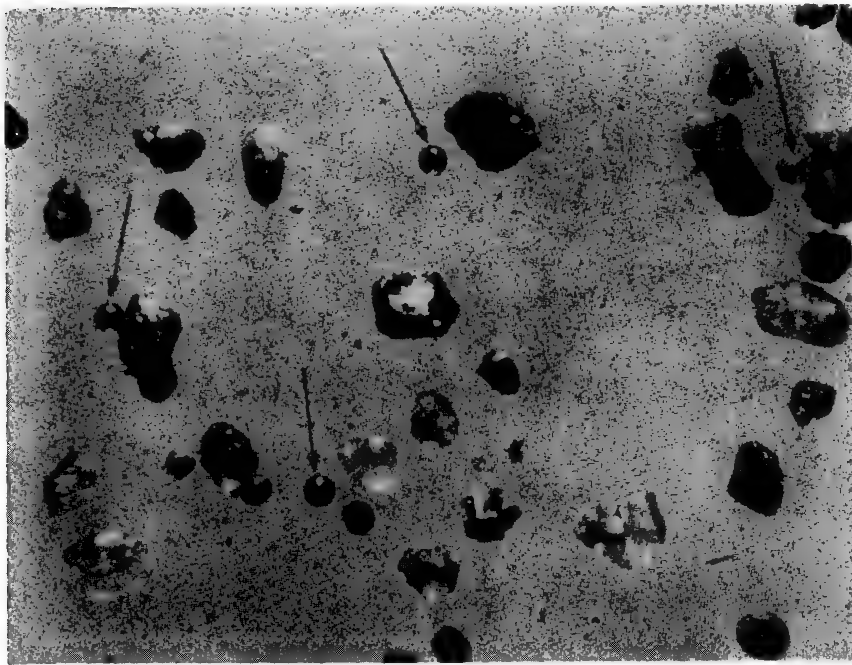


Figure 2. Optical micrograph of microspheres recovered from test explosion. Irregular shapes are particles of similar density.

# 82D

## Analysis of Microspheres

### Bead Composition(%)

	<u>Bead Lot #1</u>	<u>Bead Lot #2</u>
TiO <sub>2</sub>	96.7	91.9
Zn	.1	.2
Sr	2.2	2.1
Zr	1.0	2.5
Cd		1.3
Ce		2.0

## Analysis of Beads for Zirconium

	<u>1 Bead 10 X</u>	<u>10 Beads 1X</u>
	<u>Unpolished</u>	
Bead Lot 1	$v = 5.63$ $\bar{x} = 365(338-380)$	$v = 11.01$ $\bar{x} = 386(352-448)$
	<u>Polished</u>	
	$v = 6.21$ $\bar{x} = 368(337-401)$	$v = 6.26$ $\bar{x} = 365(338-401)$
	<u>Unpolished</u>	
Bead Lot 2	$v = 2.37$ $\bar{x} = 907(883-941)$	$v = 3.03$ $\bar{x} = 1122(1085-1167)$
	<u>Polished</u>	
	$v = 3.21$ $\bar{x} = 941(899-975)$	$v = 4.03$ $\bar{x} = 884(845-903)$

## Analysis of Beads for Zinc & Strontium

	<u>Zn</u>	<u>Sr</u>
Bead Lot 1	$v = 4.87$ $\bar{x} = 889(833-939)$	$v = 5.76$ $\bar{x} = 290(274-313)$
Bead Lot 2	$v = 6.79$ $\bar{x} = 1760(1566-1872)$	$v = 8.64$ $\bar{x} = 272(249-306)$

Data corrected for bkgd only.

25KV @ .01μA, 100 sec. counts

$$v = \frac{100}{\bar{x}} \sqrt{\frac{(x-\bar{x})^2}{n-1}}$$

## NbC MICROPROBE REFERENCE MATERIALS - AN EFFORT IN DEVELOPMENT

Fred W. Postma, Jr.  
James E. Ferguson

Union Carbide Nuclear Corporation, Development Division  
Y-12 Plant  
Oak Ridge, Tennessee

The need for homogeneous, well-characterized standards among the metal carbides has become apparent as the non-stoichiometric nature of these materials has been realized by the Y-12 Plant Microprobe Laboratory in its search for  $\text{NbC}_{1.00}$ .

Four materials were provided by Source A having chemical compositions reported as shown in Table 1. For reference, Table 1 includes the stoichiometric compositions for NbC and  $\text{Nb}_2\text{C}$  ( $\text{NbC}_{0.5}$ ) with the Y-12 Plant microprobe analyses of the four materials. The microprobe analysis of carbon in the Source A materials was not attempted using a 100 percent carbon standard due to the uncertain absorption coefficient.

The reference materials from Source A were synthesized by arc melting. From many hundred microprobe measurements on these materials over a period of months their inhomogeneity was observed to be  $\leq \pm 0.2$  weight percent  $\sigma$  with an X-ray spot diameter  $\leq 1.3$  micrometers. This precision was obtained by operating the analyzer within the region over which the instrument variations were normalized. This normalized condition was obtained by accumulating counts for fixed beam current with a specimen current on  $\text{NbC}_x$  of approximately 50 nanoamps at 20 kilovolts. If this total variation were assumed to be analysis variation, then the worst case limit of precision for the analysis of samples would be  $\pm 0.2$  weight percent.

Unfortunately, the chemical analyses provided with the Source A reference materials appeared to be in error for the  $\text{NbC}_{0.98}$  material. This error increased the imprecision of analysis for a single measurement, when using the standard curves obtained from these four materials, to  $\sigma = \pm 0.8$  weight percent for niobium and  $\sigma = \pm 0.4$  weight percent for carbon (Figure 1).

Reference materials for  $\text{NbC}_x$  were obtained from two additional sources (B and C) and were analyzed as samples using the standard curves from the Source A materials. Though the microprobe results (Table 2) were in good agreement with the Source B and C values provided, lack of chemical analysis prevents the use of these materials as standards for quantitative microprobe analysis. Finally, in an attempt to obtain  $\text{NbC}_x$  reference materials with firmly established chemical values, several  $\text{NbC}_x$  materials were prepared at the Y-12 Plant by vapor deposition.

Three of these materials, having inhomogeneities  $\leq \pm 0.1$  weight percent in excess of the instrument imprecision, were selected for complete chemical characterization. Six replicates of each material were analyzed for niobium, total carbon, and free carbon (from which combined carbon was obtained). The materials were examined by emission spectrography for trace impurities. Since the range of the chemical analyses approximated that of the microprobe measurements, these materials should constitute well-characterized reference materials (Table 3).

#### Acknowledgements:

The reference materials used as samples and early standards were provided by:

Los Alamos Scientific Laboratory  
Mid-West Probe Users Group  
Westinghouse Astronuclear Laboratory

The Y-12 reference materials were synthesized and made available by A. J. Caputo of the Development Division, Y-12 Plant.

Table 1  
COMPOSITION OF SOURCE A REFERENCE MATERIALS

Material	Weight Percent				
	Nb			C	
	Theoretical	Chemical <sup>(1)</sup>	Microprobe <sup>(3)</sup>	Theoretical	Chemical <sup>(1)</sup>
$\text{NbC}_{0.50}$	93.9			6.1	
$\text{NbC}_{0.75}$	91.2	90.8	$91.4 \pm 0.2^{(2)}$	8.8	8.5
$\text{NbC}_{0.82}$	90.4	90.3	$90.2 \pm 0.2$	9.6	8.9
$\text{NbC}_{0.90}$	89.6	89.6	$89.2 \pm 0.1$	10.4	9.8
$\text{NbC}_{0.98}$	88.8	88.8	$89.6 \pm 0.2$	11.2	11.1
$\text{NbC}_{1.00}$	88.6			11.4	

(1) Source A analysis

(2) Standard Deviation for the average

(3) Calculated using MAGIC by Colby

Table 2  
RESULTS OF ANALYSIS OF SOURCE B AND SOURCE C REFERENCE MATERIALS

Material	Weight Percent			
	Reported Composition		Microprobe Analysis Against Source A Reference Materials	
	Nb	C	Nb	C
B	88.87 <sup>(2)</sup>	11.13	88.7 ± 0.1 <sup>(1)</sup>	11.1 ± 0.1 <sup>(1)</sup>
C	88.55 ± 0.6 <sup>(3)</sup>	11.45 <sup>(3)</sup>	88.3 ± 0.1 <sup>(1)</sup>	11.0 ± 0.1 <sup>(1)</sup>

- (1) Standard Deviation ( $\sigma$ ). Accuracy unknown.  
 (2) Value obtained by difference from weight gain attributed to carbon during synthesis. Starting materials for synthesis verified to be of high purity by chemical analysis.  
 (3) Value provided by electron microprobe analysis of seven independent laboratories.

Table 3  
Y-12 REFERENCE MATERIALS

Material	Weight Percent			
	Chemical Analysis (Avg. ± $\sigma$ )		Standard Deviation of Microprobe Analysis ( $\sigma$ )	
	Nb	C	Nb*	C
V	88.66 ± 0.08	11.20 ± 0.02	± 0.2	± 0.6
W	88.76 ± 0.04	11.14 ± 0.02	± 0.3	± 0.5
Y	89.10 ± 0.04	10.83 ± 0.02	± 0.3	± 0.5



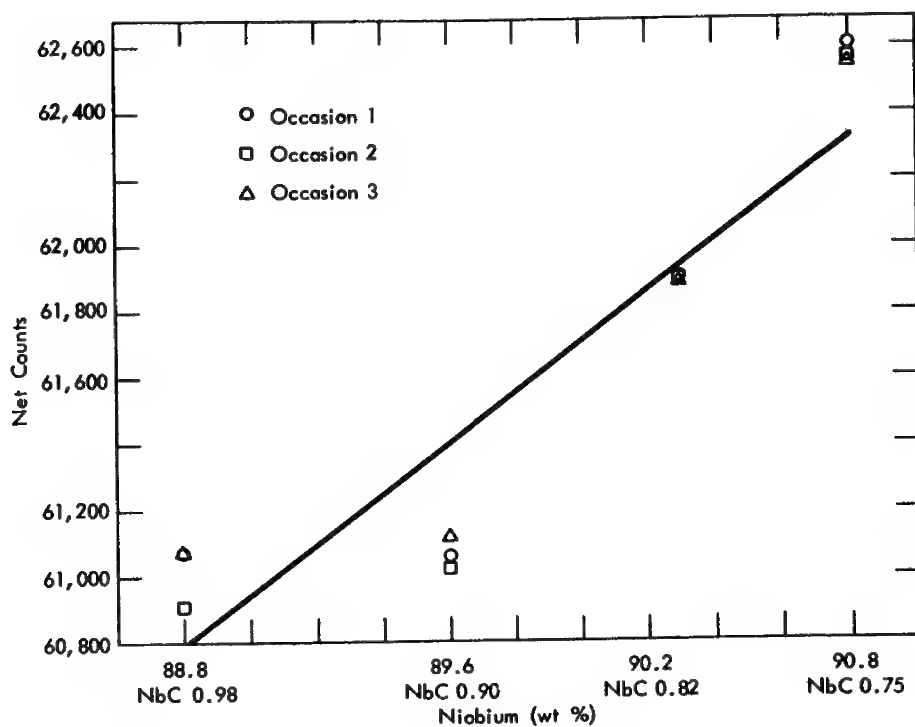
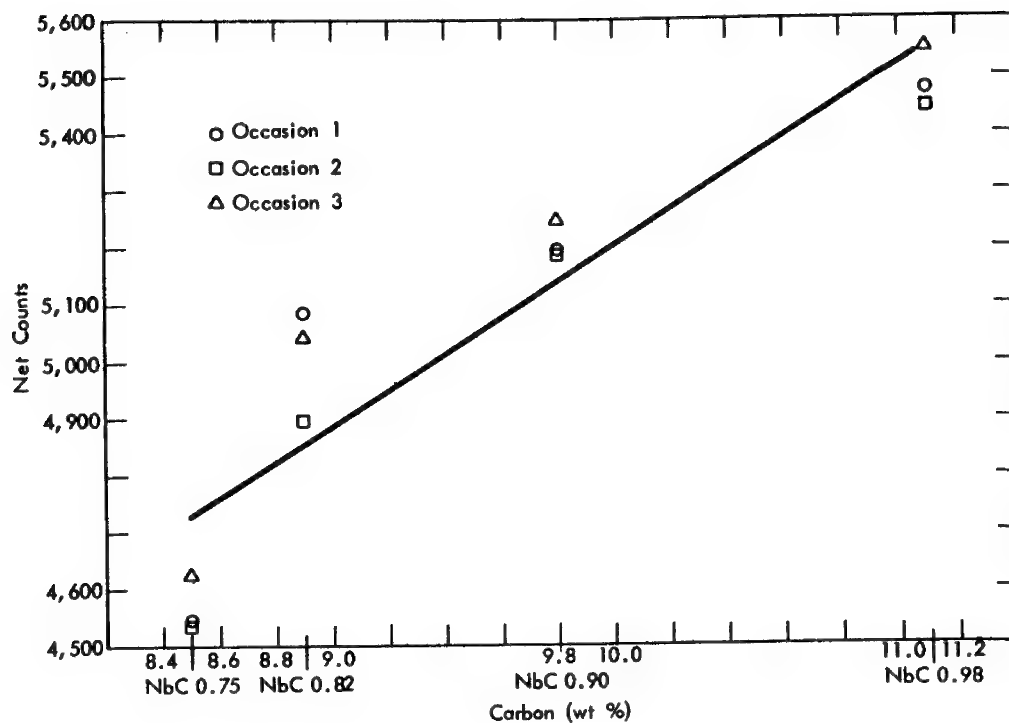


FIGURE 1. NIOBIUM AND CARBON ELECTRON MICROPROBE CALIBRATION USING SOURCE A REFERENCE MATERIALS

## AUGER ELECTRON SPECTROSCOPY IN A DIFFUSION PUMPED SEM

E. K. Brandis and R. A. Hoover

IBM Components Division

East Fishkill Facility

Hopewell Junction, New York 12533

In 1970, MacDonald et al<sup>1</sup> demonstrated that Auger electron spectroscopy could be combined with scanning electron microscopy to perform chemical analysis on a surface with submicron spatial resolution.

Auger electron spectroscopy is sensitive to the first few monolayers of the surface and requires a vacuum environment which will minimize contamination of the sample surface by polymerization of hydrocarbons. The usual approach is to operate the entire vacuum system with a pressure less than  $10^{-9}$  Torr.<sup>2</sup> For practical reasons, it is extremely difficult to convert an existing SEM to operate at such vacuum levels. However, another approach to control the number of hydrocarbons at a sample surface was first demonstrated by Castaing et al.<sup>3</sup> He showed that by directing a stream of gas onto the sample, the buildup of a layer caused by the polymerization of hydrocarbon molecules by the incident electron beam could be prevented. More recently, Brandis et al<sup>4</sup> showed this technique could also be used to minimize hydrocarbon contamination in a high-resolution SEM utilizing oil diffusion pumps and a specimen vacuum environment in the low  $10^{-7}$  Torr range.

The feasibility of controlling the number of hydrocarbon molecules near the surface of the sample was demonstrated. This indicated Auger electron spectroscopy could be performed in an oil diffusion-pumped SEM, taking advantage of its submicron spatial resolution.

A Physical Electronics Auger electron spectrometer system was attached to a Cambridge Stereoscan equipped with an anticontamination gas jet system. Figure 1 shows the carbon contamination buildup on a sputter cleaned surface as a function of time while the electron beam scans an area of 10 by  $20\mu\text{m}$ .

The escape depth of 272eV electrons is approximately  $10\text{\AA}$ , indicating a carbon buildup rate of  $0.5\text{\AA}/\text{min}$ . In Fig. 2 buildup rate is measured on a thin chromium film. In this case the rate was considerably lower, indicating the carbon contamination rate is strongly dependent on the sample. In addition, a small Physical Electronics ion sputtering gun was mounted on a sideport of the SEM. With this attachment it is now possible to clean the surface or do chemical profiling on submicron areas. A feature of the ion gun is that the sputtering rate can be adjusted so the electron beam's carbon deposition rate equals the ion gun's removal rate when operated without the anticontamination gas jet.

Directing a stream of argon gas towards the silicon sample stopped carbon buildup. The Auger peaks of carbon, as well as silicon, remained unchanged when the sample was irradiated for 45 minutes, as shown in Fig. 3. This demonstrates a very practical solution to the contamination problem that heretofore prevented Auger electron spectroscopy from being a viable scanning electron microscopy technique.

## REFERENCES

1. N. C. MacDonald, H. L. Marcus, and P. W. Palmberg, Proc. 3rd Annual Scanning Electron Microscope Symposium, IIT Research Institute, Chicago, 1970, p. 25.
2. N. C. MacDonald, Proc. 4th Annual Scanning Electron Microscope Symposium, IIT Research Institute, Chicago, 1971, p. 89.
3. R. Castaing and J. Descamp, C. R. Acad. Sci., Paris, 238, 1954, 1506.
4. E. K. Brandis, F. W. Anderson, and R. A. Hoover, Proc. 4th Annual Scanning Electron Microscope Symposium, IIT Research Institute, Chicago, 1971, 505.

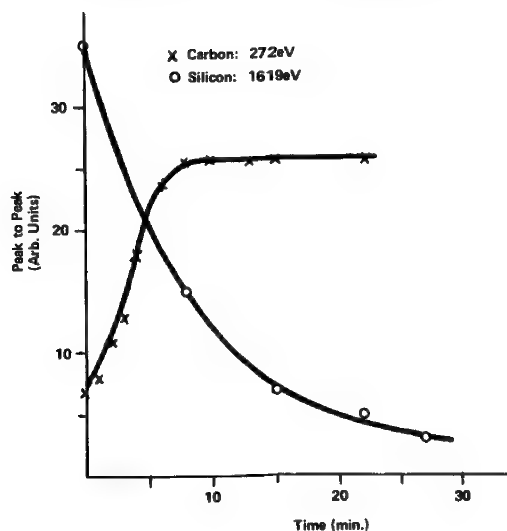


Fig. 1. Silicon and carbon Auger intensities vs time after sputter cleaning.

Sample: Si;

$E_B = 10\text{keV}$ ;

Specimen Current =  $5 \times 10^{-8}\text{ A}$ ;

Area =  $10 \times 20\mu\text{m}$

Vacuum  $\cong 5 \times 10^{-7}\text{ Torr}$

Fig. 2. Carbon and chromium Auger intensities vs time.

Sample: Cr evaporated on Si;

$E_B = 10\text{keV}$ ;

Specimen Current =  $5 \times 10^{-8}\text{ A}$ ;

Vacuum  $\cong 5 \times 10^{-7}\text{ Torr}$ ;

Area =  $10 \times 20\mu\text{m}$

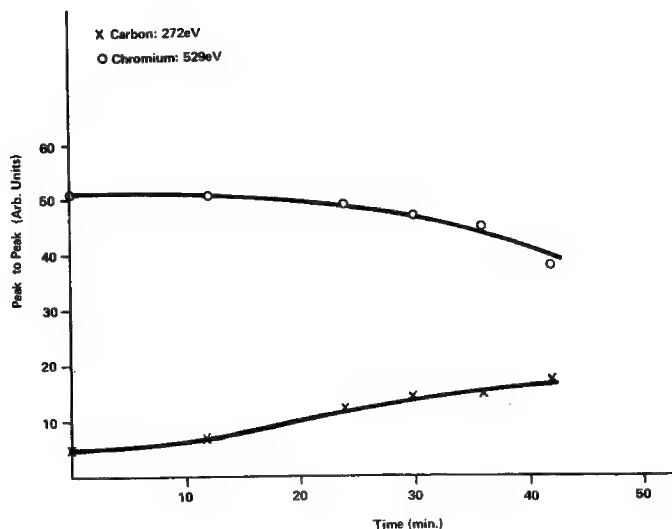


Fig. 3. Carbon and silicon Auger intensities vs time.

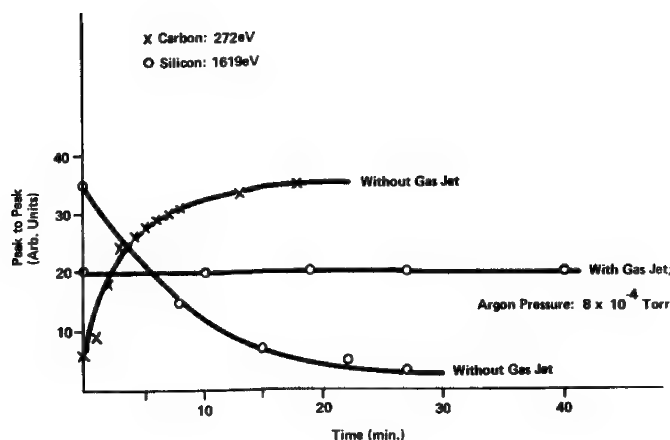
Sample: Si;

$E_B = 10\text{keV}$ ;

Specimen Current =  $5 \times 10^{-8}\text{ A}$ ;

Area =  $10 \times 20\mu\text{m}$ ;

Vacuum  $\cong 5 \times 10^{-7}\text{ Torr}$





**INDEX OF AUTHORS  
AND  
THEIR AFFILIATIONS**

# INDEX OF AUTHORS AND THEIR AFFILIATIONS

		<u>Paper Number</u>
Anderson, C. A.	Hasler Research Center, Applied Research Laboratories, 95 La Patera Lane, Goleta, California 93017	39
Armstrong, J. T.	Department of Chemistry, Arizona State University, Tempe, Arizona 85281	36
Baun, W. L.	Air Force Materials Laboratory (LN), WPAFB, Ohio 45433	11
Bayard, M. A.	W. C. McCrone Associates, Inc., 2820 South Michigan Avenue, Chicago, Illinois 60616	37
Beaman, D. R.	Dow Chemical Company, 1703 Building, Midland, Michigan 48640	7 81
Bence, A. E.	Department of Earth & Space Sciences, State University of New York, Stony Brook, New York 11790	51
Bernstein, I. M.	Department of Metallurgy & Material Science, Carnegie-Mellon University, Pittsburgh, Pennsylvania 15213	54
Besmann, T.	Department of Nuclear Engineering, 261 Sweeney Hall, Iowa State University, Ames, Iowa 50010	22
Bishop, W. R.	American Medical Association, Division of Medical Education, 535 North Dearborn Street, Chicago, Illinois 60610	23
Blanchard, M	Planetology Branch 245/5, NASA-MSC-TN6, Houston, Texas 77058	53
Bolon, R. B.	General Electric Company, Corporate Research and Development, Schenectady, New York 12345	35
Bomback, J. L.	United States Steel Corporation, Research Laboratory, 125 Jamison Lane, Monroeville, Pennsylvania 15146	54
Brandis, E. K.	IBM, East Fishkill Facility, Hopewell Junction, New York	73
Brinen, J. S.	Central Research Division, American Cyanamid Company, Stamford, Conn. 06904	9

# INDEX OF AUTHORS AND THEIR AFFILIATIONS

		<u>Paper Number</u>
Brown, J. D.	The University of Western Ontario, Faculty of Engineering Science, London 72, Ontario, Canada	5
Brown, R. W.	Lockheed Electronics Company, Inc., Houston Aerospace Systems Division, 16811 El Camino Real, Houston, Texas 77058	50
Bundtzen, R.	U. S. Public Health Service, Dept. of Health Education & Welfare, Arctic Health Research Center, Fairbanks, Alaska 99701	42
Buseck, P. R.	Department of Chemistry, Arizona State University, Tempe, Arizona 85281	36
Butler, E. M.	Argonne National Laboratory, Materials Science Division, Argonne, Illinois 60439	58
Chiu, K. Y.	University of Southern California, Department of Materials Science, Los Angeles, California 90007	14
Clanton, U. S.	NASA-MSC-TN6, Houston, Texas 77058	52
Clarke, D. R.	University of Cambridge, Department of Physics, Cavendish Laboratory, Free School Lane, Cambridge, England	17
Colby, J. W.	Bell Telephone Labs., 555 Union Boulevard Allentown, Pennsylvania 12103	67
Coleman, J. R.	University of Rochester Medical Center, Dept. Radiation Biology & Biophysics, Rochester, New York 14642	41 44 48
Conrad, W. M.	The University of Texas M.D. Anderson, 6723 Bertner Avenue, Houston, Texas 77025	46
Conty, C.	Commissariat a l'Energie Atomique, 78 Jouy En Josas, FRANCE	59
Cook, A. W.	U. S. Public Health Service, Dept. of Health Education & Welfare, Arctic Health Research Center, Fairbanks, Alaska 99701	42
Corlett, M. I.	Queen's University, Department of Geological Sciences, Kingston, Ontario, Canada	33

# INDEX OF AUTHORS AND THEIR AFFILIATIONS

		<u>Paper Number</u>
Cunningham, G.	NASA-Ames Research Center, Planetology Branch 245/5, Moffett Field, California 94035	53
DeVries, R. C.	G.E. Research and Development Center, P. O. Box 8, Schenectady, New York 12301	18
DiGiacomo, G.	IBM Component Division, B/330-145D/60A, East Fishkill Facility, Hopewell Junction, New York 12533	74
Dodd, C. G.	Philip Morris Research Center, Physics Research Division, 210 East Main Street, Richmond, Virginia 23219	12
Edie, J. W.	University of Iowa, Dental Research Laboratory (Oakdale), Iowa City, Iowa 52240	43
Eichen, E.	Ford Motor Co., Scientific Research Staff, P. O. Box 2053, Dearborn, Michigan 48121	65
Eminhizer, L. B.	317 Mineral Sciences Building, The Pennsylvania State University, University Park, Pennsylvania 16802	72
Estill, W. B.	Sandia Laboratories, Livermore, California 94550	13
Everhart, T. E.	University of California, Dept. of Electrical Engineering and Computer Sciences, Berkeley, California 94720	15
Ferguson, J. E.	Union Carbide Corp., Nuclear Division, Y-12 Plant, Oak Ridge, Tennessee 37830	
Finger, L. W.	Geophysical Laboratory, 2801 Upton Street, N.W., Washington, D. C. 20008	68
Foster, M. S.	Argonne National Lab., Chemical Engineer- ing Division, 9700 South Cass Avenue, Argonne, Illinois 60439	57
Frederickson, A. R.	Air Force Cambridge Research Laboratories (AFSC), Hanscom Field, Bedford, Massachusetts 01730	31
Fujino, N.	Department of Applied Physics, Osaka University Yamada-kami, Suita, Osaka, JAPAN	6



# INDEX OF AUTHORS AND THEIR AFFILIATIONS

		<u>Paper Number</u>
Gavrilovic, J.	Walter C. McCrone Associates, Inc., 493 East 31st Street, Chicago, Illinois 60616	62
Gair, S.	Sandia Laboratories, Livermore, California 94550	13
Guernet, J.	Commissariat a l'Energie Atomique, 78 Jouy En Josas, France	59
Greer, R.	Department of Nuclear Engineering, 261 Sweeney Hall, Iowa State University, Ames, Iowa 50010	22
Hadidiacos, C	Geophysical Laboratory, 2801 Upton St., N.W. Washington, D. C. 20008	68
Hall, T. A.	Cavendish and Biological Microprobe Laboratories, Free School Lane, Cambridge CB2 3RQ, England	40
Heil, R. H.	Image Analysis Products, Image Analysing Computers Inc., 40 Robert Pitt Drive, Monsey, New York 10952	64
Heindenreich, R. D.	Bell Telephone Laboratories, Murray Hill, N.J. 07974	26
Heinrich, K. F. J.	National Bureau of Standards, Metallurgy Division, B118 Materials Bldg., Washington, D. C. 20234	3
Henke, B. L.	University of Hawaii, Dept. of Physics and Astronomy, Watanabe Hall, 2505 Correa Road, Honolulu, Hawaii 96822	8
Hinthorne, J. R.	Hasler Research Center, Applied Research Laboratories, 95 La Patera Lane, Goleta, California 93017	39
Holdsworth, E. F.	Department of Chemistry, Arizona State University, Tempe, Arizona 85281	36
Hotz, H. P.	Qanta/Metrix Division, 120 Industrial Way, San Carlos, California 94070	78
Ingrey, S. J.	Bell-Northern Research, Box 3511, Station "C", Ottawa, Ontario, Canada	25

# INDEX OF AUTHORS AND THEIR AFFILIATIONS

		<u>Paper Number</u>
Johnson, C. E.	Argonne National Lab., Chemical Engineering Division, 9700 South Cass Avenue, Argonne, Illinois 60439	57
Judd, G.	Rensselaer Polytechnic Institute, Materials Division, Troy, New York 12181	32
Karlsson, U. L.	Dental Research Laboratory (Oakdale), University of Iowa, Iowa City, Iowa 52240	43
Keil, K.	Department of Geology and Institute of Meteroitics, The University of New Mexico, Albuquerque, New Mexico 87106	49
Keller, T. E.	Department of Computer Engineering, Case Western Reserve University, 10,900 Euclid Avenue, Cleveland, Ohio 44106	69 80
Kerrick, D. M.	317 Mineral Sciences Bldg., The Pennsylvania State University, University Park, Pennsylvania 16802	72
Kolb, A. F.	Dow Corning Corporation, Microscopy Laboratory, Midland, Michigan 48640	81
Kunz, F.	Ford Motor Co., Scientific Research Staff, P. O. Box 2053, Dearborn, Michigan 48121	65
Kushner, R. A.	Bell Telephone Laboratories, Room 2B201, Murray Hill, New Jersey 07974	28 29
Kusic, G. L.	RC406 Scaife Hall, University of Pittsburgh, Pittsburgh, Pennsylvania 15213	19
Kyser, D. F.	IBM Research Laboratory, K05-281, Monterey & Cottle Roads, San Jose, Calif. 95114	10
Ladle, G. H.	NASA-MSC-TN6, Houston, Texas 77058	52
Lewis, R. L.	Cameca Instruments, Elmsford, New York	38
Lifshin, E.	General Electric Company, Research and Development Center, P. O. Box 8, Schenectady, New York 12301	66 18 35

# INDEX OF AUTHORS AND THEIR AFFILIATIONS

		<u>Paper Number</u>
Lin, R.	GTE Laboratories Incorporated, 208-20 Willets Point Boulevard, Bayside, New York 11360	21
Lubin, P.	GTE Laboratories Incorporated, 208-20 Willets Point Boulevard, Bayside, New York 11360	21
Lund, P.K.	The University of Texas M.D. Anderson, 6723 Bertner Avenue, Houston, Texas 77025	46
Lyons, R. B.	U. S. Public Health Service, Department of Health Education & Welfare, Arctic Health Research Center, Fairbanks, Alaska 99701	42
MacQueen, H. R.	IBM Research Laboratory, K05-281 Monterey and Cottle Roads, San Jose, California 95114	10
McCaughan, D. V.	Bell Telephone Laboratories, Room 2B201, Murray Hill, New Jersey 07974	28 29
McKay, D. S.	NASA-MSC-TN6, Houston, Texas 77058	52
Marciniak, H. C.	University of Southern California Department of Material Science Vivian Hall of Engineering Los Angeles, California 90007	27
Marton, L.	Smithsonian Institution, National Museum of History and Technology, Washington, D.C. 20560	1
Massalski, T. B.	Oberlin College, 205 Barnard House, Oberlin, Ohio 44074	56
Matta, R. K.	University of Pittsburgh, RC406 Scaife Hall, Pittsburgh, Pennsylvania 15213	19
Maurer, G. S.	Oberlin College, 205 Barnard House, Oberlin, Ohio 44074	56
Melliar-Smith, C. M.	Bell Telephone Laboratories, Murray Hill, New Jersey 07974	26
Mencik, Z.	Ford Motor Company, Scientific Research Staff, Box 2053, Dearborn, Michigan 48121	70

# INDEX OF AUTHORS AND THEIR AFFILIATIONS

		<u>Paper Number</u>
Meyer, R. O.	Materials Science Division Argonne National Laboratory Argonne, Illinois 60439	58
Miller, W. G.	Illinois State Geological Survey, 425 Natural Resources Building, Urbana, Illinois 61801	75
Minetti, R. H.	Bell Laboratories, 555 Union Boulevard, Allentown, Pennsylvania 18102	38
Mishmash, H. E.	3M Company - Central Research Labs., P.O. Box 33221, St. Paul, Minnesota 55133	82
Mizer, D	Dow Chemical Co., 1703 Building, Midland, Michigan	7
Morabito, J. M.	Bell Laboratories, 555 Union Boulevard, Allentown, Pennsylvania 18103	38
Morton, R. R. A.	Bausch & Lomb, Analytical Systems Division, 830 Linden Avenue, Rochester, New York 14625	63
Murata, K.	Department of Applied Physics, Osaka University, Yamada-kami, Suita, Osaka, Japan	6
Murphy, V. T.	Room 2B201, Bell Telephone Labs, Murray Hill, New Jersey 07974	28 29
Nilsson, R.	Dept. Radiation Biology & Biophysics, University of Rochester Medical Center, Rochester, New York 14642	48
Nixon, W. C.	Engineering Dept., Cambridge University, England	2
Nishigori, N.	Department of Applied Physics, Osaka University, Yamada-kami, Suita, Osaka, Japan	6
O'Boyle, D. R.	Materials Science Division, Argonne National Laboratory, Argonne, Illinois 60439	58
Ong, P. S.	The University of Texas M.D. Anderson Hospital, 6723 Bertner Avenue, Houston, Texas 77025	46

# INDEX OF AUTHORS AND THEIR AFFILIATIONS

		<u>Paper Number</u>
Ordonez, J.	41 Hagan Drive Poughkeepsie, New York 12003	73
Palmer, T.	Planetology Branch 245/5, NASA-Ames Research Center, Moffett Field, California 94035	53
Panessa, B. J.	4 Washington Square Village, Apt. 6C, New York, New York 10012	19
Parobek, L.	Faculty of Engineering Science, The University of Western Ontario, London 72, Ontario, Canada	5
Partridge, B. C.	Image Analysis Products, Image Analysing Computers, Inc., 40 Robert Pitt Drive, Monsey, New York 10952	64
Peters, B. C.	Dow Chemical Co., 1703 Building, Midland, Michigan 48640	7
Postma, F. W.	Union Carbide Corp., Nuclear Division, Y-12 Plant, Oak Ridge, Tennessee 37830	83
Perrot, M.	Commissariat a l'Energie Atomique, 78 Jouy En Josas, France	59
Reid, A. M.	Lockheed Electronics Company, Inc., Houston Aerospace Systems Division, 16811 El Camino Real, Houston, Texas 77058	50
Ridley, W. I.	Lockheed Electronics Company, Inc., Houston Aerospace Systems Division, 16811 El Camino Real, Houston, Texas 77058	50
Reuter, W.	IBM Research Center, Yorktown Heights, New York 10593	34
Ruscica, R.	Materials Analysis Co., 1960 E. Meadow Circle, Palo Alto, California 94503	42
Russ, J. C.	EDAX Laboratories, Division of Nuclear Diodes, Inc., 4509 Lindsey Drive, Raleigh, North Carolina 27609	76
Saffir, A. J.	1343 Fieldfair Court, Sunnyvale, Calif. 94087	71
Seils, E.	Argonne National Lab., Chemical Engineering Division, 9700 South Cass Ave., Argonne, Illinois 60439	57
Shimizu, R.	Osaka University, Department of Applied Physics, Yamada-kami, Suita, Osaka, Japan	6

# INDEX OF AUTHORS AND THEIR AFFILIATIONS

		<u>Paper Number</u>
Shiraiwa, T.	Department of Applied Physics, Osaka University, Yamada-kami, Suita, Osaka, Japan	6
Simma, D. L.	Bell Telephone Laboratories, Whippany, New Jersey 07981	30
Snetsinger, K.	Planetology Branch 245/5, NASA-Ames Research Center, Moffett Field, California 94035	53
Solomon, J. S.	University of Dayton Research Institute, Dayton, Ohio 45409	11
Solosky, L. F.	Dow Chemical Co., 1703 Building, Midland, Michigan 48640	7
Springer, G.	Falconbridge Nickel Mines Limited, Metallurgical Laboratories, 8810 Yonge Street (P. O. Box 900), Thornhill, Ontario, Canada	4
Sutfin, V.	Orthopedic Research Labs, Children's Hospital Medical Center, 300 Longwood Avenue, Boston, Mass. 02115	77
Swenson, R. A.	Image Analysis Products, Image Analysing Computers Inc., 40 Robert Pitt Drive, Monsey, New York 10952	64
Thomas, R. S.	Department of Geological Sciences Queen's University, Kingston, Ontario, Canada	33
Thompson, L. F.	Bell Telephone Laboratories, Murray Hill, New Jersey 07974	26
Thresh, H. R.	Argonne National Laboratory, Dept. Materials Science, 9700 South Cass Avenue, Argonne, Illinois 60439	69 80
Tolk, N. H.	Bell Telephone Laboratories, Murray Hill, New Jersey 07974	30
Tousimis, A. J.	Biodynamics Research Corporation, 6010 Executive Boulevard, Rockville, Maryland 20852	45 47
Vannier, M. W.	Orthopedic Research Labs, Children's Hospital Medical Center, 300 Longwood Avenue, Boston, Mass. 02115	77

# INDEX OF AUTHORS AND THEIR AFFILIATIONS

		<u>Paper Number</u>
van Zuilichem, A. G.	Adriaan Pauwstraat 34, Den Haag, Holland	60
Vassamillet, L. F.	Mellon Institute of Science, Carnegie-Mellon University, 4400 Fifth Avenue, Pittsburgh, Pennsylvania 15213	55 56
Vieth, D. L.	B118 Materials Building, Metallurgy Division, National Bureau of Standards, Washington, D. C. 20234	3
Vignesoult, N.	Commissariat a l'Energie Atomique, 78 Jouy En Josas, France	59
Villaume, J. F.	The Pennsylvania State University, 317 Mineral Sciences Building, University Park, Pennsylvania 16802	72
von Rosentiel, A.P.	Adriaan Pauwstraat 34, Den Haag, Holland	60
Warner, J. L.	Lockheed Electronics Company, Inc., Houston Aerospace Systems Division, 16811 El Camino Real, Houston, Texas 77058	50
Warner, R. R.	University of Rochester, Strong Hospital, O-162 Dept. of Biophysics, Rochester, New York 14642	41 44 48
Wells, O. C.	IBM Research Center, Thomas J. Watson Research Center, Yorktown Heights, New York	16
Westwood, N. D.	Bell-Northern Research, Box 3511, Station "C", Ottawa, Ontario, Canada	25
White, C. W.	Bell Telephone Laboratories, Whippany, New Jersey 07981	30
Wiesner, J. C.	Department of Electrical Engineering and Computer Sciences, University of California, Berkeley, California 94720	15
Wilson, L. A.	Physical Measurements Applications Scientist, Instrument Division-Varian Associates, 611 Hansen Way, Palo Alto, California 94303	9
Wirth, J. L.	Sandia Laboratories, Livermore, California 94550	13

# INDEX OF AUTHORS AND THEIR AFFILIATIONS

		<u>Paper Number</u>
Wittry, D. B.	Department of Materials Science, VHE 602, University of Southern California, Los Angeles, California 90007	14 27
Wolf, E. D.	Hughes Research Laboratories, Malibu, California 90264	24
Woodhouse, J. B.	University of Illinois, Materials Research Laboratory, Urbana, Illinois 61801	61 79
Yakowitz, H	B118 Materials Bldg., Metallurgy Division, National Bureau of Standards, Washington, D. C. 20234	3
Zenobia, D. I.	Precision Metallurgical Company, Millis, Mass. 02054	71



# EPASA MEMBERSHIP LIST\*

Jerry D. Adey  
Univ. of Oregon Dental School  
611 S.W. Campus Drive  
Portland, Or. 97201

Arden Albee  
Div. of Geological Sciences  
California Institute of Tech.  
Pasadena, Ca. 91109

Leslie O. Albin  
4501 Valerie  
Bellaire, Tx. 77401

Carmelo F. Aliotta  
6 Chiarpardi Place  
Beacon, N.Y. 12508

Thomas F. Anater  
Westinghouse - Bettis  
Box 79  
West Mifflin, Pa. 15122

Chris A. Andersen  
163 Third St.  
Solvang, Ca. 93463

Charles H. Anderson  
ARL  
9545 Wentworth St.  
Sunland, Ca. 91040

D. H. Anderson  
Industrial Lab.  
Eastman Kodak Co.  
343 State St.  
Rochester, N.Y. 14650

John T. Armstrong  
Dept of Chemistry  
Arizona State Univ.  
Tempe, Az. 85281

Charles W. Andrews  
5712 Edgepark Dr.  
Brookpark, Oh. 44142

Kamal Asgar  
1011 N. University  
110 Dental School  
Ann Arbor, Mi. 48104

Clarence W. Austin, Jr.  
404 Hillmont Circle N.W.  
Huntsville, Al. 35805

Bernard Autier  
Cameca Instruments, Inc.  
101 Executive Blvd.  
Elmsford, N.Y. 10523

Donald L. Bagnoli  
RD, Horace Road  
Oak Ridge, N.J. 07438

Alexander K. Baird  
Dept of Geology  
Pomona College  
Claremont, Ca. 91711

Joseph D. Balser  
Kaiser Aluminum & Chem. Corp.  
Center for Technology  
6177 Sunol Blvd.  
Pleasanton, Ca. 94566

William G. Banfield  
National Institutes of Health  
Room 8-B-19, Bldg. 10  
9000 Rockvill Pike  
Bethesda, Md. 20014

Nicholas C. Barbi  
3459 Columbia Dr.  
LaVerne, Ca. 91750

Richard H. Barkalow  
Carnegie-Mellon Univ.  
Mellon Institute  
4400 Fifth Ave.  
Pittsburgh, Pa. 15213

R. W. Barnard  
Bell Labs.  
2000 Northeast Expressway  
Norcross, Ga. 30071

John J. Bart  
RD #2, Dix Road  
Rome, N.Y. 13440

William L. Baun  
7418 N. Dakar Drive  
Dayton, Oh. 45431

Donald W. Beard  
6801 Cochran Road  
Solon, Oh. 44139

D. R. Beaman  
515 Townsend  
Midland, Mi. 48640

Albert H. Beebe III  
29 Eichelberger Drive  
Coraopolis, Pa. 15108

Melvin H. Beeson  
664 Tamarack Drive  
Union City, Ca. 94587

A. E. Bence  
Earth & Space Sciences  
SUNY  
Stony Brook, N.Y. 11790

Leonard J. Bench  
1200 Irene Lane  
Pittsburgh, Pa. 15236

Ralph F. Benck  
316 Bynum Ridge Road  
Forest Hill, Md. 21050

Stephen L. Bender  
128 Spring St.  
Lexington, Ma. 02173

F. N. Bensey, Jr.  
725 Cumberland St.  
Harriman, Tn. 37748

Edgar Berkey  
Westinghouse Research Labs.  
Churchill Boro  
Pittsburgh, Pa. 15235

Carl Berkley  
Medical Research Technology  
Great Notch, N.J. 07424

Eugene P. Bertin  
Room E-120  
RCA Labs.  
Princeton, N.J. 08540

Deane I. Biehler  
Caterpillar Tractor Co.  
Research Dept., Tech. Center E  
Peoria, Il. 61602

Yves C. Bienvenu  
Mellon Institute  
Metal Physics Group  
4400 Fifth Ave.  
Pittsburgh, Pa. 15213

Wilbur C. Bigelow  
Dept. of Chem. & Met. Eng.  
Univ. of Michigan  
Ann Arbor, Mi. 48104

William D. Bingle  
591 Wack Drive  
Rochester, Pa. 15074

L. S. Birks  
Code 7680  
Naval Research Lab.  
Washington, D. C. 20390

Herbert L. Black  
Universal-Cyclops, Spet Steel Div.  
Research & Development Dept.  
Mayer St.  
Bridgeville, Pa. 15017

John W. Blaise  
Turbine Support Div.  
Chromalloy American Corp.  
4430 Director Drive  
San Antonio, Tx. 78219

Roger B. Bolon  
862 Saratoga Rd.  
Ballston, N.Y. 12019

John Bomback  
U.S. Steel Research Center  
Monroeville, Pa. 15146

M. J. Boris  
American Steel Foundries  
3761 Canal St.  
East Chicago, In. 46312

Lloyd G. Bostwick  
1470 Belford Court South  
Merritt Island, Fl. 32952

Janice F. Bower  
Smithsonian Observatory  
60 Garden St.  
Cambridge, Ma. 02138

Linda C. Burns  
Brown & Root - Northrop  
Manned Spacecraft Center  
Houston, Tx. 77058

Barbara Maria Chider  
Box 218  
Yorktown Heights, N.Y. 10598

David E. Boyd  
613 Salisbury Road  
Waverly, Oh. 45661

Garrett A. Busch  
Grumman Aerospace Co.  
Research Dept. PET 26  
Bethpage, N.Y. 11714

Joseph A. Chiero  
408 Lenox St.  
Oak Park, Il. 60302

Francis R. Boyd, Jr.  
126 Hesketh St.  
Chevy Chase, Md. 20015

Douglas R. Bush  
Lehigh Univ.  
Bethlehem, Pa. 18015

Kuang-Yi Chiu  
Dept. of Materials Sciences  
Univ. of Southern Calif.  
Los Angeles, Ca. 90007

Lynn L. Brandvold  
N.M. Bureau of Mines & Mineral  
Resources  
Campus Station  
Socorro, N.M. 87801

Edward M. Butler  
926 Putnam Drive  
Lockport, Il. 60441

Arthur A. Chodos  
Calif. Institute of Tech.  
Div. of Geological Sciences  
1201 E. California St.  
Pasadena, Ca. 91109

Donald D. Briglia  
849 Timlott Lane  
Palo Alto, Ca. 94303

J. W. Butler  
Argonne National Lab.  
9700 South Cass Ave.  
Argonne, Il. 60439

Boleslaus S. Chojnowski  
2 Sunderland St.  
Melville, N.Y. 11746

Edward J. Brooks  
US Naval Research Lab.  
Washington, D. C. 20390

Vincent E. Caldwell  
Armco Steel Corp.  
Research Center  
Curtis St.  
Middletown, Oh. 45042

Wesley I. Clark  
WADCO Corp.  
326 Building, 300 Area  
Richland, Wa. 99352

Dennis B. Brown  
Code 7987  
US Naval Research Lab.  
Washington, D. C. 20390

William J. Campbell  
US Bureau of Mines  
College Park, Md. 20740

Craig D. Clauser  
Materials Engineering Lab.  
Westinghouse  
Box 9175  
Philadelphia, Pa. 19113

Roy W. Brown  
Lockheed Electronics Co.  
16811 El Camino Rd.  
Houston, Tx. 77546

William T. Caneer  
307 Lookout View Ct.  
Golden, Co. 80401

Donald C. Clay  
Alabama & Pacific Ave.  
Brackenridge, Pa. 15014

Basil J. Brudnak  
504 Cheyenne Dr.  
Algonquin, Il. 60102

James D. Carl  
12 Lawrence Ave.  
Potsdam, N.Y. 13676

C. Gordon Cleaver, Jr.  
General Electric Co.  
Vallecitos Nuclear Center  
Vallecitos Road  
Pleasanton, Ca. 94566

Gary G. Brumbaugh  
3808 Arnell Place  
La Crescenta, Ca. 91214

Kenneth G. Carroll  
29 Bowdoin St.  
Cambridge, Ma. 02138

William C. Clinton  
5-A Cryton Apts.  
Rolla, Mo. 65401

George W. Bruno  
14 Walsh Road  
Bedford, Ma. 01730

James E. Cerney  
18530 S. Miles Parkway  
Cleveland, Oh. 44128

Vincent J. Coates  
Coates & Welter Instrument Corp.  
777 N. Pastoria  
Sunnyvale, Ca. 94086

Robert Buchanan  
Perkin-Elmer Ultek Div.  
Box 10920  
Palo Alto, Ca. 94303

James Cerven  
Dept. of Law Enforcement  
515 E. Woodruff Road  
Joliet, Il. 60432

Joel Arthur Cohen  
3173 Wharton Drive  
Yorktown Heights, N.Y. 10598

James R. Buckmelter  
Cambridge Research Labs.  
Hanscom Field  
Bedford, Ma. 01730

William F. Chambers  
Sandia Corp., Org. 1122  
Box 5800  
Albuquerque, N.M. 87115

J. W. Colby  
3125 Linda Lane  
Allentown, Pa. 18103

W. C. Budke  
303 North 31st Ave.  
Yakima, Wa. 98902

Wei H. Chang  
180 Prospect St., Apt. F-5  
East Orange, N.J. 07017

James R. Coleman  
Dept. of Radiation Biology &  
Biophysics  
Univ. of Rochester Medical Center  
Rochester, N.Y. 14620

David L. Burk  
Allegheny Ludlum Steel Corp.  
Research Center  
Brackenridge, Pa. 15014

W. T. Chester  
Denton Vacuum, Inc.  
Cherry Hill Industrial Center  
Cherry Hill, N.J. 08034

Donald K. Conley  
410 Hill Drive  
Allentown, Pa. 18103

George H. Conrad  
Dept. of Geology  
Univ. of New Mexico  
Albuquerque, N.M. 87116

R. Earle Conway  
2030 Wright Ave.  
Richmond, Ca. 94804

Jeanette R. Cooper  
General Electric Co.  
Nela Park  
East Cleveland, Oh. 44112

Louis Cooper  
5728 Ostin Ave.  
Woodland Hills, Ca. 91364

Paul D. Coulter  
Union Carbide Corp.  
Parma Technical Center  
Box 6116  
Cleveland, Oh. 44101

Joseph F. Cox  
1032 Winne Road  
Schenectady, New York 12309

Robert F. Craig  
370 Maple St.  
Danvers, Ma. 01923

Maria Luisa Crawford  
Dept. of Geology  
Bryan Mawr College  
Bryn Mawr, Pa. 19010

John W. Criss  
6686 Naval Research Lab.  
Washington, D. C. 20390

Robert S. Crouse  
851 West Outer Drive  
Oak Ridge, Tn. 37830

Robert F. Cunningham, Jr.  
12841 Ranchwood Road  
Santa Ana, Ca. 92705

Serge Cvikevich  
Dept. 877, Bldg. 300-84  
IBM Components Div.  
Hopewell Junction, N.Y. 12533

James M. Dahl  
1600 Huron Pkwy.  
Ann Arbor, Mi. 48106

Philip N. Dangel  
11000 Cedar Road  
Chase Brass & Copper  
Cleveland, Oh. 44106

Andrew W. Danko  
33 Buena Vista Drive  
Delmont, Pa. 15626

Randolph R. Davis  
3517 Navaho Dr.  
North Highlands, Ca. 95660

Ernest Davidson  
ARL  
9545 Wentworth  
Sunland, Ca. 91040

Mysore A. Dayanada  
School of Materials Science  
& Metallurgical Engineering  
Purdue Univ.  
Lafayette, In. 47906

Robert De Beer  
803 Highview Drive  
Chattanooga, Tn. 37415

H. S. DeBen  
5 Millbrook Lane  
Trenton, N.J. 08638

Phillip B. DeNee  
133 Marion Drive  
McMurray, Pa. 15213

George A. Desborough  
2164 Zang St.  
Golden, Co. 80401

John R. Devaney  
1499 Carroll Drive  
Altadena, Ca. 91001

R. D. Dewey  
9805 Channing Circle  
Richmond, Va. 23235

Harold A. Diehl  
Dow Chemical Co.  
Bldg 241  
Midland, Mi. 48640

Giulio DiGiacomo  
IBM Component Div.  
Bldg. 585, Dept. 60A  
East Fishkill, N.Y. 12524

Arthur S. Doan, Jr.  
Goddard Space Flight Center  
Greenbelt, Md. 20715

Charles G. Dodd  
509 West Drive Circle  
Richmond, Va. 23229

William D. Donnelly  
Dept. of Materials Sciences  
San Jose State College  
San Jose, Ca. 95114

Jean S. Donner  
101 Via Colusa  
Palos Verdes Estates, Ca. 90274

Robert F. Dragen  
Midwest Research Microscopy, Inc.  
Box 6215  
Milwaukee, Wi. 53209

Olden C. Draughn  
5734 So. Ellis  
Chicago, Il. 60637

Frank B. Drogosz  
444 S. Osceola  
Orlando, Fl. 32801

J. Stephen Duerr  
Westinghouse Electric Corp.  
Box 79  
West Mifflin, Pa. 15122

Harris W. Dunn  
Box 827  
Kingston, Tn. 37763

S. A. Durkett  
359 Garden Ave.  
Camden, N.J. 08105

Ben F. Edwards  
1438 Saxony Lane  
Houston, Tx. 77058

Erwin Eichen  
Ford Motor Co.  
Scientific Research Staff  
Box 2053  
Dearborn, Mi. 48010

J. David Eick  
Dept. of Dental Materials  
SUNY at Buffalo  
Buffalo, N.Y. 14214

Lyn Eikrem  
ARL  
9545 Wentworth  
Sunland, Ca. 91040

Leland B. Eminhizer  
Penn State Univ.  
University Park, Pa. 16802

Wesley B. Estill  
Box 969, Dw. 8311  
Sandia Labs.  
Livermore, Ca. 94550

Bernard W. Evans  
Dept. of Geological Sciences  
Univ. of Washington  
Seattle, Wa. 98105

Donald J. Evins  
MAC Div. of ETEC Corp.  
3392 Investment Blvd.  
Hayward, Ca. 94545

Richard P. Fedchenko  
1500 South Shamrock Ave.  
Monrovia, Ca. 91016

James E. Ferguson  
Rt. #3, Box 286V  
Clinton, Tn. 37716

H. Oscar Fritzsche  
4603 Moore Road  
Middletown, Oh. 45042

John T. Gilmore  
Chevron Research Co.  
576 Standard Ave.  
Richmond, Ca. 94804

James F. Ficca  
1221 McKennons Church Road  
Sherwood Park  
Wilmington, De. 19808

Roland W. Furgason  
5481 So. Packard Ave.  
Cudahy, Wi. 53172

Alice J. Gitter  
Box 363, Church St. Sta.  
New York, N.Y. 10008

David File  
807 W. Nevada  
Urbana, Il. 61801

Otto O. Gamba  
Westinghouse - Bettis  
Box 79  
West Mifflin, Pa. 15122

Keith M. Gleason  
777 N. Blue Parkway  
Lee's Summit, Mo. 64063

Kier M. Finlayson  
RCA  
Lancaster, Pa. 17601

Wilbur J. Gamblin  
Kent Cambridge  
7 Wilson Terrace  
Waldwick, N.J. 07463

Everett D. Glover  
Dept. of Geology & Geophysics  
Univ. of Wisconsin  
Madison, Wi. 53706

Mary C. Finn  
Lincoln Lab.  
244 Wood St.  
Lexington, Ma. 02173

Amalendu Ganguli  
717 Bendix Drive  
South Bend, In. 46620

J. I. Goldstein  
Dept. of Materials Science  
Whitaker Lab.,  
Lehigh Univ.  
Bethlehem, Pa. 18015

Charles E. Fiori  
NBS  
Bldg. 222, Room A-132  
Washington, D. C. 20234

Donald C. Gaubatz  
10033 Hillcrest Road  
Cupertino, Ca. 95014

George M. Gordon  
Lawrence Berkeley Lab., Bldg. 62  
Univ. of California  
Berkeley, Ca. 94720

J. J. Fischer  
5 Larch Ct.  
Suffern, N.Y. 10901

Robert Earl Gauldin  
6619 Easton St.  
Los Angeles, Ca. 90022

Jozef Graczyk  
97 Popular Ave  
Hackensack, N.J. 07601

Gordon L. Fisher  
Paul D. Merica Research Lab.  
International Nickel Co., Inc.  
Suffern, N.Y. 10901

John Gavrilovic  
Walter C. McCrone Assoc., Inc.  
493 East 31st St.  
Chicago, Il. 60616

Larry J. Gray  
Code 2511  
Naval Undersea Warfare Center  
San Diego, Ca. 92132

Francis Flaherty  
Gillette Co.  
Gillette Park  
Boston, Ma. 02106

William E. Gawthrop  
Battelle Memorial Institute  
505 King Ave.  
Columbus, Oh. 43201

Daniel B. Green  
Dept. of Endodontics  
Temple Univ. School of Dentistry  
3223 N. Broad Street  
Philadelphia, Pa. 19140

Mario M. Fornoff  
Walcott Drive  
RR #1, Box 212A  
Basking Ridge, N.J. 07920

Dale A. Gedcke  
Ortec, Inc.  
100 Midland Road  
Oak Ridge, Tn. 37830

Raymond T. Greer  
Dept. of Nuclear Engineering  
Iowa State Univ.  
Ames, Iowa 50010

Theodore F. Fox  
OCAMA/MAGCM  
Tinker AFB, Ok. 73145

George J. Georgakopoulos  
Berkeley Lawrence Lab., Bldg 62  
Berkeley, Ca. 94720

Robert Q. Gregg  
3207 Henrietta  
Bartlesville, Ok. 74003

Robert E. Frazer  
317 San Juan Way  
La Canada, Ca. 91011

Jon Gerhard  
6 Muriel Road  
Chelmsford, Ma. 01824

John S. Grosso  
Box 844  
Rochester, N.Y. 14618

Kurt Frederiksson  
Smithsonian Institution  
Washington, D. C. 20560

Mary Ann M. Giles  
810 Prospect Ave.  
Bethlehem, Pa. 18018

Carl A. Grove  
5-2 Forsyth Drive  
Troy, N.Y. 12180

William G. Fricke, Jr.  
Alcoa Tech. Center  
Box 2970  
Pittsburgh, Pa. 15230

Philip M. Giles  
Homer Research Labs.  
Bethlehem Steel Corp.  
Bethlehem, Pa. 18018

Harold E. Guina  
36853 Sunnydale  
Livonia, Mi. 48154

William S. Friedlander  
3M Co.  
3M Center  
St. Paul, Mn. 55119

John V. Gilfrich  
Code 7680  
US Naval Research Lab.  
Washington, D. C. 20390

Klaus Gumz  
Maiden Lane  
Durham, Ct. 06422

William N. Gundaker  
308 Walnut St.  
Irwin, Pa. 15642

Andrew B. Harris  
Caterpillar Tractor Co.  
Peoria, Il. 61606

Gordon E. Hitt  
Watkins Ave.  
Apalachin, N.Y. 13732

K. P. Gupta  
Materials Science Dept.  
SUNY  
Stony Brook, N.Y. 11790

Carl E. Harris  
TRW Equipment Labs.  
23555 Euclid Ave.  
Cleveland, Oh. 44117

Edward R. Holdsworth  
4621 E. Pueblo Ave  
Phoenix, Az. 85040

Ralph G. Gutmacher  
Lawrence Lab. L-404  
Univ. of California  
Livermore, Ca. 94550

Malcolm R. Harvey  
362 Encino Drive  
Livermore, Ca. 94550

Edward W. Holmes  
17 W 034 - 69th St.  
Darien, Il. 60559

Christos G. Hadidiacos  
7832 Stork Road  
Alexandria, Va. 22306

Mohan A. Hebbbar  
Westinghouse  
Materials Engineering Lab.  
Bldg. M  
Lester, Pa. 19113

Tom Huber  
JEOL Inc.  
477 Riverside Ave.  
Medford, Ma. 02155

Arnold Hakkila  
Los Alamos Scientific Lab.  
Box 1663  
Los Alamos, N.M. 87544

Robert H. Heidel  
US Geological Survey  
Bldg. 25, Rm. 2435  
Denver Federal Center  
Denver, Co. 80225

C. R. Hudgens  
6135 Teagarden Circle  
Dayton, Oh. 45449

Larry C. Hall  
Box 1530, Station B.  
Vanderbilt Univ.  
Nashville, Tn. 37203

Robert H. Heidersbach, Jr.  
US Army CERL  
Box 4005  
Champaign, Il. 61801

Robert T. Huebner  
IBM  
D/314-6, Bldg. 6-M-00  
Box 6  
Endicott, N.Y. 13760

Monte R. Hall  
1025B Montgomery Ct.  
Blacksburg, va. 24060

Kurt F. Heinrich  
804 Blossom Drive  
Rockville, Md. 20850

Ronald G. Hurley  
159 Engineering Science Bldg.  
Penn State Univ.  
University Park, Pa. 16802

George Hallerman  
Inland Steel Research Labs.  
East Chicago, In. 46312

Peter J. Heinzer  
2927 Jeanne Drive  
Parma, Oh. 44134

Thomas B. Hurshman  
IBM-OPD  
Lexington, Ky. 40505

Barry L. Hammond  
4002 Winfield Ct.  
Bowie, Md. 20715

C. G. Henderson  
1912 Arlene Drive  
Wilmington, De. 19804

Fred M. Hurwich  
Box 282  
Montrose, Ca. 91020

Bryce I. Hanna  
ARL  
9545 Wentworth  
Sunland, Ca. 91040

Paul I. Henderson  
J & L Steel Research Lab.  
900 Agnew Road  
Pittsburgh, Pa. 15230

Gudrun A. Hutchins  
Barber Pond Road  
Pownall, Vt. 05261

John C. Hannsen  
5909 Harford Ave.  
Baltimore, Md. 21207

Robert J. Henry  
1539 Lois Lane  
Bethlehem, Pa. 18018

J. D. Hutchison  
IBM  
29M/021, Box 1900  
Boulder, Co. 80302

Bruce N. Harley  
CPS Inc.  
722 E. Evelyn Ave.  
Sunnyvale, Ca. 94086

Tom Henson  
RR #2,  
Westwood Estates  
Clinton, Tn: 37716

Richard M Ingersoll  
56 Jason Ave.  
Watertown, Ct. 06795

Morton Harloe  
Perkin-Elmer Corp.  
Ultek Div.  
2205 Curtiss St.  
Downers Grove, Il. 60515

Wayne D. Hepfer  
6411 Columbine Drive  
Indianapolis, In. 46224

F. Duane Ingram  
1110 Cottonwood  
Iowa City, Ia. 52240

H. F. Harnsberger  
Chevron Research Co.  
Richmond, Ca. 94802

Jay I. Herman  
Box 279  
MIT Branch  
Cambridge, Ma. 02139

Jose A. Isasi  
Westinghouse Electric Corp.  
Box 9175  
Philadelphia, Pa. 19113

David J. Harrigan  
RD #1, Hillcrest Drive  
Towanda, Pa. 18848

James R. Hinthorne  
Hasler Research Center  
95 La Patera Lane  
Goleta, Ca. 93017

Tsugio Ito  
477 Riverside Ave.  
Medford, Ma 02155

Melvin R. Jackson  
21 Kushaqua  
RD #2  
Hewitt, N.J. 07421

Bruce Katayama  
2125 Hudson  
Richland, Wa. 99352

Curtis Knudson  
6511 Undestad St.  
Eden Prairie, Mn. 55343

Marie Jefferys  
Research & Tech. Div.  
Chromalloy American Corp.  
Blaisdell Road  
Orangeburg, N.Y. 10962

Klaus Keil  
Dept. of Geology  
Univ. of New Mexico  
Albuquerque, N.M. 87106

Lawrence Kobren  
5707 Fieldview Ct.  
Baltimore, Md. 21207

William J. Jeitner  
7 Sunset Drive  
Cherry Hill, N.J. 08034

Owen Keller  
1323 Marengo Ave.  
Forest Park, Il. 60130

Roger W. Koch  
5613 So. Trinthammer Ave.  
Cudahy, Wi. 53110

C. E. Johnson  
Argonne National Lab.  
9700 S. Cass Ave.  
Argonne, Il. 60439

Edward G. Kelso  
2509 Libson Ave.  
Alexandria, Va. 22306

Richard T. Kohler  
1381 Paddock Way  
Cherry Hill, N.J. 08034

James W. Johnson  
1353 Carolyn Drive  
Atlanta, Ga. 30329

Paul A. Kennelly  
ETEC Corp.  
3392 Investment Blvd.  
Hayward, Ca. 94545

Arnold Kolb  
1010 Willard St.  
Midland, Mi. 48648

Richard Jones  
3712 Kimberly Land  
Fort Worth, Tx. 76133

P. J. Killingworth  
Kent Cambridge  
8020 Austin Ave.  
Morton Grove, Il. 60053

N. G. Koopman  
IBM East Fishkill  
B 300-84, D877  
Hopewell Junction, N.Y. 12533

Robert Jones  
1602 N. Oak Drive  
Topanga, Ca. 90290

Chong K. Kim  
6 Fawn Drive  
Millington, N.J. 07946

Edward J. Korda  
RD #3, Hornby Road  
Corning, N.Y. 14830

William K. Jones  
A-4 Westgate  
Cambridge, Ma. 02139

Stephen L. Kimzey  
NASA  
Manned Spacecraft Center  
Houston, Tx. 77058

Marvin J. Kornblau  
GT&E  
208-20 Willets Pt. Blvd.  
Bayside, N.Y. 11360

Donald Jordan  
Cameca Instruments, Inc.  
101 Executive Blvd.  
Elmsford, N.Y. 10523

Thomas D. Kirkendell  
Box 115  
Clarksburg, Md. 20734

Donald J. Kovach  
Energy Controls Div.  
Bendix Corp.  
717 Bendix Drive  
South Bend, In. 46620

Gary Judd  
Materials Dept.  
Rensselaer Polytechnic Inst.  
Troy, N.Y. 12181

Albert S. Klainer  
Ohio State Univ.  
College of Medicine  
Columbus, Oh. 43210

William R. Kovats  
1484 - 13th St.  
Wyandotte, Mi. 48192

Charles M. Judson  
562 East Mendocino St.  
Altadena, Ca. 91001

August S. Klein  
931 Terminal Way  
San Carlos, Ca. 94070

Rose Kozak  
Gould Labs.  
540 E. 105th St.  
Cleveland, Oh. 44103

Thomas G. Jurchich  
4723 W. Braddock Road  
Apt. 200  
Alexandria, Va. 22311

Cornelis Klein, Jr.  
Dept of Geological Sciences  
Harvard Univ.  
20 Oxford St.  
Cambridge, Ma. 02138

Jerome B. Krause  
Colorado School of Mines  
Research Institute  
Box 112  
Golden, Co. 80401

W. T. Kane  
Research & Development Labs.  
Corning Glass Works  
Corning, N.Y. 14830

Jared C. Kniffen  
Univ. of Florida  
College of Medicine  
Gainesville, Fl. 32601

Frank W. Kunz  
Scientific Research Staff  
Ford Motor Co.  
Box 2053  
Dearborn, Mi. 48121

Thomas Kartelias, Jr.  
18 MacArthur Drive  
Edison, N.J. 08817

Richard N. Kniseley  
Ames Lab.  
Iowa State Univ.  
Ames, Ia. 50010

John D. Kuptsis  
Overhill Road, RD #2  
Mahopac, N.Y. 10541

Miriam Kastner  
Univ. of Chicago  
Dept. of Geophysical Sciences  
5734 Ellis Ave.  
Chicago, Il. 60637

Charles R. Knowles  
Bureau of Mining & Geology  
Univ. of Idaho  
Moscow, Id. 83843

David F. Kyser  
1258 Pampas Drive  
San Jose, Ca. 95120

Francis Laabs  
RR #3

Francis Laabs  
RR #3  
Ames, Iowa 50010

Robert Lewis  
Cameca Instruments, Inc.  
101 Executive Blvd.  
Elmsford, N.Y. 10523

William M. McMakin  
Box 1414  
Charlotte, N.C. 28201

Carl W. Laakso  
4080 N.W. 190th Ave.  
Portland, Or. 97229

John Leys  
3-M Center St.  
St. Paul, Mn. 55101

William R. McMillan  
3407 Bradford Road  
Cleveland Heights, Oh. 44118

Tracy Lamanec  
Box 292, Crawford Road, RD 3  
Schenectady, N.Y. 12306

Eric Lifshin  
General Electric Research &  
Development Center  
Schenectady, N.Y. 12300

H. R. MacQueen  
346 Avenida Nogales  
San Jose, Ca. 95123

F. Parks Landis  
2177 Story Ave.  
Schenectady, N.Y. 12309

Wen-Nan Lin  
3730 McClintock Ave.  
Apt. 433  
Los Angeles, Ca. 90007

Victor G. Macres  
2952 Sherwood Ct.  
San Carlos, Ca. 94070

D. K. Landstrom  
698 S. Fifth St.  
German Village  
Columbus, Oh. 43206

Lloyd H. London, SPINE 6070  
Union Carbide Corp.  
Tarrytown Technical Center  
Box 65  
Tarrytown, N.Y. 10591

William Maguire  
Perkin-Elmer Corp.  
131 Danbury Road, MS #380  
Norwalk, Ct. 06852

Arthur M. Langer  
Environmental Sciences Lab.  
Mt. Sinai School of Medicine  
100th St. & Fifth Ave.  
New York, N.Y. 10029

Paul Lublin,  
GT&E Labs.  
208-20 Willets Point Blvd.  
Bayside, N.Y. 11360

James S. Makosey  
98 Locust St.  
Irwin, Pa. 15642

T. E. Lannin  
General Electric Co.  
Vallecitos Nuclear Center  
Vallecitos Road  
Pleasanton, Ca. 94566

Paul K. Lund  
Rogers Memorial Hospital  
Rogers, Ar. 72756

Victor J. Malasauskas  
6806 S. Bell  
Chicago, Il. 60636

Elma Lanterman  
Research Center  
Borg-Warner Corp.  
Des Plaines, Il. 60018

R. Lunn  
Nuclear Diodes  
Box 135  
Prairie View, Il. 60069

E. S. Malizie  
478 - 79th St.  
Niagara Falls, N.Y. 14304

Richard R. Larson  
7310 - 24th Ave.  
Hyattsville, Md. 20783

Charles E. Lyman  
Rm. 13-4006  
Mass. Inst. of Tech.  
Cambridge, Ma. 02139

Genvant Maniar  
Carpenter Steel Co.  
Reading, Pa. 19603

Wayne A. Lasch  
2913 Huntington Road  
Snaker Heights, Oh. 44120

Harvey W. Lyon  
American Dental Association  
211 E. Chicago Ave.  
Chicago, Il. 60611

Lolly Marie Marchant  
202 E. Hinckley Ave.  
Ridley Park, Pa. 19078

Joseph Lebedzik  
Materials Research Lab.  
University Park, Pa. 16802

James L. Mc Call  
505 King Ave.  
Columbus, Oh. 43201

Hans C. Marciniak  
3923 West 110th St.  
Englewood, Ca. 90303

John R. LeBlanc  
Brockway Glass Co.  
R & D Bldg.  
Brockway, Pa. 15824

Gene E. McCorkle  
4309 Ponderosa, N.E.  
Albuquerque, N.M. 87110

Vincent C. Marcotte  
Kuchler Drive, RD #1  
La Grangeville, N.Y. 12540

A. J. Leeper  
Nuclear Chicago  
Des Plaines, Il. 60015

Michael J. McGuire  
Route 1, Box 58  
Warrenville, Il. 60555

William S. Margolis  
5712 Winifred Drive  
Fort Worth, Tx. 76133

John W. Lenke  
American Dental Ass'n.  
Research Institute  
211 E. Chicago Ave.  
Chicago, Il. 60611

T. D. Mc Kinley  
E. I. du Pont de Nemours & Co.  
Pigments Dept.  
Experimental Station  
Wilmington, De. 19898

Paul W. Martin  
281 Andover St.  
Danvers, Ma. 01923

Charles W. Lewis  
Dept of Pathology  
Baylor College of Medicine  
Houston, Tx. 77025

Patrick J. McMahon  
Film-Vac Inc.  
Englewood, N.Y. 07631

Richard T. Martin  
5692 Berkeley Road  
Goleta, Ca. 93071

L. L. Marton  
Museum of History & Tech.  
Room 5025  
Smithsonian Institution  
Washington, D. C. 20560

Helen Mateer  
216 W. Fairview  
Oak Ridge, Tn. 37830

Richard K. Matta  
267 Ridge Road  
RD #4  
Irwin, Pa. 15642

H. G. Matthews  
Canberra Insustries  
45 Gracey Ave.  
Meriden, Ct. 06450

Gregory S. Maurer  
6230 Fifth Ave.  
Pittsburgh, Pa. 15232

James D. Meiggs  
11512  
Albuquerque, N.M. 87112

Robert G. Meisenheimer  
2093 Essenay Ave.  
Walnut Creek, Ca. 94596

G. F. Melde  
6051 Prince Drive  
San Jose, Ca. 95129

Robert W. Merchant  
8 Melody Lane  
Schenectady, N.Y. 12309

Wolfgang J. Mergner  
Dept of Pathology  
School of Medicine  
31 So. Greene St.  
Baltimore, Md. 21201

Arthur B. Merkle  
467 Corby Dr.  
Baton Rouge, La. 70810

Harvey B. Merrill, Jr.  
Scientific Instruments & Sales Co.  
Box 11628  
Atlanta, Ga. 30305

Alexander S. Michaelson  
Tech. Research Int'l. Corp.  
5057 N. Tripp Ave.  
Chicago, Il. 60630

John R. Mihalisin  
545 Mountain Ave.  
North Caldwell, N.J. 07006

Alex S. Miller  
Box 835  
Alliance, Oh. 44601

Emmett L. Miller  
5301 Bolsa Ave.  
Huntington Beach, Ca. 92647

John L. Miller, Jr.  
133 Nebraska Ave.  
Oak Ridge, Tn. 37830

N. Carlile Miller  
3211 Chadbourne Road  
Shaker Heights, Oh. 44120

H. Edward Mishmash  
3M Co.  
3M Center  
St. Paul, Mn. 55101

Arthur R. Mlodozieniec  
Advanced Tech.  
Hoffman LaRoche, Inc.  
Nutley, N.J. 07110

Sheldon H. Moll  
Advanced Metals Research Corp.  
149 Middlesex Turnpike  
Burlington, Ma. 01803

William G. Morris  
GE Research & Development Center  
Box 8  
Schenectady, N.Y. 12301

Roger A. Morton  
Bausch & Lomb  
820 Linden Ave.  
Rochester, N.Y. 14625

John E. Mulhern, Jr.  
Dept. of Physics  
Univ. of New Hampshire  
DeMeritt Hall  
Durham, N.H. 03824

Ernest H. Muller  
570 N. Kenmore, Apt. 401  
Los Angeles, Ca. 90004

Norman A. Mulvenon  
Ortec, Inc  
799 Roosevelt Road  
Glen Ellyn, Il. 60137

Lee Munz  
Ortec, Inc.  
Box 485  
Oak Ridge, Tn. 37830

Anthony Murawski  
20513 W. Outer Drive  
Dearborn, Mi. 48124

A. P. Murphy  
Procter & Gamble Co.  
Miami Valley Labs.  
Box 39175  
Cincinnati, Oh. 45239

Judith A. Murphy  
Electron Microscopy Center  
Southern Illinois Univ.  
Carbondale, Il. 62901

Thomas E. Murphy  
Route #4, Box 259  
Williamsburg, Va. 23185

Karl E. Muszar, Jr.  
7820 Scarborough Blvd, E. Drive  
Indianapolis, In. 46256

Margaret Ryan Myers  
IIT Research Institute  
19 West 35th St.  
Chicago, Il. 60657

Robert L. Myklebust  
Route #1  
Frederick, Md. 21701

David J. Nagel  
Code 7685, Naval Research Lab.  
X-Ray Optics Branch  
Washington, D. C. 20390

Samuel K. Nash  
400 S. Camac St.  
Philadelphia, Pa. 19147

John Francis Natale, Jr.  
Chromalloy American Corp.  
Research & Tech. Div.  
Orangeburg, N.Y. 10962

Ontario Nestor  
6838 Mohawk Lane  
Indianapolis, In. 46260

Hermann Neuhaus  
280 Waverly St, #6  
Menlo Park, Ca. 94025

Livingston A. Newberg  
21 W. 518 Thorndale  
Medinah, Il. 60157

Herbert A. Newborn  
MIT  
326 Memorial Drive, Room 534  
Cambridge, Ma. 02139

Thomas J. Nichol  
6-4 Nott Drive  
Troy, N.Y. 12180

J. B. Nicholson  
ARL  
9545 Wentworth St.  
Sunland, Ca. 92040

Robert F. Nickerson  
Lawrence Livermore Lab.  
Box 648  
Livermore, Ca. 94550

James A. Nicolino  
BRC-Instruments  
Biodynamics Research Corp.  
6010 Executive Blvd.  
Rockville, Md. 20852



Henry Nikkel  
28 Neff Drive  
Canfield, Oh. 44406

J. R. Norris  
ARL.  
9545 Wentworth  
Sunland, Ca. 91040

L. R. Norville  
Scientific Instruments Dept.  
Perkin-Elmer Corp.  
Box 10920  
Palo Alto, Ca. 93403

Robert L. Novak  
229 Parkside Ave.  
Pittsburgh, Pa. 15228

Charles R. Obermeyer  
The Smithsonian Institution  
Tenth & Constitution Ave.  
MNH E-425  
Washington, D. C. 20560

Dennis O'Boyle  
Metallurgy Div.  
Argonne National Lab.  
Argonne, Il. 60439

Robert E. Ogilvie  
Metallurgy Dept.  
MIT  
Room 13-4009  
Cambridge, Ma. 02139

John R. Ogren  
4782 Amerwood Ave.  
La Palma, Ca. 90620

Ray H. Olsen  
113 S.W. 207th St.  
Seattle, Wa. 98166

(Carl) Marcus Olson  
RD #2, Box 378  
Hockessin, De. 19707

Harlen E. Olson  
Lawrence Livermore Lab.  
Box 808  
Livermore, Ca. 94550

Poen Sing Ong  
M. D. Anderson Hospital  
Texas Medical Center  
Houston, Tx. 77025

Joseph Ordonez  
41 Hagen Drive  
Poughkeepsie, N.Y. 12603

John A. O'Rourke  
2557 - 45th St.  
Los Alamos, N.M. 87544

Bernard Ostrofsky  
670 N. Tippecanoe St.  
Gary, In. 46403

Thomas R. Padden  
Westinghouse  
Advanced Reactors Div.  
Box 158  
Madison, Pa. 15663

George N. Panagis  
National Steel Corp.  
Weirton, W.V. 26062

Barbara J. Panessa  
4 Washington Square Village  
New York, N.Y. 10012

Donald L. Parker  
9705 Jackie Lane  
St. Louis, Mo. 63123

Robert R. Parmerter  
Eastman Kodak  
Industrial Lab., B-34  
Rochester, N.Y. 14650

William Parrish  
Dept. K05, IBM Research Lab.  
Monterey & Cottle Roads  
San Jose, Ca. 95114

John M. Parsons  
PPG Industries Inc.  
Glass Research Center  
Box 11472  
Pittsburgh, Pa. 15238

Bisweswar Patnaik  
#5 Wenliss Terrace  
Wappingers Falls, N.Y. 12590

William Paxton  
IAC  
13558 Cedar  
Cleveland, Oh. 44118

Irene D. Payne  
440 River Road  
Chatham, N.J. 07928

John E. Pearson  
4075 - 52nd St. N.  
St. Petersburg, Fl. 33709

Edward Peters  
A. D. Little  
Acorn Park  
Cambridge, Ma. 02140

Paul S. Phillips, Jr.  
NCR  
Central Research Div. Office  
Dayton, Oh. 45409

Jerome J. Pickett  
5 Meadowbrook Road  
Bedford, Ma. 01730

Frances D. Pidgeon  
24510-H Clareshire Drive  
North Almsted, Oh. 44070

Howard M. Piolet  
244 Kelton St.  
Allston, Ma. 02134

Stephen D. Piner  
Canberra Industries  
45 Gracy Ave.  
Meriden, Ct. 06480

Heinz W. Pinsler  
300 Alexander St.  
Rochester, N.Y. 14607

Ronald J. Plenzler  
1700 N. Westwood  
Toledo, Oh. 43607

Larry E. Plew  
US Naval Ammo. Depot  
Code 30313, Bldg. 2044  
Crane, In. 47522

Fred W. Postma, Jr.  
105 Mowhawk Road  
Oak Ridge, Tn. 37830

John Carl Potosky  
6602 Pico Vista Road  
Pico Rivera, Ca. 90660

Harley W. Prentiss  
1658 Lowell Ave.  
Claremont, Ca. 91711

Robert F. Quirk  
28 Appleton St.  
Saugus, Ma. 01906

Dennis Radcliffe  
Dept. of Geology  
Univ. of Georgia  
Athens, Ga. 30601

J. N. Ramsey  
IBM, Dept. 286, Bldg. 300-97  
Hopewell Junction, N.Y. 12533

Gutti V. Rao  
109B Materials Research Center  
Rensselaer Polytechnic Inst.  
Troy, N.Y. 12181

T. S. Rao-Sahib  
Univ. of Southern California  
Dept. of Materials Science (VHE 602)  
Los Angeles, Ca. 90007

Stanley D. Rasberry  
A-125 Chemistry  
NBS  
Washington, D. C. 20234

H. Paul Rasmussen  
Horticulture Dept.  
Michigan State Univ.  
East Lansing, Mi. 48823

Madison William Reed, Jr.  
15514 Diana Lane  
Houston, Tx. 77058

W. J. Runkle  
6411 Carrollton Ave.  
Indianapolis, In. 46220

Herbert Schreiber, Jr.  
Bell Labs., Room 1-A-35  
Murray Hill, N.J. 07974

Theodore S. Renzema  
SUNY at Albany  
Physics Dept.  
1400 Washington Ave.  
Albany, N.Y. 12203

Robert J. Ruscica  
MAC Div. of ETEC Corp.  
3392 Investment Blvd.  
Hayward, Ca. 94545

Thomas P. Schreiber  
22918 Sunnyside  
St. Clair Shores, Mi. 48080

Wilhad Reuter  
IBM Research  
Box 218  
Yorktown, N.Y. 10598

Malcolm J. Rutherford  
Dept. of Geology  
Brown Univ.  
Providence, R.I. 02912

David Schroeder  
729 Harden Drive  
Pittsburgh, Pa. 15229

Paul H. Ribbe  
Dept. of Geology  
Virginia Polytechnic Institute  
Blacksburg, Va. 24061

William E. Rutherford  
RR #2, Box 225  
Russiaville, In. 46979

Robert Seibert  
Texline Instrument Co.  
5223 Valkeith Dr.  
Houston, Tx. 77035

Neil A. Richard  
Battelle Memorial Institute  
505 King Ave.  
Columbus, Oh. 43201

Clayton O. Ruud  
Univ. of Denver  
Denver, Co. 80210

Ursula Setz  
851 Springfield Ave., Apt. 9C  
Summit, N.J. 07901

Mary E. Richardson  
Environmental Protection Agency  
2000 So. Eads St.  
Arlington, Va. 22202

Joseph R. Ryan  
122 Windson Drive  
Irwin, Pa. 15642

J. Shaffer  
Hi-Rel Industries  
2116 Huntington Drive  
San Marino, Ca. 91108

David H. Riefenberg  
Dow Chemical Co.  
Rocky Flats Div.  
Box 880  
Golden, Co. 80401

Irving B. Sachs  
4402 Vale Circle  
Madison, Wi. 53711

John W. Shaffer  
Western Electric  
555 Union Blvd.  
Allentown, Pa. 18103

William L. Robison  
774 Canterbury Ave.  
Livermore, Ca. 94550

Arthur Saffir  
1343 Fieldfair Court  
Sunnyvale, Calif. 94087

A. M. Sheble  
Hi-Rel Industries  
2116 Huntington Drive  
San Marino, Ca. 91108

Henry J. Roden  
875 Perry Ct.  
Santa Barbara, Ca. 93105

Edward J. Saller  
708 W. St. Gertrude Place  
Santa Ana, Ca. 92707

Thomas P. Sheehy  
American Smelting & Refining Co.  
Park Ave. & Oak Tree Road  
South Plainfield, N.J. 07080

J. D. Rodgers  
Phillips Electronics  
750 S. Fulton Ave.  
Mt. Vernon, N.Y. 10550

Theodore E. Sargent, Jr.  
96 South Main St.  
Mansfield, Ma. 02048

Rex Sherwood  
1 Timber Trail  
Suffern, N.Y. 10901

Peter A. Romans  
US Bureau of Mines  
Albany, Or. 97321

Stephen Sawruk  
Mobil Oil Corp.  
Research Dept.  
Paulsboro, N.J. 08066

James M. Short  
Xerox Corp.  
Research Labs.  
Xerox Square, Room W-114  
Rochester, N.Y. 14603

Elmer A. Rosauer  
Iowa State Univ. (EM Lab.)  
120 Engineering Annex  
Ames, Io. 50010

William H. Scheub  
Attn: Research Library  
The Timken Co.  
Canton, Oh. 44706

M. A. Short  
Scientific Research Staff  
Ford Motor Co.  
Box 2053  
Dearborn, Mi. 48121

H. S. Rosenbaum  
General Electric Co.  
Vallecitos Nuclear Center  
Vallecitos Road  
Pleasanton, Ca. 94566

Manfred A. Schippert  
Advanced Metals Research Corp.  
149 Middlesex Turnpike  
Burlington, Ma. 01803

John E. Shott, Jr.  
Gulf R & D. Co.  
Box 2038  
Pittsburgh, Pa. 15230

Mark Rosenblum  
1730 Manor Place  
Dayton, Oh. 45406

Leon J. Schkolnic  
American Can Co.  
Princeton Lab.  
Box 50  
Princeton, N.J. 08540

Vivian E. Shull  
Dept. of Horticulture  
Michigan State Univ.  
East Lansing, Mi. 48823

J. T. Rozsa  
3819 Roselawn Road  
Woodmere Village  
Cleveland, Oh. 44122

Richard E. Schmunk  
814 Raymond Drive  
Idaho Falls, Id. 83401

L. A. Siegel  
American Cyanamid Co.  
1937 West Main St.  
Stamford, Ct. 06904

Sylvester F. Simchick  
1518 La Crosse Ave.  
Reading, Pa. 19607

Rene Simon  
Webb Scientific Co.  
18530 S. Miles Parkway  
Cleveland, Oh. 44128

Warren Singer  
Cameca Instruments, Inc.  
101 Executive Blvd.  
Elmsford, N.Y. 10523

Charles B. Slack  
ARL  
9545 Wentworth  
Sunland, Ca. 91040

Robert Smid  
Westinghouse-Bettis  
Box 79  
West Mifflin, Pa. 15122

James Patrick Smith  
Texas Instruments, Inc.  
Box 5936, M/S 147  
Dallas, Tx. 75222

Joseph V. Smith  
Univ. of Chicago  
Dept of Geophysical Sciences  
Chicago, Il. 60637

Robert E. Smith  
3815 Ansley Road  
Birmingham, Al. 35243

Todd N. Solberg  
924 N. Rosevere  
Dearborn, Mi. 48128

J. L. Solomon  
2342 Citation Ct.  
Reston, Va. 22070

James S. Solomon  
1031 Dellwood  
Troy, Oh. 45373

Lawrence F. Solsky  
3612 Chestnut Hill  
Midland, Mi. 48640

Donald F. Solum  
2636 - Sixth Ave. S.W.  
Rochester, Mn. 55901

Charles J. Spengler  
168 Paree Drive  
Pittsburgh, Pa. 15239

Nathan Spielberg  
Dept. of Physics  
Kent State Univ.  
Kent, Oh. 44240

Lawrence S. Staikoff  
Case Western Reserve Univ.  
10900 Euclid Ave.  
Cleveland, Oh. 44106

Norbert Stalica  
158 Whiteland Hunt Road  
Downingtown, Pa. 19335

Wayne J. Steele  
Lawrence Livermore Lab.  
Livermore, Ca. 94550

Jeffrey J. Stepek  
606 Old Leechburg Road  
Pittsburgh, Pa. 15239

Richard E. Stevens  
Ernest F. Fullam, Inc.  
Box 444  
Schenectady, N.Y. 12301

Robert P. Stevens  
A. P. Green Refractories Co.  
Mexico, Mo. 65265

J. H. Stewart, Jr.  
171 North Seneca Road  
Oak Ridge, Tn. 37830

Heribert Stindl  
Dept. of Geology  
Institute of Mineral Research  
Michigan Tech. Univ.  
Houghton, Mi. 49931

Philip A. Stine  
139-2 Airport Road  
West Lafayette, In. 47906

George R. Strabel  
5632 Norcross Road  
Columbus, Oh. 43224

Bernard M. Strauss  
Gulf R & D Co.  
P.O. Drawer 2038  
Pittsburgh, Pa. 15230

Paul A. Sullivan  
515 S. St. Andrews Pl., Apt. 1  
Los Angeles, Ca. 90020

Selby E. Summers  
Ernest F. Fullam, Inc.  
Box 444  
Schenectady, N.Y. 12301

Lloyd V. Sutfin  
5 Halsey Way  
Natick, Ma. 01760

Walter J. Sutkowski  
West Redoubt Road  
Fishkill, N.Y. 12524

George W. Swanson  
High Voltage Engineering  
South Bedford St.  
Burlington, Ma. 01803

B. Swaroop  
Kelsey-Hayes R & D Center  
2500 Green Road  
Ann Arbor, Mi. 48105

Albert E. Symonds, Jr.  
130 Vivion Drive  
Aiken, S.C. 29801

Jack Tabock  
19185 Mendota  
Detroit, Mi. 48221

Charles M. Taylor  
Box 7087  
Stanford, Ca. 94305  
Richard S. Thomas

Richard S. Thomas  
Western Regional Research Labs.  
US Dept. of Agriculture  
Berkeley, Ca. 94710

Henry R. Thresh  
11000 Cedar Ave.  
Cleveland, Oh. 44106

Kenneth R. Tiek  
RR #2  
Linton, In. 47441

Anastasious J. Tousimis  
Biodynamics Research Corp.  
6010 Executive Blvd.  
Rockville, Md. 20852

Lucien F. Trueb  
Denver Research Institute  
University Park  
Denver, Co. 80210

Thomas P. Turnbull  
939 Northumberland Drive  
Niskayana  
Schenectady, N.Y. 12309

R. G. Vadimsky  
Bell Labs.  
R & D Unit, Mountain Ave.  
Murray Hill, N.J. 07974

Joseph Vallone  
Esso Research & Engineering Co.  
Box 101  
Florham Park, N.J. 07932

Michael W. Vannier  
Orthopedic Research Lab. CHMC  
300 Longwood Ave.  
Boston, Ma. 02115

Peter F. Varadi  
10500 Rockville Pike  
Rockville, Md. 20852

Lillian A. Vargo  
Turbine Support Div. of Chromalloy  
4430 Director Drive  
San Antonio, Tx. 75219

Lawrence F. Vassamillet  
4400 Fifth Ave.  
Pittsburgh, Pa. 15213

Jack Wagman  
4504 Pamlico Drive  
Raleigh, N.C. 27609

Paul Walitsky  
Westinghouse  
Dept. 82010-5  
1 Westinghouse Plaza  
Bloomfield, N.J. 07003

Gilbert H. Walker  
Star Route Box 60  
Gloucester Point, Va. 23062

Harry Walker  
Philips Electronic Inst.  
750 S. Fulton Ave.  
Mount Vernon, N.Y. 10550

Charlie M. Wall  
3600 Duncanville Road  
Dallas, Tx. 75211  
C. J. Walsh

C. J. Walsh  
Nuclear Diodes, Inc.  
Box 135  
Prairie View, Il. 60069  
Joseph M. Walsh

Joseph M. Walsh  
6 Birch Hill Drive  
Wapping, Ct. 06087

Norman M. Walter  
The Boeing Co.  
Vertol Div., Boeing Center  
Box 16858  
Philadelphia, Pa. 19142

Ronald R. Warner  
23 Asbury St.  
Rochester, N.Y. 14620

Raymond E. F. Weaver  
8 Sterrett St.  
Pittsburgh, Pa. 15205

Stephen Hon Yin Wei  
Dept. of Pedodontics  
College of Dentistry  
Univ. of Iowa  
Iowa City, Ia. 52240

Paul W. Weiblen  
Dept. of Geology  
Univ. of Minnesota  
Minneapolis, Mn. 55455

William W. Welbon  
1571 Alexander Road  
Clearwater, Fl. 33516

Oliver C. Wells  
1324 Leland Drive  
Yorktown Heights, N.Y. 10598

Leonard M. Welter  
Coates & Welter Inst. Corp.  
Subsidiary of American Optical Corp.  
777 N. Pastoria Ave.  
Sunnyvale, Ca. 94086

Jon E. Wergedal  
Seattle VA Hospital  
4435 Beacon Ave.  
Seattle, Wa. 98108

Thomas H. West, Jr.  
Gulf General Atomic  
Box 608  
San Diego, Ca. 92122

Edwin J. Westerman  
327 Conway Drive  
Danville, Ca. 94526

Norman E. Weston  
Engineering Materials Labs.  
DuPont Experimental Station  
Wilmington, De. 19898

Gerald W. Whelan  
Armco Steel Corp.  
Meddletown, Oh. 45042

David C. Wherry  
211 South Cherry St.  
Denver, Co. 80222

Eugene W. White  
1119 Houserville Road  
State College, Pa. 16801

Robert R. Whitlock  
7405 - 18th Ave. #205  
Hyattsville, Md. 20783

Marion R. Wiemann  
Box 386  
Chesterton, In. 46304

J. P. Williams  
Corning Glass Works  
R & D Center  
Corning, N.Y. 14830

Timothy Williams  
Chromalloy American Corp.  
R & D Div.  
Orangeburg, N.Y. 10962

Donald E. Wilson  
106 Rocky Road  
Shelton, Ct. 06484

Arlo L. Wingirt  
5212 S.W. Charleston  
Seattle, Wa. 98116

Nelson H. Winquist  
5344 Parkline Drive  
Columbus, Oh. 53227

Walter N. Wise  
2776 River Road  
Hamilton, Oh. 45015

David B. Wittry  
Univ. of Southern California  
Materials Science Dept.  
University Park  
Los Angeles, Ca. 90007

Edward D. Wolf  
18627 Kinzie St.  
Northridge, Ca. 91324

Richard C. Wolf  
883 Lilac Lane  
Los Altos, Ca. 94022

George J. Wolfe  
Box 102  
Norvelt, Pa. 15674

David R. Wonsidler  
Bell Labs.  
555 Union Blvd.  
Allentown, Pa. 18103

W. G. Wood  
Qanta/Metrix Corp.  
120 Industrial Way  
San Carlos, Ca. 94070

John B. Woodhouse  
Materials Research Lab.  
Univ. of Illinois  
Urbana, Il. 61801

Harvey Yakawitz  
NBS  
Gaithersburg, Md. 20706

Nelson C. Yew  
ETEC Corp.  
3392 Investment Blvd.  
Hayward, Ca. 94545

G. Robert Zechman, Jr.  
Dept. of Geophysical Sciences  
Univ. of Chicago 331  
5734 S. Ellis Ave.  
Chicago, Il. 60637

William H. Zeigler  
Penn State Univ.  
University Park, Pa. 16803

Louis Zeitz  
SKI  
410 E. 68th St.  
New York, N.Y. 10021

Carolyn Zelek  
Scientific Research Staff  
Ford Motor Co, Rm 1029, Dept 9023  
2000 Rotunda Drive  
Dearborn, Mi. 48121

William F. Zelezny  
78 Isleta  
Los Alamos, N.M. 87544

Mary Anne Zemitis  
126 Yorkshire Blvd.  
Dearborn Heights, Mi. 48127

Donald Zenobia  
Precision Metallurgical Corp.  
1360 Main St.  
Millis, Ma. 02045

Thomas O. Ziebold  
9701 Fields Road, Apt. 600  
Gaithersburg, Md, 20760

P. William Zingaro  
22 Clubway  
Hartsdale, N.Y. 10530

#### CANADA

James D. Brown  
95 Cumberland Acres  
London, Ontario, Canada

Laurence C. Brown  
Dept. of Metallurgy  
Univ. of British Columbia  
Vancouver 8, B.C., Canada

Michel Pierre Cescas  
Faculty of Agriculture  
Laval Univ.  
Quebec 10, Province of Quebec  
Canada

Eric J. Chatfield  
Dept. of Physics  
Ontario Research Foundation  
Sheridan Park, Ontario, Canada

L. C. Coleman  
Univ. of Saskatchewan  
Saskatoon, Saskatchewan  
Canada

Arthur Cox  
Box 460  
Hamilton, Ontario,  
Canada

Ramon Coy-Yll  
Ecole Polytechnique  
2500 Marie Guyard Avenue  
Montreal, Quebec, Canada

Mark Firth  
Dept. of Metallurgical Engineering  
McGill Univ.  
Montreal, Quebec, Canada

Elvira Gasparrini  
Dept. of Geology  
Univ. of Toronto  
Toronto, 5  
Ontario, Canada

E. D. Ghent  
Geology Dept.  
Univ. of Calgary  
Calgary 44, Albert, Canada

Warren E. Gibbs  
International Nickel Co.  
of Canada  
Sheridan Park, Mississauga  
Ontario, Canada

Donald C. Harris  
1435 Morisset Drive  
Ottawa, Ontario, Canada

Sidney I. Ingrey  
9, Birchdale Ave.  
Ottawa 14, Ontario  
Canada K2B 5Z5

Claude P. Lechene  
195 Bryand  
Sherbrooke, Quebec, Canada

Wallace H. Mac Lean  
334 Regent St.  
Mc Gill Univ.  
Dept. of Geology  
Montreal, Quebec, Canada

Charles E. Makepeace  
2314 Elmira Drive  
Ottawa, Ontario, Canada

Rodney H. Packwood  
1284 Greyrock Crescent  
Ottawa, Ontario  
Canada K1S 3H3

Lubomir Parobek  
275 Windemere Road, Apt. H  
London 72, Ontario, Canada

A. G. Plant  
601 Booth St.  
Ottawa, Ontario, Canada

John Rucklidge  
Dept. of Geology  
Univ. of Toronto  
Toronto, Canada

Anton Sawatzky  
5 Tupper  
Pinawa, Manitoba, Canada

D. G. W. Smith  
Dept. of Geology  
Univ. of Alberta  
Edmonton, Alberta, Canada

Gunter Springer  
Box 900  
Thornhill, Ontario, Canada

R. J. Traill  
Geological Survey of Canada  
601 Booth St.  
Ottawa, Canada

#### FOREIGN

Caterina Ricci Bitti  
Centro Sperimentale Metallurgico  
Castel Romano  
Roma, Italy 00129

Ahron Batt  
Israel Institute of Metals  
Technion City  
Haifa, Israel

Flavio Borile  
Via Resegone, 10  
Carnate  
Milano 20040  
Italy

Raymond Castaing  
Univ. of Paris  
Faculte Des Sciences  
Orsay, France

Amram Eshel  
Dept. of Botany  
Tel-Aviv Univ.  
Tel-Aviv  
Israel

Colin Fisher  
Image Analyzing Computers Ltd.  
Melbourn, Royston, Herts  
England

Nobukatsu Fujino  
Central Research Labs.  
Sumitomo Metal Industries, 3  
1-Chome Nichinagasu  
Amagasaki, Japan

Pierre Galle  
37 Avenue Arouet  
92 - Antony  
France

Bidyut K. Ganguly  
C P Gavea 38008  
Rio de Janeiro  
G B Brazil

Petrus Jongenburger  
Lab. voor Metaalkunde  
T. H. Delft  
Rottendamseweg 137  
Delft, The Netherlands

Andre Lanchli  
Fachbereich Biologie (10)  
der Technischen Hochschule Darmstadt  
D-6100 Darmstadt,  
Germany

Cesar Mario Libanati  
Alvear 800  
Martinez, Argentina

Henry J. Noebels  
Beckman Intern'l Tech. Center  
32 Avenue Frontenex  
Geneva, Switzerland

Werner Nowacki  
Sahlistrasse 6  
3000 Bern, Switzerland

Pierre Jean-Louis Pinard  
26, Chemin de Chalin  
69 - Eucully, France

Guy Remond  
BRGM Laboratoire de Microsonde  
BP 818 Orleans, France

T. Shiraiwa  
Central Research Labs.  
Sumitomo Metal Inds.  
3, 1-Chome Nichinagasu  
Amagasaki, Japan

Arnold P. von Rosenstiel  
Adriaan Pauwstraat 34  
Den Haag, Holland

Wisichard T. Weiser  
c/o Bundesanstalt fuer  
Bodenforschung  
Alfred-Bentz-Haus  
Hannover, Germany D-3000

# THE QUANTITATIVE MICROANALYSIS OF BORON IN TUNGSTEN-BORON SYSTEMS

I. B. BOROVSKII

Baikov Institute, Academy of Science, Moscow, USSR

The quantitative microprobe analysis of light elements remains one of the most difficult analytical problems to date. In particular, great difficulties arise in attempting to determine the content of light elements in systems containing elements with atomic numbers  $Z \approx 40$ . This situation exists due to the lack of accurate values of mass self-absorption coefficients  $\mu_{mA}^A$  for the  $K\alpha$  radiation of element "A" being analyzed as well as the lack of accurate values of mass absorption coefficients  $\mu_{mA}^A$  for  $K\alpha$  radiation of light elements in matrix "a". If one introduces the corrections into the measured intensity ratios of element "A" in the specimen and standard,  $I_A^*/I_A$ , with the use of any set of the conventional correction formulas [1], the calculated weight concentration  $C_A$  of element "A" will depend on the adopted numerical values of  $\mu_{mA}^A$  and  $\mu_{ma}^A$ . The meaning becomes quite obvious if we list, for example, the values of  $\mu_{mA}^A$  and  $\mu_{ma}^A$  for the light elements given in table #1 [2,3,4,5]. The evaluation of all correction formulas indicate that they are not suitable for large overvoltage values  $V = E_o/E_q$ , the case which happens to exist in the analysis for light elements. As a consequence, a search for new methods of quantitative analysis is still of great importance.

In our report we shall consider a new method based on the extrapolation of the value  $\underline{P} = I_A^*/I_A \cdot i^*/i_A$  to the critical excitation potential of X-ray characteristic spectra. In this expression  $I_A^*$  and  $I_A$  are the intensities of  $K\alpha$ ,  $L\alpha$ , etc. lines of element "A"

NOTE: This abstract was prepared from Dr. Borovskii's hand written notes during the conference so that it could be distributed to the attendees. Any error in content, technical or otherwise, is the sole responsibility of the printing committee.

measured in the analyzed sample and pure element standard respectively. The terms  $i_A^*$  and  $i_A$  are the "absorbed electrons" in the analyzed sample and pure element standard respectively. The authors have checked their method for 165 cases where the analyses were for middle and large atomic number elements. The method allows one to determine the weight concentration of any element in an analyzed sample on the basis of the measured values of  $\underline{P}$  at various  $E_0$  and does not require a knowledge of the full composition of the specimen, i.e.;  $\left| \lim_{E_0 \rightarrow E_c} \underline{P} \right| = C_A$ . The feasibility of this new method for the quantitative analysis of light elements has so far been insufficiently investigated. In their published paper the authors of this new method do not offer a simple and accurate way for the extrapolation of the  $\underline{P} = f(E_0)$  curves to the critical excitation voltage. In our investigation presented here we offer a simple solution which we employed for our latest task.

It is well known from theoretical and experimental research that the curves  $I = f(E_0)$  have a maximum at the large values of the overvoltage  $V_0$ . The position of this maximum depends on  $Z$  and  $E_q$ . In our work [7] we have obtained an analytical expression for  $\bar{U}$  which determines the position of  $I_{\max}$ . It follows from this work that in the analyses of the elements of middle and high atomic numbers, using the K, L or M lines for which  $\bar{U} \sim 3-5$ , the maximum of the  $I = f(E_0)$  curve is not attained, then the dependence of  $\underline{P}$  on  $E_0$  is approximately linear. However, for the light elements optimum values of  $\bar{U}$  range from 10 to 200 and the maximum of the curves are attainable.

It follows from this reasoning, in order to make an unambiguous extrapolation to the excitation potential  $E_q$ , one must change the scale of the Y axis. If we plot the value of  $\text{Log } \underline{P}$  versus  $E_0$ , then, the curves with a maximum can be approximated by two intersecting straight lines. The inflection points correspond to the maximum values of  $I$  at the optimal value of  $\bar{U}$ . This conclusion has been checked for the case of analysis of binary alloys containing boron and tungsten. This system is especially difficult to analyze with conventional microprobe analysis using conventional formulas for the correction.



Our first task was to determine an optimal value of  $\bar{U}$  for boron which has been analyzed with the use of its  $K_{\alpha}$  band as well as for boron in the single-phase samples  $W_2B$ ,  $WB$ , and  $W_2B_5$ . The theoretical calculation as compared with the experiment gives rise to a maximum position shifted toward the higher energies (approximately 10 KV). Further, the dependence of the intensity of  $W L_{\alpha}$  and  $W M_{\alpha}$  lines in pure tungsten on the accelerating voltage has been measured within the region from 3 to 30 KV. This dependence is about linear for the  $L_{\alpha}$  line ( $\lambda = 1.48 \text{ \AA}$ ) and has a maximum at 20 KV for the  $M_{\alpha}$  line ( $\lambda = 6.92 \text{ \AA}$ ). A slight disagreement between the theory and experiment for the case of one-phase specimens can be explained by the lack of accurate values of the measured absorption coefficients for boron and by the fact that in [7] the effect of take-off angle has not been taken into account.

The intensity measurements of  $B K_{\alpha}$  bands on one-phase borides have provided the choice of the voltage region which is favorable for the quantitative analysis of boron. This region includes an optimal value of  $\bar{U}$  and a maximum value of intensity; it extends from 2 to 15 KV.

The content of tungsten for the three borides mentioned above has been determined with the use of  $L_{\alpha}$  and  $M_{\alpha}$  lines at the accelerating voltages from 5 to 30 KV taken in 8 steps. Similar weight concentrations of tungsten in these samples have been obtained. Figure 3-4 shows the results of boron determination in the sample at 2 to 20 KV also taken in 8 steps. For the element boron,  $\log P$  versus  $E_0$  is plotted on figure #4. The resulting analyses are given in table #2, which is the summary of the quantitative determination of the boron and tungsten weight concentrations. It is seen from this table that although the tungsten-boron system is extremely difficult to analyze, we have obtained rather good results using the extrapolation method to determine the content of a light element in a heavy matrix. The relative error in boron determination is in the region of  $\sim 1.5\%$  to  $5\%$ . The error in tungsten determination is  $\sim 0.5\%$  to  $2\%$ .

We can point out that we have found in practical analyses the existence of the system  $WB_6$ , however, we did not find the system  $WB_{12}$  in our analyses [8,9,10].

## REFERENCES

1. For example, see P. M. Martin, D. M. Poole, Metals Materials and Metallurgical Reviews., V.5, N3, 19-46, 1971.
2. R. D. Devtey: "Progress in Nuclear Energy". Ser. 9, Anal. Chem., vol. 9, 1969. Hand book of X-ray and microprobe data.
3. K. F. J. Heinrich, X-ray Optics and X-ray Microanalysis, Paris, 1961.
4. Henke, Advances in X-ray Analysis, 13, 1970.
5. D. Vollath, Microchimica Acta Suppl. III, II-18, 1968.
6. T. A. Kuprijnova, S. A. Dizman, Zawodskoja Laboratorija, 36, No 11, 1970. Apparatura Methody Rontgenovskogo Analyza, V. IX, p. 171, 1971.
7. I. B. Borovskii and W. I. Rydник, Quantitative Electron Probe Microanalysis, NBS, N-298.
8. B. Post, F. Glaser, J Chem. Phys., 20, 1050, 1952.
9. E. Rudy, F. Benesovsky, L. Toth, Z. Metal Runde, 54 N 6, 345, 1963.
10. K. T. Portnoi, K. Romashev, et al, Poroshkovaja Metallurgia, n 5, 1962.

TABLE #1

	$WL_{\alpha_1}$	$WM_{\alpha_1}$	$BK_{\alpha_1}$	$MoL_{\alpha_1}$
$\lambda(\text{\AA})$	1,48[2]	6,98[2]	67,64[2]	5,39[2]
$\mu/\rho$ B	2,75[2] 2,2[3]	203,126 [2]	3390 [4] 11087,7[2] 7324,9 [5]	103,93[2] 90,8 [3]
$\mu/\rho$ C	4,581[2] 4,1 [3]	338,255 [2]	10020,26[2] 6600 [4] 12727 [5]	173,16[2] 162,8 [3]
$\mu/\rho$ Mo	139,8[3]	1378 [2]		705,489[2] 728,0 [3]
$\mu/\rho$ W	150,8[3] 137,3[2]	6036,7[2]	49459,24[2]	3776,68[2] 3145,2 [3]

TABLE #2

Experimental values in Weight %									
	Result From Stoichiometric Relationship in Weight %		Results of chemical analysis in Weight %						
	$C_W$	$C_B$	$C_W$	$C_B$	$C_{W/L\alpha_1}$	$C_{W/M\alpha_1}$	$C_{WZp}$	$C_{BK\alpha_1}$	
$W_2B$	97,0	3,0	96,9	3,1	96,0 ( $\pm 0,5$ )	95,5 ( $\pm 0,6$ )	95,7 ( $\pm 0,6$ )	3,1 ( $\pm 0,1$ )	
$WB$	94,4	5,6	94,45	5,55	93,9 ( $\pm 0,3$ )	94,0 ( $\pm 0,5$ )	93,9 ( $\pm 0,4$ )	5,9	
$W_2B_5$	87,9	12,1	89,88	10,12	35,0 ( $\pm 0,4$ )	36,0 ( $\pm 0,4$ )	86,0 ( $\pm 0,4$ )	12,0 ( $\pm 0,2$ )	

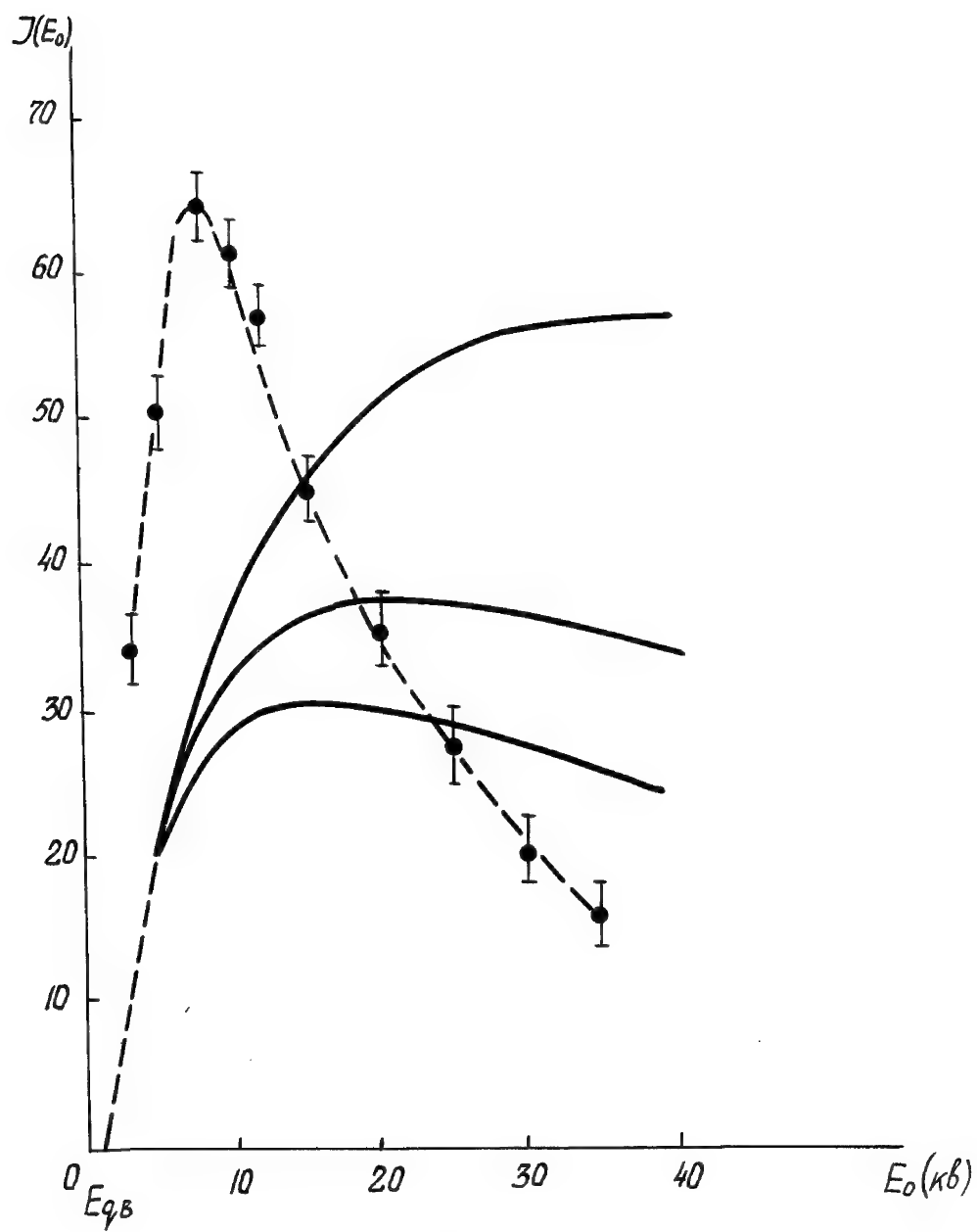


FIGURE #1

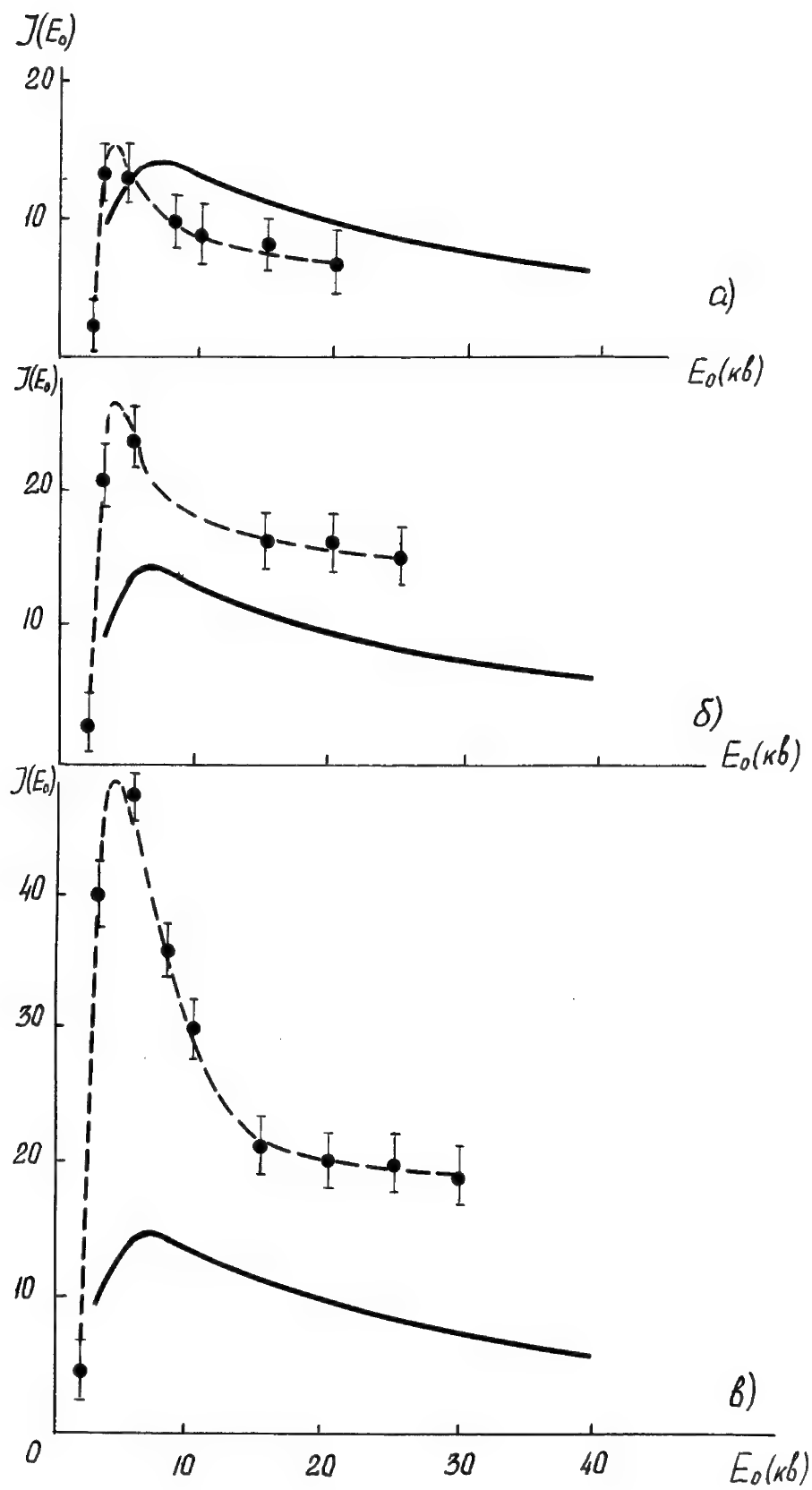


FIGURE #2

## "DOUBLE MIRROR" X-RAY ANALYZER

I. B. BOROVSKII, A. T. KOZLENKOV, W. G. BOGDANOV

Institute of Metallurgy, Academy of Science, Moscow, USSR

The "double mirror" method and the apparatus based on this method represent the improvements of the differential reflecting filter method (DRFM) which has been developed earlier [1, 2]. In the conventional DRFM some mirrors of different curvature, angle of incidence and coating material are placed in the path of an X-ray primary beam emitted by the specimen (target). The reflected beam falls into the detector slit.

A disadvantage of this method is that the mirror reflects into the detector not only the  $K\alpha$  line of the light element to be analyzed, but also part of the  $K\alpha$  line intensity of an element whose  $Z$  is greater by unity, if such element happens to be present in the specimen. It also reflects the lines of the other series as well as the continuous background radiation due to heavier elements with wavelengths shorter than the wavelength of  $K\alpha$  radiation of the sought element, but longer than the critical wavelength corresponding to the threshold of reflection of a given mirror. This is explained by the fact that for all known coatings and permissible grazing angles  $\alpha$  the reflection coefficient ( $R$ ) near the short wave threshold varies from a maximum to a minimum gradually, and the spectral region with which this change takes place, exceeds the wavelength separation between the  $K\alpha$  lines of light elements with adjacent atomic numbers.

In the apparatus with a single mirror, the ratio of the intensities of the  $K\alpha$  lines recorded by the detector for the adjacent light elements with atomic numbers  $Z$  and  $Z + 1$  is proportional to the ratio of  $R$  ( $R_Z/R_{Z+1}$ ), for the wavelengths of the  $K\alpha$  lines of these elements.

When use is made of two consecutively reflecting mirrors having the same coating and the same radius of curvature positioned at one and the same angle

NOTE: This abstract was prepared from Dr. Borovskii's handwritten notes so that it would be available for distribution to the attendees during the conference. Any error in content, technical or otherwise, is the sole responsibility of the printing committee.





to the incident beam, this ratio becomes  $(R_Z/R_{Z+1})^2$ . For all known coatings and angles of incidence the ratio  $R_Z/R_{Z+1}$  is anywhere between 10 and 30. When use is made of two identical mirrors arranged in tandem, this ratio is from 100 to 900, while with  $n$  mirrors used it will be from  $10^n$  to  $30^n$ . This implies that in analysis of an element  $Z$  by means of two or more series-arranged mirrors it is possible to cut off practically all interfering radiation of the element with atomic number  $Z + 1$  and the background radiation. The accompanying attenuation of the  $K\alpha$  line of the sought element is significant, since the  $R$  for the wavelength  $\lambda$  of the line  $R_\lambda$  is very near unity. As an example, when analyzing boron in B-C compounds or mixtures it is possible to attenuate the intensity of C  $K_\alpha$  lines by the factor of 100 - 200, whereas the intensity of B  $K_\alpha$  line decreases only by 10% - 20%. Figures 1, 2, and 3 illustrate the principle of the improved method.

Figure #1 is the block diagram of the apparatus, #2 is the plot of reflected intensity at the output versus the  $\lambda$ , #3 is one of the embodiment of the apparatus. There are two concave mirrors, 2 and 3, placed in the path of the X-ray beam excited in the specimen-target 1. Both mirrors have the same curvature and identical coating material; for example, both will be metallic. The choice of the coating material is predetermined by the wavelength region, corresponding to the light element being analyzed.

The beam of X-rays emitted in the specimen under electron bombardment passes through an opening in the wall separating the specimen chamber and mirror chamber (omitted in Fig. #1 and #3) and falls upon the first concave mirror 2. The mirror reflects the primary beam of X-rays emitted by the specimen-target through an angle  $\alpha$  which is smaller than the angle of total external reflection of X-rays in the specified wavelength region. The radiation reflected from the mirror 2 strikes the additional concave mirror 3 at the angle equal to the angle of incidence of the primary beam on the entrance mirror 2. The reflected beam is accepted by the detector. It should be borne in mind that total angle of deflection (deviation) measured from the direction of the primary beam incidence upon the first mirror 2 at the angle  $\alpha$  amounts to  $4\alpha$  after being reflected from the additional mirror 3, while after reflection from  $n$  additional mirrors the angle of deflection becomes  $2n\alpha$ . Because the angle  $\alpha$  is small, ranging from  $2 - 10^\circ$ , and the radius of the mirrors



is large, the increase in the angle of deflection from the original direction is of considerable importance, since this is what makes possible the elimination of background radiation scattered by the mirror holder and other objects.

In order to eliminate the  $K\alpha$  lines of light elements with atomic numbers smaller than that of the element being analyzed, and also to attenuate the interfering lines with a wavelength longer than that of the  $K\alpha$  line of the sought element, use may be made of an absorbing filter with films of varying thickness fabricated from nitro-cellulose or other material, placed in the path of the X-ray beam between the additional mirror and the detector.

Figure #3 shows one of the possible embodiments of an apparatus for X-ray microprobe analysis of specimens containing several elements. This apparatus has several entrance mirrors 5, 6, 7, and equal number of additional mirrors 8, 9, and 10. The entrance mirrors 5-7 are mounted one above the other in a mount 11 and set up on a carriage 12 free to move in a vertical direction. The mirrors, 5 and 8, 6 and 9, 7 and 10, make up respectively, operating pairs; that is, the mirrors in each pair have the same reflecting coating and the same curvature.

The entrance mirrors 5, 6 and 7 differ between each other in the material of the coating and the angle they make with the primary beam  $\alpha_1$ ,  $\alpha_2$ ,  $\alpha_3$ , respectively. Thus each mirror reflects X-rays within a specified wavelength region. The additional mirror, say 8 in each pair, say 5 and 8, works with the reflected beam travelling from the respective entrance mirror 5, the same angle which the concave mirror 5 makes with the primary beam of X-rays. By moving and placing the carriage 12 in a desired position, the selected mirror, say 5, is arranged in the X-ray primary beam, thereby providing the choice of a specified wavelength region. Since the entrance mirrors differ in angle of incidence, the radiation reflected from the selected first mirror 5 can only reach the corresponding stationary additional mirror 8 and then the detector.

In changing over to analysis of some other element, another mirror, say 6, is brought in line with the primary beam, so that X-rays reflected by this mirror strike the additional mirror 9, and then reach the detector.

The additional advantage of the apparatus is that the angle of incidence on each of the entrance mirrors is maintained exactly constant. The design of the new microprobe analyzer was based on the principle described above. The



apparatus is comprised of two channels with the mirror arranged in a common volume with four gas-filled proportional counters to detect the radiation reflected by the entrance and output mirrors in each channel, two titanium vacuum pumps, high-voltage supplies, amplifiers and other electronic means. The new apparatus\* is shown in figure #4. The X-ray beam is excited under the following conditions: Accelerating voltage is from 5 to 15 KV; beam current 20 - 300  $\mu$ A, 6 concave mirrors, 3 for each channel. The coating materials are Al, Cr, Au and polystyrene.

The results of preliminary experiments have shown that all advantages of the reflection filter method were the same as in the earlier designed analyzer with a single mirror (very high intensity) while the signal to background radiation has varied from 50 or more. As a result of our improved design we have experienced an increase in the limit of detectibility for the elements beryllium, boron and carbon in alloys to 0.1% to 0.05%.

#### REFERENCES

1. I. B. Borovskii, A. P. Lukirskii, Optics and Spectroscopy, 24.267, (1968).
2. I. B. Borovskii, A. I. Kozlenkov, A. E. Mirkin, W. G. Bogkanov, J. Microscopy, 8.889 (1969).

\* Reflecting Mirror Microprobe: RMM-250  $\equiv$  RM3-250 in Russian library.

Note: The figures were not available for the preparation of this abstract.

